

# University of Napoli Federico II



Doctorate in  
*STRUCTURAL, GEOTECHNICAL ENGINEERING AND  
SEISMIC RISK*

XXXIII CYCLE

## **BIO-INDUCED PARTIAL SATURATION AS A LIQUEFACTION MITIGATION TECHNIQUE**

Giuseppe Astuto

### **Supervisors**

Prof. Alessandro Flora  
Prof. Emilio Bilotta

### **PhD Coordinator**

Prof. Luciano Rosati



# SUMMARY

1 CHAPTER 1 .....	7
1.1 INTRODUCTION.....	7
1.2 GENERAL REMARKS AND CASE HISTORY .....	8
1.3 AN INTRODUCTION TO LIQUEFACTION .....	11
1.3.1 LIQUEFACTION SUSCEPTIBILITY .....	14
1.3.2 LIQUEFACTION TRIGGERING .....	24
1.4 GENERAL FRAMEWORK AND GOAL OF THE WORK .....	30
2 CHAPTER 2 .....	33
2.1 TRADITIONAL LIQUEFACTION MITIGATIONS TECHNIQUES .....	33
2.1.1 DYNAMIC AND VIBRO-COMPACTION .....	34
2.1.2 COMPACTION GROUTING.....	37
2.1.3 LOW PERMEATION GROUTING .....	40
2.1.4 SOIL MIXING .....	42
2.1.5 JET GROUTING.....	45
2.1.6 DRAINAGES SYSTEMS.....	47
3 CHAPTER 3 .....	53
3.1 INDUCED PARTIAL SATURATION AS LIQUEFACTION MITIGATION TECHNIQUE.....	53
3.1.1 PARTIALLY SATURATED SOILS MODELLING: FOUNDAMENTAL CONCEPTS .....	58
3.1.2 EQUIVALENT PORE FLUID COMPRESSIBILITY .....	59
3.2 INDUCED PARTIAL SATURATION: A MULTIDISCIPLINARY APPROACH.....	65
3.2.1 INDUCED PARTIAL SATURATION: POSSIBLE MITIGATION TECHNIQUES ....	68
3.2.1.1 <i>Drainage Recharge</i> .....	69
3.2.1.2 <i>Air Injection</i> .....	70
3.2.1.3 <i>Water Electrolysis</i> .....	71
3.2.1.4 <i>Use of Chemicals: Sodium Perborate</i> .....	72

3.3 USE OF BIOGAS .....	74
3.3.1 BIOLOGICAL FRAMEWORK .....	74
3.3.2 BACTERIAL DENITRIFICATION AS A PROCESS DRIVING IPS .....	78
4 CHAPTER 4 .....	85
4.1 BIO-CHEMICAL EXPERIMENTAL INVESTIGATION: INTRODUCTION .....	85
4.2 MICROORGANISMS ISOLATION FROM SLUDGE TREATMENT PLANT .....	85
4.3 NITRATES TO AMMONIA TESTS REDUCTION .....	88
4.4 BUBBLES NUCLEATION TESTS- FROM NITRATES TO NITROGEN GAS N <sub>2</sub> .....	90
4.5 MOLECULAR BACTERIA CHARACTERIZATION.....	93
4.6 ENVIRONMENTAL ANALYSES .....	97
5 CHAPTER 5 .....	104
5.1 GEOTECHNICAL TESTING .....	104
5.2 TESTED SOILS .....	104
5.3 DESATURATION TESTS .....	107
5.3.1 PERMEAMETER TESTS .....	108
5.3.2 TIME-DEPENDENT METABOLISM ANALYSIS .....	118
5.3.3 DESATURATION TESTS ON BACK-PRESSED SAMPLES .....	123
5.4 OPTICAL ANALYSES ON BUBBLE NUCLEATION.....	126
6 CHAPTER 6 .....	131
6.1 MONITORING TECHNIQUES .....	131
6.2 ELECTRICAL RESISTIVITY .....	131
6.2.1 SMALL SIZE PHYSICAL MODEL: ELECTRICAL RESISTIVITY MEASUREMENTS .....	133
6.3 P-WAVES VELOCITY .....	142
6.3.1 BENDER ELEMENTS TESTS AND TESTING PROGRAMME .....	143
6.3.2 EXPERIMENTAL RESULTS.....	148
6.3.2.1 <i>Time-Domain Analyses</i> .....	151
6.3.2.2 <i>Frequency-Domain Analyses- Corrected Output Signals</i> .....	155

6.3.2.3 <i>Experimental correlation between P-waves velocity and degree of saturation</i> .....	160
6.3.3 NUMERICAL MODELLING OF BENDER ELEMENTS TESTS.....	165
7 CHAPTER 7 .....	172
CONCLUSIONS AND REMARKS.....	172
8 REFERENCES.....	175
9 APPENDIX- QUARTZ SAND CYCLIC CHARACTERIZATION .....	183



# **1 CHAPTER 1**

## **1.1 INTRODUCTION**

Within the background of geotechnical engineering, enlarging attention is being dedicated to the ever increasing branch of the ground improvement, which often offers attractive and innovative solutions with respect to a wide range of engineering problems. In fact, such an approach is frequently adopted to face geotechnical issues, instead of applying more expansive and usual interventions. On the other hand, although ground improvement techniques are gaining a relevant role in the civil engineering landscape, such field still suffers a certain degree of uncertainty, especially at the design phases. This depends both on the complexity of soil behaviour, that makes some of the ground improvement solutions difficult to model, and to the commercial pressure of industry, that pushing on new solutions makes it often difficult to settle experiences and modelling results into a robust design framework. Thus, efforts to build up a solid and reliable background, play a key role to improve knowledge on new and innovative ground improvement solutions. The goal of this Thesis is to contribute to such an effort.

It is widely known that ground improvement solutions are suitable to face both static and dynamics issues ranging, for example, from retaining structures to seismic isolation of foundations. Actually, a leading issue which absorbs more and more research efforts is represented by the mitigation of liquefaction effects, on which increasing focus has been demonstrated in the last few years. This is mainly due to the heavy impact of potentially catastrophic events driven by liquefaction, as demonstrated by several circumstances all over the world: Niigata (Japan, 1964), Marina District, San Francisco (U.S.A. 1989), Kobe (Japan, 1995), Kocaeli (Turkey, 1999), Christchurch (New Zealand, 2011), Emilia Romagna (Italy, 2012) are only few examples of liquefaction phenomena occurred, leading to heavy damages in terms of both economical and human loss.

Thus, since liquefaction triggering can cause severe damages, reliable solutions are needed to solve or, at least, minimize its impact on the built environment. Therefore new, innovative, low-cost, environmentally friendly and efficient methodologies to improve shear strength and stiffness of loose sands during seismic shaking are needed. Among the copious techniques suitable to reduce liquefaction risk, more or less innovative, academic research is more and more focusing on the implementation of a desaturation technique, that has proven to be very effective to this aim (Mele et al. 2018, Mele and Flora 2019). As it will be shown in the following sections, such technique represents an attractive solution since it highly increases liquefaction resistance.

The present work aims to the development of a bio-Induced Partial Saturation (bio IPS) technique able to generate gas bubbles within the pores of the soil and, at the same time, to the development of a reliable monitoring technique. Starting from the identification and isolation of specific microorganisms able to generate gas bubbles, the work aims first at evaluating the capability of the selected microorganisms to nucleate bubbles. Then, the environmental compatibility of the metabolism's products is investigated by performing preliminary chemical and biological tests, in order to verify the applicability of the technique.

Successively, with the aim to quantify the amount of generated gas, desaturation tests are carried out for different experimental conditions, monitoring at the same time environmental parameters of interest as well. Once the nucleation process has been widely explored, and the environmental compatibility has been ensured, the experimental setup has been finally focused on possible monitoring techniques able to control and verify the degrees of saturation achieved with the IPS technology. Basically, two possible monitoring parameters have been investigated, i.e. electrical resistivity and P-waves velocity. Their sensitivity to the degree of saturation of a soil will be analysed in detail as it follows, showing that such parameters are well suited to quantify the desaturation level achieved with the bio-IPS technique and, on the other hand, that a delicate interpretation of the data must to be taken into account. It will be highlighted that a combination of the two technologies is likely the best possible monitoring solution.

## **1.2 GENERAL REMARKS AND CASE HISTORY**

In this section, a qualitative framework about soil liquefaction is reported: general remarks about the liquefaction risk are underlined and some cases history are shown.

Liquefaction represents a rapid loss or decrease of shear strength and stiffness of granular soils, as a consequence of a dynamic event, due to the release of elastic energy that propagates through the subsoil. Soils subjected to this type of failure mechanisms are usually granular materials under fully saturated conditions. When an earthquake occurs, undrained conditions can be achieved, because of either the rapidity of the seismic event or the presence of impervious boundary conditions, and the soil exhibits pore pressures build up which can decrease effective stresses, until the granular material decreases or loses completely its shear strength. In such conditions, soil behaves temporarily as a viscous fluid, losing any bearing capacity. This can result in heavy damages to structures and infrastructures, which can also present nothing but damages under a geotechnical point of view, while no significant structural damages are presented, as reported in Figure 1-1, (rocking example due to liquefaction triggering).



*Figure 1-1 Example of rocking caused by liquefaction*

In 1964 in Niigata, Japan, a violent earthquake of magnitude  $M_w = 7.6$ , with hypocentre of about 40 km depth, struck the town: more than 3000 houses were destroyed and over 11,000 damaged. Liquefaction affected large areas, with devastating effects (Figure 1-2). Settlements up to 150 cm were registered, because of the stiffness loss and redistribution hydraulic boundary conditions as well (Ishihara and Koga 1981).

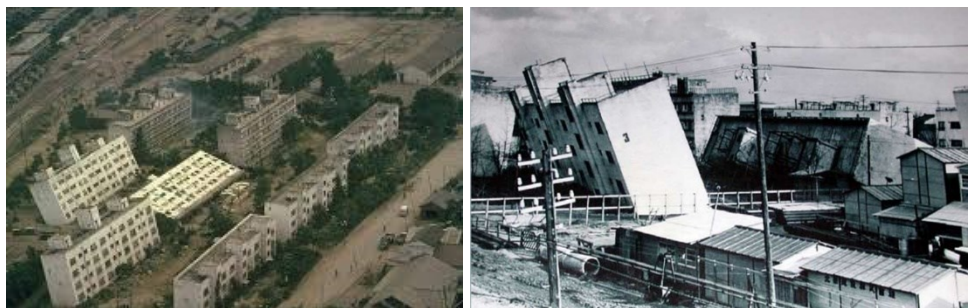


*Figure 1-2 Niigata, Japan 1964*

Again in Japan, the Kobe earthquake, 1995  $M_w=6.8$ , led to catastrophic damages in terms of human (6000 victims) and economic loss (Soga 1998). After the seismic event, several studies were carried out in order to unravel the phenomena and model, as clear as possible, the mechanical behaviour leading to liquefaction collapses (Figure 1-3).



*Figure 1-3 Kobe, Japan 1995*

Another seismic event that led to soil liquefaction occurred in Turkey, Kocaeli in the 1999 (Figure 1-4). Several studies were developed to quantify the plastic settlements caused by the *lateral spreading* (Cetin et al. 2004), a liquefaction consequence due to the loss of confinement stresses thanks to which liquefaction collapse can be induced also in non-liquefiable soils.



Figure 1-4 Kocaeli, Turkey 1999

A more recent earthquake, occurred in the 2010-2011, was the Christchurch seismic events that caused several damages because of the very superficial hypocentre of about 5 km. Figure 1-5 shows the post-seismic effect of liquefaction, in which the soil recovered strength and stiffness after the transient phase of viscous fluid. Central business district and eastern suburbs were totally destroyed by liquefaction. Almost one thousand commercial buildings were unable to be used and were later demolished (Taylor et al. 2012).



Figure 1-5 Christchurch, New Zealand 2010-2011

Moreover, in May 2012, liquefaction evidences have been recorded during the Italian earthquake in Emilia Romagna in which, for the first time in Italy, liquefaction phenomena have been clearly detected during a dynamic event. Even in this case, several damages occurred to structures and infrastructures, and changes in the hydrological regime have been recorded as well. The effects of liquefaction, followed by the 2012 earthquake in Northern Italy, have been immortalized and reported in several research works (Alessio et al. 2013; Lai et al. 2015; Lombardi and Bhattacharya 2014; Sciarra et al. 2012; Vannucchi et al. 2012).

Thus, as the brief case histories above underline, liquefaction represents a potential high-impact phenomenon that needs to be studied thoroughly, in order to evaluate the main triggering factors first, and define technical solutions and methodologies able to reduce the risk related to such type of collapse.

As it will be showed in details in the next sections, liquefaction triggering is strictly correlated to several factors such as saturation, relative density and others, which substantially affects the susceptibility, and consequently the risk, of granular materials subjected to a dynamic event to be potentially liquefied. In fact, the recognition of the causes that lead to the liquefaction of soils represents the basis of the identification and development of improvement technique, acting on different factors that affect the mechanical behaviour of the soil itself.

### 1.3 AN INTRODUCTION TO LIQUEFACTION

Liquefaction concerns loose, saturated cohesionless deposits, and represents a phenomenon in which the soil undergoes a phase transformation, changing its behaviour from solid to liquid (Ishihara 1993). Different definitions of *Liquefaction* have been given by several authors during the years and a growing attention has been dedicated towards that type of collapse. One of the first definition of liquefaction was probably given by Terzaghi & Pack in the 1948, that coined the expression “*spontaneous liquefaction*” to indicate the rapid change of state from a friction-resistance material to a viscous fluid. Kramer and Seed (1988) defined liquefaction failure as mechanism that leads to the development of instabilities in large masses of soil. Again, Poulos et al. (1988) defined liquefaction as decrease of the shear resistance of a mass of soil, during a monotonic, cyclic or dynamic loading, with no variations in volume.

Because of the contractive behaviour of loose granular materials, positive pore pressures develop under undrained shearing. Since seismic shaking causes conditions that are only partially drained or fully undrained even in coarse soils, such pore pressure increments induce a corresponding reduction of the effective stresses, eventually leading to a (transient) condition of nihil shear strength and stiffness.

$$\Delta\sigma = \Delta\sigma' + \Delta u = 0 \quad \Delta\sigma' = -\Delta u$$

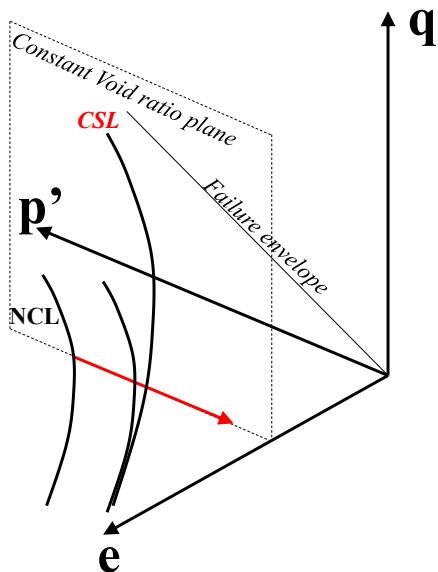


Figure 1-6 Qualitative stress path at constant volume during a seismic event

$$\tau_{lim} = \sigma' \cdot \operatorname{tg}\varphi = 0$$

Equation 1-1

Recently, Lirer and Mele (2019) have demonstrated that at a deeper insight it can be shown that the phase transition from solid to liquid can be best investigated by looking at the equivalent viscosity of the soil. In particular, they have shown that a sharp drop of such a viscosity is the clearest possible marker of the phase transformation, and that it takes place before the effective stresses reach zero. As a consequence, in engineering terms it is of the utmost importance to highlight that not only the zero effective stresses conditions have to be avoided, but that values of pore pressure increments well below the critical values have to be granted for the sake of safety.

Indeed, it is conceptually important to underline that the liquefaction can lead to different types of collapse: a first one, not due to any shear failure mechanism, since the stress path during the pore pressure increase does not reach the critical state line, rather the effective stresses point to the axis origin in a  $(\tau; \sigma)$  or a  $(q; p')$  plane. On the other hand, if an upper structure is present, the pore-pressure's rise, leading to a decreasing in effective stresses, can activate failure mechanisms which are prior to the complete fluidification of the soil, such as bearing capacity failure.

Focusing on the former mechanism, Figure 1-6 shows conceptually the stress path leading to liquefaction in a plane with constant void ratio (no volume changes). It is quite clear that the path does not intersect the *Critical State Line*, which lies in a 3D space actually. Thus, the liquefaction failure mechanism can be strictly correlated to the loss of the intergranular contacts caused by the pore pressure build up.

Obviously, the entire mechanisms involved in the process and the factors that influence the susceptibility of the soil are quite wide and complex, and an exhaustive characterization will be provided in the next section.

Liquefaction of granular materials, under fully saturated and loose state conditions, can occur in both static and cyclic loading paths when the drained behaviour is not permitted (Kramer and Seed 1988). Even though monotonic loading can cause the transient fluidification of the soil, main efforts have been dedicated to the understanding of the triggering factors related to the dynamics path developed during a seismic event.

Regardless of the stress path condition, it is well known that loose granular materials show a contractive behaviour under cyclic or static loading. When the drainage is not permitted and the soil is fully saturated, pore pressure rises because of the soil skeleton's tendency to contract and the effective stresses therefore decrease. In this condition, liquefaction phenomena potentially activated can be subdivided into two groups: *flow liquefaction* and *cyclic mobility* (Kramer 1996). The former is less frequent in field collapses, but causes much higher damages while, on the other hand, the latter occurs more frequently but its consequences are usually less dangerous.

The main difference between the two type of collapses regards the shear stress required to guarantee the equilibrium:

- In case of *flow liquefaction*, the shear stresses acting are greater than the shear strength required. This results in large deformations of the soil caused essentially by static shear stresses: cyclic loading leads the soil in an unstable condition, allowing the static stresses to produce flow liquefaction. Generally, this type of collapse leads to rapid and sudden deformations.
- In case of *cyclic mobility*, the shear stresses induced by the seismic event are lower than the shear strength of the liquefied soil. For this type of phenomena, the decrease of stiffness is less rapid, and the permanent displacements do not suddenly develop, rather they gradually increase during the cyclic loading. Finally, the permanent displacement caused

by the cyclic mobility is due to both static and cyclic shear stresses, and it is largely known as *lateral spreading*.

In order to evaluate the liquefaction hazard, it is common in the geotechnical practice to evaluate first if the soil can be susceptible to liquefaction. Once the susceptibility has been assessed, it is necessary to understand if liquefaction can be triggered and, consequently, which type of damages can affect eventual upper structures. This conceptual scheme leads necessarily to own instruments in order to evaluate, quantitatively, the liquefaction hazard. To this aim, a comprehensive evaluation is needed about three fundamental aspects of liquefaction hazard: susceptibility, initiation and effects (Kramer 1996).

### 1.3.1 LIQUEFACTION SUSCEPTIBILITY

The assessment of liquefaction susceptibility of liquefiable soil is preliminary to develop a reliable analysis of the seismic hazard, potentially leading to flow liquefaction or cyclic mobility. Several criteria are available in the literature, some of them also developed for low-plasticity silt and clays (Boulanger et al. 2006). However, remaining in the framework of the “classic” liquefiable soils, (or rather granular well or poor graded materials) the following main criteria can be reported (Kramer 1996):

- Historical criteria
- Geologic criteria
- Compositional criteria
- State Criteria

*Historical criteria* are fundamentally based on post-earthquake site characterization, showing that the liquefaction susceptibility is markedly higher for sites in which no significant changes, in terms of soils and groundwater conditions, have been detected (Youd 1984). Thus, historical seismic events review can be useful to determine a liquefaction susceptibility map, as described by Youd (1991). For example, Ambraseys (1988) developed a relationship between limiting epicentral distances of sites at which liquefaction has been observed and moment magnitude for shallow earthquakes, by conducting an historical worldwide data collection. As it is clearly shown in Figure 1-7, the higher is the magnitude of the seismic event, the higher is the epicentral distance needed so that liquefaction could not be observed. Other charts are also available in the literature, for different data collection (Papadopoulos and Lefkopoulos 1993).

On the other hand, by its intrinsic nature, historical criteria do not allow to make any type of consideration on the geology and the seismic response of the site.

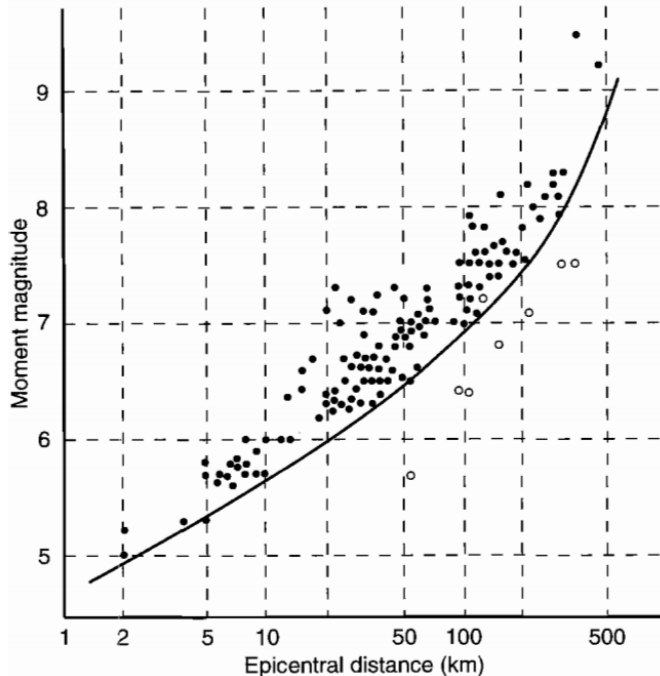


Figure 1-7 Historical criteria correlation (Ambraseys, 1988)

*Geological criteria* are based on geological consideration regarding the soil deposits and the groundwater level depth. Since soils in looser state are more susceptible to be liquefied, the depositional environment and age of a soil deposit can drive to a preliminary susceptibility analysis. Indeed, a relatively small range of geological environment includes soil potentially liquefiable (Youd 1991b). In addition, more attention has to be focused on alluvial deposits, since the deposition processes leads to a looser state condition, and human-made soil deposits as well, since for the latter the in-situ compaction actions, provided during the deposition itself, could not be sufficient to avoid the liquefaction susceptibility. Obviously, the groundwater table plays a key role since liquefaction can occur only in fully saturated deposits. By this point of view, the deeper is the groundwater table, the lower is the liquefaction susceptibility: commonly, liquefaction is triggered when groundwater is within a few meters from the ground surface.

By increasing the refinement of the susceptibility assessment, a more reliable criterion is represented by the *compositional* one. In this case, several intrinsic parameters have to be investigated in order to assess the liquefaction susceptibility of the soil. If it was common thought that only quasi-monograngular soils (particularly clean sands) were subjected to liquefaction, research activities have demonstrated that even finer soils can be subjected to liquefaction, since the collapse is driven by the pore pressure build up during shear loading. Many authors' work (Chu et al. 2004; Martin et al. 2004) have underlined the possibility of triggering liquefaction in low-plasticity silts and clays, leading to significant ground failures. The presence of low-plasticity fine soil within the pores of a poor-graded

sandy material can significantly affect the liquefaction potential, by changing the fabric of the soil, thus its mechanical behaviour. A schematic representation of the particle arrangement has been made by Karim and Alam (2014) and it is shown in Figure 1-8. It is possible to identify a limit fine content (LFC) at which the mechanical behaviour, in terms of pore pressure build up, become independent by the silt content. From *a*) to *b*), the soil structure is sand- dominated, with silt contained in a sand-skeleton, whereas in configuration *c*) there is enough fine such that the sand grains loose contact with each other and the soil structure becomes silt-dominated.

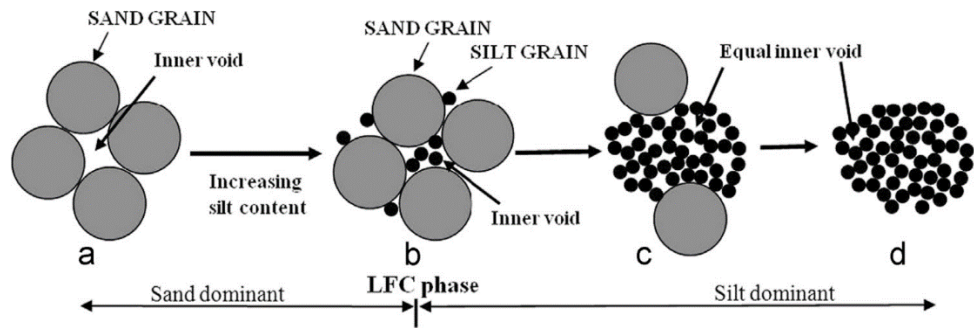


Figure 1-8 Schematic diagram demonstrating particle arrangement of sand–silt mixture with the variation of silt content (Karim and Alam 2014)

This results in an increase of the liquefaction susceptibility with increase of the low-plasticity fine content up to the LFC, after which the liquefaction resistance tends to remain constant (Figure 1-9).

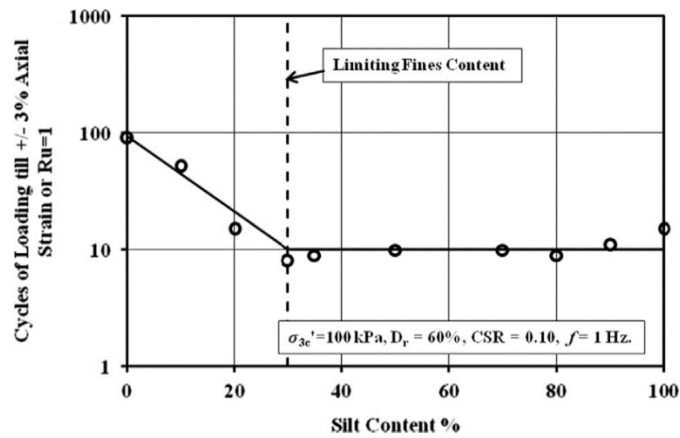


Figure 1-9 Experimental correlation between the number of cyclic loading leading to liquefaction and silt content (Karim and Alam 2014)

Wang (1979) suggests that if a fine-grained soil satisfies each of the following criteria, the material has to be considered as liquefiable:

- Fraction finer than  $0.005 \text{ mm} < 15\%$

- Liquid limit,  $LL < 35\%$
- Natural water content  $> 0.9 LL$
- Liquidity index  $< 0.75$

As far as soil gradation is concerned, which affects the liquefaction potential as well, the Italian Code (NTC 2018) establishes a granulometric range, defining the soil potentially liquefiable, as a function of the uniformity coefficient,  $U_c$ , defined as the ratio between  $d_{60\%}$  and  $d_{10\%}$  (Figure 1-10).

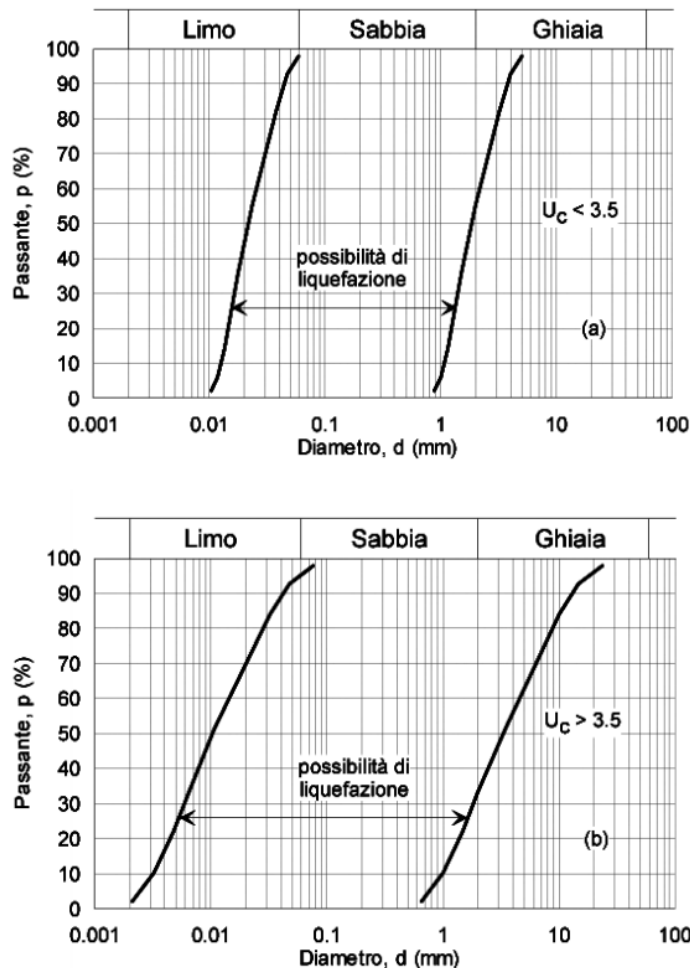


Figure 1-10 Granulometric range for potentially liquefiable soils: a)  $U_c < 3.5$  b)  $U_c > 3.5$  (Italian Code NTC 2018)

Generally, a well graded material shows a higher liquefaction resistance because of the more efficient interlocking between the grains and a lower tendency to contract in volume, since the smaller voids are filled with finer grains.

Liquefaction susceptibility is markedly dependent on the particle shape as well. Angular or sub-angular grains lend a higher liquefaction resistance, while soils constituted by round particles are more susceptible, since the contractive behaviour, under applied shear loading, is emphasised.

The criteria discussed above are not sufficient to reliably assess the susceptibility of the soil to liquefaction, rather a state criterion must be adopted to that aim. The mechanical behaviour of a granular material and, consequently, its volumetric changes, are strongly dependent by:

- Void ratio,  $e$ , or equally the relative density,  $D_r$ ;
- Initial stress condition,  $\sigma_c'$

The combination of these two state parameters is essential to define the volumetric deformations that will develop, leading either to contractive or dilative behaviour. The fundamental knowledge about the granular materials behaviour was found out by Casagrande, (1936), by performing drained, strain-controlled tests on loose and dense sand specimens, under the same initial effective confining stresses. In Figure 1-11 results in both plains ( $q; \varepsilon_a$ ) and ( $q; e$ ) are reported.

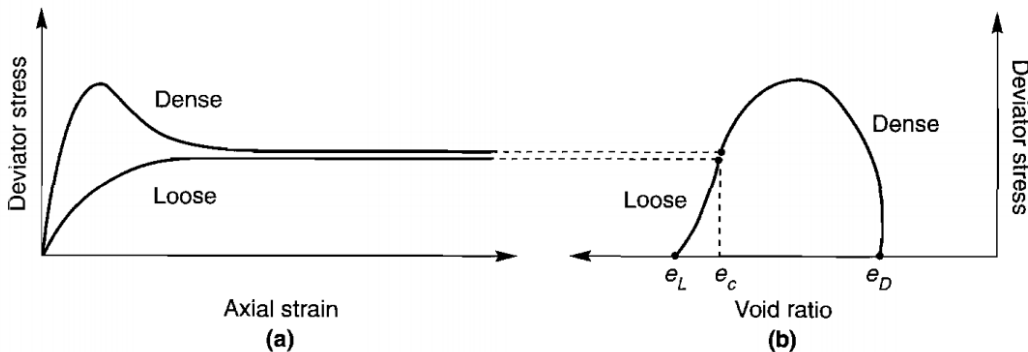


Figure 1-11 Drained, strain-controlled tests on loose and dense sand (Casagrande, 1936): a)stress; strain b) stress; void ratio (Kramer 1996)

The looser sample suddenly exhibits a contractive behaviour, and the stress-strain path shows no peak strength detection. On the other hand, the denser one exhibits initially a contraction, to lately show a dilatative behaviour, resulting in a higher strength in the ( $q; \varepsilon_a$ ) plane. Regardless the stress-strain relationship, the key outcome was that, even though the initial void ratio was completely different for the two tested specimens, for high strain levels soils reached the same “*critical*” void ratio, continuing to shear with constant deviatoric stresses. Such void ratio,  $e_c$ , is, for a given confining pressure, independent from the initial density of the sample.

Thus, if different tests are carried out at different confining pressures, a locus of  $e_c$  can be obtained, as shown in Figure 1-12. The locus, called *Critical Void Ratio*, separates the contractive from dilative behaviour for a given material. Thus, the mechanical behaviour of granular materials, in term of volumetric strains, can be preliminary defined by investigating simultaneously the initial void ratio

and effective confining stresses acting in-situ: by knowing the state parameters of a granular deposit, it is possible to distinguish soils susceptible or not to liquefaction phenomena.

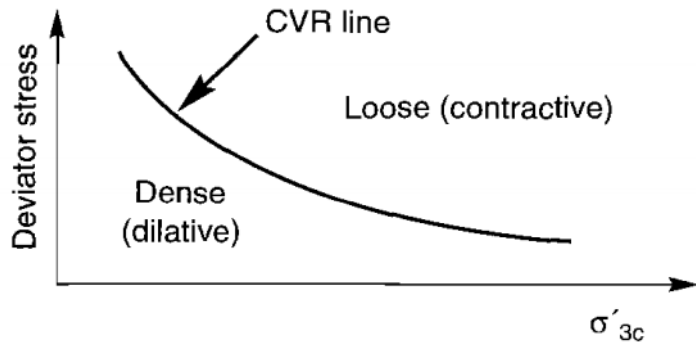


Figure 1-12 Critical void ratio CVD, defined by Casagrande (Kramer 1996)

Obviously, if undrained tests are carried out, positive or negative pore pressures will rise, respectively for loose and dense specimens. Thus, the following assumption can be made (as showed in Figure 1-13):

- Drained conditions: for a given  $\sigma_{c,0}'$ , the final void ratio will be  $e_c \neq e_0$  with  $\sigma_{c,0}' = \sigma_{f,0}'$
- Undrained conditions: for a given  $\sigma_{c,0}'$  the final void ratio will be  $e_c = e_0$  with  $\sigma_{c,0}' \neq \sigma_{f,0}'$

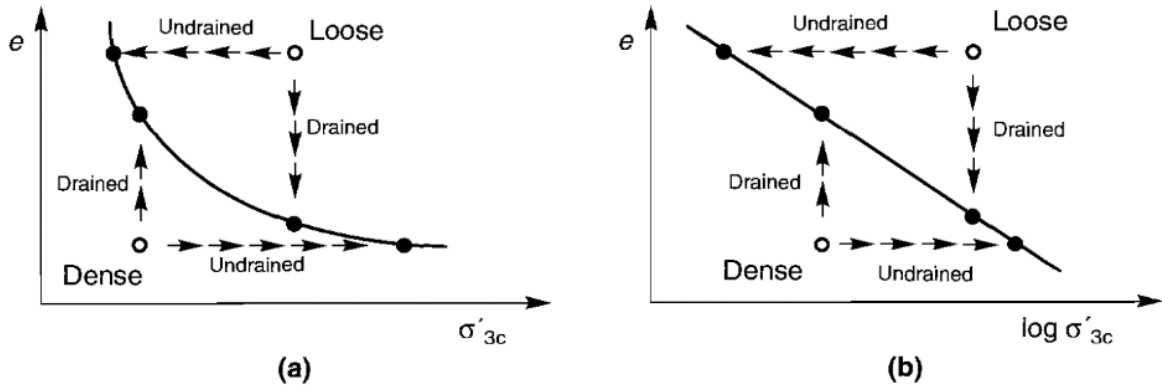


Figure 1-13 Drained and undrained paths leading to the critical void ratio locus (Kramer 1996)

Knowing the initial state conditions, in terms of void ratio and affective stresses, can be useful to evaluate the “*state position*” related to the CVR line: soils lying above are considered to be subjected to flow liquefaction, vice versa soils are not susceptible to liquefaction collapses.

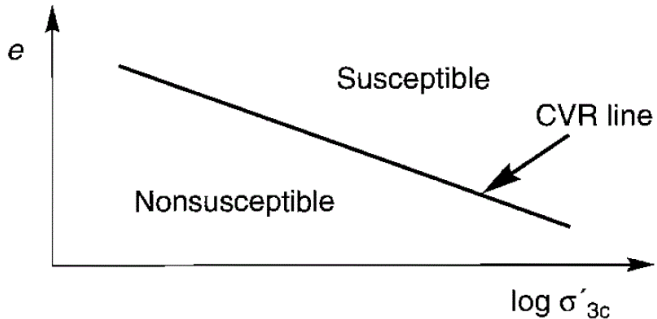


Figure 1-14 CVR line in the  $(e; \sigma'_{3c})$  plane (Kramer 1996)

Thus, if a soil is loose enough to be placed above the locus, it will generate positive pore pressure increments and flow liquefaction will be triggered. If the soil is denser, the tendency to dilate will generate, in undrained conditions, negative pore pressure increments, and no liquefaction should be achieved.

Actually, some historical events have shown that denser configuration can lead to soil liquefaction as well. It is the case of Fort Peck Dam in Montana, where flow liquefaction occurred during the stage construction, in the 1938 (Middlebrooks 1942). Post-failure-back analysis showed that, for that specific material, the state conditions were such to be plotted below the CVR line; nevertheless, flow liquefaction failure of its upstream slope was observed. A hypothesis was given by Casagrande: the previous laboratory tests was conducted in strain-controlled conditions. Sure enough, in situ collapses are generally caused in stress-controlled conditions. Moreover, when a soil is leaded to flow liquefaction (by means of stress controlled loading), grains show the tendency to rotate continuously, in order to achieve a minimum friction resistance structure (Casagrande 1976). In fact, during his initial tests, Casagrande was not able to conduct stress-controlled loading, resulting in the impossibility of simulating this type of soil behaviour, until the late 1960s.

In addition (Castro 1969), undrained tests were performed, for different density, under anisotropically consolidated conditions and monotonic loadings. The stress-strain relationship allowed to identify three types of mechanisms, depending on the initial density of the specimen. The following behaviour can be detected:

- *liquefaction*
- *limited liquefaction*
- *dilation*

Tests results, reported in Figure 1-15, show in details the stress paths developed during the shear phases.

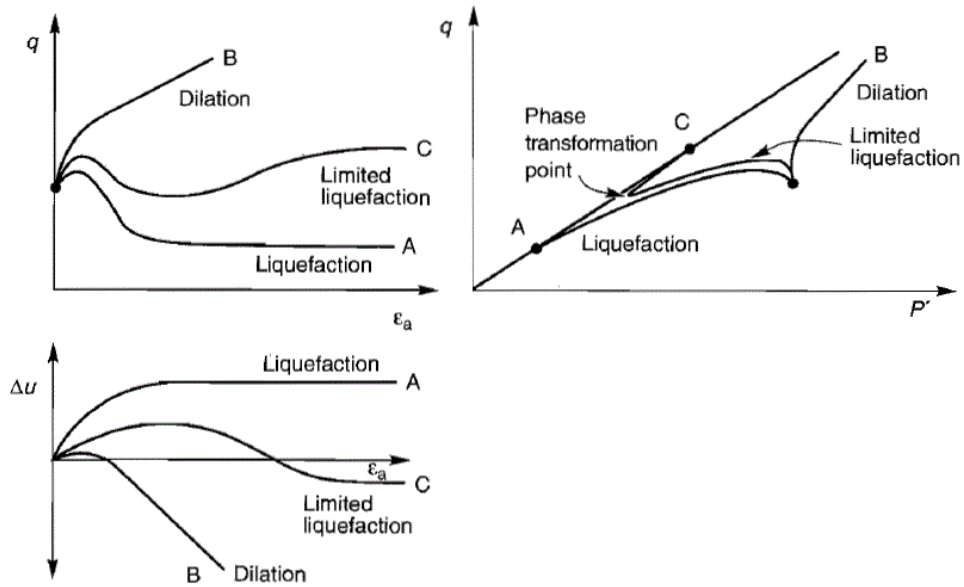


Figure 1-15 Undrained-anisotropically consolidated tests for different densities: liquefaction (a), dilation (b) and limited liquefaction (c) (Kramer 1996)

The looser specimen (test *a*) shows suddenly a contractive behaviour: positive pore pressures rise, and a peak strength is reached at very low strain level. Afterwards, a heavy drop in the shear strength is observed, and the soil completely liquefies, collapsing in a “*flow condition*”, developing high strains at constant shear stresses and very low effective confining pressures. The denser one shows first a very low contractive behaviour, then dilative behaviour is developed, and shear strength increases with an increase in the effective confining stresses (test *b*). Sample tested in intermediate conditions (test *c*), shows a softening-post peak behaviour, during a contractive phase, and then starts to dilate at higher strains. Soil develops the dilative behaviour once the phase transformation line (point of contraction- dilative reverse) is reached. Such behaviour was then termed *limited liquefaction*. In these tests, effective stresses reached at large strains shape a curve in the plane  $e-\sigma'_3$  that is below and almost parallel to the CVR line. This curve is called *steady state line (SSL)* (Castro and Poulos 1977; Poulos 1981). In this state the soil shows a constant volume (in case of drained tests), effective confining pressure and deformation velocity. Flow of soil structure and the orientation of the soil particles during stress-controlled conditions may be the causes of the difference between the curves CVR and SSL. The soils with an initial void ratio below the SSL do not show flow liquefaction whereas the soils with a void ratio above the SSL show flow liquefaction. The locus mentioned above is actually a projection of a curve (in the  $q;p'$  plane) that lies in a 3D space  $q;p',e$ .

or, equally,  $\tau, \sigma', e$  (as also revealed in the previous section in Figure 1-6). The 3D locus is thus conceptually fundamental to better understand the behaviour of a soil and the stress path leading to liquefaction (Figure 1-16).

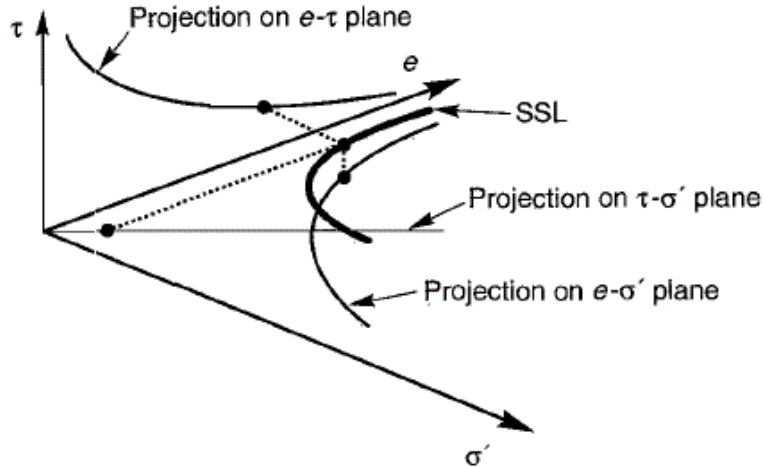


Figure 1-16 Three-dimensional steady state line and its projections (Kramer 1996)

Indeed, the knowledge of the SSL line is useful to preliminary define the potential susceptibility of the soil regarding the flow liquefaction (Figure 1-17), by plotting the soil state conditions, in terms of combination of initial void ratio and stresses:

- if the soil state plots above the SSL line, and the static stress is greater than the undrained shear strength,  $S_{su}$ , soil is susceptible to flow liquefaction;
- if the soil state plots below the SSL line, soil is not susceptible to flow liquefaction.

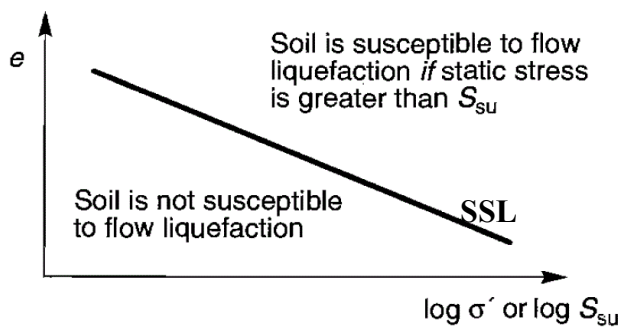


Figure 1-17 State criteria for soil liquefaction susceptibility (Kramer 1996)

Thus, the void ratio only, at which the soil lies in the in-situ condition, is not sufficient to ensure or not the liquefaction susceptibility. Since the soil shows markedly a non-linear behaviour, because

of its elastic-plastic nature, the stress conditions must be correlated to the initial void ratio. Thus, since the SSL line can divide the “shear-volumetric” coupled behaviour, a conceptual parameter that includes the state conditions can be useful to assess the liquefaction susceptibility. Indeed, such parameter have been named *state parameter* and it is defined as (Been and Jefferies 1985):

$$\psi = e - e_{ss} \quad \text{Equation 1-2}$$

In other terms, the state parameter quantify, for a precise state condition, the distance of the soil state from the SSL locus, preliminary providing the liquefaction susceptibility (Figure 1-18): if  $\psi$  is positive, soil will show contraction; vice-versa, soil behaviour will be dilative. In addition, at least theoretically speaking, soils having the same state parameter, with different values of  $\sigma'$ ;  $e$ , should exhibit the same type of shear-volumetric behaviour.

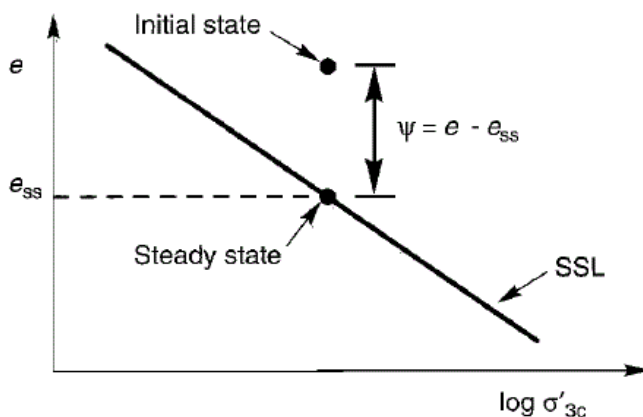


Figure 1-18 State parameter (Kramer 1996)

Despite the state parameter  $\psi$  may be limited to characterize the soil behaviour especially for loose sand under low confinement, several studies have been developed in order to link  $\psi$  to different parameters such as friction angle, dilation angle, CPT resistance (Been et al. 1986), PMT and DMT results (Yu, 1994,Konrad, 1988).

Unfortunately, even if the state parameter  $\psi$  is conceptually useful to evaluate liquefaction susceptibility, it is quite difficult to assess with a high accuracy the position of SSL line in laboratory testing. In fact, several uncertainties regarding the SSL line have been investigated by several authors (Been et al. 1991, Flora et al. 2012), showing that granular material can exhibit a non-linear correlation between  $\sigma'$  and  $e$ , at steady state conditions, and there is no particular reason why the SSL should be linear in the semi- logarithmic compression plane other than a mathematical convenience.

### 1.3.2 LIQUEFACTION TRIGGERING

Even if a granular material has been assessed as susceptible to liquefaction, this is not sufficient to ensure the triggering of liquefaction itself. To trigger liquefaction phenomena, a strong enough disturbance must be detected, and its evaluation is one of the most critical parts of a liquefaction hazard evaluation. Anyway, both flow liquefaction and cyclic mobility can be seismically triggered but, historically, the first understanding of flow liquefaction are mostly related to the static conditions, which represents the basis to assess the liquefaction triggering under cyclic or dynamic stress conditions.

Under monotonic shear stress loading, loose soils exhibit a mechanical behaviour that can lead to flow liquefaction as conceptually described in Figure 1-19.

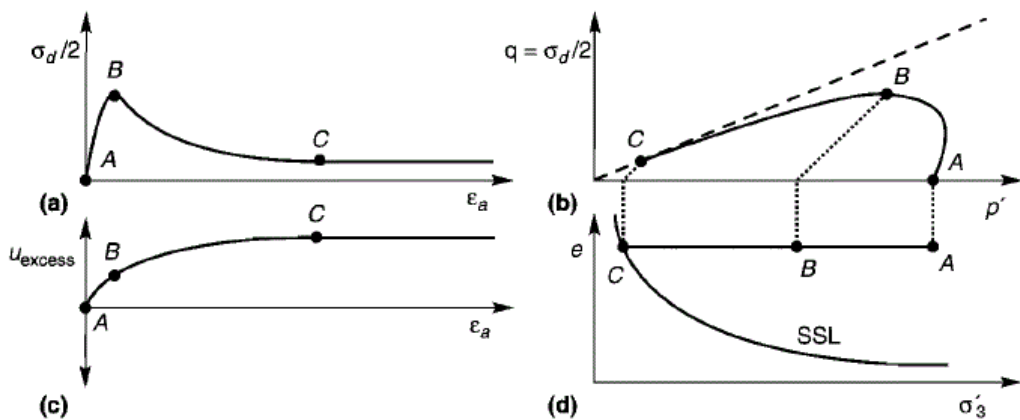


Figure 1-19 Monotonic loading leading to flow liquefaction in different planes of interests (Kramer 1996)

Starting by an isotropic consolidation, if a shear stress in undrained conditions is applied, soil exhibits rapidly a contractive behaviour, resulting in a pore-pressure build up ( $A-B$ ). If a pore pressure ratio  $r_u$  is defined as:

$$r_u = \frac{\Delta u_w}{\sigma'_c} \quad \text{Equation 1-3}$$

it could be asserted that, in point  $B$ ,  $r_u$  is much lower than one (i. e. effective confining stresses still being higher than zero). At this point, reached for relatively low strain levels, a peak in the  $q; \varepsilon_a$  plane is detected. Afterwards, the soil specimen shows a decrease in the deviator, resulting in a collapse of the soil itself, leading to high strain levels. Concurrently, from point  $B$ , the specimen becomes unstable, a rapid excess pore pressure is developed, and effective stresses dramatically reduce, until

point  $C$  is reached. From point  $B$  to point  $C$ , the soil is thus subjected to *flow liquefaction*, initiated when the specimen became irreversibly unstable (point  $B$ ).

If the same types of undrained test are conducted for different effective confining stresses, with the same void ratio (Figure 1-20), a locus of instability points can be detected.

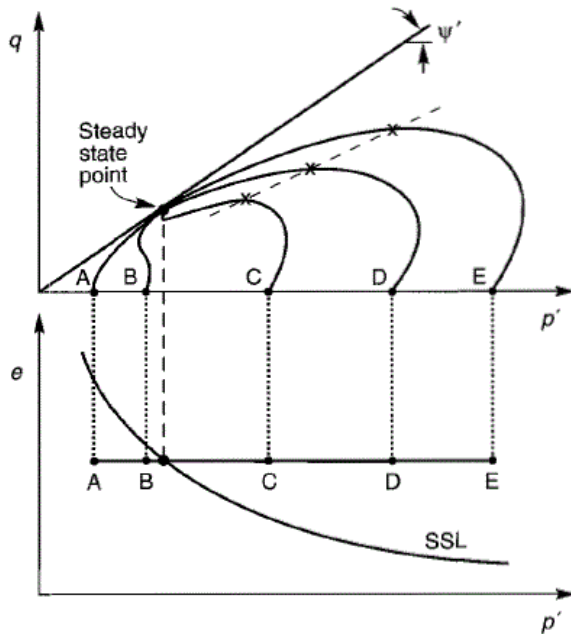


Figure 1-20 Locus of instability points for static undrained tests

As it has been discussed in the previous sections, since the tests  $A$  and  $B$  lie below the SSL, they will exhibit a dilative behaviour and they will reach the steady state point increasing their effective stresses (i. e. increasing their volume in drained conditions). Thus, in this case, liquefaction cannot be triggered. Points  $C$ ,  $D$  and  $E$  lie above the SSL instead. All the three tests start to exhibit an unstable behaviour when the deviator peak is reached. Afterwards, flow liquefaction is triggered. The locus of points at which the unstable behaviour is activated lead to the definition of a straight line, where at the effective stress conditions correspond the initiation of flow liquefaction (Hanzawa et al. 1979; Vaid and Chern 1983).

The definition of the instability points results in the definition of the so-called *Flow liquefaction surface (FLS)* in the stress path space (Figure 1-21), and represents the boundary between stable and unstable states in undrained shear conditions. In other words, if the stress path does not lie on such surface, the soil failure is due to the classic shear mechanisms, vice versa static flow liquefaction is triggered. In addition, since flow liquefaction cannot occur if the stress path is below the steady-state point, the FLS is truncated at that level (Kramer 1996).

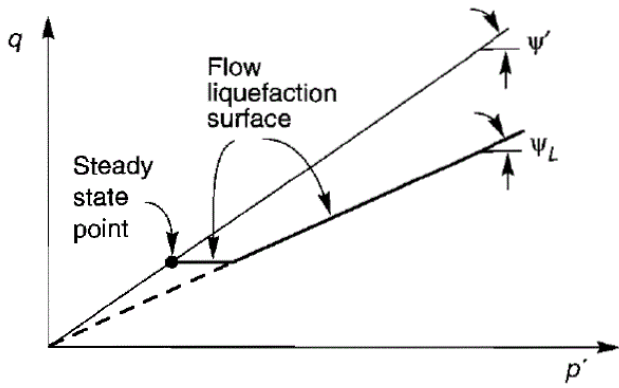


Figure 1-21 Flow liquefaction surface (Kramer 1996)

Hence, the use of the *flow liquefaction surface* has been applied in both static and cyclic loading conditions, showing for the latter that *FLS* triggering criteria can be applied as well (Vaid and Chern 1983). Actually, in the case of cyclic loading, several studies have shown that liquefaction is triggered when the stress path is somewhere within the *FLS* surface, but the actual trigger point still to be covered by a certain degree of uncertainty. Anyway, in Figure 1-22 is conceptually reported the initiation of liquefaction for both static and cyclic loading.

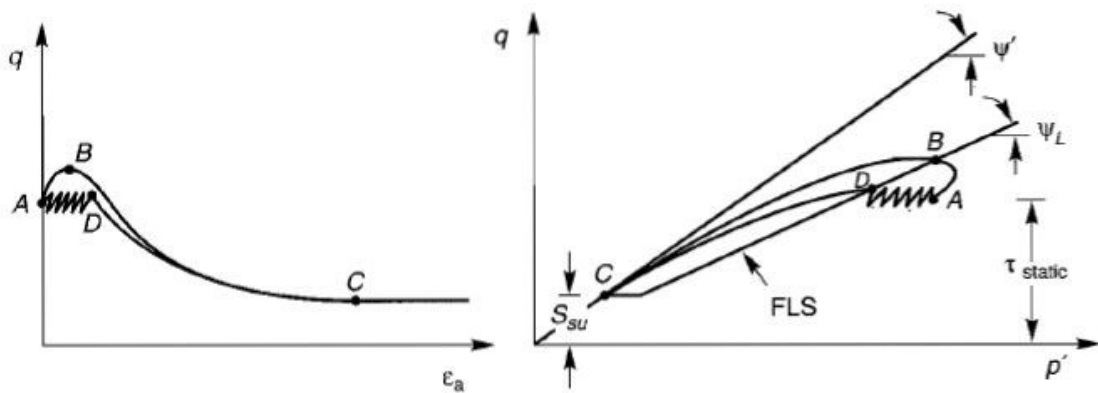


Figure 1-22 Initiation of liquefaction under static and cyclic loadings

For what it concerns the cyclic condition, by starting by a  $K_0$  consolidation, the cyclic loading applied leads to the development of excess pore water pressure leading the stress path to slide towards the axis origins, until the *FLS* surface is reached. Once the soil is in point *D*, the specimen becomes unstable and liquefaction is initiated, and the steady state point is gained (point *C*). On the other hand, the statically loaded specimen shows a different point of liquefaction initiation (point *B*), but the same steady state point is achieved when fully liquefaction is detected. Therefore, the *FLS* is able to mark the boundary from which the soil will show instability producing flow liquefaction.

In order to increase the detail level regarding liquefaction phenomena, it is possible to assert that flow liquefaction can be conceptually subdivided in two stages:

- a first stage, at which pore water pressures are generated, at relatively small strains level;
- a second stage in which, once the *FLS* is reached because of pore pressures build up, soil becomes unstable, showing a strain-softening driven by the shear stresses required for the equilibrium (Kramer 1996).

Obviously, the increments in pore water pressure play a key role in the liquefaction phenomena, since they represent the “*driven reason*” of what has been discussed so far. If no pore pressures are generated, no matter static or cyclic or dynamic loading, liquefaction will be not triggered.

In case of cyclic loading, both flow liquefaction and cyclic mobility can be reached, depending on the shear stress magnitude and the initial conditions in terms of proximity to the *FLS*.

Usually, static in-situ stresses remain essentially constant during a dynamic shaking, at least until large deformations are achieved. When the shear stresses required for the static equilibrium are greater than the steady state strength, flow liquefaction can occur since the stress path inevitably falls into the *FLS*. In other words, if initial state lies in the shadow region of Figure 1-23, soil is susceptible to flow liquefaction.

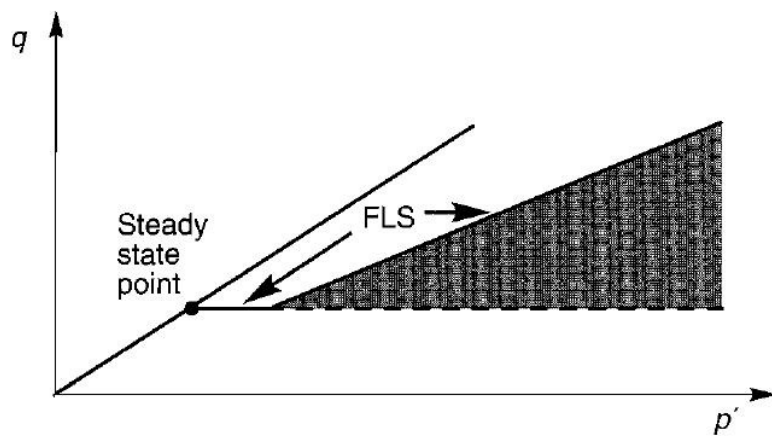


Figure 1-23 Initiation zone in case of flow liquefaction

On the other hand, cyclic mobility can be activated in the complementary zone, as reported in Figure 1-24, when the shear stresses required for the equilibrium are lower than the steady state strength. No flow liquefaction is detected, but considerable settlements can be achieved anyway.

If triaxial tests are conducted to assess the cyclic mobility behaviour, mainly three different configurations can be achieved (Figure 1-25):

- a)  $\tau_{\text{static}} - \tau_{\text{cyc}} > 0$  and no exceedance of steady state strength;
- b)  $\tau_{\text{static}} - \tau_{\text{cyc}} > 0$  and exceedance of steady state strength is reached temporarily;
- c)  $\tau_{\text{static}} - \tau_{\text{cyc}} < 0$  and no exceedance of steady state strength.

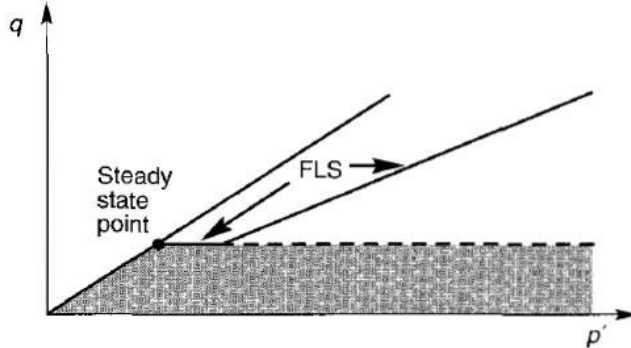


Figure 1-24 Zone of susceptibility to cyclic mobility

In all the three type of stress-paths, no flow settlements can be developed; even if the soil exhibits instantaneous and/or transient stages at  $\sigma'=0$  (e.g. case C), and permanent strains and, consequently deformations, accumulate incrementally. Moreover, even when the stress-path is cycling upon the failure drained envelope, a residual shear strength is available, as shown in Figure 1-26.

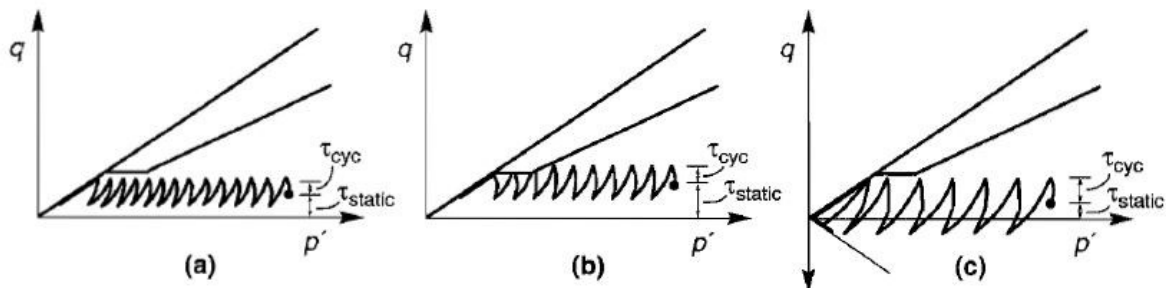


Figure 1-25 Possible cases of cyclic mobility

Indeed, once cyclic mobility has been fully developed and static shear is applied, the soil exhibits a shear strength resulting from the dilative behaviour until the steady state point is reached. Significant permanent strains may accumulate during cyclic loading, but flow failure cannot occur.

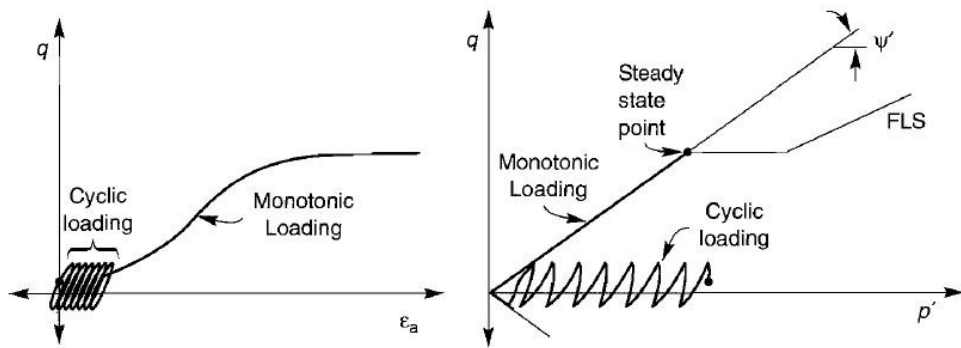


Figure 1-26 Post-Cyclic-Mobility static loading

In addition, laboratory tests are particularly useful to investigate the pore pressure build-up during the cyclic loading. To that aim, several authors have developed correlation able to predict the rises in the pore water pressure,  $r_u$ , as a function of the number of cycles. In particular, Lee and Albaisa (1974) and DeAlba et al. (1975), basing on cyclic tests, have developed the following relationship:

$$r_u = \frac{1}{2} + \frac{1}{\pi} \sin^{-1} \left[ 2 \left( \frac{N}{N_l} \right)^{\frac{1}{\alpha}} - 1 \right] \quad \text{Equation 1-4}$$

in which:

- $N$  is the current number of cycles;
- $N_l$  is the number of cycles required to reach liquefaction;
- $\alpha$  is an experimental parameter taking into account soil properties and tests conditions.

*Equation 1-4* is thus useful to predict the pore pressures that could arise, for a given soil, even for events that do not lead the soil to be fully liquefied, as shown in Figure 1-27.

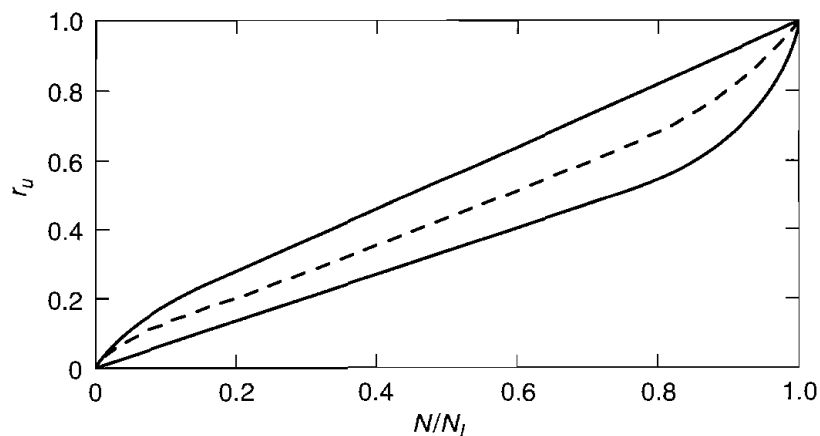


Figure 1-27 Pore pressure build-up as a function of the number of cycle

In fact, if a given seismic event is such to not completely liquefy the soil, pore pressure rises anyway. Thus, even if fully liquefaction is not reached, a decrease in the effective stresses is achieved because of the pore pressure increment, resulting in a lower shear strength of the soil. In such conditions ( $r_u < 1$ ), failure mechanisms different from the pure liquefaction can be activated (e.g. loss of bearing capacity), or settlements due to the effective stresses reduction can result incompatible with regards to an existing structure. Therefore, the aim of liquefaction mitigation actions is to avoid fully liquefaction certainly, but also to guarantee that pore pressure increment is compatible regarding to the above-mentioned failure mechanisms or excessive settlements. Indeed, when a mitigation action is needed, the design  $r_u$  is generally chosen referring to the allowable settlements or to the bearing capacity of shallow foundations (Fasano et al. 2019).

The thesis work aims to the development of a bio-IPS technique, by means of gas bubbles nucleation within the soil, in order to increase the cyclic resistance of granular liquefiable materials. By its nature, the technique is suitable to reduce the pore pressure build-up thanks to the higher compressibility of the nucleated gas. Since pore pressure rises anyway, a specific  $S_r$  has to be assessed in design phase, by applying possible design procedures available in the literature (e.g. Mele and Flora, 2019). Once the  $S_r$  target has been evaluated, design of the bio-IPS is needed, in order to guarantee the desired degree of saturation.

## 1.4 GENERAL FRAMEWORK AND GOAL OF THE WORK

The present thesis has been funded in the framework of PON 2014-2020 as “*Innovative PhD with industrial characterization*”. The work has been developed at the *University of Napoli, Federico II* within the Department of Structures for Engineering and Architecture (*Structural Engineering, Geotechnics and Seismic Risk PhD course*) and in collaboration with the industrial partner *Tecno-In S.p.A.* and the “*Faculdade de Engenharia, University of Porto* “. The work has been developed as follows:

Chapter 1 contains an introduction to the main topics: an introduction to liquefaction as well as cases history are reported, briefly underlining the main aspects of interest. Afterwards, the goal of the research work is presented.

Chapter 2 introduces the main traditional mitigation techniques, in order to evaluate the current landscape.

Chapter 3 expounds the *Induced Partial Saturation* as a liquefaction mitigation technique and the fundamental concepts about partially saturated soils, underlining the configuration that has to be achieved to face the liquefaction phenomena with this type of mitigation action. Several possible IPS

techniques are presented, focusing on the possibility of linking the bio-chemical potential of some IPS solutions with respect to the geotechnical engineering. In addition, the involved biochemical processes are discussed.

Chapter 4 reports on the biological experimental investigation, which represents the basis for the development of the present research work, carried out in collaboration with the *Department of Biology of Federico II*.

In Chapter 5 the experimental program carried out at DICEA *geotechnical laboratory of the University of Napoli Federico II* is presented, showing the potential of the adopted bio-chemical solutions to induce partial saturation in sand. Desaturation tests and optical analysis are discussed.

Chapter 6 is focused on possible monitoring techniques able to verify and quantify the degree of saturation achieved during the ground improvement process. In detail, both electrical resistivity and P-wave velocity are discussed. The experimental programme on the latter is carried out at *Faculdade de Engenharia, University of Porto* by means of bender element tests. Laboratory analyses and data interpretation are discussed. In addition, numerical modelling based on bender element tests is performed, by means of FEM code PLAXIS 2D, in order to verify and validate the laboratory experimental data.

Chapter 7 contains a summary of the entire thesis work, underlining its key points. Finally, conclusions and remarks are discussed.

As previously shortly mentioned, the present thesis aims to the development of a non-invasive Induced Partial Saturation technique able to reduce the susceptibility of granular materials to liquefaction. In addition, monitoring techniques have been investigated in order to assess the efficiency of the treatment in terms of final degree of saturation achieved with the IPS technology.

The experimental work is subdivided as follow:

- Identification of a biological process able to generate gas bubbles within the pores by means of microorganism metabolism;
- Isolation of different bacteria lineages collected by a sludge treatment plant;
- Identification of the bacteria lineages able to carry out denitrification processes, resulting in the nucleation of gas bubbles, by means of biological testing in controlled environment;
- Assessment of optimum bacteria growth by means of chemical broth solution;
- Analysis on the environmental compatibility of the generated gas compounds and bacteria metabolism' sub products;

- Identification of several tested soils;
- Desaturation tests able to assess and quantify the generated gas, leading to the desaturation of specimen;
- Bio-chemical transient analysis aiming to investigate the biological paths and products generated during bacteria's activity;
- Optical analysis on bubbles nucleation;
- Monitoring testing by means of electrical resistivity and P-waves velocity measurements;
- Numerical modelling of P-waves propagation to validate the experimental data.

Thus, the thesis work tries to cover the entire process of IPS improvement technique, starting by the nucleation process, in order to assess the final  $S_r$  that can be achieved, with the final goal to set up a reliable monitoring technique able to verify, in real scale problems, the efficiency of the treatment by means of indirect monitoring methodology. The latter presents very delicate issues because of the heavy heterogeneity of the soil and the complex behaviour of the tri-phase material, composed by soil-gas-water. Nevertheless, the implementation of indirect monitoring techniques is needed, in order to ensure the effectiveness of the induced partial saturation technique during in-situ treatment.

## 2 CHAPTER 2

### 2.1 TRADITIONAL LIQUEFACTION MITIGATIONS TECHNIQUES

In this section a brief framework about mitigation techniques, able to reduce liquefaction potential, is reported. Several techniques have been studied and developed during years, and the selection of one of them rather than others is strictly correlated to several factors, depending on the specific site and soil to be improved as well. One of the most binding aspects is the urbanization of the area: the higher is the site's degree of anthropization the lower will be the invasiveness of the technology that will be used. This aspect is fundamental for the right choice of the most efficient methodology to carry on, ensuring highly reliable results in terms of liquefaction resistance increment.

The first step to develop efficient mitigation techniques is to identify the soil characteristics that influence the soil's tendency to liquefy. Thus, if the predisposing factors are known and determined, improvement techniques can be implemented, acting on a soil's factor rather than others. As pointed out in the previous section, liquefaction susceptibility is deeply related to:

- Density;
- Cementation;
- Gradings;
- Boundary conditions;
- Saturation.

Thus, starting by the knowledge of the triggering factors, mitigation techniques can be implemented, by applying either traditional methods or more innovative mitigation actions.

Huang and Wen (2015) proposed the following classification for liquefaction mitigation techniques, by classifying three different categories:

- Soil reinforcement
- Drainage
- Saturation degree reduction

Regarding the soil reinforcements, different methodologies can be considered, such as soil replacement, soil densification and bonding of grains. More precisely, goals mentioned above can be achieved with several technologies, depending on the site characteristics. For example, if a soil densification wants to be reached, the main technologies suitable to the aim are:

- Dynamic compaction
- Vibro-compaction

- Compaction grouting

Thanks to the application of the technologies mentioned above, it is possible to densify the soil skeleton and consequently decreasing the soil susceptibility to liquefaction phenomena. Usually, the design of the densification technique is based on the individuation of either target relative density or cyclic resistance ratio (CRR). A check of the effectiveness of the treatment can be done by some empirical methods based on the interpretation of the CTP results (e.g. Boulanger and Idriss, 2014).

### 2.1.1 DYNAMIC AND VIBRO-COMPACTATION

Starting by the dynamic compaction, such technique is surely applicable for new construction, located in a non (or low) urbanized area. The technique, indeed, consists in high energy impacts of a heavy soil mass on the ground surface, producing noise and vibrations, resulting in the inapplicability in urban environment. The kinetic energy allows to densify the soil beneath the ground surface. As pointed out by Lukas (1995), the efficiency of the treatment is a function of the grain size distribution, plasticity index and permeability of the soil, resulting in three regions of soil grain distribution that assess the applicability of the dynamic compaction on a given soil (Figure 2-1).

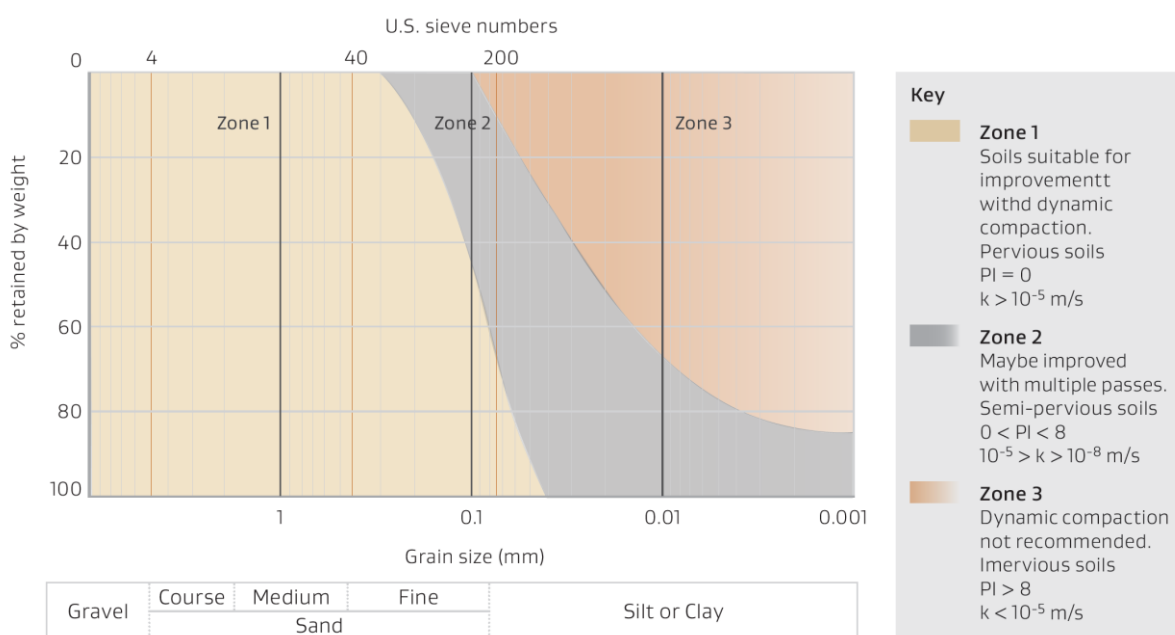


Figure 2-1 Soils suitable for dynamic compaction (Lukas 1995)

Sure enough, the areas interested by the treatment, and its effectiveness, decrease with the increasing of the considered depth.



Figure 2-2 Dynamic compaction example

Figure 2-2 shows operatively the technique application. If  $H$  is the falling height,  $W$  is the weight of the falling mass, the energy of the single impact is simply:

$$E_1 = W \cdot H \quad \text{Equation 2-1}$$

and, consequently, the specific energy for unit area as:

$$E = \frac{E_1 \cdot n}{A} \quad \text{Equation 2-2}$$

where  $n$  is the number of impacts and  $A$  the treated area. In addition to quantify the treated depth by the single impact the following empirical correlation can be used:

$$D = K \cdot (W \cdot H)^{0.5} \quad \text{Equation 2-3}$$

Where  $K$  is a normalizing factor, taking into account the soils characteristics, heterogeneity of the subsoil, degree of saturation and other technical factors (if no data are available, it is common practice to use  $K=0.5$ ). Finally, in Figure 2-3, an example of operative sequence is reported for such improvement technique.

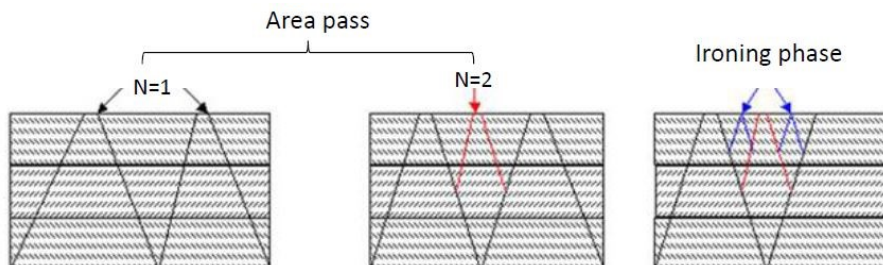
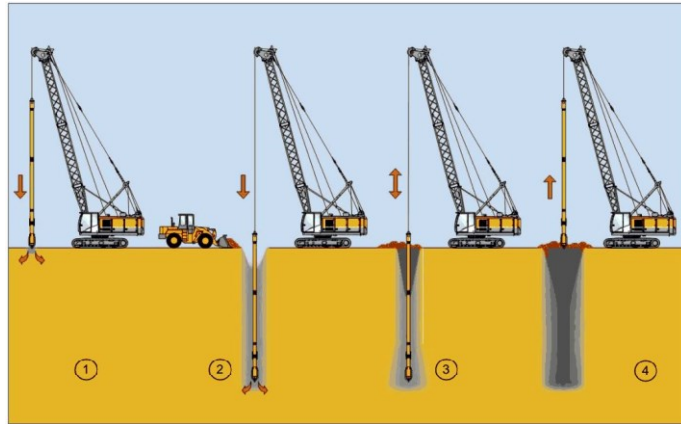


Figure 2-3 Example of operative sequence of dynamic compaction

On the other hand, vibro-compaction method consists of the insertion of a vibrating mass within the soil and, thanks to an eccentric acceleration of the instrument's tip, inducing a densification of the surrounding soil itself. An example of the operative sequence is shown in Figure 2-4.



*Figure 2-4 Example of operative sequence of vibro compaction*

For the application of this kind of vibro-compaction, the fines content should be lower than 15%. For larger fines content the method faces difficulties in densifying the soil with the pure application of vibrations. In addition, water flushing is usually applied to ease the penetration of the vibrating tube.

Unfortunately, the efficiency of the vibrator and his motion as well, even using accelerometers at the tip of the vibrating mass, is not reliably assessable, resulting in lacking information for the densification of the surrounding soil and occurring fluidisation or liquefaction phenomena around the vibrator (Triantafyllidis and Kimmig 2019).

Even if the technique is supposed to be highly efficient, especially for clean sands, no particularly reliable methodologies are available to predict precisely the final improvement carried out by the vibro-operation. This is mainly due to the complexity of the induced deformation near the vibrating tip, as schematically shown in Figure 2-5, where authors identify three different zones, respectively a fluidification zone, a compacted zone and an elastic zone.

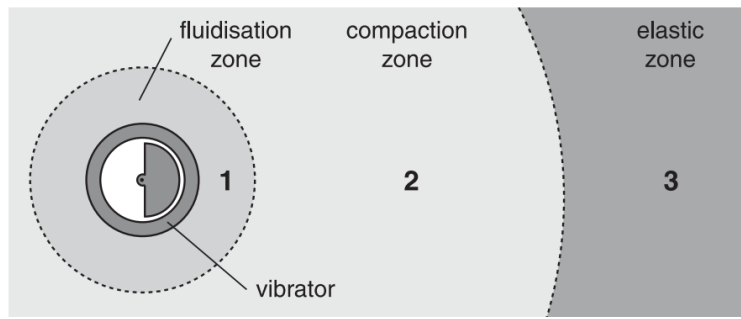


Figure 2-5 Simplified scheme of the treated zone with vibro-compaction techniques (Triantafyllidis and Kimmig 2019)

In addition, the cavity created by probe penetration should be filled by a soil with a specific grains size distribution to increase the compaction degree, some recommendations on particle size recommendations are given by Elias et al. (2006).

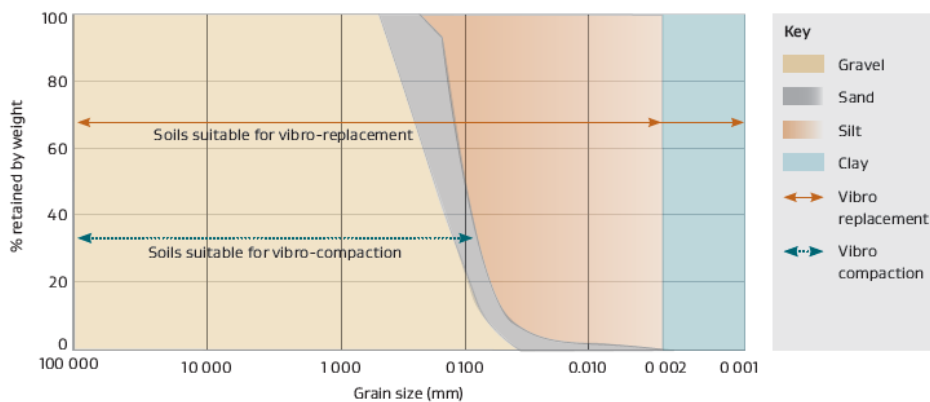


Figure 2-6 Soils suitable for vibro-compaction (Elias et al. 2008)

Details on design issues regarding this type of technique are not treated in the present work.

## 2.1.2 COMPACTION GROUTING

Finally, regarding the soil densification framework, compaction grouting represents an alternative technique to reduce the liquefaction susceptibility of granular materials.

Compaction grouting is a technique to increase the strength of loose, liquefaction susceptible soils, by increasing their relative density. First, the susceptible soil is reached by a grout pipe casing and then, a stiff cement-grout mixture is injected through the pipe. The procedure is then repeated at different stages in order to form expanding grout bulbs within the soil mass. The bulbs of grout displace the soil nearby and densify the surrounding zone. Furthermore it inherently densify the loosest soil in proximity of the grout pipe and thus treat the most susceptible material (Miller and Roycroft 2004). In Figure 2-7 a qualitative sequence of compaction grouting application is shown.

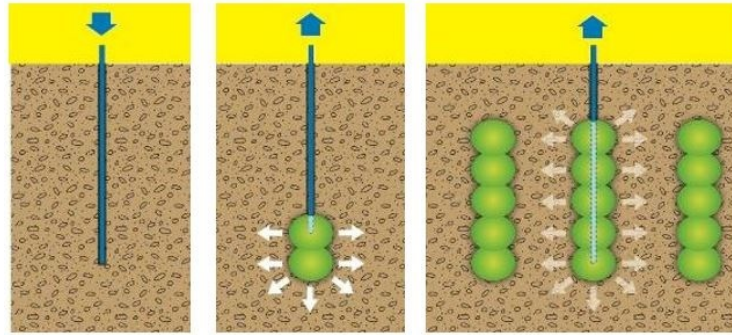


Figure 2-7 Qualitative sequence of compaction grouting application

Unfortunately, compaction grouting involves several soil parameters due to different possible soil conditions as well as grouting variables. The application of the method, however, is deeply bound by practical experience and empiricism. A mechanistic model that rationally considers the different variables involved in the process and allows for optimized design is not available (El-Kelesh et al. 2001). Indeed, the improvement of soil due to the compaction grouting technique is usually assessed by comparing the pre-treatment and post-treatment penetration resistances of the standard penetration test or cone penetration test (El-Kelesh et al. 2012).

However, several theoretical schemes have been studied during the years, referring to different types of mechanisms, as reported in Figure 2-8.

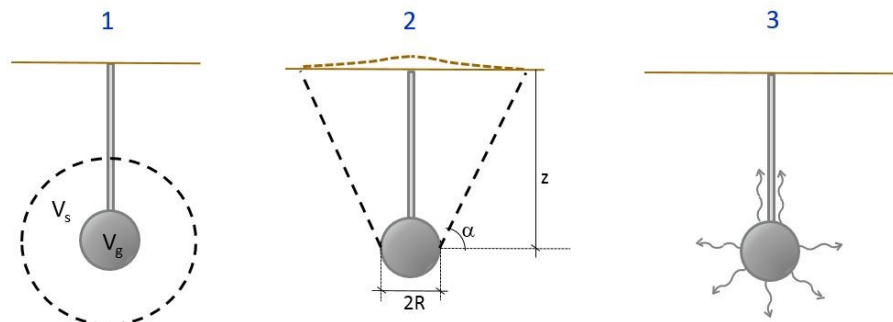


Figure 2-8 Different compaction grouting mechanisms: 1) Expansion of Grout Bulb; 2) Conical Shearing Failure; 3) Grout permeation (no compaction grouting is carried out)

These three different schemes lead to different theoretical evaluation of the treatment. The first scheme refers to an ideal expansion of a spherical cavity in an isotropic elastic-plastic continuum, in which the surrounding soil behaves first elastically, until the yield locus is reached (Figure 2-9), determined by the Mohr-Coulomb criterion (El-Kelesh et al. 2001). Under a strain point of view, the following relationship can be assumed:

$$\varepsilon_{v,s} = \frac{V_g}{V_s} \quad \text{Equation 2-4}$$

$$\gamma_{s,0} = \frac{P_s}{V_s} \quad \text{Equation 2-5}$$

$$\gamma_{s,1} = \frac{P_s}{V_s - V_g} \quad \text{Equation 2-6}$$

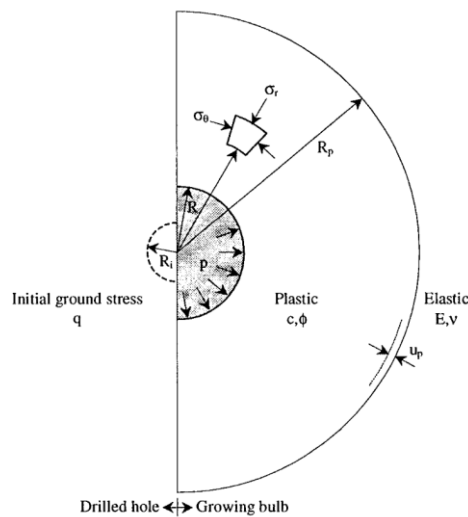


Figure 2-9 Cavity expansion scheme (El-Kelesh et al. 2001)

On the other hand, by considering the conical shearing failure mechanism in Figure 2-8, starting by the assumption reported in Figure 2-10, Wong (1974) proposed the following relation linking the treatment radius,  $R$ , to the limiting pressure,  $P_{g,max}$ , as follow:

$$p_{g,max} = \gamma \cdot z \cdot \frac{\left(\frac{z}{R}\right)^3 + 3\left(\frac{z}{R}\right)\tan\alpha + 3\tan^2\alpha}{3\tan^2\alpha} \cdot \left(1 + \frac{2(1 - \sin\varphi)\cos(180 - \alpha + \varphi)}{\cos\varphi \cdot \cos\alpha}\right) \quad \text{Equation 2-7}$$

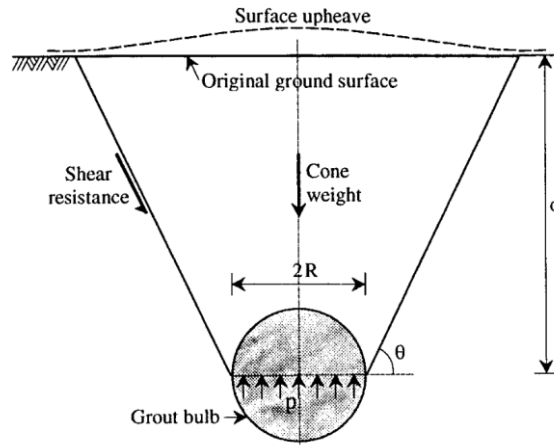


Figure 2-10 Conical shearing failure mechanism

Regarding to the third example in Figure 2-8, such a mechanism has to be neglected or, at least, reduced to a minimum, since it could lead to a permeation of the grout through the soil voids, leading to a different consolidation technique, but not a compaction grouting one.

Moreover, grain cementation is an alternative goal that can be achieved to improve the mechanical behaviour of granular soils, increasing their resistance to liquefaction phenomena. The main techniques that can be applied to that aim are mainly represented by:

- Low permeation grouting technique;
- Soil mixing technique;
- Jet grouting technique.

These techniques do not induce a densification of the soil, rather they carry on a cementation of the grains, resulting in an additional cohesive rate, improving the cyclic behaviour, and they are becoming even more reliable improvement techniques thanks to the increasing efforts faced in the geotechnical engineering practice and research.

### 2.1.3 LOW PERMEATION GROUTING

The low permeation grouting technique consists in the injection of a grout that permeates within the soil voids, with a relative low pressure of injection. The aim of the technique is such to develop a specific rate of cementation without dislocating the soil particles. In other words, the grout is slowly injected in order to not change significantly the effective stresses acting in situ. Thus, the technique represents an innovative mitigation solution, especially in developed sites with existing structures. In particular, a solvent- type silicate-based material diluted by water can be injected into the ground to replace the existing pore water and form a permanent gel which binds the particles of soil together

(Rasouli et al. 2016). A qualitative sequence of application is reported in Figure 2-11, in which four different stages are presented:

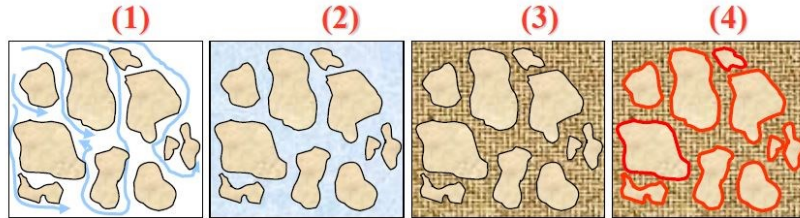


Figure 2-11 Qualitative scheme of low permeation grouting application

1. A grout, with relative low viscosity, is injected within the soil voids; without changing the soil's fabric;
2. The grout, in a fluid state initially, starts to increase its viscosity,
3. The grout begins to solidify, carrying out cementation bounds;
4. Cementation bounds are fully developed, and the soil's mechanical behaviour has been improved.

The main issue related to the application of the low permeation grouting, is an estimation of the treated volume by the grout injection. Several theoretical relationships are available, even if their previsions are heavily affected by the soil heterogeneity. For example, under a cylindric filtration hypothesis, the following relationship, at constant injection pressure, can be carried out:

$$t = \frac{\gamma_m \cdot n \cdot S}{4 \cdot p_i \cdot k_m} \left( 2 \cdot \ln \left( \frac{R}{R_0} \right) \cdot R^2 + R_0^2 - R^2 \right) \quad \text{Equation 2-8}$$

in which:

- $\gamma_m$ : unit weight of the injected grout;
- $n$ : porosity;
- $S$ : soil's degree of saturation;
- $p_i$ : injection pressure;
- $k_m$ : permeability of the soils to the injected grout;
- $R_0$ : radius of the injection borehole.

Thus, Equation 2-8 links the radius of the treatment to the injection time, which is upper bounded by the gelling time,  $t_{gel}$ , represented by the specific time from which the grout starts to increase significantly its viscosity, resulting in a null, or very low, injectability of the grout itself.

## 2.1.4 SOIL MIXING

Soil Mixing represents versatile consolidation technique consisting in the insertion a rotating device into the ground, on which propellers and / or mixing blades are installed, ensuring the disintegration and in-situ mixing of the soil, thanks to a binder inserted by means of special nozzles. An element (column, septum, etc.) is formed, and the resulting material shows higher shear strength resistance, lower deformability and permeability with respect to the surrounding soil. The mechanical and physical properties of the treated soils do not depend only on the type of binding agent used, but also on the way in which it was added and mixed to the soil and on the site-specific conditions of maturation. The advantage of the soil mixing technique lies in its wide range of applicability, with respect to the type of soil to be treated. Indeed, with the soil mixing technique it is possible to treat soils spacing from clean sands and gravels to clays (Bruce 2000). Typical soil mixing improving actions are qualitatively reported in Figure 2-12, in terms of possible geometry of treatment.

Soil mixing technique can be involved by means of two different methods, depending on the in-situ characteristics of the soil. Thus, these two different methods are:

- Soil mixing *Dry Method*;
- Soil mixing *Wet Method*.

In the dry method, binding is activated directly within the treated soil (it has to present sufficient natural water content to that aim). On the other hand, the wet method provides the chemical grout to be injected directly in a liquid state within the soil. Figure 2-13 and Figure 2-14 represent schematically the in-situ application, for the dry and wet method respectively.

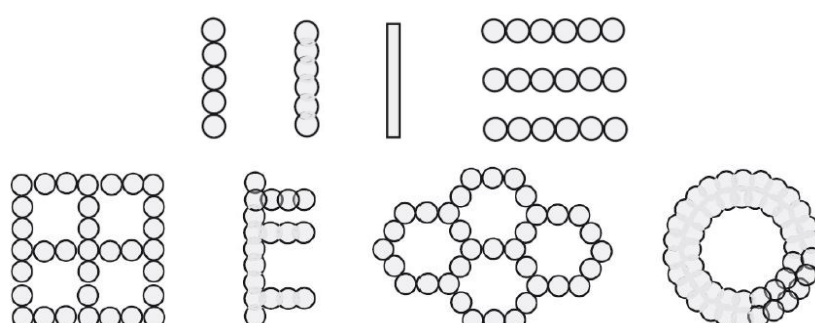


Figure 2-12 Typical Soil Mixing applications

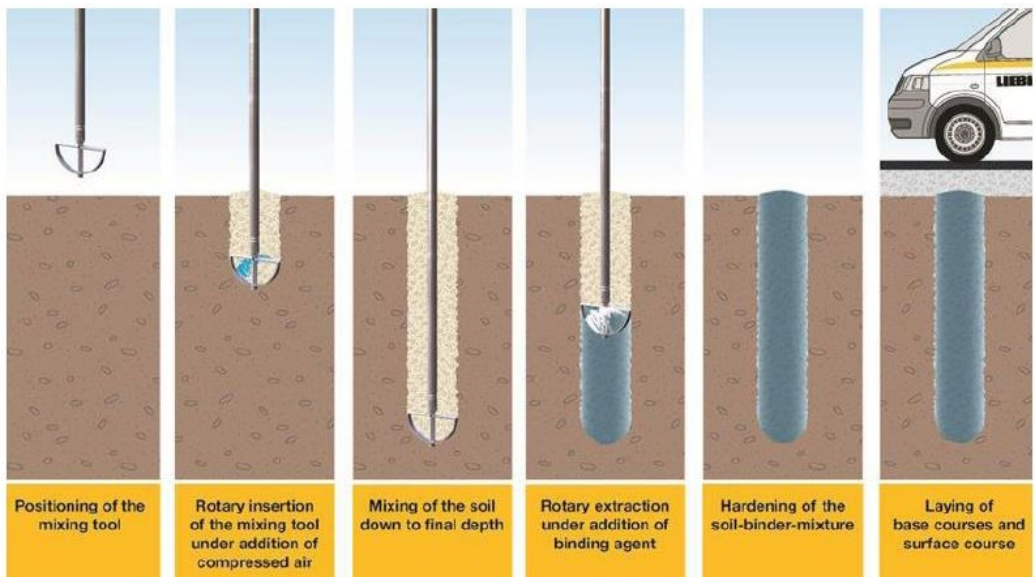


Figure 2-13 Example of dry method application

Regardless the applied method, different stages application can be considered. The final characteristic of the treated soil can be optimized by changing the execution procedures, as a function of the virgin soil and its stratigraphy. In Figure 2-15 different execution procedures are reported.

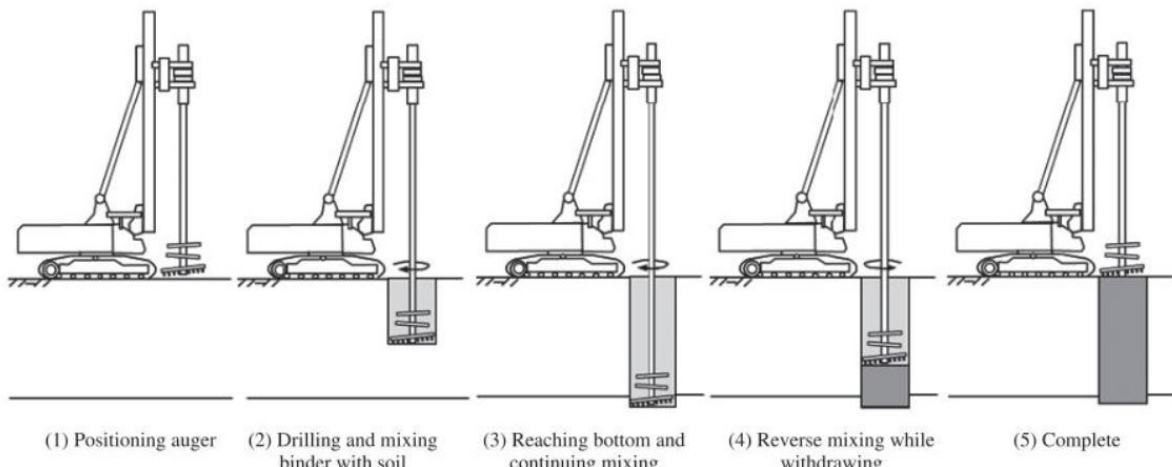


Figure 2-14 Example of wet method application

As it is shown, the following execution procedures can be carried out:

- Without or with bottoming;
- With reversal during penetration;
- With bottom restroking;
- With stepped restroking during withdrawal;

e) With full depth restroking.

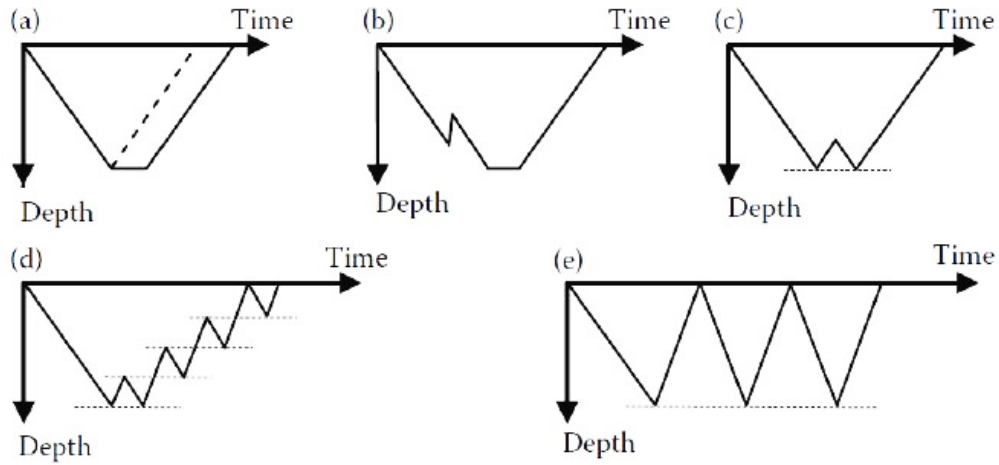


Figure 2-15 Typical execution procedures of deep soil mixing (Topolnicki 2004)

The choice of an execution procedure rather than others is a function of the stratigraphy and the different layers of soils that lie in the treated volume.

The soil mixing technique is often applied to carry on liquefaction mitigation actions, since it is a very versatile technique, applicable practically in all soils type and a wide range of geometry can be achieved as well. For example, a “*Lattice Type Configuration*” (Figure 2-16) is often applied to face liquefaction issues, since it represents a high efficiency measure against lateral spreading failures.

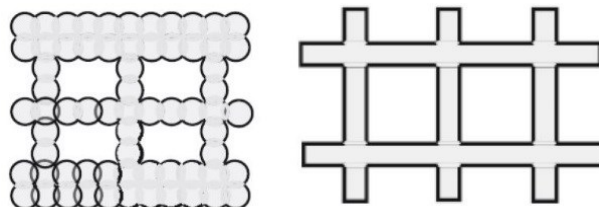


Figure 2-16 Lattice Type treatment

In Figure 2-17 a qualitative example of liquefaction mitigation action by means of soil mixing technique is reported.

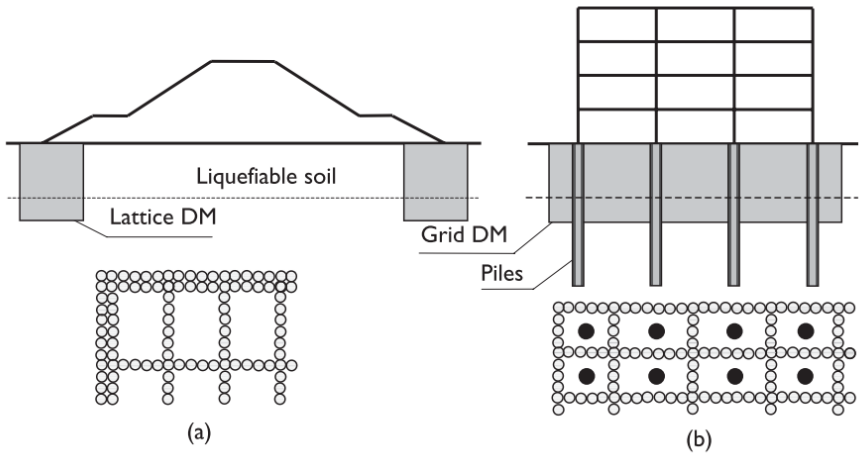


Figure 2-17 Examples of DM application for liquefaction mitigation (schematic): (a) protection of a river dyke; (b) improvement of the lateral resistance of piles (Topolnicki 2004)

## 2.1.5 JET GROUTING

Finally, regarding the cementation techniques, another reliable mitigation action is represented by the *Jet Grouting* technique. Jet grouting is a ground improvement technique able to carry out treated columns of soil-grout mixture, by means of the injection at very high velocities of a grout.

The technique involves a first perforation phase and a second phase in which the mixture is injected as the equipment rises (Figure 2-18). Practically, during the treatment the in-situ soil is disintegrated by the injection fluid, thanks to its high kinetic energy and then re-mixed, with consequent improvement of the relative mechanical and / or hydraulic properties. Since the disintegration is due to the high velocity jet, rather it is not a pure mechanical re-mixing— as for the soil mixing—, the generated columns are deeply influenced by the shear strength of the treated soil. Thus, the dimensions of the improved volumes are not constant with the depth, rather they will be variable as the mechanical characteristics of the soil change.

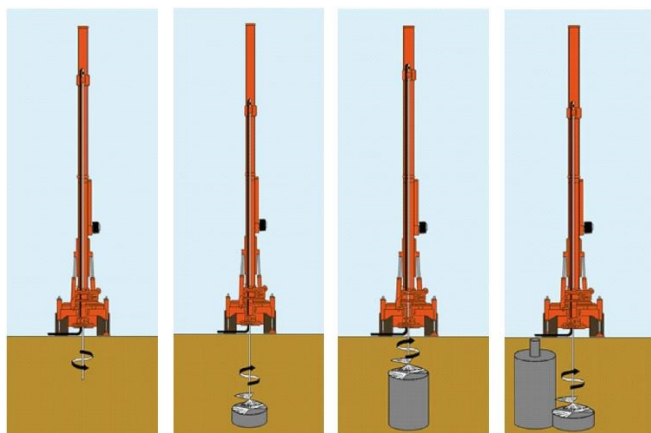


Figure 2-18 Jet grouting application phases

Several authors have widely investigated the relationship between the jet energy, the grout viscosity and technological parameters as well, with the final diameter of the obtained column. Flora et al. (2013) pointed out that a simple yet sound way to quantify soil resistance to erosion is to relate it to the soil shear strength. Thus, starting by the knowledge of in-situ testing (*SPT or CPT tests*) as well as the knowledge of the specific energy at the nozzles ( $E_{s,u}$ ), it is possible to estimate the final diameter using the following equations:

$$E_{s,u} = \frac{m \cdot v_u^2}{2 \cdot L} = \frac{\pi}{8} \cdot \frac{\rho \cdot M \cdot d^2 \cdot v_u^3}{v_r} \quad \text{Equation 2-9}$$

$$D_a = D_{ref} \cdot \left( \frac{\alpha \cdot \Lambda^* \cdot E_{(s,u)}}{7.5 \cdot 10} \right)^\beta \cdot \left( \frac{N_{SPT}}{10} \right)^\delta \quad \text{Equation 2-10}$$

$$D_a = D_{ref} \cdot \left( \frac{\alpha \cdot \Lambda^* \cdot E_{(s,u)}}{7.5 \cdot 10} \right)^\beta \cdot \left( \frac{q_c}{1.5} \right)^\delta \quad \text{Equation 2-11}$$

in which:

- $V_u$  is the velocity at the nozzle;
- $\rho$  is the grout density;
- $M$  is the number of nozzles;
- $d$  is the nozzle diameter;
- $v_r$  is the rise velocity;
- $\alpha$  is an empirical parameter depending on the technology used (*single/double/triple-fluid*);
- $D_{ref}$  is a reference diameter obtained with a single fluid jet grouting having  $\omega=1$ ,  $E_{(s,u)}=10$  MJ/m and  $q_c=1.5$  MPa or  $N_{SPT}=10$  (depending on the soil type);
- $\beta$  and  $\delta$  are empirical parameters to be calibrated by means of new or pre-existing field data;
- $\Lambda^*$  is a hydrodynamic dimensionless parameter (*Hinze, 1948*) taking into the interaction between the jet and the surrounding fluid.



Figure 2-19 Example of double fluid jet grouting field trial (Flora et al. 2013)

Thus, jet grouting as liquefaction mitigation technique can be used to reduce the susceptibility of granular deposits, since it is in fact a high efficiency treatment in cohesionless material. The cementation of the grains totally inhibits pore pressure rises, and the high execution speed of the technique makes the jet grouting suitable to liquefaction mitigation issues. On the other hand, because of the very high velocity of the jet, the technique is not applicable in urbanized area.

The brief framework discussed above, regarding the possible cementation techniques, represents only a limited range of the possible mitigation actions to face liquefaction phenomena. An alternative branch of ground improvement techniques is represented by drainage systems. Such mitigation actions, at which increasing attentions have been dedicated in the last years (Fasano et al. 2019; Ben Salem et al. 2015), allow to reduce pore pressure build up by means of the insertion of high-permeability devices. The presence of boundary surfaces able to drain rapidly the pore pressures induced by the seismic event can reduce significantly the liquefaction potential of granular deposits.

## 2.1.6 DRAINAGES SYSTEMS

Within this type of mitigation techniques, different solutions in the geotechnical engineering's panorama are available, such as the installation of prefab drains- vertical or horizontal- or the installation of stone columns. Regarding the possibility of taking advantage of prefab drains, an innovative design method is available in the literature for horizontal drains as liquefaction mitigation action.

Fasano et al. (2019) suggest design charts which link the pore pressure ratio,  $r_u$ , with the spacing between the horizontal drains and their diameter. Starting by the *Equation 2-12*, authors have developed design charts reported in Figure 2-20.

$$T_{ad} \left( \frac{\partial^2 r_u}{\partial \left(\frac{x}{d}\right)^2} + \frac{\partial^2 r_u}{\partial \left(\frac{y}{d}\right)^2} \right) = \frac{\partial r_u}{\partial \left(\frac{t}{t_d}\right)} - \frac{N_{eq}}{\pi A N_l} \cdot \frac{1}{\left( \frac{N_{eq}}{N_l} \cdot \frac{t}{t_d} \right)^{1-\frac{1}{2A}} \cdot \cos \left( \frac{\pi}{2} r_u \right)} \quad \text{Equation 2-12}$$

where:

- $A$  is a parameter shape for pore pressure build-up curve;
- $d$  is the drain diameter;
- $N_{eq}$  is the number of equivalent cycles of the shaking;
- $N_l$  is the number of cycles required to cause liquefaction;
- $r_u$  is the pore pressure ratio;
- $t$  is the time variable;
- $T_{ad}$  is the dimensionless time factor;
- $t_d$  is the significant duration of the shaking;
- $x$  and  $y$  are the space-domain coordinates.

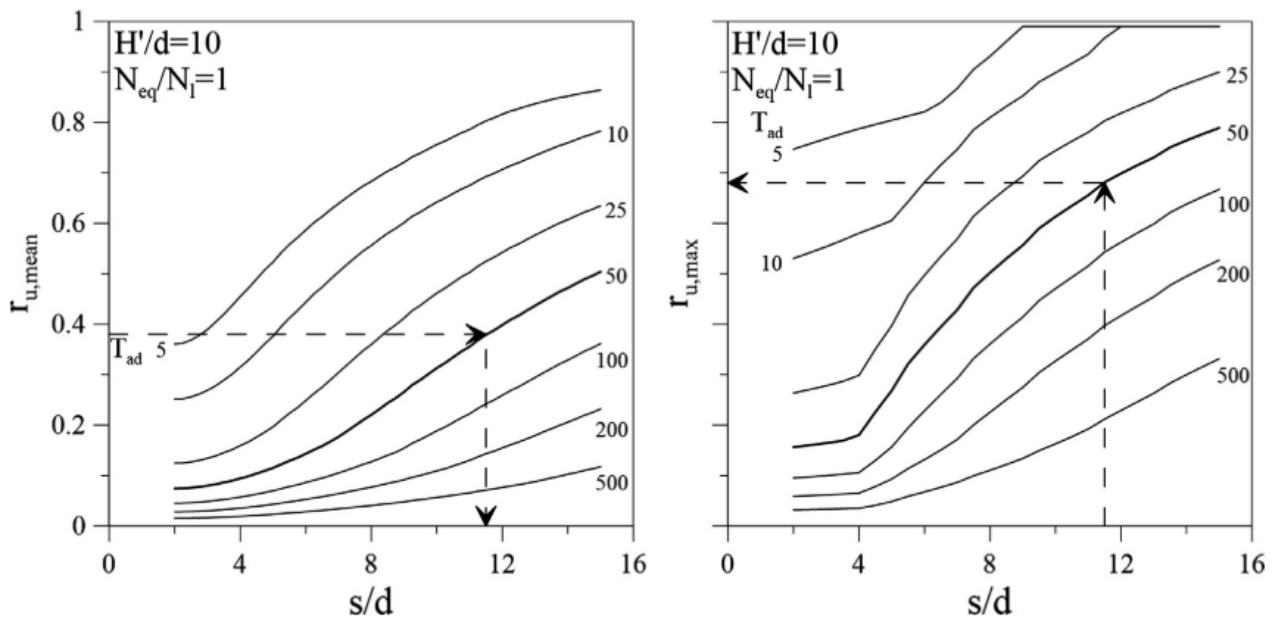


Figure 2-20 Design charts for horizontal drains (Fasano et al. 2019)

Thus, the above charts represent a very innovative approach to reliable design horizontal drains installation by imposing a pore pressure ratio target,  $r_u$ , and the significant duration of the shaking-by means of  $T_{ad}$ . As results, the ratio  $s/d$  can be easily obtained.

Ben Salem et al. (2015) studied the performance of reinforcement with granular columns as a method for the liquefaction mitigation. The installation of stone columns leads to the dissipation of

excess pore pressure due to the higher permeability of the inserted material. Actually, reinforcement can mitigate the risk of liquefaction through additional mechanisms, including the increase in the soil density during installation process of granular columns, and the increase in the lateral effective confining stress in the soil. Authors analyse numerically the influence of the changes in the permeability of the surrounding soil, by identifying a disturbed and undisturbed zone due to the stone column installation (as shown in Figure 2-21).

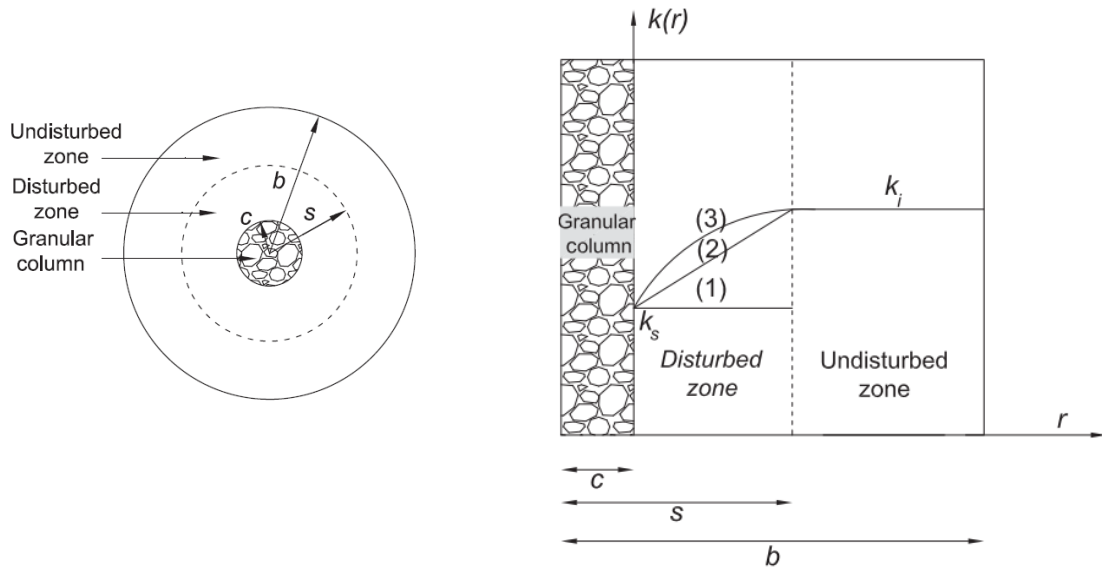


Figure 2-21 Variation of horizontal soil permeability: (1) reduced constant permeability, (2) linear variation of soil permeability, (3) parabolic variation of soil permeability (from Ben Salem et al. 2015)

Design charts are provided as a function of the permeability variation in the surrounding soil, for reduced constant (Figure 2-22), linear (Figure 2-23) and parabolic variation (Figure 2-24) of the soil permeability itself.

Authors also provide charts in which the peak of  $r_u^{\max}$  is related to the ratios  $s/c$  and  $k_i/k_s$  (Figure 2-25), pointing out that with the increase of granular-column spacing, the generation of excess pore pressure increases. Besides, the installation of granular column has significant influence on the generation and the dissipation of excess pore pressure; reduced soil permeability, and a larger disturbed zone around the granular column increases the peak value of the maximum pore pressure ratio  $r_u^{\max}$ . With linear variation of soil permeability in the disturbed zone higher values of the maximum pore pressure ratio  $r_u^{\max}$  are predicted, and the lowest values are obtained when reduced constant permeability is considered. The installation of the granular drains inevitably affects the permeability of the surrounding soil, thus a different permeability has to be considered certainly. In fact, the hypothesis of reduced constant permeability is not realistic: changes in soil permeability will

be lower as higher distances from the drains are considered. Thus, the linear variation of soil permeability is preferred, since it better models the installation effect of the granular columns and it is more conservative as well, since higher pore pressure ratio  $r_u^{\max}$  are predicted.

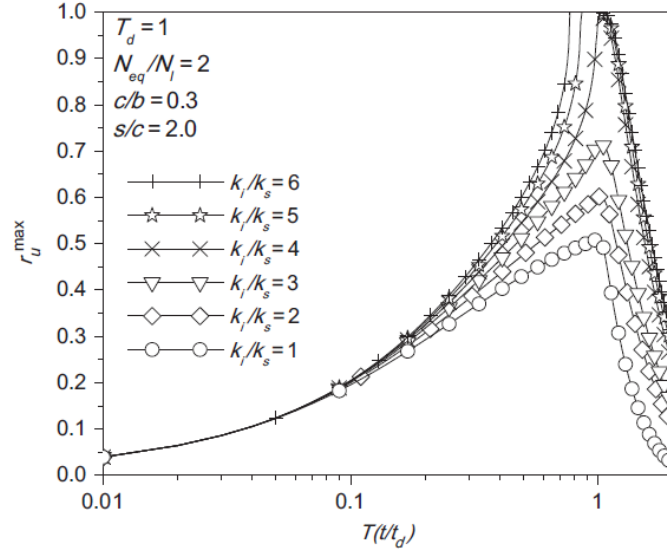


Figure 2-22 Variation of  $r_{\max} u$  with  $T(t / t_d)$  for different  $k_i / k_s$  in the case of reduced constant permeability in the disturbed zone

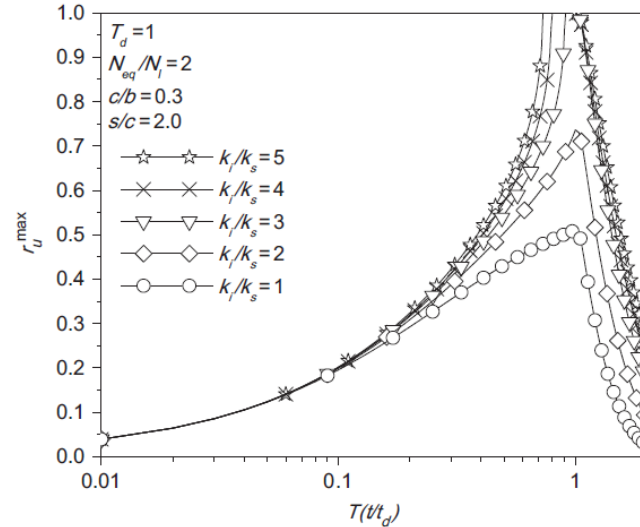


Figure 2-23 Variation of  $r_{\max} u$  with  $T(t / t_d)$  for different  $k_i / k_s$  in the case of linear variation of soil permeability in the disturbed zone

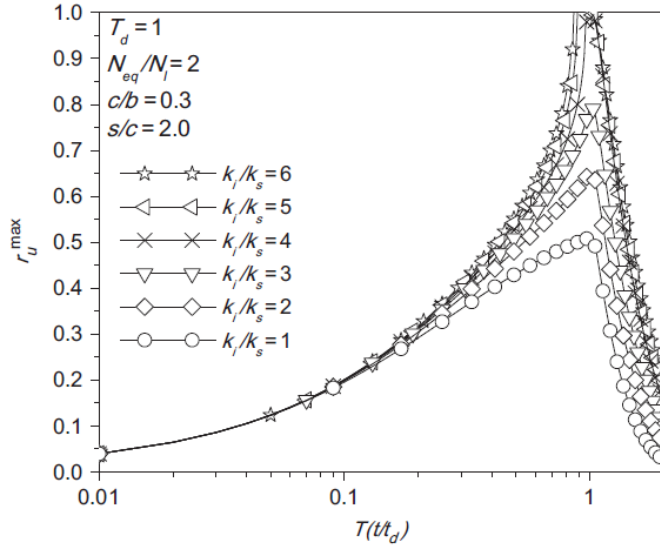


Figure 2-24 Variation of  $r_{u\max}$  with  $T(t / t_d)$  for different  $k_i / k_s$  in the case of parabolic variation of soil permeability in the disturbed zone

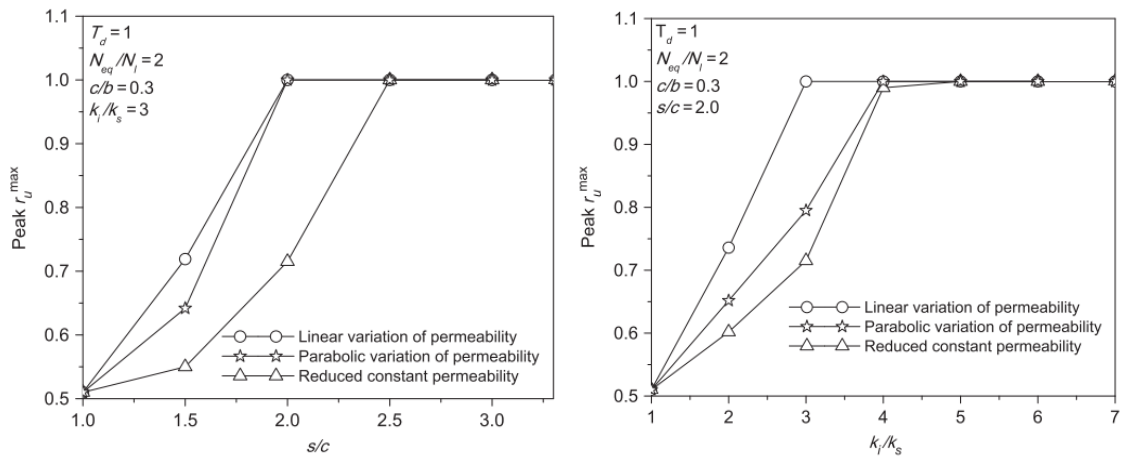


Figure 2-25 Variation of the peak values of  $r_{u\max}$  with radius ratio  $s/c$  (left) and  $k_i/k_s$

Finally, the saturation degree reduction, on which particular attention will be dedicated in the next sections, represent an alternative method to improve the cyclic behaviour of saturated cohesionless soils. Indeed, laboratory triaxial tests (Tsukamoto et al. 2014; Mele et al. 2018b) and centrifuge tests (Zeybek and Madabhushi 2017) have shown that the mechanical behavior of granular soils depends strongly on the degree of saturation. Cyclic undrained tests have demonstrated that even a small reduction in the degree of saturation can lead to a considerable increase of the cyclic resistance ratio. Different methods have been tested in previous studies, such as air injection (Okamura et al. 2011), water electrolysis (Yegian et al. 2007), chemical-sodium perborate (Eseller-bayat et al. 2013). Thus, in the next section a solid and wide framework about induced partial saturation (IPS) technique will

be reported, in order to underline the main aspects that make such technique a very useful one to face liquefaction risk mitigation.

### **3 CHAPTER 3**

#### **3.1 INDUCED PARTIAL SATURATION AS LIQUEFACTION MITIGATION TECHNIQUE**

Thanks to the ever more rapid development of science, technologies and inter-disciplinary approaches, liquefaction mitigation risk can be faced taking advantage of several innovative techniques. The increasing collaboration between different branches within the academic world is leading to the growth of innovative and reliable technologies, which look promising within the liquefaction risk mitigation framework, but still confined in the research environment so far. Thus, implementation, research, field trial tests, laboratory research as well as an ever more deeply understanding of all the processes involved using such technologies represent a key role for the industry to take advantage of these new potential applications.

Indeed, in the last few years, the solid link consolidated between different disciplines- not necessary included in the engineering ones- have led to different technologies such as the use of colloidal silica, bentonite or laponite. Among them, the development of an Induced Partial Saturation technique, using either chemical or biological approaches, represents a promising mitigation application, able to reduce the liquefaction risk with low or null disturbance on a hypothetic structure nearby. Several methodologies, as it will be seen in the following, can be carried on to lower the degree of saturation. Anyway, all of them aim to the achievement of a tri-phase-soil configuration, that is:

- a solid phase (grains);
- a liquid phase (pore water);
- a gas phase (e.g. air, nitrogen).

The presence of a gas phase- regardless its spatial distribution- leads to an important increase in the cyclic resistance of granular deposits, due to the higher volumetric compressibility of the gas itself, with respect to the water compressibility (practically incompressible in the pressures range of interest). The capability of the gas to compress itself- thus to change in volume- leads to a decrease in the pore pressures build up.

As it has been shortly underlined previously, laboratory tests have widely investigated the increase in the CRR due to the presence of the gas within the soil's pores. In Figure 3-1 and Figure 3-2 laboratory tests results are reported, ensuring that even a relatively small reduction of  $S_r$  leads to considerable increase in the cyclic resistance (*e. g. from 100% to 82-90%, Figure 3-1*).

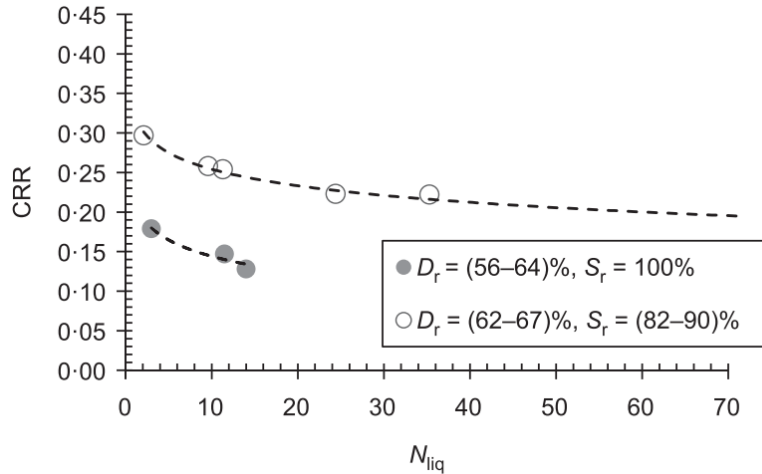


Figure 3-1 CRR for saturated and partially saturated sandy soils (Mele et al. 2019)

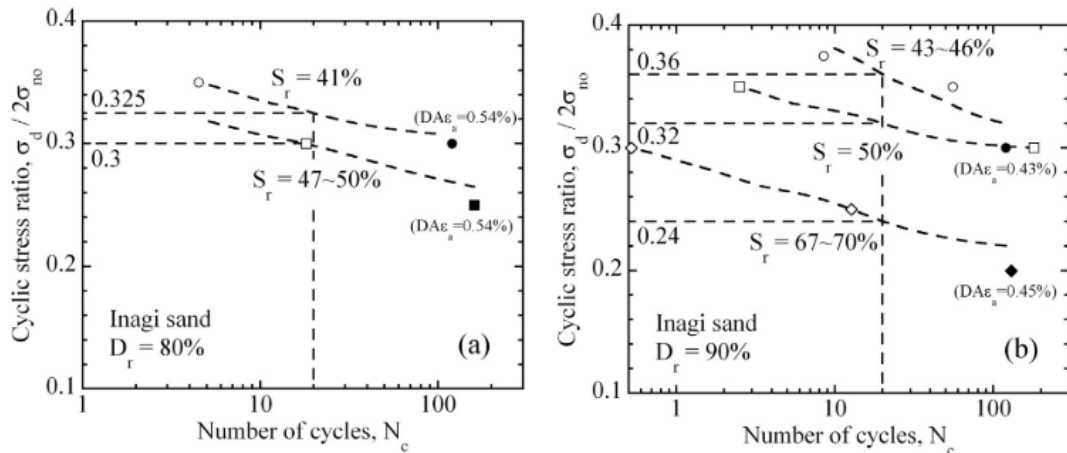


Figure 3-2 CRR for partially saturated soils (Tsukamoto 2018)

Thus, if the presence of a gas phase leads to a different mechanical behaviour of the soil, it is necessary to deeply understand first its possible configuration within the soil skeleton. Once the several gas phase distributions have been studied, it will be possible to differentiate the soil cyclic response as a function of the gas distribution itself.

To that aim, in Figure 3-3 possible gas phase distributions are reported (Leroueil et al. 2015), in which they are subdivided as follows:

- Continuous gas/discontinuous water;
- Continuous gas/continuous water;
- Discontinuous gas/continuous water (*small bubbles*);
- Discontinuous gas/continuous water (*large bubbles*).

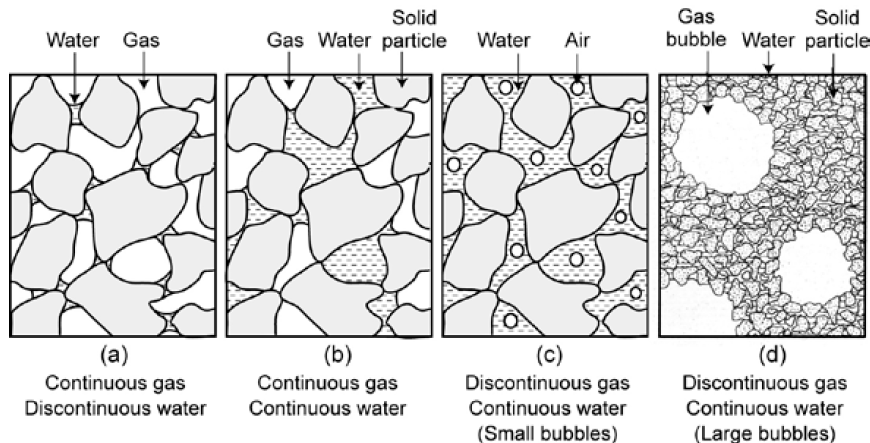


Figure 3-3 Possible gas phase distributions (Leroueil et al. 2015)

First of all, since the whole liquefaction processes are most influenced by the pore pressure rises, it is useful to identify a simple parameter able to take into account the presence of the gas- and its spatial distribution. To this aim, a first differentiation can be made on the basis of the well-known Skempton parameter,  $B$ , which can be easily obtained in triaxial tests as the ratio between  $\Delta u/\Delta \sigma_c$ . By using the  $B$ -value as a function of the degree of saturation, several authors (Kamata et al. 2009; Tsukamoto et al. 2014) proposed a conceptual subdivision of non-saturated soils, as will be discussed later on.

In fully saturated conditions, interparticle pores are completely filled with water, and no gas phase is present. In such conditions, a soil specimen subjected to an isotropic increase in total stress  $\Delta\sigma$ , in undrained conditions, assuming the fluid as practically incompressible, shows an increase in the pore pressure,  $\Delta u$ , equal to the total stress increment. This behavior leads the pore pressure coefficient  $B=\Delta u/\Delta\sigma$  to be equal to 1.

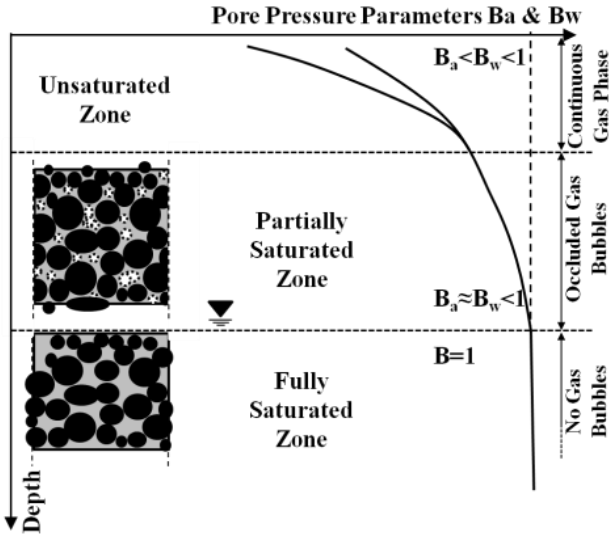


Figure 3-4 Schematic configurations of gas phases (adapted from Tsukamoto et al. 2014)

Actually, if soil is not fully saturated, under a total stress increment pore air and pore water pressure show different rates of increments and can be quantified (Vaughan 2003) by specializing the pore pressure parameters, always lower than 1, as  $B_a = \Delta u_a / \Delta \sigma$  and  $B_w = \Delta u_w / \Delta \sigma$ . Figure 3-4 shows, as a function of depth, the conceptual subdivision discussed above. Thus, following this type of subdivision, soils having a gas phase can be finally defined as (Tsukamoto 2018):

- Unsaturated, when the gas phase is continuous;
- Partially saturated, when the gas phase is discontinuous, i.e. the presence of the gas results in occluded gas bubbles fitting the pore spaces among the grains.

As pointed out by Leroueil et al. (2015), unsaturated soils can be detected when:

- soils are deposited above the water table, remaining unsaturated;
- soils are compacted to degrees of saturation lower than the degree of saturation at the optimum water content;
- When desiccation leads to gas entry at the soil-gas boundary.

On the other hand, partially saturated soils conditions can be mainly achieved when:

- soils are compacted to degrees of saturation higher than the degree of saturation at the optimum water content;
- soils containing dissolved gas are subject to a reduction in pore water pressure;
- gas is generated directly within the soil, for example recent sediments containing organic matter: microbiological processes can be involved, with consequent generation of gas (e.g. methane);

- When gas is trapped in some type of application, for example by wetting of soils in which the gas was previously continuous as a result of drying or compaction dry of optimum water content.

Successively, it is necessary to deeply investigate the laws and mechanisms that influence the gas phase. First of all, laws controlling gas conditions must to be taken into account. To this aim, both Boyle's (*Equation 3-1*) and Henry's (*Equation 3-2*) laws has to be considered:

$$P_g V_g = N_{mg} R T_k \quad \text{Equation 3-1}$$

$$P_{pg} = h_{wg} \left( \frac{N_{msg}}{N_{mw}} \right) \quad \text{Equation 3-2}$$

where  $N_{mg}$ = number of moles of gas,  $R$  = universal gas constant,  $T_k$ = absolute temperature,  $h_{wg}$ = constant of dissolution of gas in water,  $N_{msg}$ = number of moles of dissolved gas and  $N_{mw}$  = total number of moles of water.

On the other hand, under a mechanical point of view, it is fundamental the knowledge of laws controlling the mechanical behaviour. With regards to a continuous gas phase distribution, at the interface water-gas is present a surface tension,  $T_s$ , which plays a key role in the unsaturated soil mechanics. In particular, the surface tension is able to sustain extension stresses resulting in the possibility of the air pressure to be different from the water pressure. When the interface gas-water is curved, menisci exist and the difference between the air and water pressure is given by the following equation:

$$(u_a - u_w) = 2 \frac{T_s}{R_s} \quad \text{Equation 3-3}$$

which is the well-known capillarity law. In *Equation 3-3* is present the radius of the meniscus,  $R_s$ , and the previously discussed surface tension,  $T_s$ , which is equal to 73 mN/m for a temperature of 20°C at atmospheric pressure. The difference between air and pore water is called *matric suction*,  $s=(u_a - u_w)$  and results in an additional normal force between the grains (Wheeler and Karube 1995). Thus, the presence of the suction confers an additional shear strength to the soil itself. This mechanism results in unsuitability of the effective stresses principle, rather it is necessary to model the mechanical behaviour with a different approach.

### **3.1.1 PARTIALLY SATURATED SOILS MODELLING: FUNDAMENTAL CONCEPTS**

In the present section a simple and brief overview about partially saturated soil is reported, in order to frame the main concepts useful for the thesis' work. Possible gas phase configurations are discussed as well as their main conceptual implication regarding the soil's behaviour.

As previously discussed, a reliable parameter to divide unsaturated and partially saturated conditions is represented by the B-value. When a change in confining pressure is applied, both air and water pressures increase, and their rise can be evaluated by means of the different pore pressure parameters  $B_a$  and  $B_w$ . These two parameters show different values and are lower than 1 due to surface tension of pore water within soil aggregates (Tsukamoto 2018). In these conditions, the higher is the increment in the confining stresses, the lower becomes the matric suction. Conceptually, a transformation phase between continuous and discontinuous gas phase distribution will take place. Once the continuity of the gas phase is lost, a different configuration will exist: soils voids will be then partially filled by occluded gas bubbles. Theoretically, a difference in air and pore water pressure still exists, due to the presence of the surface tension (*Equation 3-3*). In fact, in such conditions, the water phase does not interact with the grains anymore. Suction is still present- in terms of difference of pressure between the bubble and pore water- but, since no interaction in terms of menisci is involved, suction can be neglected. Thus, no more additional shear strength will affect the mutual normal forces between the grains. The phase transformation leads the soil to be modelled differently. Indeed, since the existing bubbles are occluded and do not interact with the soil skeleton anymore, soil - which is tri-phase actually - can be seen as a bi-phase material, composed by a soil skeleton and an equivalent pore fluid composed of water and bubbles. As it will be seen in detail in the following, the bi-phase modelling of the material is useful to predict desaturation effects in engineering terms and therefore to face liquefaction mitigation risk by means of IPS technique.

In any case, even though the pore pressure coefficient represents a good parameter to explain the partially saturated configuration, the physical parameter ruling the phenomenon is the degree of saturation, obviously. Indeed, if the B-value is a reliable marker, it represents simply a total response of the soil to a change in its degree of saturation. As it has been reported in Figure 3-5, B-value is strictly correlated to the degree of saturation,  $S_r$ . The phase transformation from unsaturated to partially saturated conditions is deeply related to the grain size distribution of the soil itself. Anyway, if granular soils are investigated, a first order of magnitude of  $S_r$ - dividing the continuity/discontinuity of the gas phase- can be assumed to be near the 80% (Tsukamoto 2018).

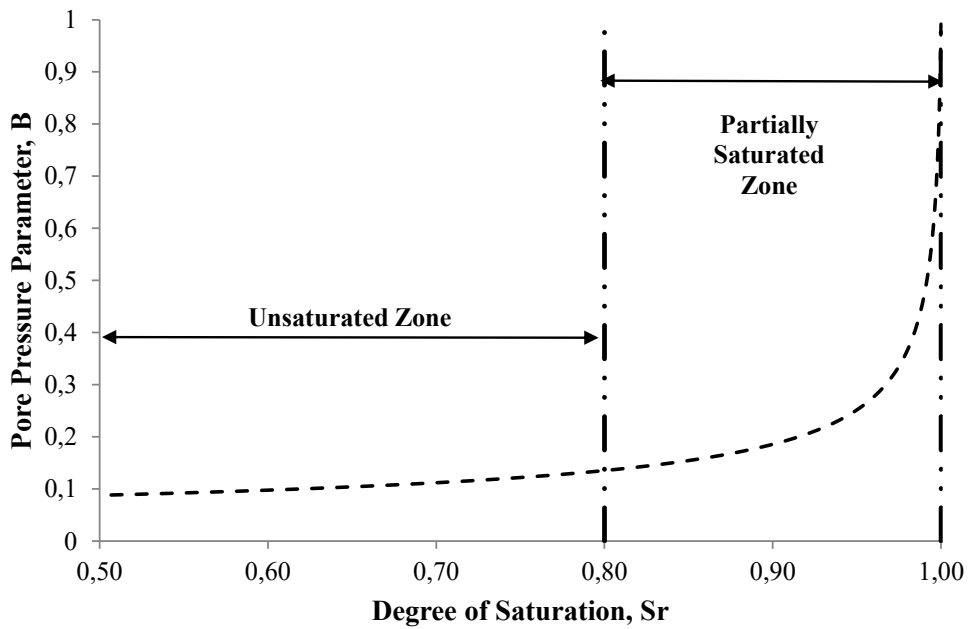


Figure 3-5 Correlation between degree of saturation and pore pressure parameter- transformation phase

Thus, the presence of occluded gas bubbles leads to a modelling of the soil as bi-phase material, represented by the soil skeleton and the equivalent pore fluid (*bubbles+water*), without changing the effective stresses since the intergranular forces keep unchanged (this is the reason why IPS is a low-impact technique, appealing for pre-existing structures). To that aim, the compressibility of the equivalent pore fluid must be taken into account, mainly influenced by the gas and concurrently the degree of saturation. Indeed, the equivalent compressibility represents the key parameter to deeply investigate the cyclic mechanical behaviour and, more important, the increase in the liquefaction resistance of the soil. In the following section the results of a wide investigation about the equivalent compressibility are reported.

### 3.1.2 EQUIVALENT PORE FLUID COMPRESSIBILITY

As previously reported in Figure 3-5, a correlation between Sr and B-value can be assumed. The change in the B-value is a simple consequence of a change in the degree of saturation. In order to increase the detail level, in Figure 3-6 a similar theoretical relationship is reported (from Tsukamoto, 2018), by assuming the theory of wave propagation through a poro-elastic medium (Tsukamoto et al. 2002).

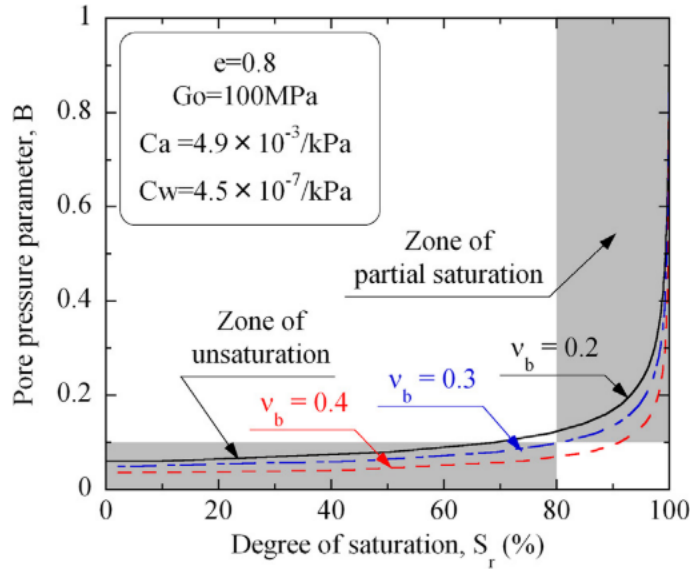


Figure 3-6 Degree of saturation versus pore pressure parameter (Tsukamoto 2018)

A change in  $S_r$  leads to a change in  $B$  which is connected, in turn, to the compressibility of the equivalent pore fluid. Kamata et al. (2009) suggest the following equation:

$$S_r = \frac{C_a - \frac{C_b(1-B)}{nB^2}}{C_a - C_w} = \frac{C_a - \frac{3}{2G_0n} \frac{1-2v_b}{1+v_b} \frac{1-B}{B^2}}{C_a - C_w} \quad \text{Equation 3-4}$$

Where:

- $C_a, C_w$  and  $C_b$  are the compressibility of pore air, pore water and soil skeleton respectively;
- $n$  is the porosity;
- $G_0$  is the initial shear modulus;
- $v_b$  is the skeleton Poisson's ratio.

Equation 3-4 leads to the relationship shown in Figure 3-6. The pore pressure parameter  $B$  has a sudden decrease as the degree of saturation drops from 100 to 80%. In this range of  $S_r$ , soils can be considered partially saturated and occluded air bubbles are contained within the pore spaces. The dependence of  $B$  on the initial shear modulus is also shown in Figure 3-5: the lower is  $G_0$ , the higher is the pore pressure parameter value to guarantee the same degree of saturation.

Equation 3-4 is able to predict, at a certain  $B$ -value, the corresponding degree of saturation taking into account the air compressibility. Actually, it is possible to define directly an equivalent compressibility of the homogeneous pore fluid using the following equation, derived by Fredlund & Rahardjo, 1993:

$$C_{aw} = S_r C_w B_w + (1 - S_r + HS_r) \frac{B_a}{u_a} \quad \text{Equation 3-5}$$

Where:

- $C_w$  is the compressibility of the pore water;
- $S_r$  is degree of saturation;
- $H$  is the volumetric coefficient of solubility for air in water;
- $u_a$  is the absolute air pressure.

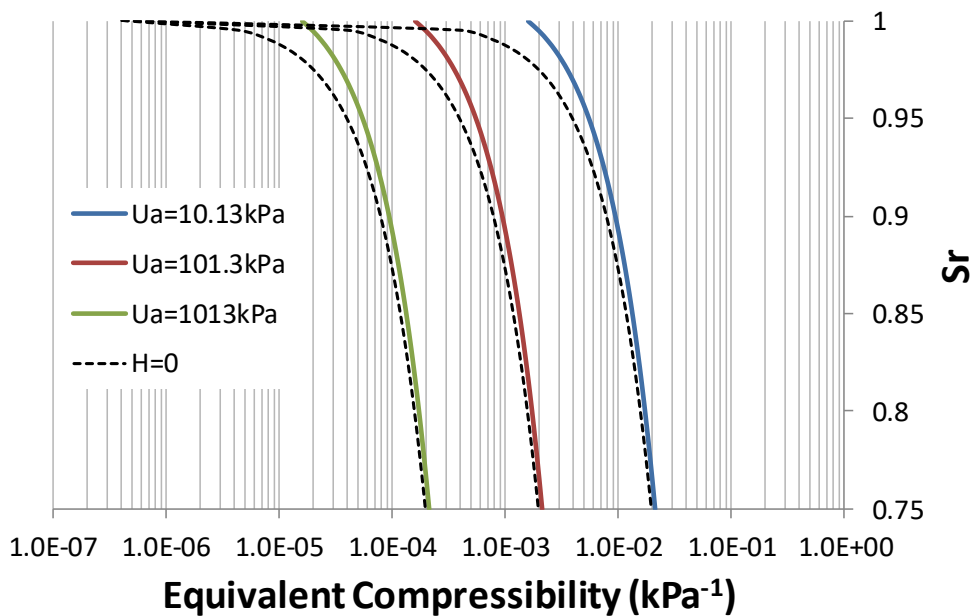


Figure 3-7 Correlation between degree of saturation and equivalent fluid compressibility

Equation 3-5 is plotted in Figure 3-7, for three different absolute air pressures. As it can be noted, at the same degree of saturation, the higher is the absolute pressure, the lower will be the equivalent pore fluid compressibility. In addition, it is possible to study the effect of the gas bubbles going under solution, by means of the volumetric solubility coefficient,  $H$ . Indeed, by considering the solubility of the gas, it can be ascertained that the presence of gas itself under solution can lead to sensitive changes in the equivalent compressibility, especially for degree of saturation close to 100%. Small reductions in degree of saturation below 100% have a major impact in increasing the compressibility of the pore-water-air mixture while, for decreasing  $S_r$ , the equivalent compressibility tends to be quite constant. On the other hand, the derivation does not consider surface tension effects, and so the effect of bubble size.

Schuurman, 1966, pointed out that the bulk modulus of water containing air bubbles,  $K_{aw}^*$ , can be given by the following equation:

$$K_{wa}^* = (V_a + V_w) \left( \frac{(V_{a0} + V_s)p_{a0}}{(V_a + V_a)^2} - \frac{4T}{3d_0} \frac{1}{V_a} \left( \frac{V_{a0}}{V_a} \right)^{\frac{1}{3}} \right) \quad \text{Equation 3-6}$$

where:

- $P_{a0}$  is the atmospheric pressure;
- $d_0$  and  $V_{a0}$  are the diameter and volume of air bubbles at atmospheric pressure;
- $V_w$  is the volume of water;
- $V_s$  is the volume of dissolved air into the water;
- $V_a$  is the volume of air bubbles.

Furthermore,  $V_s$  and  $V_a$  can be expressed as:

$$V_s = HV_w \quad \text{Equation 3-7}$$

$$V_a = \frac{(V_{a0} + V_s)p_{a0}}{p_a} - V_s \quad \text{Equation 3-8}$$

where it is possible to note that  $V_s$  will be dependent on the volume of water. The water pressure at a given air pressure can be expressed as follows:

$$p_w = \frac{V_{a0} + V_s}{V_a + V_s} \left( p_{w0} + \frac{4T_s}{d_0} \right) - \frac{4T_s}{d_0} \left( \frac{V_{a0}}{V_a} \right)^{1/3} \quad \text{Equation 3-9}$$

where  $p_{w0}$  is the initial water pressure. Thus, it is possible to take into account the effects of size and solubility of air bubbles on the degree of saturation as:

$$S_r = \frac{V_w}{V_a + V_w} \quad \text{Equation 3-10}$$

Finally, thanks to the framework reported above, it is possible to determine the B-value of a partially saturated soil containing air bubbles as:

$$B^* = \frac{1}{1 + \frac{n \left( \frac{1}{K_{wa}} - \frac{1}{K_s} \right)}{\left( \frac{1}{K_d} - \frac{1}{K_s} \right)}} \quad \text{Equation 3-11}$$

The role of compressibility of the air-water mixture have also been studied by Okamura and Soga (2006). Starting by the theoretical identification of the volumetric changes due to the presence of gas, authors investigated the impact of the back pressures at which the bubbles are present, in terms of cyclic resistance ratio. In detail, the volumetric changes caused by a change  $\Delta p$  in the pore pressure can be defined as follows, respectively for air and water:

$$\varepsilon_a = \frac{K_a}{\Delta p} \quad \text{Equation 3-12}$$

$$\varepsilon_w = \frac{K_w}{\Delta p} \quad \text{Equation 3-13}$$

In addition, the volumetric change of the equivalent pore fluid, composed by air and water, can be expressed as:

$$\varepsilon_{vf} = \frac{\Delta p}{K_f} = [(1 - S_r)\varepsilon_a + S_r\varepsilon_w] = \Delta p \left( \frac{1 - S_r}{K_a} + \frac{S_r}{K_w} \right) \quad \text{Equation 3-14}$$

where:

- $K_a$  is the bulk modulus of air;
- $K_w$  is the bulk modulus of water;
- $K_f$  is the bulk modulus of the equivalent pore fluid.

In *Equation 3-14*, the term  $S_r/K_w$  can be neglected, since  $K_w \gg K_a$ . Thus, considering soils grains as uncompressible and introducing the Boyle's law, volumetric strains can be expressed as:

$$\begin{aligned} \varepsilon_v &= \frac{\Delta p}{K_a} (1 - S_r) \frac{e}{1 + e} = \frac{\Delta p}{p_0 + \Delta p} (1 - S_r) \frac{e}{1 + e} \leq \frac{\sigma'_c}{p_0 + \sigma'_c} (1 - S_r) \frac{e}{1 + e} \\ &= \varepsilon_v^* \end{aligned} \quad \text{Equation 3-15}$$

in which  $p_0$  is the absolute pressure of the fluid and  $e$  its void ratio. If  $\Delta p$  reaches the maximum value, equal to  $\sigma'_c$ , then  $\varepsilon_v^{max} = \varepsilon_v^*$ .

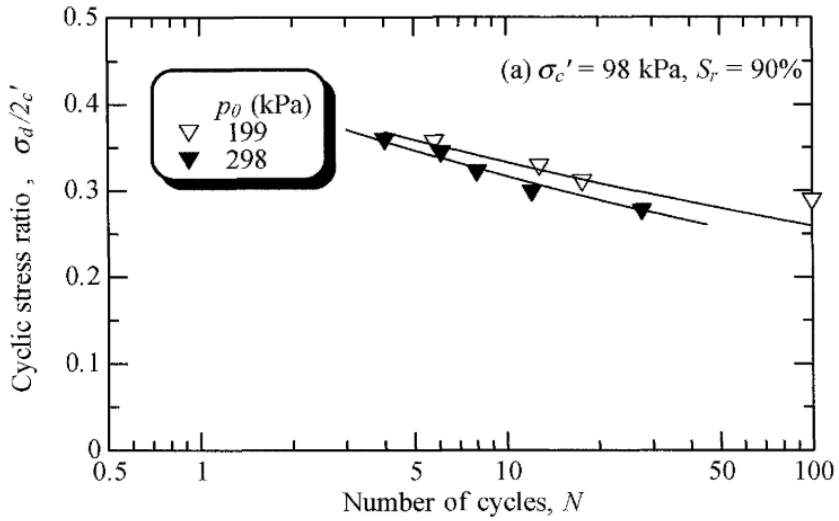


Figure 3-8 Influence of back pressure (hence equivalent pore fluid compressibility) on liquefaction resistance (Okamura and Soga 2006)

The results obtained by Okamura and Soga (2006), by means of triaxial tests on Toyoura sand and reported in Figure 3-8, underline the importance of considering the air-water mixture compressibility. At the same degree of saturation, hence at the same volume of air within the soils' voids, the number of cycles needed to reach liquefaction decreases with increasing back pressures- if the same cyclic stress ratio is applied. These results confirm that, even if the same Sr is achieved, the degree of saturation alone is not sufficient to assess the increase in the cyclic resistance of the cohesionless soil, rather it must be taken into account the pressures at which bubbles are subjected. The higher is the pressure, the lower will be the bubble's capability to sustain pore pressures rises- by decreasing its volume- hence, the compressibility will be lower.

The framework reported so far leads to the basic knowledge about the liquefaction phenomena. The main mechanisms leading to soil liquefaction have been examined as well as the triggering factors. Besides, several criteria to assess liquefaction susceptibility of granular saturated deposits have been discussed. Once the most recent research results have been reported, the main geotechnical engineering methodologies to face this type of failure have been presented. As it has been shown, several ground improvement techniques can be adopted to reduce liquefaction risk, depending on the type of site and soils. Among them, the induced partial saturation represents an alternative and low-cost solution. Its potential lies in the low invasive nature of the application itself, since the formation of occluded bubbles does not change the effective stresses. The principal mechanical aspects, regarding the gas phase distribution as well as the key role of the equivalent pore fluid compressibility, have been discussed. Thus, to face liquefaction issues using IPS technologies, it was necessary to study adequately the right way to model the partially saturated soil. To this aim, a brief

subdivision of the two main possible configurations has been made. The following section will be dedicated to different approaches able to obtain partially saturated conditions. In particular, different interdisciplinary solutions will be reported. Among them, the present work will be focused on a biochemical approach to induce the partial saturation by means of biological microorganisms, able to generate gas bubbles through their own metabolism.

### **3.2 INDUCED PARTIAL SATURATION: A MULTIDISCIPLINARY APPROACH**

As it has been previously discussed, mitigation actions such as drainage, densification, desaturation, as well as addition of plastic fine content, can be implemented to reduce pore-pressures build-up and therefore to increase the liquefaction resistance of granular soils under both static and dynamic loads. Even though most of the existing mitigation actions can be reliably designed, they are quite expensive and often unsuitable in case of urbanized area, in which pre-existing structures are present.

The main requirements to develop innovative techniques to tackle with the liquefaction risk are:

- non-disruptive mitigation techniques;
- large improvement area at low cost;
- environmentally compatible improvement techniques.

For example, most of the traditional techniques can cause deformations and/or vibrations during the installation, leading to non-compatible interferences with structures nearby (Gallagher et al. 2007). In addition, even if compatible sites are treated, traditional mitigation actions can be of high-energy consumption and often quite expensive (Khodadadi and Bilsel 2012).

Hence, induced partial saturation by means of non-invasive injection technique is appealing as it leads to an increase in the compressibility of the pore fluid. Hence, pore pressure build up is reduced and an increase in the soil cyclic resistance is achieved without affecting the structures nearby. Actually, desaturation can be induced either by lowering the groundwater table or by generating gas bubbles within the soil pores (Yoshimi et al. 1989). The former is more invasive, and a high desaturation is achieved, the latter is less invasive and a wide range degree of saturation can be obtained, depending on the amount of gas bubbles induced within the soil. The present work is focused on an IPS technique able to generate gas bubbles directly within the soil voids, allowing to a discontinuous distribution of the gas phase itself.

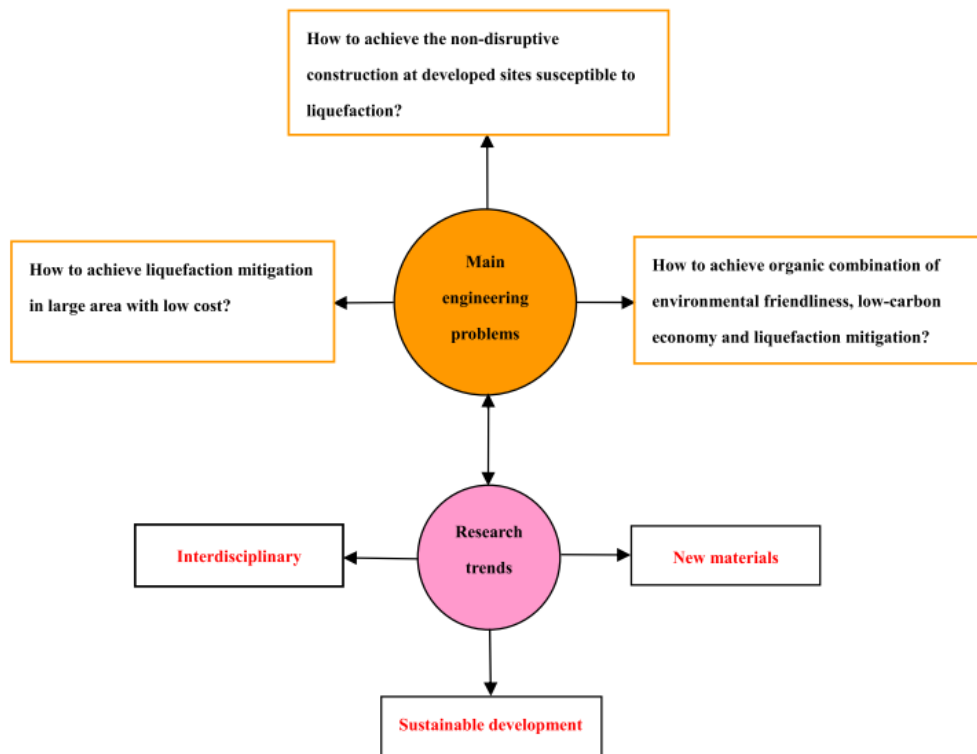
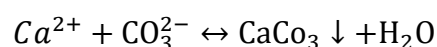


Figure 3-9 Main engineering problems and research trends of liquefaction mitigation (from Huang and Wen 2015)

Indeed, in the last few years increasing attention has been focused on innovative techniques, developed under a multidisciplinary approach, leading to the collaboration between several branches-not strictly involved in the geotechnical engineering panorama. Currently, researchers are focused on applying recyclable materials and developing liquefaction mitigation methods that can lower carbon emissions (Baharuddin et al. 2013). The research direction is continuously evolving, and the focus is to achieve low-cost and non-disruptive mitigation (Towhata 2008; Huang and Wen 2015).

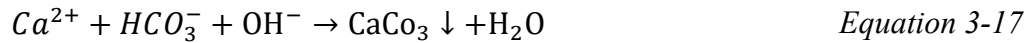
An example of multidisciplinary approach is given by the application of the so called MICP method (*Microbial-Induced Carbonate Precipitation*). The MICP does not lead to the generation of gas bubbles, rather it takes advantage of bacteria metabolism to induce a bio-chemical reaction leading to the formation of carbonate. Thus, even if MICP does not represent a pure IPS technique, it shows the potential of collaboration between different disciplines.

The creation of calcium carbonate (calcite) cement occurs as a consequence of bacterial metabolic activity that raises the pH of the proximal environment (DeJong et al. 2006). The main reactions leading to the formation of calcium carbonate are reported in the following:



Equation 3-16

which represents the overall equilibrium reaction. Furthermore, microbiologically induced calcite precipitation occurs according to the reactions (Ramakrishnan et al. 2001).



Once the cementation structure has been developed thanks to bacteria metabolism, granular soils-MICP treated show an increase in their cyclic resistance, due to the precipitation and subsequent calcification of  $CaCO_3$ . The improvement of mechanical behavior can be assessed through triaxial undrained tests as well as bender element tests. As an example, Figure 3-10 shows the increase, during time, of  $V_s$  velocities (by means of bender element tests) due to the cementation carried out during a MICP method application. The increasing in  $V_s$ , hence the increasing in soil's stiffness, leads to an increase in the liquefaction resistance of the soil itself.

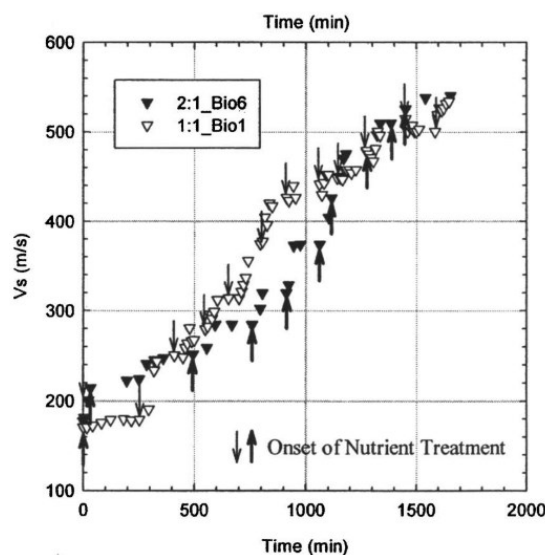


Figure 3-10 Increasing in shear wave velocities after a MICP treatment (DeJong et al. 2006)

In addition, Van der Ruyt and van der Zon, 2009 tested MICP treated soil under unconfined conditions. Tests results in terms of UCS (uniaxial compressive strength) are reported in Figure 3-11. It can be pointed out that UCS strength increases with increasing calcium carbonate content. For normal applications, the UCS strength required is less than 3 MPa (Chu 2016), which could be easily achieved with a calcium content of 100 to 200 kg/m<sup>3</sup>. To achieve the same UCS strength for sand using cement grouting, the amount of cement used would be between 250 to 300 kg/m<sup>3</sup>.

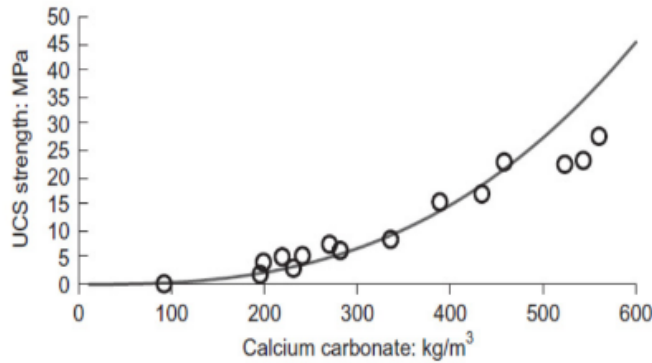


Figure 3-11 Unconfined compression strength (UCS) versus calcium carbonate content relationship for biocement treated sand (after Van der Ruyt and van der Zon, 2009)

On the other hand, MICP can lead to the formation of ammonia and ammonium, that need to be removed, due to their environmental incompatibility. As it will be shown in detail in the following sections, alternative bio-chemical improvement techniques can be adopted to neglect the formation of incompatible sub-products.

Anyway, this brief introduction aims to the underlining the potential of multidisciplinary approach, leading to the development of interesting, promising and innovative techniques. Such a collaboration can cover and solve different issues related to different area of study, allowing to the identifications of innovative technologies focusing on their effectiveness in terms of geotechnical results as well as of low-cost application and, most of all, environmental compatibility. In the next section, different multidisciplinary approaches will be presented, focusing on technologies able to induce a partial saturation of the soil.

### 3.2.1 INDUCED PARTIAL SATURATION: POSSIBLE MITIGATION TECHNIQUES

In order to induce the partial saturation within the soil, several applications have been considered in the recent research panorama. Indeed, different techniques have been proposed to induce partial saturation in sand to mitigate liquefaction hazard (Ciardi 2017). The tested techniques, which differ for physical, chemical or bio-chemical approach, are mainly:

- Drainage-recharge;
- Air injection;
- Water electrolysis;
- Use of chemicals;
- Use of biogas.

### 3.2.1.1 Drainage Recharge

The drainage recharge technique aims to entrapping air bubbles within the pores, by means of lowering and successively recharging the water table. During the lowering phase, the extraction of the pore fluid from the voids leads necessarily the air to replace the pore water. At a later time, ground water level is supposed to be gradually re-established to the initial value. Hence, the process allows to the entrapment of the previously generated air. With this technique, a partially saturated condition is then achieved. In addition, such a technique has been tested by Yegian et al. (2007) at laboratory scale. Authors induced the partially saturation by recharging procedure starting by a fully saturated Ottawa sand specimen in a flexible liquefaction box, able to induce a simple shear deformation generated by a shaking table excitation (hence able to investigate the effectiveness of the treatment). Once the full saturation has been ensured, the pore water has been slowly drained from the bottom of the box. Afterwards, the drained water was reintroduced at a slow rate from the top of the specimen, as reported in Figure 3-12.

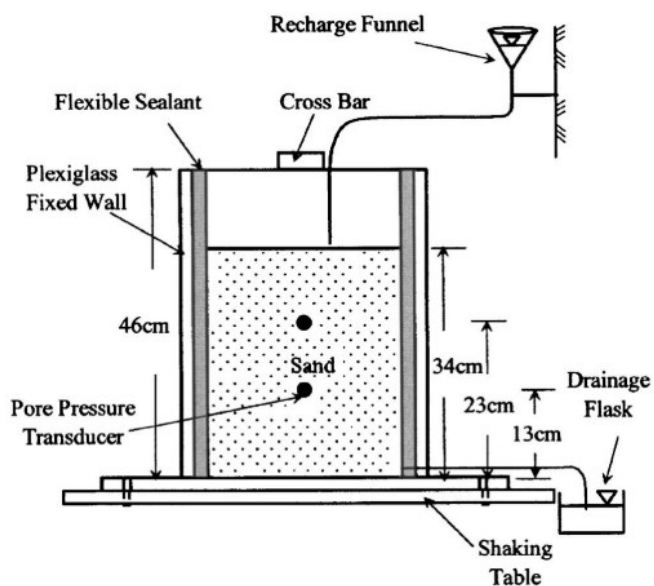


Figure 3-12 Induced partial saturation setup for recharge procedure (from Yegian et al. 2007)

After reintroducing all the drained water, a significant amount of water remained above the surface of the sand specimen indicating entrapment of air during recharge. The recharge method could represent a reliable technique to induce the partial saturation but, since the lowering of the ground water level (in field scale) is needed necessarily, significant changes in the effective stresses will be induced- hence, ground level deformations- resulting in a low applicability for urbanized area and/or pre-existing structures.

### 3.2.1.2 Air Injection

An alternative technique to physically induce the partial saturation is represented by the possibility of directly injecting an amount of air in a susceptible layer, simply by pumping a specific volume of gas. Actually, the air injection technique finds its original application in the environmental engineering, with the aim to reduce pollutions of heavy metal within the soil (the so-called *air-sparging* technique). Anyway, several authors have examined the potential applicability of the technique. Okamura et al. (2011) pointed out that, if the effectiveness of air injection needs to be investigated, it is necessary to own solid basis- as well as reliable implementation system- able to predict and asses the airflow pattern and the influence zone. Yasuhara et al. (2008) pointed out that the zones of influence depend on soil type, soil stratifications, and air-injection pressure and depth.

The flow of air injected through saturated soils will be initiated where air pressure at the injection point surpasses the value enabling air to penetrate pore water (Okamura et al. 2011). In other words, to trigger air flow, the injection pressure must overcome a specific pressure, equal to the sum of the hydrostatic and capillarity pressures- that could arise from the presence of soil- (Marulanda et al. 2000). For a cohesionless material the injection pressure could be expressed as follow:

$$P_{inj}^{max} = \min(\sigma'_{vertical}; \sigma'_{horizontal}) \quad \text{Equation 3-19}$$

Operatively, IPS by means of air injection could be easily carried out by pumping air from the ground surface, as conceptually shown in Figure 3-13.

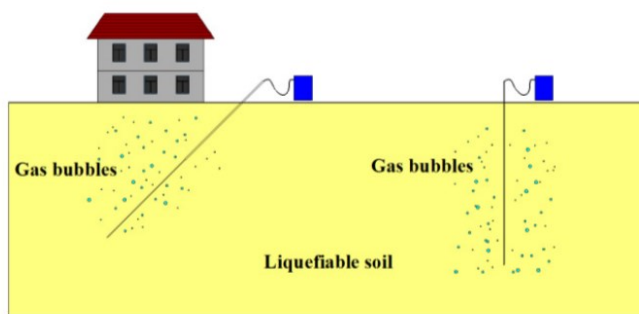


Figure 3-13 Conceptual example of air injection application (Chu 2016)

Flora et al. (2020) performed a trial field to test the effectiveness of IPS – by means of air injection – at a true scale in a site located in Pieve di Cento, Emilia Romagna region, in Italy (where liquefaction occurred in the 2012 earthquake). Innovative well screens were set in place: they are made of micro-pored polyethylene and have been designed to minimize flow resistance by means of

a greater porosity -compared to conventional ones- uniformly distributed along the pipe's entire length. The pipes were installed by means of a Directional Drilling Technique DDT (Figure 3-14).



*Figure 3-14 Directional drilling equipment (Flora et al. 2020)*

Authors additionally pointed out that, by using such an installation technique, the disturbance on a possible overlying structure is heavily minimized, as reported in Figure 3-15.

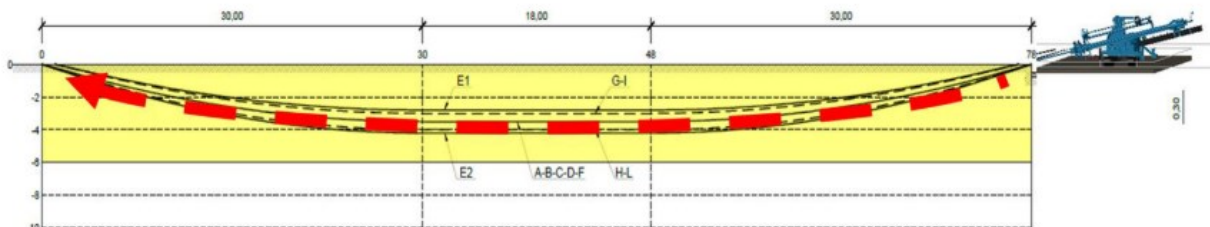


*Figure 3-15 IPS air injection application by means of directional drilling installation (Flora et al. 2020)*

Thus, the air injection technique represents an appealing ground improvement action, since it can be suitable for existing structures – thanks to the limited installation disturbance – and low-cost. On the other hand, the distribution of gas bubbles introduced by pumping will not be uniform for all the treated area. Furthermore, the gas pumped into the ground tends to aggregate in gas pockets rather than producing individual bubbles. As a result, the gas tends to escape from the ground.

### **3.2.1.3 Water Electrolysis**

Another technology that can be used for liquefaction mitigation is represented by water electrolysis. This technique is largely used for the enhancement of in situ remediation of contaminated soils (Acar and Alshawabkeh 1993). Actually, since the water electrolysis process leads to the formation of gas, it has been recently adopted to face liquefaction risk or, at least, to be investigated

in laboratory tests. Practically, electrolysis consists in the ionization of hydrogen and oxygen gases when an electrical current is induced within the water by using electrodes.

As reported by Yegian et al. (2007), electrolysis was selected as an efficient application to induce partial saturation since it introduces gas into the soil pores without application of any pressure. Oxygen and hydrogen are produced by water electrolysis, respectively at the anode and cathode, following the ensuing chemical reactions:



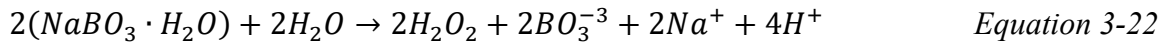
It is conceptually important to underline that, since  $H_2$  is produced by the electrolysis process, it must be lower than critical quantities, seeing as how hydrogen is considered the most unstable gas with respect to safety explosion hazard. Thus, gases produced by electrolysis should be enough to ensure the target increment in the liquefaction resistance and, concurrently, they must be lower than specific quantities with respect to safety hazard issues. However, authors pointed out that electrolysis produced variation in the degree of saturation high enough to significantly increase the cyclic resistance, without exceeding critical quantities.

Desaturation tests on initially saturated specimens, performed in a shaking table equipped with electrodes, allowed the authors to determine the level of current and length of time needed to generate an appreciable amount of gas. The process of electrolysis was maintained until hydrogen bubbles were generated at the cathode and migrated through the soil specimen toward the anode (Yegian et al. 2007). In addition, visual inspection and probing confirmed that the process was able to reduce the average degree of saturation of the specimen. However, water electrolysis method needs a current to be applied to the soil, resulting in a probably high-cost application of the technique itself. Moreover, the current application leads to a non-uniform distribution of the gas bubbles within the sand specimens, as pointed out by Eseller-Bayat et al. (2013).

### **3.2.1.4 Use of Chemicals: Sodium Perborate**

An alternative approach to achieve partially saturated conditions lies in the employment of chemical compounds able to generate gas bubbles. To this aim, as reported by Eseller-Bayat et al. (2013), sodium perborate monohydrate ( $NaBO_3 \cdot H_2O$ ) can be used to reduce the degree of saturation.

This chemical compound, also known as *PBS-1*, is able to generate oxygen following the chemical reaction with water:



Under a chemical point of view, sodium perborate monohydrate reacts with water and generates hydrogen peroxide ( $\text{H}_2\text{O}_2$ ), which is a ready source of oxygen gas. Hence, thanks to chemical reaction reported in *Equation 3-23*,  $\text{O}_2$  gas is formed, and partially saturated conditions can be achieved. Operatively, authors carried out a wet pluviation of *dry sand+PBS-1* to set up partially saturated samples. After the preparation, a high-resolution camera was used to assess the uniformity of the desaturation process. As shown in Figure 3-16, the use of sodium perborate monohydrates can lead to even distribution of gas bubbles within the soil voids as well as to a degree of saturation also lower than 80%.

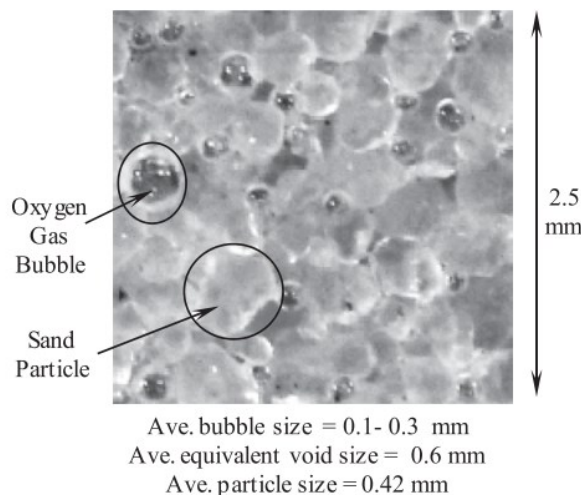


*Figure 3-16 High resolution frame of a sand specimen desaturated by means of sodium perborate (Eseller-bayat et al. 2013)*

In conclusion, sodium perborate monohydrate can be used to achieve degree of saturation also lower than 80%, ensuring a good distribution- in terms of uniformity- of the oxygen generated bubbles. On the other hand, the use of PBS-1 in real scale mitigation actions could be difficult, due to its very fast reaction with water, resulting in a low applicability of the process itself.

### **3.3 USE OF BIOGAS**

Under a biological point of view, soil represents an ecosystem. There are typically 40 million bacterial cells in a gram of soil and a million bacterial cells in a milliliter of fresh water (Wu 2015). Thus, if a different prospective is assumed, soil can be seen as a complex living system, allowing microorganisms to carry out a wide range of simultaneous processes (DeJong et al. 2011). Actually, most of the combined bio-geotechnical ground improvement methods start by scaling classic environmental application to civil engineering issues. The increasing knowledge about microorganism's metabolism, as well as the processes they are able to carry on, leads to the opportunity of adapting biological processes as alternative and innovative real scale applications.

#### **3.3.1 BIOLOGICAL FRAMEWORK**

Since microorganism natural activities lead to an important amount of produced gas- on a worldwide scale- it is reasonable to take advantage of specific bio-chemical reactions to face specific geotechnical issues, such as liquefaction phenomena. Indeed, if a desaturation of the soil is needed, several microorganism skills can be exploited to generate a gas phase within the liquefiable layers.

Microorganisms can be grouped in three different categories: archaea, fungi and bacteria. Fungi are eukarya and hence more closely related to plants and animals than to bacteria or archaea. Like all eukarya, including humans, fungal cells contain membrane-bound nuclei with chromosomes that contain DNA. On the other hand, bacteria and archaea are the smallest independently living, single-celled organisms on earth. Typical cells range from 0.5 to 1.0  $\mu\text{m}$  in diameter (Aislabie et al. 2013). All such microorganisms are key players in the turnover of soil organic carbon (*SOC*) in the large carbon storages (Tveit et al. 2015).

Thus, their metabolisms can lead to the formation of several gases, depending on the type of biochemical reaction involved in the process. The main gases produced by microorganisms are represented by:

- Carbon dioxide,  $\text{CO}_2$ ;
- Carbon monoxide,  $\text{CO}$ ;
- Nitrogen,  $\text{N}_2$ ;
- Methane,  $\text{CH}_4$ ;
- Nitrous oxide,  $\text{N}_2\text{O}$ ,

Each of the gases mentioned above are produced by both bacteria and archaea, depending on the type of sources available in the soil as well as the type of environment in which microorganism are present. A typical profile of the soil and microbials' habitat is shown in Figure 3-17.

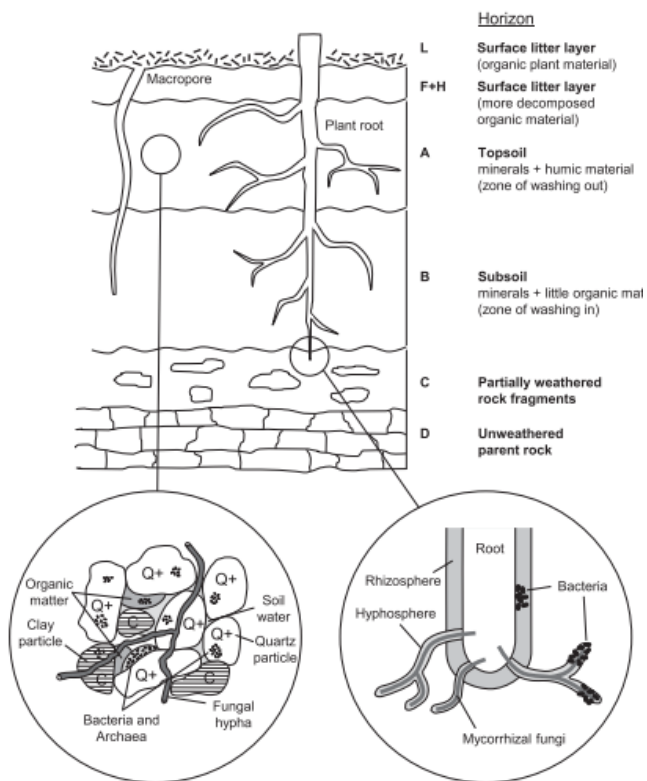


Figure 3-17 Typical soil profile showing horizons and microbial habitats (Aislabie et al. 2013)

If one of these gases would to be used to induce a partial saturation, definition of the bio-chemical reactions involved is needed first. To this aim, in Figure 3-18 the carbon cycle is shown. It is possible to note as, thanks to microbial activity, both  $CH_4$  and  $CO_2$  are produced. Actually, their production is linked in turn, as shown in Figure 3-19. Under strictly anaerobic conditions, *methanogens* – a particular type of microorganisms, belonging to archaea – can use the available hydrogen to reduce dioxide carbon,  $CO_2$  and produce methane gas,  $CH_4$ . When methane gas rises in the shallower soil layers it can be oxidized by *methanotrophs*, that are microorganisms consisting mainly of bacteria. As results,  $CO_2$  is produced. However, both  $CH_4$  and  $CO_2$  are not suitable to be used for IPS, since they have high environmental impact. Indeed, both gases are among the main impacting *green house gases* (GHG), absorbing and emitting radiant energy within the thermal infrared range. In addition, especially dioxide carbon shows a high solubility in water. As result, if  $CO_2$  is supposed to be the generated gas from a IPS mitigation action, an important amount of  $CO_2$  would be under solution, leading to a lower amount of the same  $CO_2$  under occluded gas bubbles conditions.

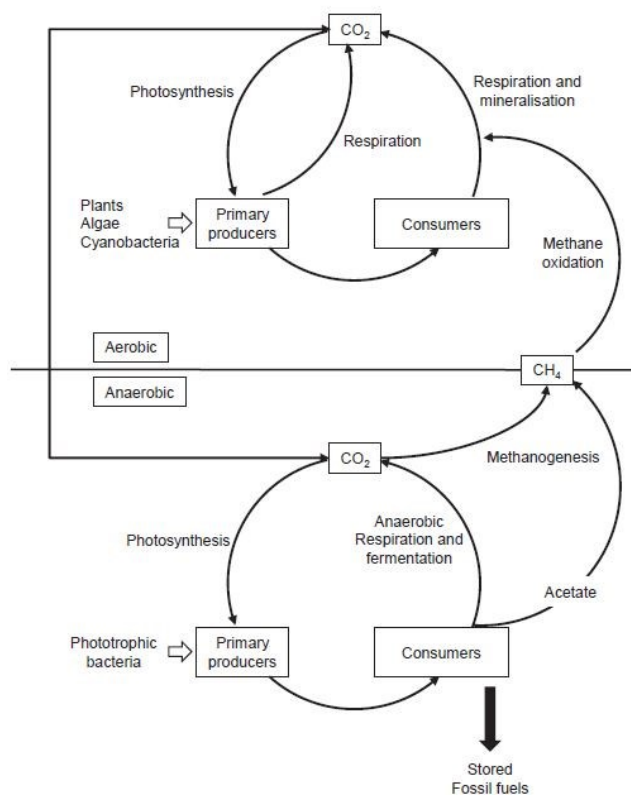


Figure 3-18 Carbon cycle (Aislabie et al. 2013)

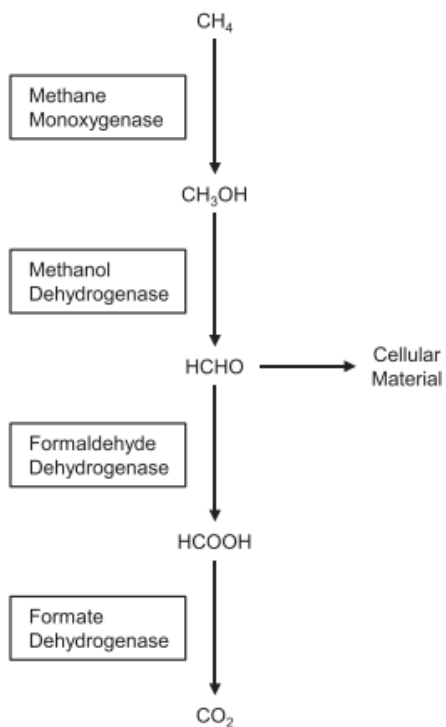


Figure 3-19 Carbon dioxide production (Aislabie et al. 2013)

On the contrary, nitrogen gas  $N_2$  could be an appealing gas to be used inducing the partial saturation. Its properties, under both chemical and environmental perspectives, are highly suitable as will be underlined in the following. Nitrogen gas is essential for all organisms, since it is essential element in protein and nucleic acids (Aislabie et al. 2013). Therefore, microbes play a key role in the nitrogen cycle, as reported in Figure 3-20. The bio-chemical reactions involved in the nitrogen cycle are different, and many of them can be carried out only if specific lineages of microorganisms are present.

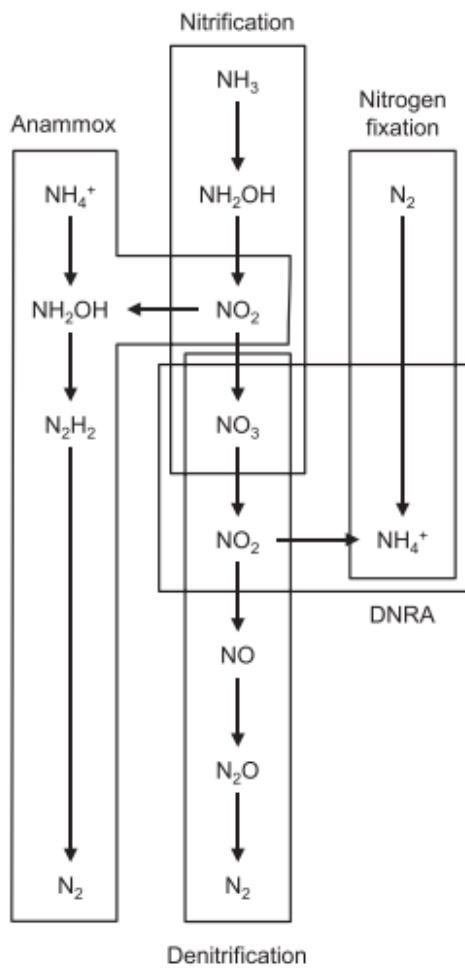


Figure 3-20 Main bio-chemical reactions carried out by microorganisms in the nitrogen cycle (Aislabie et al. 2013)

In details, microbes' activities lead to several type of processes that can be grouped as:

- Nitrogen fixation;
- Dissimilatory nitrate reduction to ammonia (DNRA);
- Nitrification;
- An-Amm-Ox;
- Denitrification.

The reactions reported above are often carried out in a simultaneous way, and the chemical tendency to follow majorly a process rather than others depends strictly by several factors such as enzymes owned by particular microorganisms. Actually, Aislabilie et al. (2013) pointed out that “*some steps in the nitrogen cycle are mediated by few microbial groups (e.g. nitrogen fixation or nitrification) and are referred to as narrow processes, whereas others are mediated by many groups (e.g. DNRA) and are considered broad processes. The release of ammonium from soil organic matter during decomposition is known as ammonification. Only bacteria and archaea carry out biological nitrogenfixation (N-fixation), the reduction of atmospheric nitrogen gas to ammonium. N-fixation is the only natural process through which new N enters the biosphere, so it is critically important for ecosystem function. N-fixation is catalysed by the enzyme nitrogenase. This enzyme is extremely sensitive to oxygen, requiring a low oxygen environment for activity. The ammonium produced through N-fixation is assimilated into amino acids and subsequently polymerised into proteins*”. Overall, denitrification is a microbial respiratory process during which soluble nitrogen oxides are used as an alternative electron acceptor when oxygen is limiting. It consists of the sequential reduction of nitrate ( $NO_3^-$ ), nitrite ( $NO_2^-$ ) and nitric oxide ( $NO$ ) to the green-house gas nitrous oxide ( $N_2O$ ) or benign nitrogen gas ( $N_2$ ). It occurs predominantly in waterlogged areas that have become anaerobic. Complete denitrification (to  $N_2$ ) is the major biological mechanism by which fixed N returns to the atmosphere from soil and water, completing the nitrogen cycle (Aislabilie et al. 2013).

Thus, the identification of several processes leading to the formation of  $N_2$  gas could represent an appealing and possible IPS methodology, since the nitrogen gas owns the following several advantages:

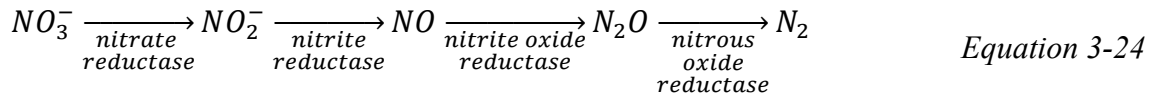
- it is chemically inert, hence not involved in possible sub-biochemical processes;
- it is environmentally compatible;
- it is of low solubility in water.

Certainly, with respect to practical applications, the process should be engineered in order to avoid or, at least, minimize as much as possible intermediate products which can undermine its application. The goal that needs to be achieved is that of setting up a bio-IPS process, mainly by means of denitrification phenomenon, optimizing the  $N_2$  formation. To that aim, a focus on the chemical paths is needed, trying to define the key factors leading to a high efficiency bio-IPS mitigation technique.

### **3.3.2 BACTERIAL DENITRIFICATION AS A PROCESS DRIVING IPS**

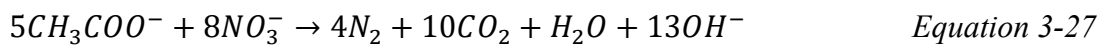
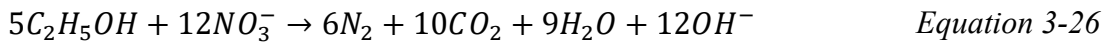
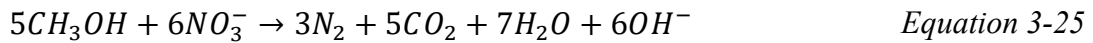
Nitrogen gas is formed in the subsurface when denitrifying microorganisms are provided with a solution containing nitrate and dissolved organic matter. This process may be referred to as

dissimilatory reduction of nitrate, or denitrification (Van Paassen et al. 2018). Generally, denitrification is a biological anoxic process where nitrates are reduced to nitrogen gas by the following reaction:



This process might not lead to a 100% efficiency of the  $N_2$  generation. In fact,  $N_2O$  might be produced anyway, and its amount depends on several factor such as: the presence of specific genes encoding the required enzymes in the bacterial species involved in the process (Rebata-Landa and Santamarina 2012), the ratio C/N (Chung and Chung 2000); the soil acidity and aeration, the soil texture and nutrient status (Johns et al. 2004); and the soil moisture (Davidson et al. 1993). In addition, to promote the efficient and full reduction of nitrate to nitrogen gas, selecting the right substrate composition is essential (O'Donnell 2016, Pham et al. 2016). Too much nitrate may lead to accumulation of intermediate compounds, while leaving a large excess of organic substrate would be inefficient (Van Paassen et al. 2018).

However, several reactions can be suitable to the  $N_2$  gas production, as reported by the following equations:



Electron donors are almost all organic compounds. In the examples reported above, biogas production in denitrification's reactions is achieved by using methanol, ethanol, or sodium acetate as electron donors. Besides, in Figure 3-21 the *N-cycle* is reported in order to frame conceptually the process identified by the mentioned reactions.

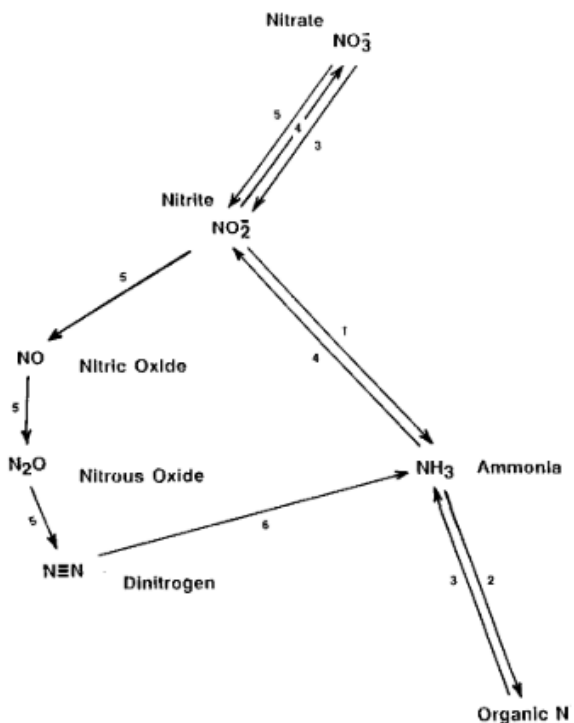


Figure 3-21 Nitrogen cycle 1=assimilatory nitrate reduction, 2=nitrogen immobilization into organic nitrogen, 3=ammonification, 4=nitrification, 5=denitrification, 6=nitrogen fixation. (from Bachofen 1991)

Actually, bio-chemical processes involved in the bio-IPS do not follow pure denitrification reaction, rather several parallel paths are carried on. Indeed, as pointed out by Rebata-Landa and Santamarina (2012), beyond the denitrification, an ammonification process is often developed, depending on specific enzymes catalysing a battery of reactions. Thus, the main processes resulting in the decomposition of the  $\text{NO}_3^-$  can be grouped as shown in Figure 3-22.

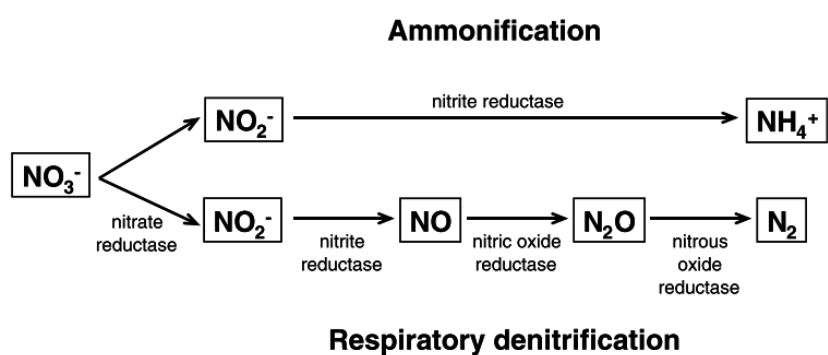


Figure 3-22 Reduction of nitrates and nitrites (Rebata-Landa and Santamarina 2012)

By the ammonification process, ion ammonium,  $\text{NH}_4^+$ , is produced. Such ion has to be minimized as much as possible, since its limit concentration is restricted by local codes; however, this issue will be analysed and discussed later. Even so, the main biological processes leading to the nucleation of

occluded gas bubbles- by means of denitrification respiratory mainly- have been discussed under a strictly bio-chemical point of view. Once the reactions involved have been studied and assessed, remarks about dynamics of bubbles nucleation could be useful to deeply understand the whole process leading to the application of the bio-IPS technique.

Generally speaking, prior to the presence of N<sub>2</sub> (or others) under occluded gas bubble configuration, biogenic gases go under solution within the pore fluid: a specific threshold of supersturation exists, at which the increase in the biogenic gas results in the nucleation of the bubble (Ronen et al. 1989). In addition, as pointed out by Hemmingsen (1977) and Lubetkin (2003), three different processes can lead to the spontaneous formation of gas bubbles, respectively:

- depressurization to a vapor pressure below that of the pure liquid;
- temperature increase until the vapor becomes more stable than the pure liquid;
- dissolution of gas from a supersaturated liquid when the supersaturation exceeds certain threshold values.

Indeed, with regards to the latter, the supersaturation can be defined as (Rebata-Landa and Santamarina 2012):

$$\sigma = \frac{c_{gen}}{c_{eq}} - 1 \quad \text{Equation 3-28}$$

where

- $c_{gen}$  is the gas concentration in the fluid;
- $c_{eq}$  is the gas concentration soluble in the liquid under the prevailing experimental conditions.

The nucleation of the gas bubble is thus strongly dependent on the supersaturation threshold which is, in turn, a function of molecular interactions between the gas and the fluid. Theoretically, such a threshold should be constant, in fact heterogeneous bubble nucleation at substantially lower supersaturations are reached because of the presence of mineral surfaces (Blander and Katz 1975) (Gerth and Hemmingsen 1980). In order to make bubble form, supersaturation has to be reached. At this point, the pressure in the liquid tends to equalize that of the gas. Obviously, as previously discussed, the concentration in the gas under solution is linked with the pressure of the gas by the Henry's law (*Equation 3-2*), through the Henry's constant  $h_{wg}$ .

On the other hand, once the bubble nucleates, a critical radius of the bubble itself will exist. In particular, bubbles showing a radius lower than the critical one, will tend to go under solution again.

On the contrary, bubbles will be stable or tend to coalesce in greater ones. Starting by this assumption, Lubetkin (2003) pointed out that, when Henry's law is applied – hence *Equation 3-28* is valid – the critical radius can be expressed as follows (reported graphically in Figure 3-23):

$$r_{critical} = \frac{2T_s}{u \cdot \sigma} \quad \text{Equation 3-29}$$

where:

- $\sigma$  is the supersaturation;
- $u$  is the nucleation pressure (the pressure at which bubble nucleates);
- $T_s$  is the surface tension ( $=0.072 \text{ N/m}$  for water at  $20^\circ\text{C}$ ).

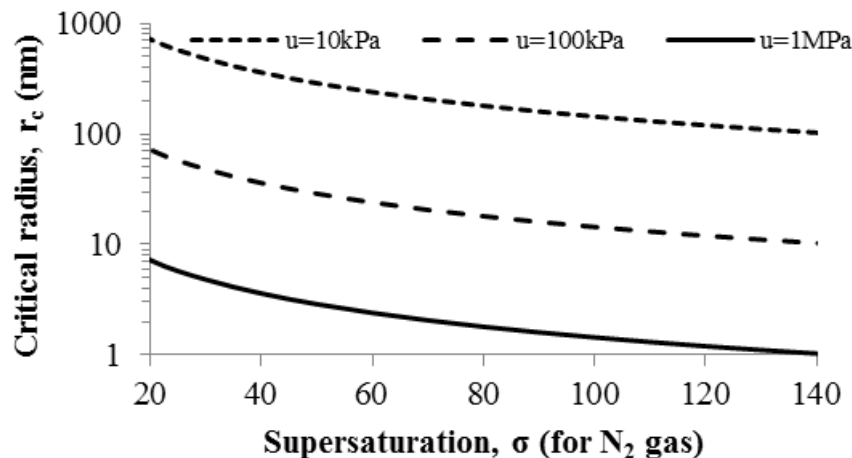


Figure 3-23 Critical radius for a  $N_2$  nucleated bubble (Equation 3-29)

Table 3-1 Measured values of supersaturation needed to cause bubble nucleation in aqueous solutions, (from Lubetkin 2003)

Gas	Measured supersaturation needed
Carbon dioxide, $CO_2$	4.62-20
Hydrogen, $H_2$	80-90
Nitrogen, $N_2$	19-140
Methane, $CH_4$	80

In Table 3-1 supersaturation needed to cause nucleation is reported. Note that supersaturation for  $N_2$  gas is higher than that for the  $CO_2$ . On the other hand, carbon dioxide presents a higher solubility in water than that of the nitrogen gas. For this reason,  $N_2$  is still the most suitable gas to induce the partial saturation, as well as it is of null or low environmental impact and chemically inert.

Although denitrification is the main reaction producing  $N_2$ , it is not the only path through which nitrates are reduced. As previously introduced, a parallel path- named ammonification- through which ammonium  $NH_4^+$  is produced, is involved in the bio-chemical process (as already shown in Figure 3-22). The ammonia production leads to another type of biochemical step able to reduce the  $NH_4^+$  ion into  $N_2$  by means of the anammox reaction (Anoxic-Ammonia-Oxidation) as follows:



Accordingly, the amount of nitrogen gas bubbles produced is carried out by the denitrification and concurrently by the anammox: the former is the main process and a higher quantity of  $N_2$  is produced; the latter leads to a lower production of nitrogen gas and at the same time allows to the ion ammonium reduction. Finally, Figure 3-24 shows schematically the different biochemical paths involved in the production of nitrogen gas bubbles, by summarizing the whole processes discussed previously.

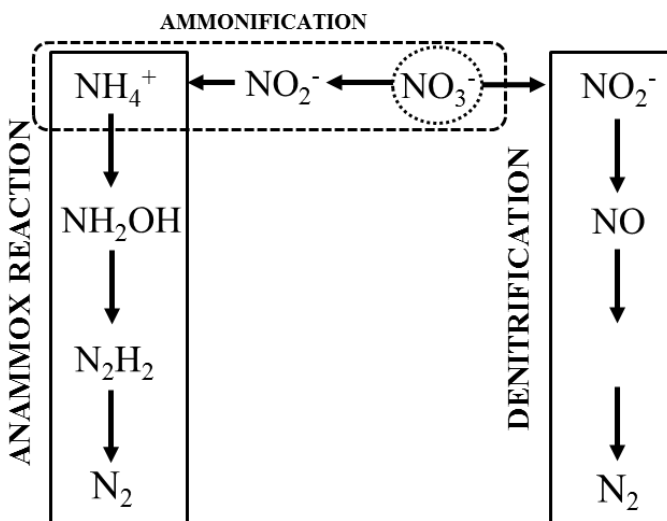


Figure 3-24 Biochemical paths involved in the nucleation process

As it will be discussed in the experimental section, it is pivotal to consider the entire processes involved in the bio-IPS technique. The ammonium is not a desired product to be formed but, on the other hand, it will represent a transient sub-product from which an additional amount of  $N_2$  is produced. Obviously, the steady state conditions have to ensure that the presence of undesired chemical compounds -nothing but  $N_2$ - must be bounded in specific limits, in order for the bio-IPS technique to be applicable in real scale filed mitigation actions.

In the next sections the experimental program is reported. First, microbiological experimental setup is shown, starting by the isolation of bacteria. Successively, the preliminary tests are described. Such tests were carried out in order to ensure the bacteria capability to nucleate nitrogen gas bubbles.

Once a solid microbiological framework has been achieved, geotechnical desaturation tests have been performed, as later discussed. Finally, the bio-chemical analyses on transient chemical compounds are reported, aimed at ensuring the environmental compatibility of the bio-IPS process.

## **4 CHAPTER 4**

### **4.1 BIO-CHEMICAL EXPERIMENTAL INVESTIGATION: INTRODUCTION**

In order to set up a bio-chemical solution able to induce the partial saturation within the soil, a preliminary biological investigation is needed. The availability of microorganisms able to carry out denitrification processes is thus unavoidable to define and develop a reliable bio-IPS technique. First of all, isolation of denitrification bacteria is needed certainly, in order to evaluate the possibility of bacteria themselves to reduce nitrates. Bacteria's identification and isolation have been carried out starting by a sludge treatment plant sample, from which a significative number of microorganisms can be pulled out. Progressively, thanks to a microbiological identification approach, a limited number of bacteria lineages could be identified and isolated, in order to consequently proceed to specific tests able to assess qualitatively the bacteria's capability to reduce nitrates and, concurrently, generate gas bubbles as final product of their own metabolism. In addition, several tests have been performed in order to assess the rate of nitrates reduced, as a result of the denitrification metabolic processes. Furthermore, several analyses on the generated gas composition have been carried out, aiming to check that nitrogen gas was the main product of the process.

In the following sections the results of the bio-chemical experimental programme will be reported. The goal is to own the main basis instruments- under a strictly biochemical point of view- needed to power up the geotechnical experimental set-up, resulting in the assessment of the desaturation potential of the bio-IPS technique, by means of specific lineages previously identified and tested.

### **4.2 MICROORGANISMS ISOLATION FROM SLUDGE TREATMENT PLANT**

In order to preliminary isolate a wide range of microorganisms, a sludge sample was taken from a civil and industrial wastewater treatment plant and the culture medium *Plate Count Agar (PCA Oxoid)* was used at the Department of Biology of the University of Napoli Federico II in order to grow different microorganisms' lineages. Such a culture medium contains glucose and yeast extract used for the total bacterial count in food microbiology (e.g. in milk, meat, meat products and other foods) and for environmental analyses. It is also used in pharmacy and cosmetic industry.

Considering the characteristics of the typical organisms of some process phases of wastewater purification plants, the sample was subjected to enrichment in liquid medium.

In this work, a typical composition of the culture medium was used, constituted by (for 1 liter of culture medium):

- Tryptone: 5,0 g;
- Yeast extract: 2,5 g;

- Glucose: 1,0 g;
- Bacteriological Agar: 12,0 g.

The nutrients provided by tryptone, the vitamins contained in the yeast extract and the energy source represented by glucose support the growth of most bacteria.

Subsequently the plates were incubated in aerobiosis, anaerobiosis and microaerophilia conditions at  $30 \pm 1$  ° C. In particular, for the matrix isolation 10 g have been diluted with 90 mL of 0.9% NaCl solution. After having adequately homogenized the sample, decimal dilutions were performed at different concentrations and subsequent surface sowing in accordance with ISO 7218: 2007 / Amd.1: 2013 (E). The surface seeding technique -or spatula method- involves the use of a sterile pipette to transfer a small quantity (generally 100 µL) of the liquid sample or initial suspension onto the previously prepared agar plate. The maximum PCA medium was used in the trial in question. It is necessary to repeat the inoculation for the subsequent decimal dilutions (where the colonies to be counted will be related to the relative dilution factor). Using a sterile plastic spatula, the inoculum is distributed as quickly as possible and evenly on the agar surface without touching the side walls of the Petri dish, then the sample is completely absorbed for about 15 minutes at room temperature. The spatula seeding technique allows to produce superficial colonies on agar plates with considerable advantages compared to the deep seeding method: the morphology of the colonies is easily observable and distinguishable; furthermore, the microorganisms not exposed to the heat of the molten agar medium were sent to obtain higher counts.

After incubating the plates in aerophilic, microaerophilic and anaerobic conditions at  $30 \pm 1$  ° C for 24h, the resulting colonies were selected on morphological diversity (example in Figure 4-1) and then subcultured, with the smear seeding method.

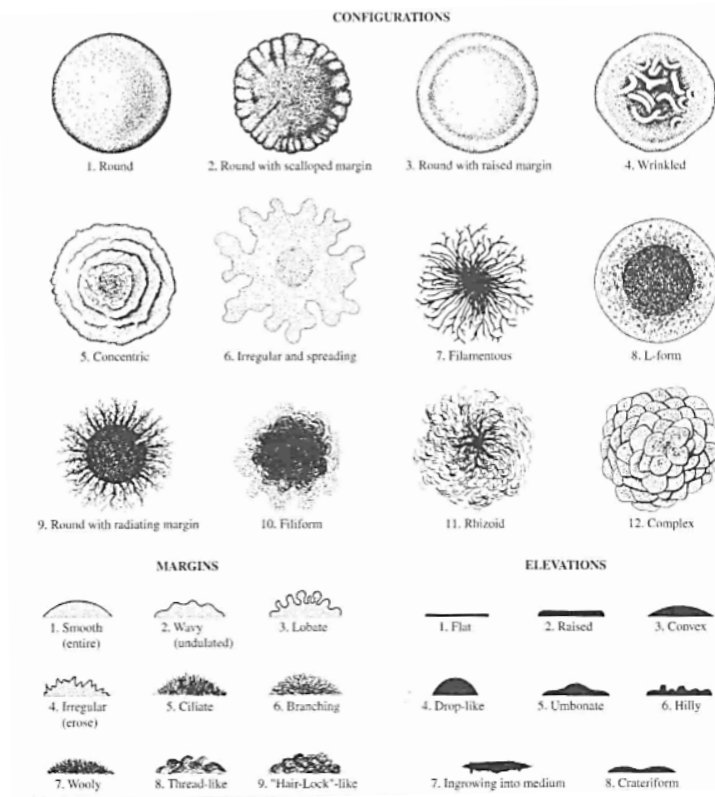


Figure 4-1 Example of optical subdivision of bacteria lineages

This technique involves the use of a sterile loop and Petri dishes with previously agarized medium (also in this case PCA) on the surface of which, by making parallel lines -not superimposed- a progressive decrease in the density of the inoculum is promoted, so that along the edges of the last smears develop isolated colonies. This allows to isolate single colonies from others and to consider each single colony as "pure", as theoretically deriving from a single cell.

Thus, by applying the above-mentioned technique, a high number of several microorganisms (about 183) have been isolated, as shown in Figure 4-2. At this point, taking advantage of optical preliminary identification, a first subdivision of microorganisms themselves have been performed, as shown in Figure 4-3.

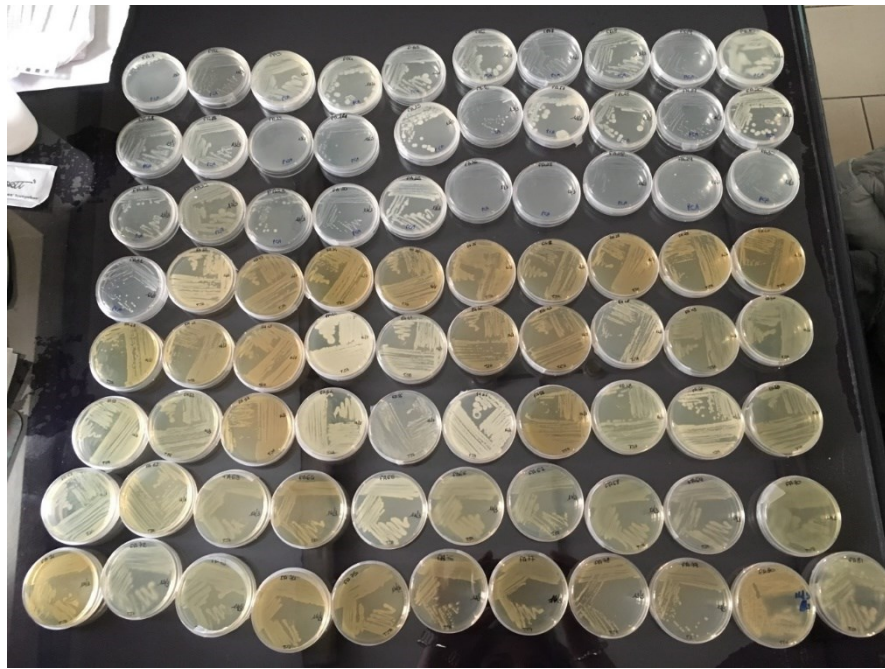


Figure 4-2 Culture of microorganisms isolated from a sludge treatment plant under aerophilia, microaerophilia and anaerobiosis conditions, at 30 + 1 °C

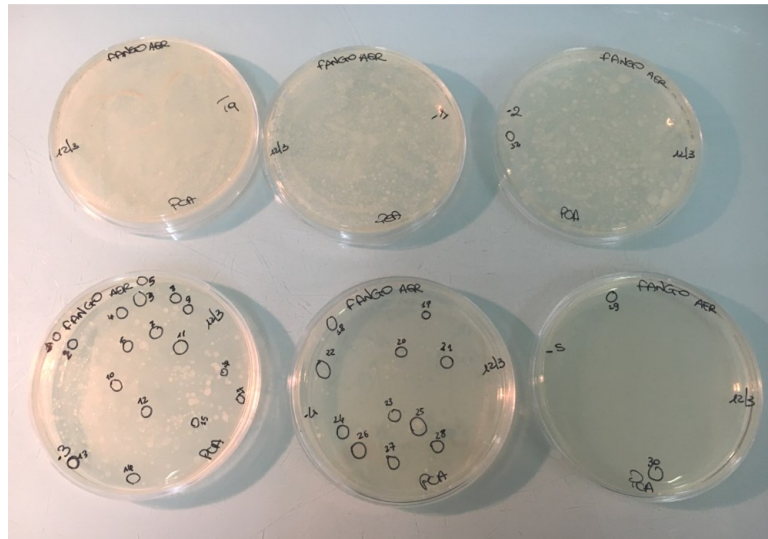


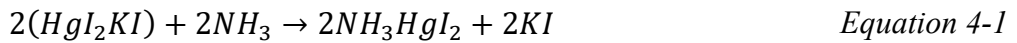
Figure 4-3 Colonies morphological distinction after surface seeding on Petri's dishes

After the preliminary distinction of microorganisms' lineages, a deeper analysis on bacteria metabolism has been carried out.

#### 4.3 NITRATES TO AMMONIA TESTS REDUCTION

The first test conducted is aimed to the spectrophotometric determination of ammonia using Nessler's reagent (which is an alkaline compound becoming deeper yellow in presence of ammonia)-

according to the APAT IRSA-CNR method. In 24-well multiwells, 2.5 mL of the same concentration of the isolated bacteria ( $10^8$  CFU / mL), in nitrate broth were added with 100 $\mu$ L of Nessler's reagent. Generally, the Nessler reagent allows the qualitative and quantitative recognition of ammonia, more precisely if it is present as an ammonium ion in aqueous solution. It consists of an alkaline solution of potassium tetraioduromercurate, which in the presence of ammonia gives the following reaction:



developing an intense yellow-orange color, due to the iodide of oxamidodimercury which, over time, in case of a sufficiently high concentration, flocculates and precipitates. It is a very sensitive reaction, which allows to detect the presence of ammonia even at concentrations of the order of 0.1 mg / l (0.1 ppm) and the absorbance of the colored complex is measured at the wavelength of 420 nm. In order to examine the metabolism of the selected bacteria, the broth solution have been set up by mixing:

- $NaCl$ ;
- $KNO_3$ , necessary to activate bacteria metabolism, as source of nitrates, containing two of the most important elements for the growth and sustenance of flora and microfauna: potassium and nitrogen;
- Tryptone, which is a pancreatic digestion product of casein. This protein hydrolyzate, particularly rich in amino acids and peptides. It is used for the preparation of culture media for microbiology and as a nutrient source in the production of antibiotics, toxins, enzymes and other biological products.

Thus, the test for reducing nitrates to ammonia, in a broth with minimal nourishment and rich in potassium nitrate, was carried out in order to select the microorganisms with metabolism able to successively reduce nitrates to nitrogen, by adding the above-mentioned Nessler's reagent. This addition in equal quantities (100  $\mu$ L) to the same concentration of the isolated bacteria ( $10^8$  UFC / mL), allowed to carry out an evaluation based on the colorimetric variation. The microorganisms present in the wells in which there was a colour change tending to orange brown were selected (starting by the initial 80 subcultures, 15 of them were selected). Colorimetric tests results are reported in Figure 4-4.

Once a first analysis has been performed, and the bacteria capability to form ammonia- as a result of nitrate reduction- has been ensured, additional tests on the pure  $N_2$  gas bubbles nucleation have been carried out.

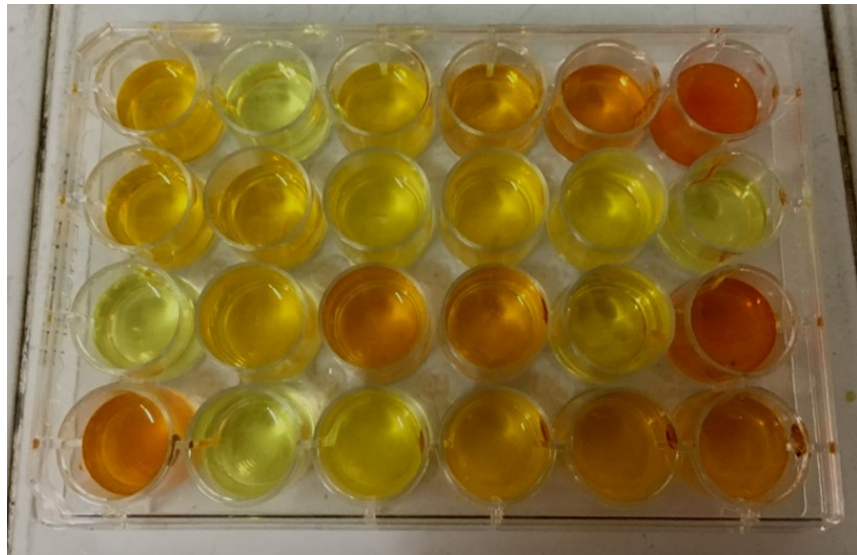


*Figure 4-4 Nitrate reduction to ammonia tests*

#### **4.4 BUBBLES NUCLEATION TESTS- FROM NITRATES TO NITROGEN GAS $N_2$**

Once several bacteria lineages have been selected, the test was prepared to check the reduction of nitrates to molecular nitrogen ( $N_2$ ), in a broth rich in potassium nitrate, taking advantage of Durham tubes (Figure 4-5). The method was first reported in 1898 by the British microbiologist Herbert Durham. These tubes are smaller test tubes inserted upside down in a larger test tube. Initially, the small tube is immersed in the solution in which the microorganisms grow and it is filled with it; if any gas is produced after inoculation and incubation, the nucleated gas bubbles will be visibly trapped inside the bell itself. During the tests, the nitrate broth was inoculated inside Durham's tubes with the bacterial culture under examination and incubated at the optimal growth temperature for 2-3 days. After the incubation period, the ability of the microorganisms to reduce the nitrate ion is verified by evaluating the state of reduction achieved, by analyzing the presence of gas in the Durham tube for the formation of molecular nitrogen.

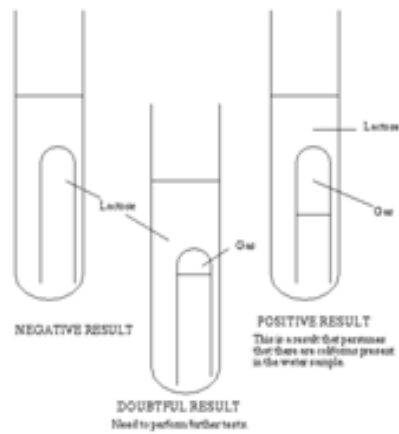


Figure 4-5 Durham's tube

Lately, an evaluation of the production of microbubbles with known concentrations of the isolated microorganisms was carried out. Starting from initial inoculations obtained by diluting the samples in nitrate broth with a sterile 10 µL inoculation loop, after appropriate decimal dilutions and verification of the optical density with the spectrophotometer, it was possible to obtain bacterial cultures at different concentrations ( $10^7$ ,  $2 \times 10^7$ ,  $10^8$  UFC / mL) combined at different concentrations of potassium nitrate (1, 4, and 40 g/L). Actually, the first test was carried out at unknown concentrations of the microorganisms to verify their ability to reduce the nitrate ion by evaluating the state of reduction achieved, in particular analyzing the presence of gas in the Durham's tube for the formation of molecular nitrogen (Figure 4-6).

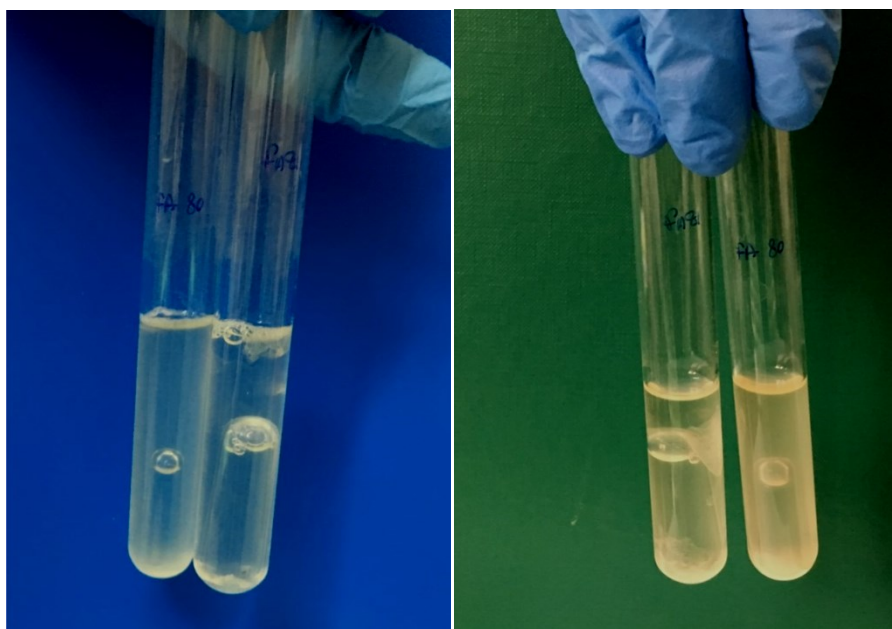


Figure 4-6  $N_2$  nucleation tests in Durham's tubes (at unknown bacteria concentration)

Successively, tests at precise and different concentrations have been carried out, as showed in Figure 4-7.



Figure 4-7  $N_2$  nucleation tests in Durham's tubes (at specific bacteria concentration)

These tests confirm the capability of bacteria metabolism to reduce nitrates. Bubbles nucleation is strongly developed, but the amount of produced gas is not quantified yet at this stage. In fact, all these preliminary tests aim to ensure the bacteria tendency to produce nitrogen gas bubbles as final product of their own metabolism. In addition, a qualitative approach it has been necessary first, because of the high number of microorganisms that have been isolated from the sludge sample. Once the main bacteria lineages have been selected – thanks to the last Durham's tube tests (Figure 4-7) – a final check on the bacteria metabolism has been carried out, by introducing the soil matrix. In particular, a liquefiable silty sand has been gently and poorly pluviated within the tubes, in order to verify the capability of the selected bacteria to reduce nitrates – and consequently nucleate  $N_2$  bubbles – even in presence of soil particles. Such soil – and its characteristics – will be reported in §5.2, being one of the tested materials for the geotechnical experimentation. In Figure 4-8, check tests by using the silty sand are shown.

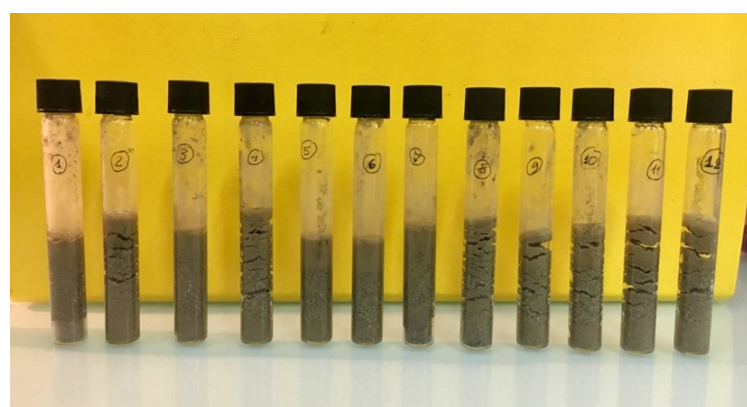


Figure 4-8 Check tests on bacteria metabolism on a liquefiable silty sand

Tests show that – depending on the specific bacteria lineage – sand grains are dislocated as a consequence of bubbles nucleation, since no confinement was imposed at the sample. Thus, a qualitative distinction on the amount of produced gas, as a function of different bacteria metabolism, has been performed, as reported in Table 4-1. On this basis, bacteria lineages have been selected to be subjected to a molecular characterization, as shown in the next section.

*Table 4-1 Qualitative assessment of bubbles production*

Sample ID Code	Bubbles Production
<b>01</b>	++++
<b>02</b>	+++
<b>03</b>	++
<b>04</b>	+++
<b>05</b>	++++
<b>06</b>	+++++
<b>07</b>	++++
<b>08</b>	+++
<b>09</b>	+++
<b>10</b>	+++
<b>11</b>	+++
<b>12</b>	++++

## 4.5 MOLECULAR BACTERIA CHARACTERIZATION

In the present section a brief and basic framework regarding the molecular characterization is reported, evidencing the main general steps needed. As well as the tests reported above, the molecular characterization has been carried out thanks to the collaboration with the Laboratory of the Department of Biology. Thus, the main steps needed to the characterization are:

1. Bacteria DNA extraction;
2. PCR (Polymerase chain reaction);
3. Agarose gel electrophoresis;
4. Sequencing.

1. Within the molecular approach, the first step consists in the extraction of bacterial DNA in adequate quantities and with a high degree of purity -by means of methods developed in

research laboratories or commercial kits- from low quantities of sample (0.2 -5 mg), in both optimum quantity and quality, for subsequent amplification reactions in vitro using the Polymerase Chain Reaction (PCR) technique. In particular, the extraction was carried out by heat treatment. A colony was taken from the plate, containing the pure culture, and diluted with 70  $\mu$ L of ultrapure water in a sterile 200 $\mu$ L Eppendorf pipette (Figure 4-9). The centrifugation is carried out at 8000 rpm for 5 minutes at 4 ° C and the supernatant was recovered. The DNA present in the aqueous phase, transferred into vials, was used for Polymerase Chain Reaction.



Figure 4-9 Eppendorf pipette

2. The Polymerase Chain Reaction is a technique that automates the DNA duplication process, through which multiple copies of a DNA sequence can be obtained in vitro. This technique was invented by the American biochemist Kary Mullis, in 1983. PCR consists in 3 steps, that are briefly reported below.

- **Step 1: Denaturation**

As in DNA replication, the two strands in the DNA double helix need to be separated. The separation happens by raising the temperature of the mixture, causing the hydrogen bonds between the complementary DNA strands to break. This process is called denaturation.

- **Step 2: Annealing**

Primers bind to the target DNA sequences and initiate polymerisation. This can only occur once the temperature of the solution has been lowered. One primer binds to each strand.

- **Step 3: Extension**

New strands of DNA are made using the original strands as templates. A DNA polymerase enzyme joins free DNA nucleotides together. This enzyme is often Taq polymerase, an

enzyme originally isolated from a thermophilic bacterium called *thermus aquaticus*. The order in which the free nucleotides are added is determined by the sequence of nucleotides in the original (template) DNA strand. The result of one cycle of PCR is two double-stranded sequences of target DNA, each containing one newly made strand and one original strand.

These three steps, necessary for the PCR to be carried out, are conceptually shown in Figure 4-10.

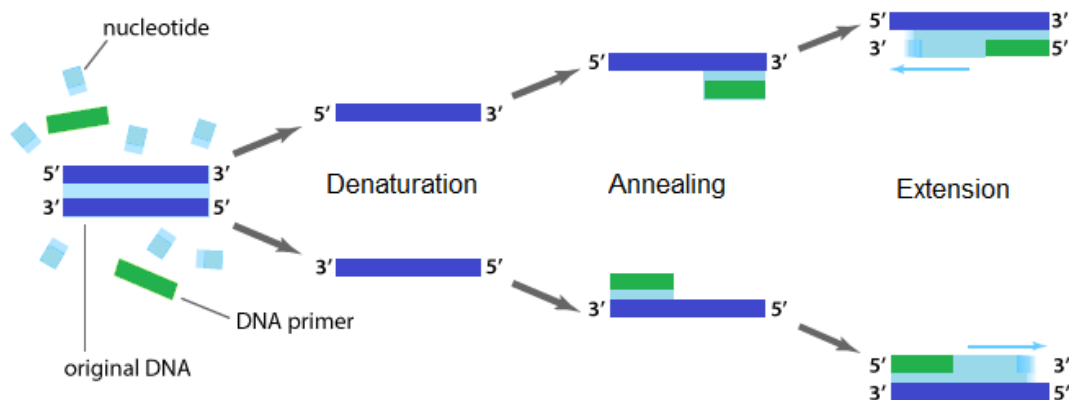


Figure 4-10 Polymerase Chain Reaction Processes

3. Electrophoresis on agarose gel consists of the differentiated migration in an electric field of electrically charged molecules. Electrophoresis is conducted on an inert and homogeneous support (gel or matrix), the sample is dissolved in a suitable buffer in which any support is saturated in order to allow the conduction of the current. The matrix in question used is Agar: a non-toxic mixture obtained from red algae, of two polymers derived from galactose, namely agarose and agarpectin. The 1.5% agarose gel was prepared with a saline buffer called TAE buffer. The agarose concentration determines the fibrous structure of the gel and therefore the migration of the sample. After mixing agarose and TAE buffer under heat, ethidium bromide was added, intercalating the bases and responsible for the emission of UV fluorescence. In the wells 4µL of the amplified were loaded together with 1µL of BBF (bromophenol blue). In the first well, 100bp DNA ladder was added as a reference. To highlight a visible result, the electrophoretic run is performed for 25-30 minutes at 70V. The visualization of the bands inside the agarose gel, exposed to a UV transilluminator (590 nm) will indicate the effectiveness of the amplification (Figure 4-11).



*Figure 4-11 Visualization of the bands inside the agarose gel, exposed to a UV transilluminator*

4. DNA sequencing is the process of determining the nucleic acid sequence – the order of nucleotides in DNA. It includes any method or technology that is used to determine the order of the four bases: adenine, guanine, cytosine, and thymine. In the present work, an external corporation carried out the sequencing of the DNA samples. The sequencing method used is that of Sanger or enzymatic sequencing. The sequence provided in the form of an Electronferogram was converted into FASTA format and identified by means of the bioinformatics software Blast (Basic Local Alignment Search Tool), evaluating the results according to the alignment with the database of sequences already present in the program. Afterwards, samples of interests were finally identified.

Thanks to the specific procedures performed during the bio-experimental program, three different bacteria lineages have been selected to further develop the IPS technique by means of bio-gas bubbles nucleation. Indeed, after the molecular characterization, every type of the 12-above-mentioned isolated microorganisms have been characterized, as reported in Table 4-2.

*Table 4-2 Final characterization of isolated microorganisms*

Sample ID Code	Bubbles Production	Identified Microorganisms
01	++++	<i>Aeromonas caviae</i> strain HAMBI 1972
03	++	P3
05	++++	P2
06	+++++	<i>Aeromonas caviae</i> strain HAMBI 1972
07	++++	<i>Aeromonas caviae</i> strain HAMBI 1972
09	+++	P1
10	+++	P1
12	++++	P1

Thus, thanks to the molecular characterization, the nucleation tests, as well as the chemical reduction tests, five different kind of bacteria have been selected to speed up the bio-IPS technique as a liquefaction mitigation action, respectively named **P1**, **P2** and **P3** in Table 4-2. All the bacteria belong to *Pseudomonas* species, which is one the most well-known kind of denitrifying bacteria. Obviously, the selected microorganisms have been tested in order to ensure their non-pathogenic nature, thus being appealing to be used in the civil engineer panorama. Actually, the final group of bacteria that will be used in all the further tests have been restricted beyond, resulting in the three lineages reported in Table 4-3- such distinction has been performed on the basis of the amount of produced gas, as previously discussed.

*Table 4-3 Final selection of bacteria to be applied in the bio-IPS experimentetion*

Sample ID Code	Bubbles Production	Identified Microorganisms
<b>03</b>	++	<b>P3</b>
<b>05</b>	++++	<b>P2</b>
<b>12</b>	++++	<b>P1</b>

Once biological assessments have been performed and suitable bacteria have been isolated and detected, it has been necessary to investigate their metabolism's compatibility under an environmental point of view. To that aim, several analyses have been performed at the Laboratory of Analysis and Environmental Research of the Department of Civil, Architectural and Environmental Engineering (DICEA), of the University of Napoli Federico II. Such tests, necessary for the successive application in the field, are discussed in the following section.

## 4.6 ENVIRONMENTAL ANALYSES

In order to preliminary asses the environmental compatibility of the metabolic products of bacteria's activity, several environmental analyses have been performed. In particular, two main aspects have to be meticulously evaluated, in order to guarantee a safe bio-IPS mitigation action, which are:

- Nitrates concentrations at the end of gas bubbles nucleation process have to be compatible with limit-values imposed by Italian codes (*D.Lgs. 11/1999, n. 152; D.Lgs. 02/2001 n. 31; D.Lgs 02/2016 n. 9*);
- Gas composition of the nucleated bubbles has to be evaluated in order to ensure the formation of molecular nitrogen gas,  $N_2$ .

To those aims two different tests have been carried out, respectively:

- Ion exchange chromatography, for the analyses of initial and final nitrates in the biochemical solution;
- Gas chromatographic analysis, for the assessment of the generated gas.

Briefly, ion-exchange chromatography (or Ion chromatography) separates ions and polar molecules based on their affinity to the ion exchanger. It works on almost any kind of charged molecule including large proteins, small nucleotides, and amino acids. Thanks to such type of analyses it is possible to evaluate the concentration of the desired ion- nitrates- in order to further investigate the efficiency of bacteria metabolism. Indeed, if the initial concentration is well known – thanks to the controlled setup of the chemicals – the final concentration of nitrates depends strictly on bacteria activity, and their capability to reduce them. Thanks to the biological experimental analyses previously reported, it is sure enough that selected bacteria are able to activate their own metabolism reducing nitrates, but nothing is known yet under a quantitative point of view. Thus, to quantify the efficiency of the biochemical denitrification process, a trial sample has been setup and further analysed. In particular, chemical has been developed by the following composition:

- Nitrate broth containing about 2000 p.p.m. of  $\text{NO}_3^-$  (resulting of the 60% of  $\text{KNO}_3$ );
- Bacteria concentration equal to  $10^4$  CFU.

The compound has been gently mixed in a vial, appropriately sealed in order to ensure anaerobic conditions. A first sample has been taken immediately, to check the initial  $\text{NO}_3^-$  concentration to be equal to the desired one. Successively, the sample has been left in such anaerobic conditions for a sufficient time to ensure the complete bacteria activity. Afterwards, a final sample has been collected, in order to later assess the nitrate concentration in steady state. The knowledge of initial and final concentration of  $\text{NO}_3^-$  is fundamental to assess the environmental applicability of the bio-IPS technique. Thus, once samples have been collected, ion-exchange chromatography tests have been performed. Actually, samples were prior diluted by 1:100 – due to technical issues related to the measurement instrument – and successively analysed. Obviously, outputs will be related to the real chemical conditions. Usually, the interpretation of ion exchange chromatography tests results is made by comparing the retention time of the sample peaks with the retention time of the reference solutions. The concentration is determined by comparing the peak area with the calibration curve of the analyte constructed using a series of reference solutions at different concentrations.

Figure 4-12 shows the results regarding the initial conditions of the bio-chemical solution. In particular, the detected peak related to the  $\text{NO}_3^-$  concentration is underlined by the dashed red line. Results show that the  $\text{NO}_3^-$  concentration of the diluted chemical is equal to 20.314 p.p.m., which

corresponds easily to  $[NO_3^-] = 2031.4$  p.p.m. of the original (undiluted) bio-chemical solution according to the stoichiometric previsions related to the injected  $KNO_3$ .

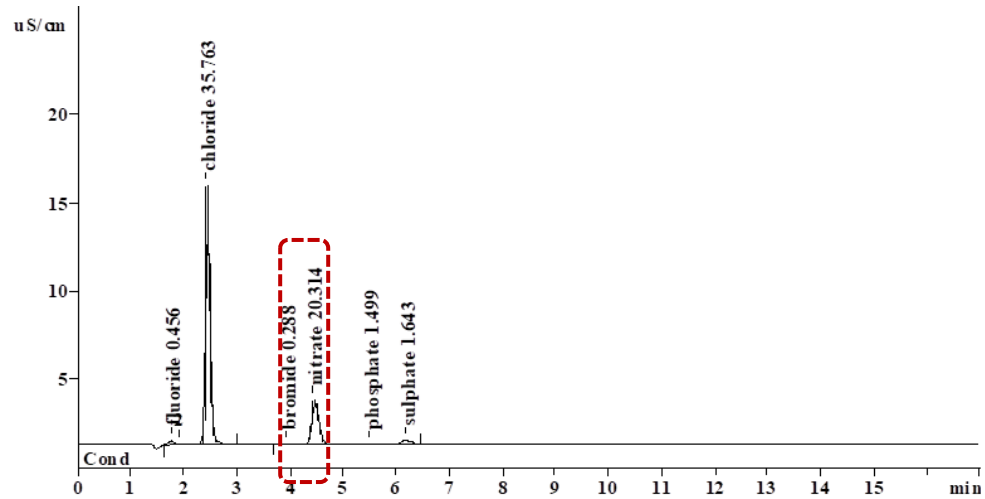


Figure 4-12 Ion exchange chromatography test's results for initial conditions of the bio-chemical solution

Afterward, the steady state has been analysed, to characterise the final metabolic activity of bacteria. In Figure 4-13 steady state results are reported, in which the nitrates concentration has been underlined as in Figure 4-12. The test has been performed after 10 days of bacteria activity.

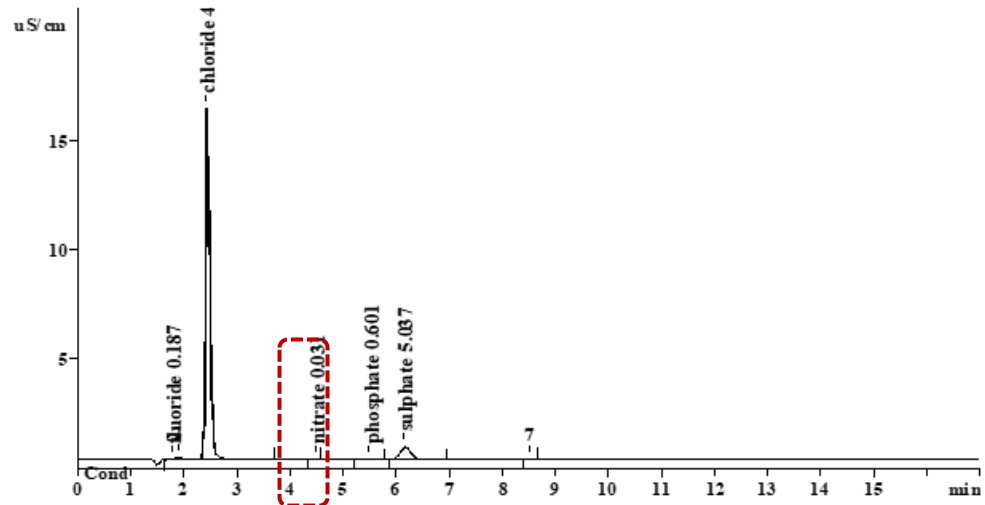


Figure 4-13 Ion exchange chromatography test's results for steady state conditions of the bio-chemical solution

As before, the  $NO_3^-$  concentration of the diluted chemical is equal to 0.031 p.p.m., which corresponds to  $[NO_3^-] = 3.1$  p.p.m. of the original bio-chemical solution. Thus, it is possible to ascertain that bacteria metabolism is highly able to reduce nitrates with a very high denitrification process efficiency, since  $[NO_3^-]$  has been reduced from 2031.4 p.p.m. to 3.1 p.p.m., as briefly reported in Table 4-4.

Table 4-4 Ion exchange chromatography tests' results

$[NO_3^-]$ initial	$[NO_3^-]$ final	$(\Delta[NO_3^-])/[NO_3^-]$ initial
2031.4 p.p.m.	3.1 p.p.m.	99.84%

To sum up, the ion exchange chromatography tests assess the reliable ability of bacteria metabolism to reduce a very high amount of the initial nitrates. These have to be present in a sufficient quantity to ensure the activation of bacteria metabolism but, at the same time, their final concentration has to be sufficient lower, in order to be compatible with the limit value imposed by codes. For example, Italian codes (*D.Lgs. 11/1999, n. 152; D.Lgs. 02/2001 n. 31; D.Lgs 02/2016 n. 9*) declares that, regarding “*Provisions on water resources*”, the upper limit of nitrates is fixed equal to 50 p.p.m. Thus, even if a very high concentration of  $NO_3^-$  should be needed to induce the required partial saturation, the steady state concentration of nitrates is compatible with the limiting values, thus showing the potential of the bio-IPS technique presented in the current work.

Once the denitrification efficiency has been evaluated, a gas composition analysis is needed, in order to ensure the formation of the desired gas, which is the  $N_2$  as widely discussed in the previous sections. To this aim, a gas chromatographic tests have been carried out. The performed tests are reported in Table 4-5, in which both initial bacteria and nitrates concentrations are shown.

Table 4-5 Gas chromatographic tests

Test	$[NO_3^-]$ initial	Bacteria Concentration
GCT1	$\approx 2000$ p.p.m.	$10^4$ CFU
GCT2	$\approx 2000$ p.p.m.	$2 \cdot 10^4$ CFU

In order to test the generated gas – by means of bacteria metabolism – it has been necessary to activate bacteria activity in a controlled equipment able to:

- Ensure the initial anaerobic conditions;
- Minimize the possible pollution during the sampling due to the atmospheric gases.

To this aim, a Falcon® tube has been conveniently modified (Figure 4-14) in order to avoid the issues discussed above. In particular, a drainage tube with a non-return valve has been installed at the top of the Falcon itself (carefully sealed previously), in order to be further able to sample the generated gas- the more undisturbed as possible. In addition, once the chemical has been inserted and gently mixed, the atmospheric gases present anyway in the upper part of the Falcon have been suctioned.

Thanks to this procedure, bacteria activity has been activated in an anaerobic condition and with no-initial gases- because of the imposed vacuum.



Figure 4-14 Modified Falcon® tube for the generated gas sampling

Finally, the generated gas has been sampled after sufficient time to ensure the end of bacteria metabolism, to be further analysed. Results are reported in Figure 4-15 and Figure 4-16, respectively for the GCT1 and GCT2, in which the detected  $N_2$  gas is underlined by the red dashed lines.

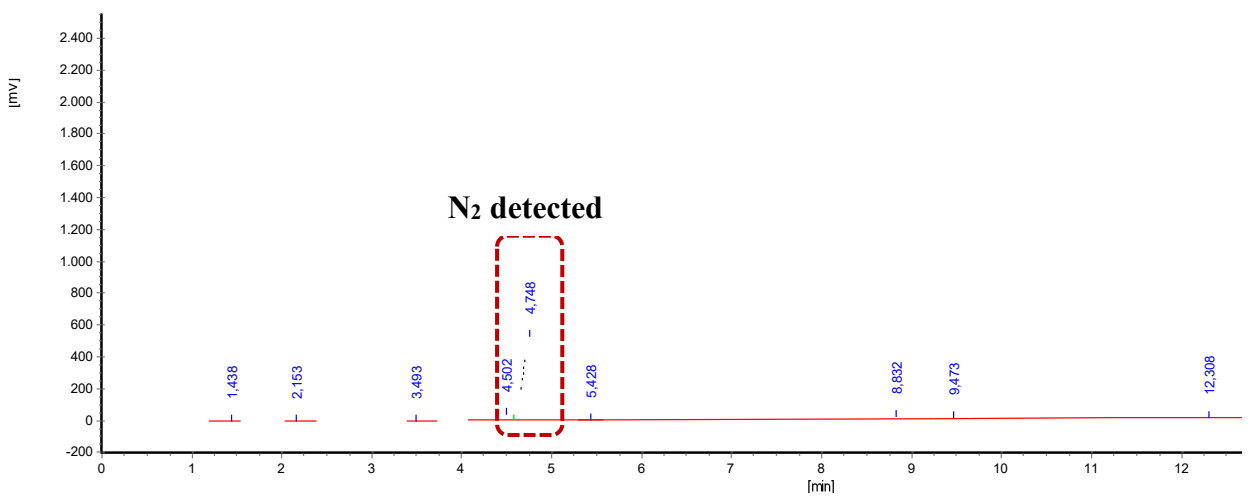


Figure 4-15 GTC1 Test results

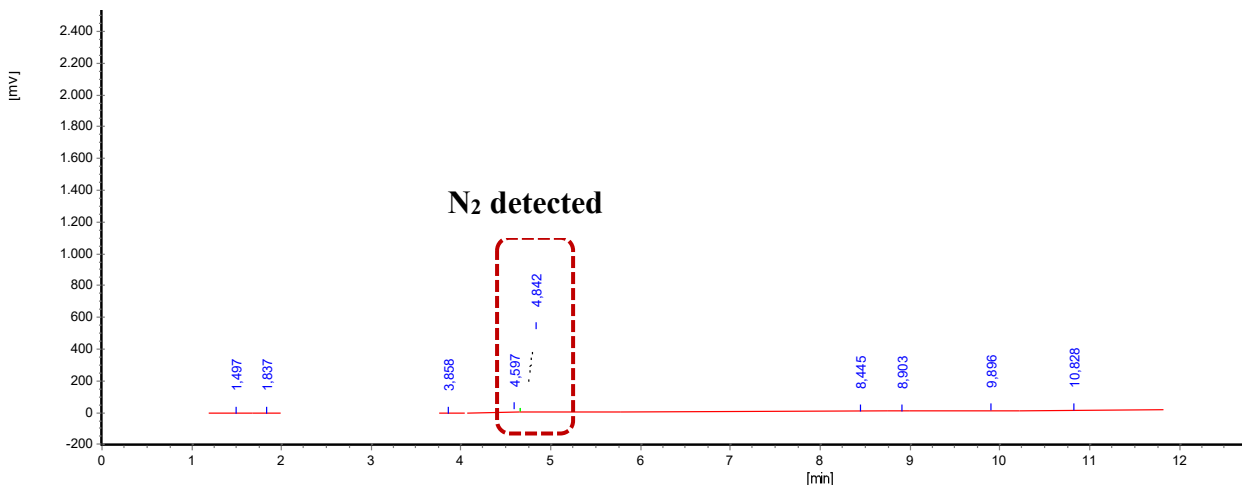


Figure 4-16 GCT2 Test results

In order to interpret data from the gas chromatography analyses, it is necessary to normalize the detected percentages to the atmospheric ones. This is due to the impossibility of sampling the gas without altering, even in a minimum part, its real composition. Indeed, during the extraction and injection in the GC apparatus, an amount of atmospheric gas will alter the sampled gas anyway, although the precautions adopted on the Falcon® device. Thus, by applying the above-mentioned normalization, it is possible to conclude that the two GC tests lead to the following percentages of  $N_2$  and  $CO_2$  gas (Table 4-6), considering that no  $O_2$  has been generated by bacteria metabolism (since the anaerobic conditions have been ensured):

Table 4-6 Gas chromatography tests results

Test	$N_2$ %	$CO_2$ %
GCT1	98.19	1.81
GCT2	98.32	1.68

Tests results show that a very high percentage of nitrogen gas ( $\approx 98\%$  in both tests) is generated, with a very low amount of  $CO_2$ . In addition, for the GCT2, an acid solution has been added to allow the formation of  $CO_2$  gas, which was already present in the liquid phase. After the acidification, the gas chromatography test has been repeated, and output results are showed in Figure 4-17, in which the  $CO_2$  detected gas is underlined by the black dashed line.

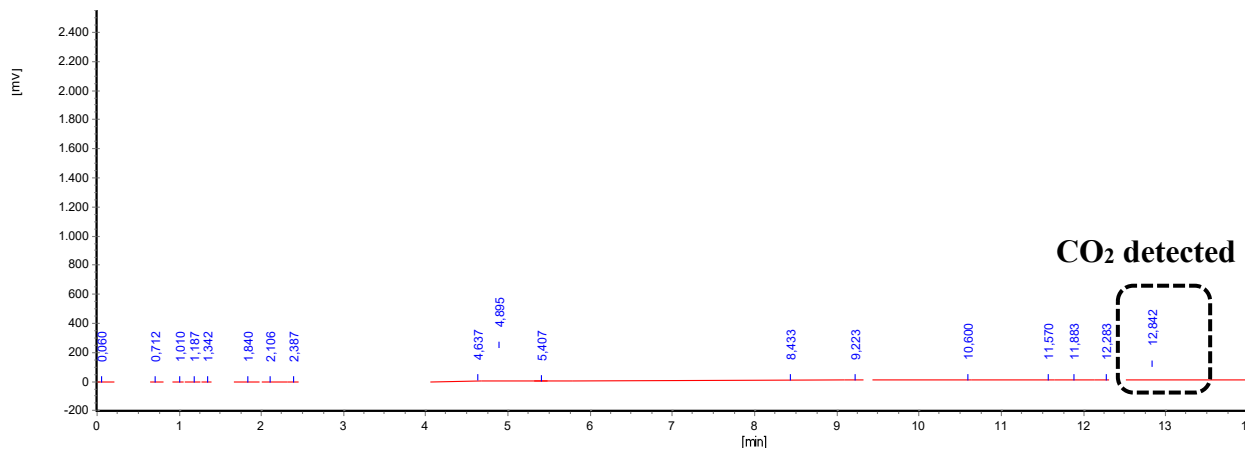


Figure 4-17 GCT2- Acidified solution to detect  $\text{CO}_2$  gas

As it can be seen, by acidifying the chemical, an amount of  $\text{CO}_2$  is detected, conversely for the first two tests reported previously. This result confirms that, although  $\text{CO}_2$  is formed during the bioprocess, it lies in the liquid phase and it is not present as Greenhouse Gas. In conclusion, gas chromatography tests have ensured the nitrogen gas formation, in very high percentages. In addition, no  $\text{CO}_2$  in gas phase is generated – at least not in notable amount. Thus, both nitrates and generated gas tests certify the applicability of such a bio-IPS technique, being very efficient and environmentally compatible:

- Selected bacteria are able to reduce even a very high initial concentration of nitrates, verifying that a very high efficiency of the denitrification process is carried out. In addition, steady state  $\text{NO}_3^-$  concentration are compatible with the limiting code values;
- Generated gas from respiratory denitrification is mainly formed by  $\text{N}_2$  gas, which is the desired one because of its low solubility, chemically inert and environmentally compatible.

Finally, thanks to the biological and chemical-environmental tests discussed above, the applicability of the selected bacteria has been evaluated, aiming to induce the partial saturation as a liquefaction mitigation technique. These results are fundamental for the development of the technique, by means of desaturation tests on an initial fully saturated soil sample. Indeed, as it will be widely reported in the following chapter, several desaturation tests – in different conditions – have been performed, in order to quantify the amount of produced gas and thus, as a consequence, to evaluate and assess the degree of saturation obtained at steady state conditions, after the bio-respiratory denitrification had been carried out.

## 5 CHAPTER 5

### 5.1 GEOTECHNICAL TESTING

Once the applicability of the selected bacteria to carry on respiratory denitrification processes has been evaluated- from a biochemical point of view- it has been necessary to develop a geotechnical experimental setup, in order to verify and quantify the Induced Partial Saturation within the soil. The aim of the geotechnical testing is to evaluate the transient process carried out by bacteria activity and to quantify the generated gas volume, in order to assess the degree of saturation at the end of the biochemical process.

In this section, desaturation tests will be reported. In particular, three different apparatuses have been used- as it will be shown. In addition, several bio-chemical measurements have been carried out during some of the tests, in order to better understand bacteria metabolism and its effects on the final configuration of the treated soil. The tested soils are represented by three different type of sands- all liquefiable. Their grain size distributions are quite different and, most important, they show different amount of natural organic matter- thus carbon sources- that, as it will be underlined in the follow, can slightly affect the transient process. Furthermore, optical analyses on bubble nucleation have been performed, trying to investigate its dimension and stability. Tests have been carried out on the biochemical solution alone and in presence of soil to be treated. All these aspects will be detailed in the next sections.

### 5.2 TESTED SOILS

As previously mentioned, three different soils have been tested. All of them fall well within the liquefiable granulometric range defined by the Italian code NTC 2018. Thus, the tested soils will be named as follows:

- *PdC silty sand*: a silty sand retrieved from Pieve di Cento site (Emilia Romagna, Italy), in which several liquefaction phenomena were detected during the North Italian earthquake of the 2012;
- *Quarto sand*, a poorly graded sand;
- *Quartz sand*, an artificial monogranular quartz sand.

In Figure 5-1 all the three granulometric curves are shown while, in Table 5-1, the main parameters are reported.

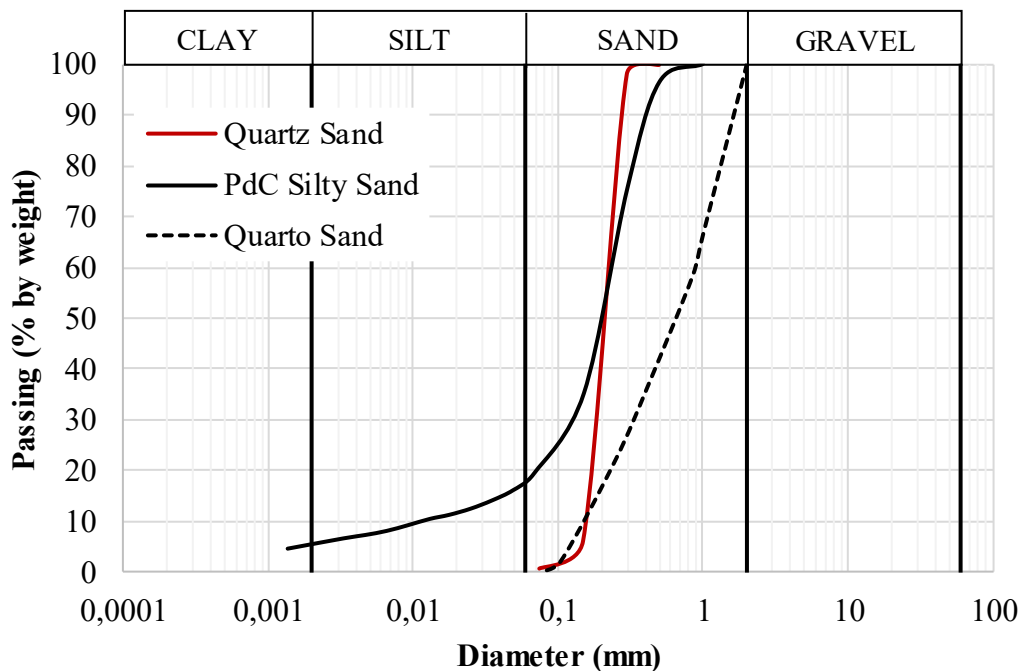


Figure 5-1 Granulometric curves of tested soils

Table 5-1 Tested soils intrinsic parameters

Soil (-)	$G_s$ (-)	$e_{max}$ (-)	$e_{min}$ (-)	$D_{50}$ (mm)	$U_c$ (-)	FC (%)
PdC Silty Sand	2.685	0.884	0.442	0.200	20.00	18
Quarto Sand	2.710	0.728	0.368	0.680	5.44	0
Quartz Sand	2.640	0.769	0.512	0.215	1.45	0

Since the coefficient of uniformity,  $U_c$ , is quite different for the three material, a subdivision of the soils regarding the liquefiable ranges has been made. To this aim- with respect to the above-mentioned granulometric ranges adopted by the NTC 2018 Italian code- soils are grouped in Figure 5-2 and Figure 5-3, as a function of  $U_c$ .

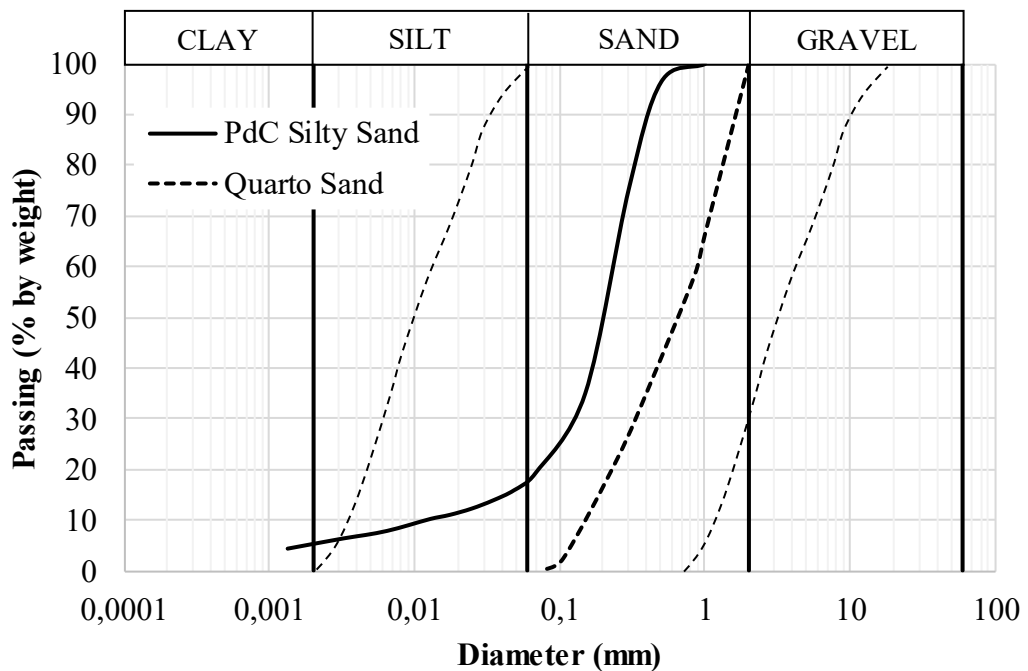


Figure 5-2 PdC silty sand and Quarto sand granulometric distributions for  $U_c > 3.5$

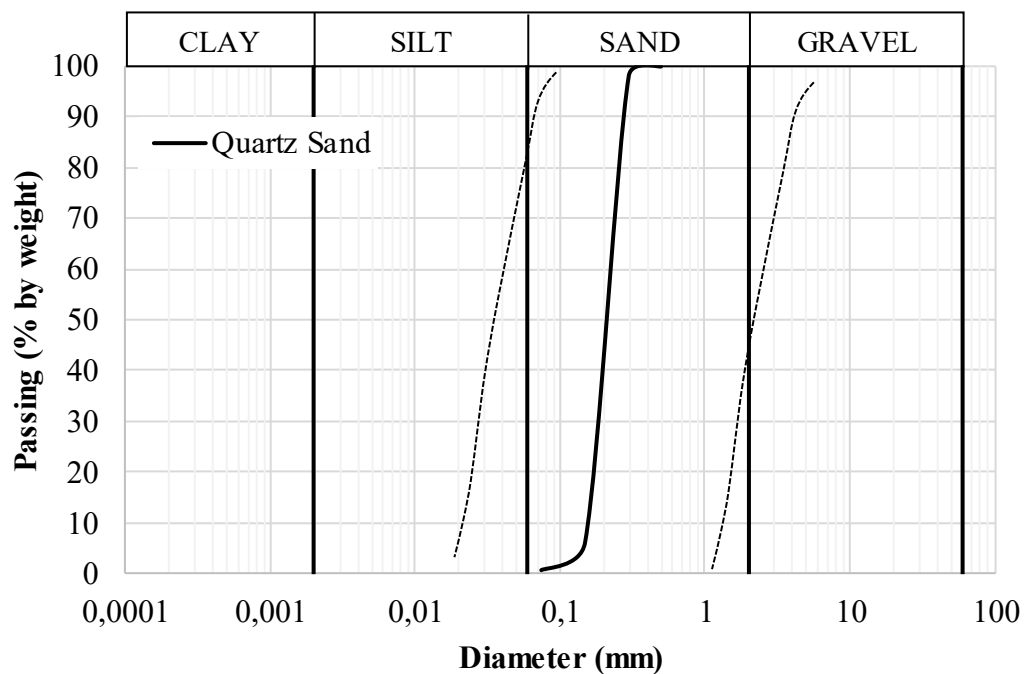


Figure 5-3 Quartz sand for granulometric distributions for  $U_c < 3.5$

It is easy to ascertain that all the tested soils lie within the specific granulometric susceptible ranges, resulting in a liquefiable granulometric zone.

### **5.3 DESATURATION TESTS**

To the aim of quantifying the generated gas volume by means of nitrogen gas bubbles nucleation, several desaturation tests have been performed. Desaturation tests have been carried out using different apparatuses - as will be shown in detail in the following - in which the tested materials are pluviated at the same void ratio and in fully saturated initial conditions. To ensure the initial fully saturation, a wet pluviation sample preparation method has been adopted. Thus, the dry soil has been carefully and gently pluviated, at a controlled drop height, directly within the bio-chemical solution. The latter was previously prepared by mixing the selected bacteria and the nitrate broth- both prepared at different concentrations- immediately before the soil pluviation. Samples preparation procedure has been kept unchanged for all tests, regardless of the apparatus used. Indeed, as previously mentioned, desaturation tests have been carried out in three different equipments, which will be named in the following as:

- Permeameters (DTP Tests);
- Desaturation testing cell (DTC Test);
- Resistivity Cell (DRC Tests).

These three different equipments have increasing dimensions (from the first to the third), in order to investigate any possible change in bacteria metabolism caused by the environmental dimensions. Their setting up as well as their characteristics will be explained in detail in the relative section of interest.

However, for each test, the generated gas volume has been indirectly measured by measuring the expelled pore fluid. Indeed, if the sample starts in fully saturated conditions, bacteria metabolism will activate a filtration process due to the nucleation of the bubbles, with consequently generation of pore pressures. Those pore pressure increments, at the surface of the generated bubbles, determine a pore pressure gradient that will result in an expulsion of the pore fluid. Thus, if the expelled pore fluid is measured, the basic and fundamental assumption for the desaturation tests is that the volume of generated gas bubble within the soil pores is equal to the volume of the expelled pore fluid itself. Thanks to this, if any soil state parameter is known and controlled, it is possible to assess- both in transient and steady state conditions- the degree of saturation achieved with the bio-IPS technique.

In the following sections, desaturation tests- and the relative equipment used as well as the soil tested- will be reported. Table 5-2 shows briefly the type of test, the apparatus used and the tested material.

Table 5-2 Summary of desaturation tests

Test	Equipment used	Tested soil
DTP1	Permeameter	PdC Silty Sand
DTP2	Permeameter	PdC Silty Sand
DTP3	Permeameter	PdC Silty Sand
DTP4	Permeameter	PdC Silty Sand
DTP5	Permeameter	PdC Silty Sand
DTP6	Permeameter	PdC Silty Sand
DTP7	Permeameter	PdC Silty Sand
DTC	Desaturation testing cell	PdC Silty Sand
DRC1	Resistivity Cell	Quarto Sand
DRC2	Resistivity Cell	Quartz Sand

### 5.3.1 PERMEAMETER TESTS

Permeameter desaturation tests have been performed by testing the PdC silty sand (Figure 5-2). In order to verify its susceptibility to liquefaction, cyclic triaxial tests have been carried out on saturated specimens, with an effective confining pressure of 50 kPa and an average relative density of 40%. The obtained cyclic resistance curve is reported in Figure 5-4 (Astuto et al. 2019).

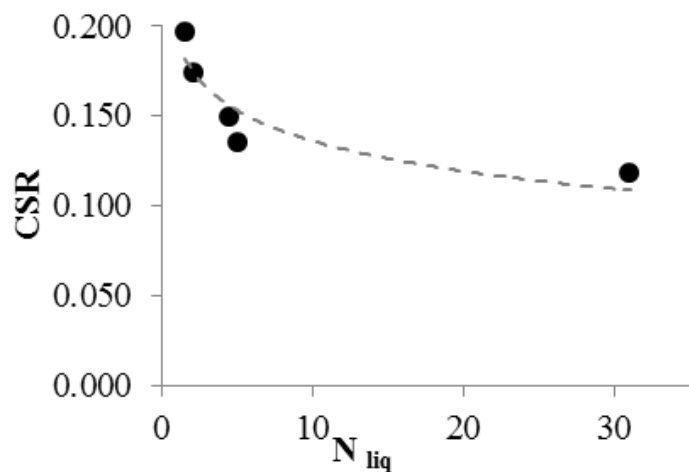


Figure 5-4 Cyclic resistance curve for PdC silty sand ( $\sigma'_{c,0}=50$  kPa;  $D_{r,avr}=40\%$ ) (Astuto et al. 2019)

Desaturation tests are carried out using classic permeameters ( $\Phi=50$  mm,  $H=100$  mm) (Figure 5-5) in which the silty sand is pluviated at the same void ratio and in a fully saturated condition. The wet pluviation is made directly in the solution containing both bacteria and nitrates, and it has been performed in order to obtain an average relative density of all the specimens equal to  $\approx 40\%$ . Permeameters are equipped with two porous metal plates, one at the top and one at the bottom. Prior to pluviation, metal plates have been carefully saturated with the biochemical solution, to ensure the initial complete saturation and to minimize any approximation during the expelled pore fluid measurements. In each test a different concentration of bacteria and nitrates is tested. Measurements of the expelled pore fluid are made by an upper drainage of the permeameter connected to a collection system (Figure 5-6) while, obviously, the lower drainage is kept closed during the entire test. In detail, the measurements of the expelled pore fluid have been assessed by weight measurements of the entire system connected to the permeameter itself. To this aim, cables are equipped with an open/close valve, able to isolate the entire collection system during each measurement of the expelled pore fluid's weight. Regarding the pore pressures applied to the sample, the liquid phase is directly connected to the atmosphere, resulting in a pressure of the pore fluid to be equal to the atmospheric one. In addition, during some of the tests, measurement of  $NH_4^+$  concentration have been carried out to verify the biochemical paths discussed in the previous section. Such results will be reported and discussed in the §5.3.2.

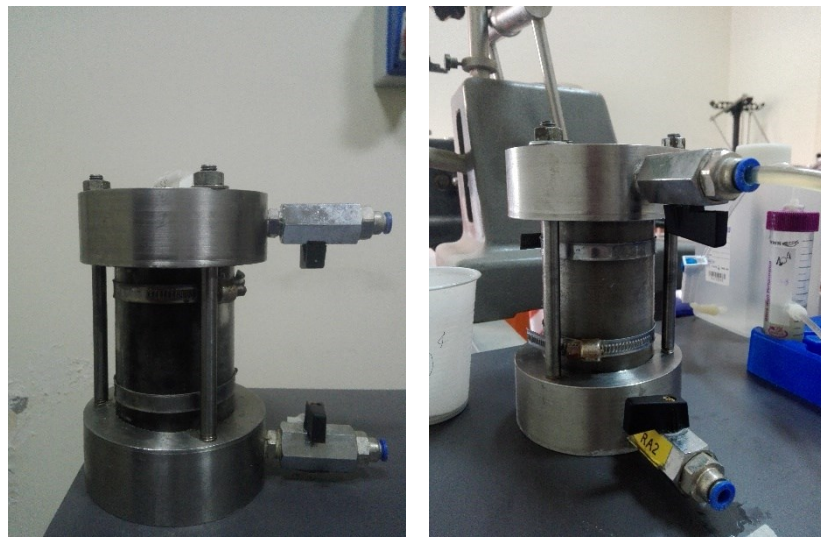


Figure 5-5 Classic permeameters used for DTP tests

In Table 5-3 a summary of the desaturation permeameter tests is reported. As mentioned before, different initial concentrations of both bacteria and  $NO_3^-$  have been tested.

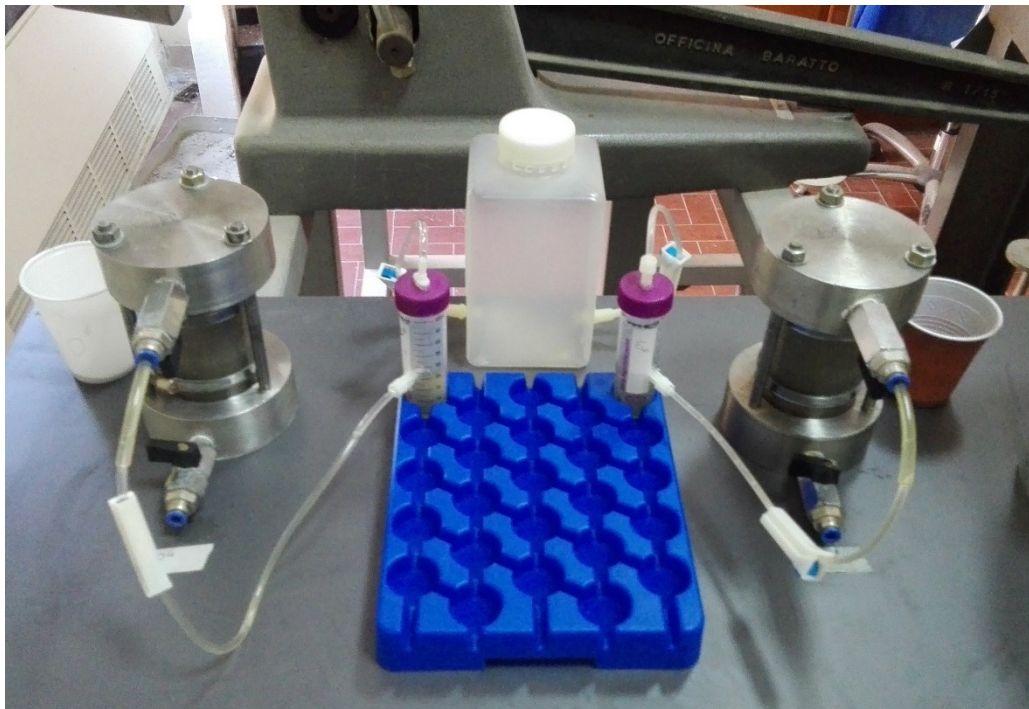


Figure 5-6 DTP set up

Table 5-3 Permeameters desaturation tests

Tests (-)	Bacteria Concentration (C.F.U.)	Nitrate Concentration (mg/L)	Sr (%)	NH <sub>4</sub> <sup>+</sup> Measurements (-)
DTP1	1,00E+08	2500	59,90%	✓
DTP2	1,00E+04	2500	62,80%	✓
DTP3	1,00E+04	240	81,90%	✗
DTP4	1,00E+04	24	94,90%	✗
DTP5	1,00E+04	200	81,30%	✗
DTP6	1,00E+04	2000	69,14%	✗
DTP7	1,00E+04	2000	63,83%	✗

The tests reported in Table 5-3 show a  $NO_3^-$  concentration ranging from 2500 mg/L to 24 mg/L, thus varying over a range of two orders of magnitude.

In Figure 5-7 desaturation tests for DTP1, DTP2, DTP6 and DTP7 tests ( $[NO_3^-] = 2000/2500$  mg/L) are reported- in terms of generated gas-, as a function of the normalized time (defined as  $t_i/t_{\text{steady state}}$ ). In Figure 5-8 the same tests results are reported, in terms of degree of saturation.

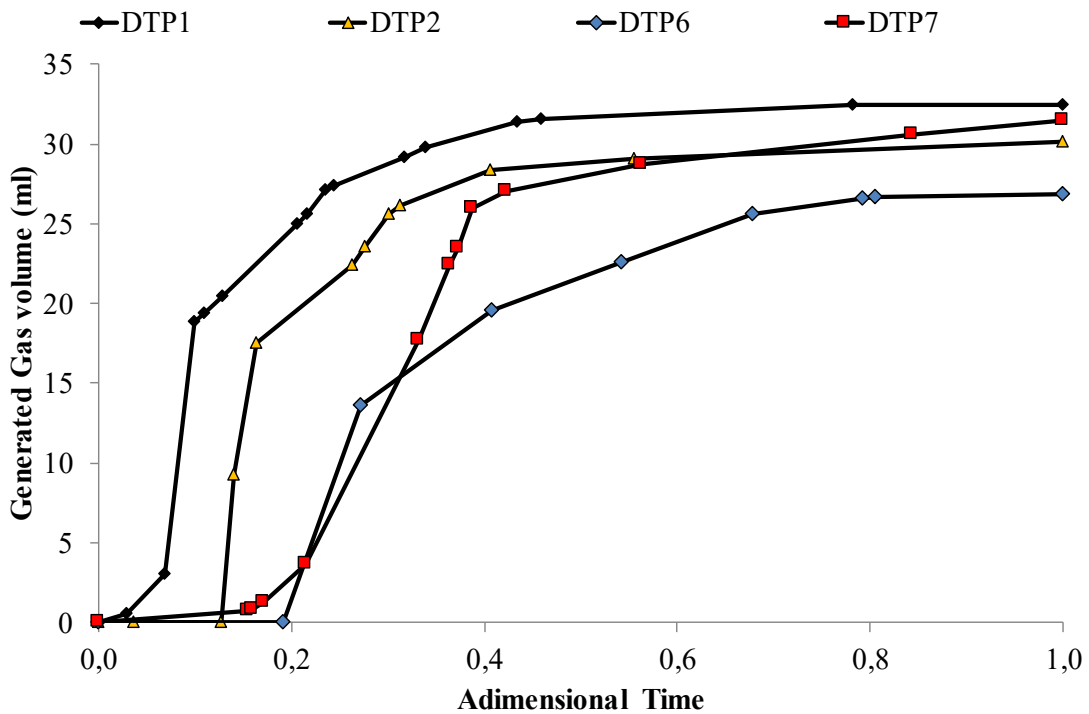


Figure 5-7 Desaturation tests results for DTP1, DTP2, DTP6 and DTP7- Generated gas volume

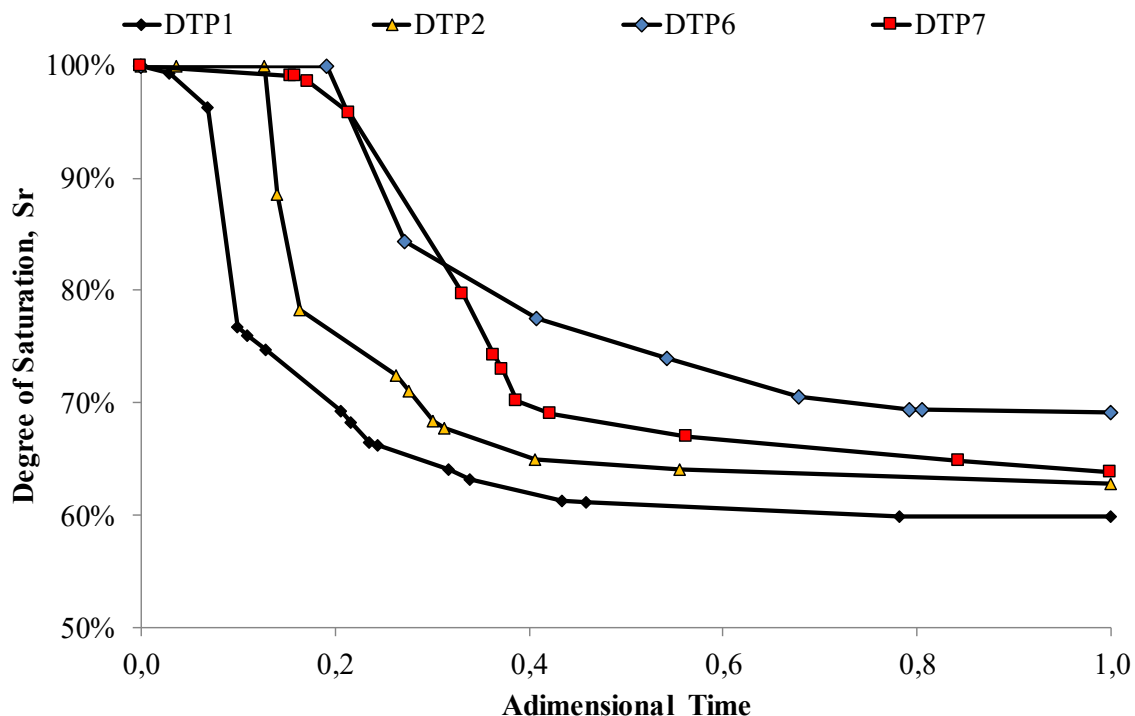


Figure 5-8 Desaturation tests results for DTP1, DTP2, DTP6 and DTP7- Degree of saturation

The calculation of the variation of the degree of saturation with time has been easily performed by measuring the expelled pore fluid. Indeed, if the sample is initially fully saturated and the state parameters are known, it is possible to calculate immediately the water content as:

$$w_{sat} = \frac{P_{w,sat}}{P_S} \quad \text{Equation 5-1}$$

$$S_r = \frac{w_{sat} \cdot \gamma_s}{\gamma_w \cdot e} = 1 \quad \text{Equation 5-2}$$

Once the  $w_{sat}$  is known, by measuring each time the expelled pore fluid, it is easy to re-calculate the water content and, consequently, the degree of saturation as:

$$w = \frac{P_{w,sat} - P_{expelled \ pore \ fluid}}{P_S} \quad \text{Equation 5-3}$$

$$S_r = \frac{w \cdot \gamma_s}{\gamma_w \cdot e} \quad \text{Equation 5-4}$$

Results show that an important decrease of the degree of saturation can be achieved, by using an initial concentration of nitrates ranging from 2000 to 2500 mg/L. For such concentrations,  $S_r$  lower than 70% can be reached.

On the other hand, in Figure 5-9 and Figure 5-10 tests results for a lower (but not the lowest tested)  $NO_3^-$  concentration are reported, respectively showing the generated gas volume and the degree of saturation achieved. For these tests the steady state degree of saturation is about of 80%.

Finally, the DTP 4 desaturation test has been performed by using the lowest  $NO_3^-$  concentration, equal to 24 mg/L. Test results are showed in Figure 5-11 and Figure 5-12, in terms of generated gas volume and degree of saturation- as for the previously presented tests results. As it was expected, final degrees of saturation are much higher if compared to the rest of the tests. This is obviously due to the very low nitrates concentration of the bio-chemical solution, resulting in a very low efficiency of bacteria to nucleate gas bubbles. Indeed, by following the bio-chemical processes reported in the previous sections, if a low amount of nutrients-  $NO_3^-$ -are available for bacteria to be reduced, it will result in a low amount of  $N_2$  generation.

Thus, once permeameter test results have been grouped and showed- as a function of  $[NO_3^-]_0$ , it is useful to compare all the entire tests in a unique chart, as reported in Figure 5-13.

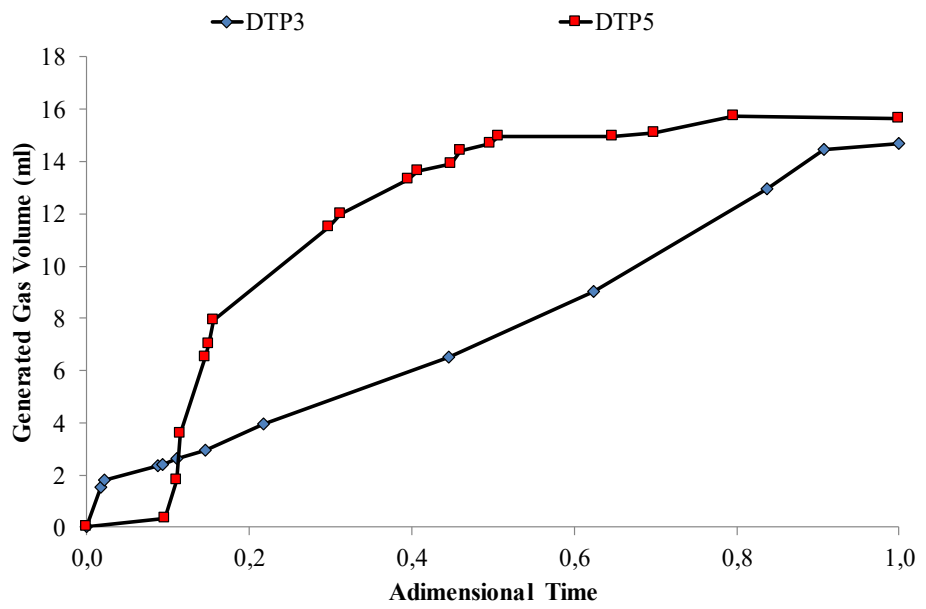


Figure 5-9 Desaturation tests results for DTP3 and DTP5- Generated gas volume

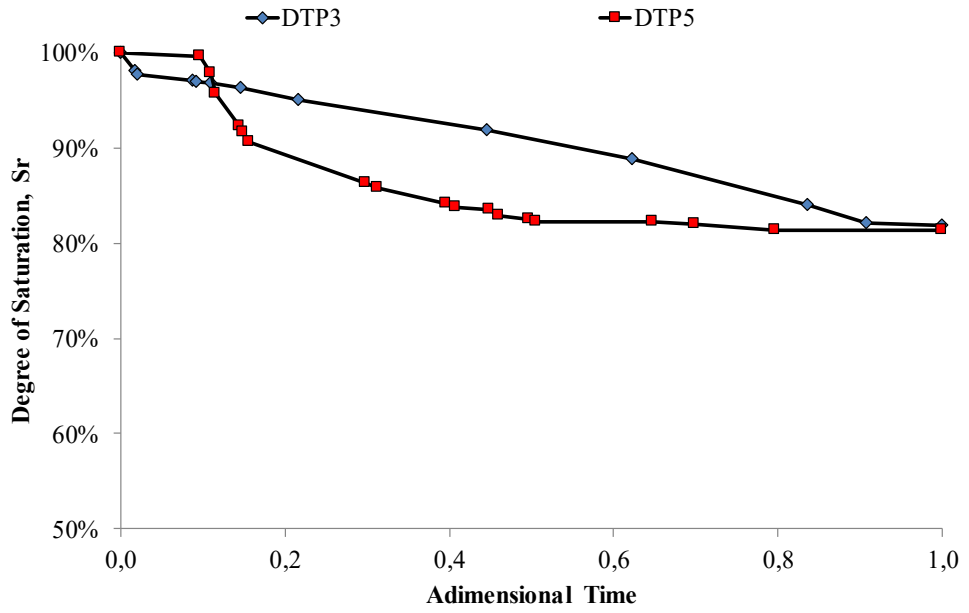


Figure 5-10 Desaturation tests results for DTP3 and DTP5- Degree of saturation

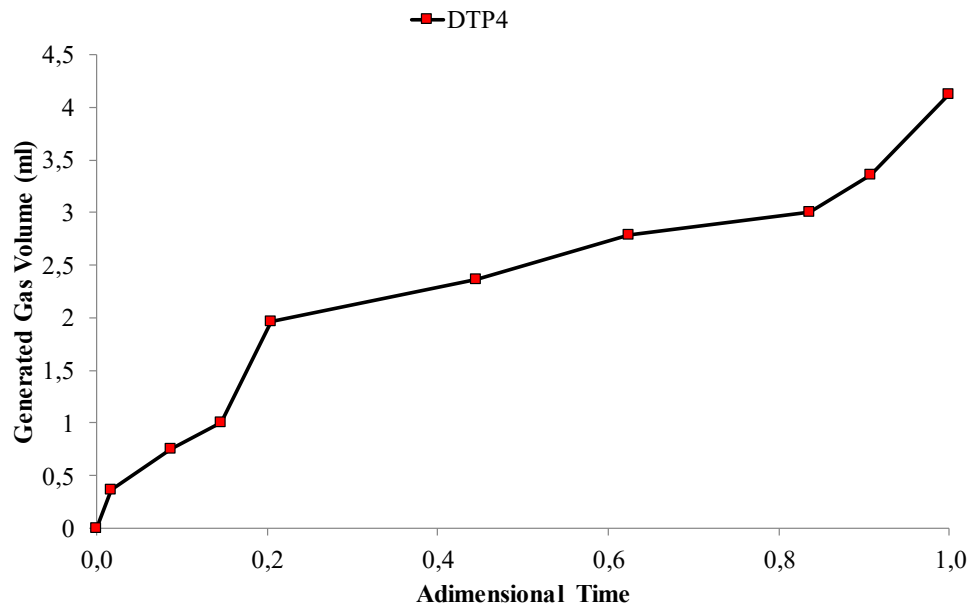


Figure 5-11 Desaturation tests results for DTP4- Generated gas volume

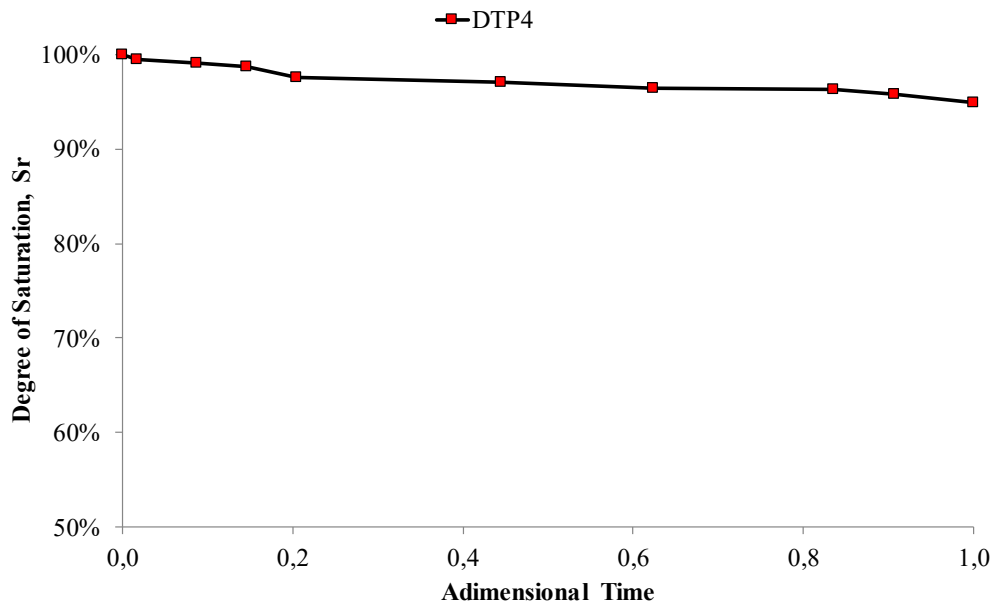


Figure 5-12 Desaturation tests results for DTP4 - Degree of saturation

Tests results show that the induced partial saturation process leads to a wide range of degrees of saturation, depending on the amount of nutrients available for the selected bacteria- as the biochemical theory predicts. In particular, it is interesting to focus on the transient phases that lead to the gas bubbles nucleation. Indeed, two “stages” can be qualitatively detected:

- A first one, in which the gradient of the generated gas- and thus the reduced degree of saturation- is particularly high. In this stage, gas bubbles nucleation seems to be very

efficient, resulting in a high desaturation potential of the bacteria lineages, which lies in the range of normalised time between 0.1 and 0.4, especially for the DTP tests presenting a higher quantity of  $NO_3^-$ . Besides, a good consistency between the tests is achieved, except for the DTP3 test, in which no particularly high generated gas gradients are detected, but almost the same steady state  $S_r$  is reached anyway;

- A second one, in which the gradients of the generated gas tends to be lower. In this stage, desaturation goes on anyway, presenting gas generation velocities much lower than the first “stage”.

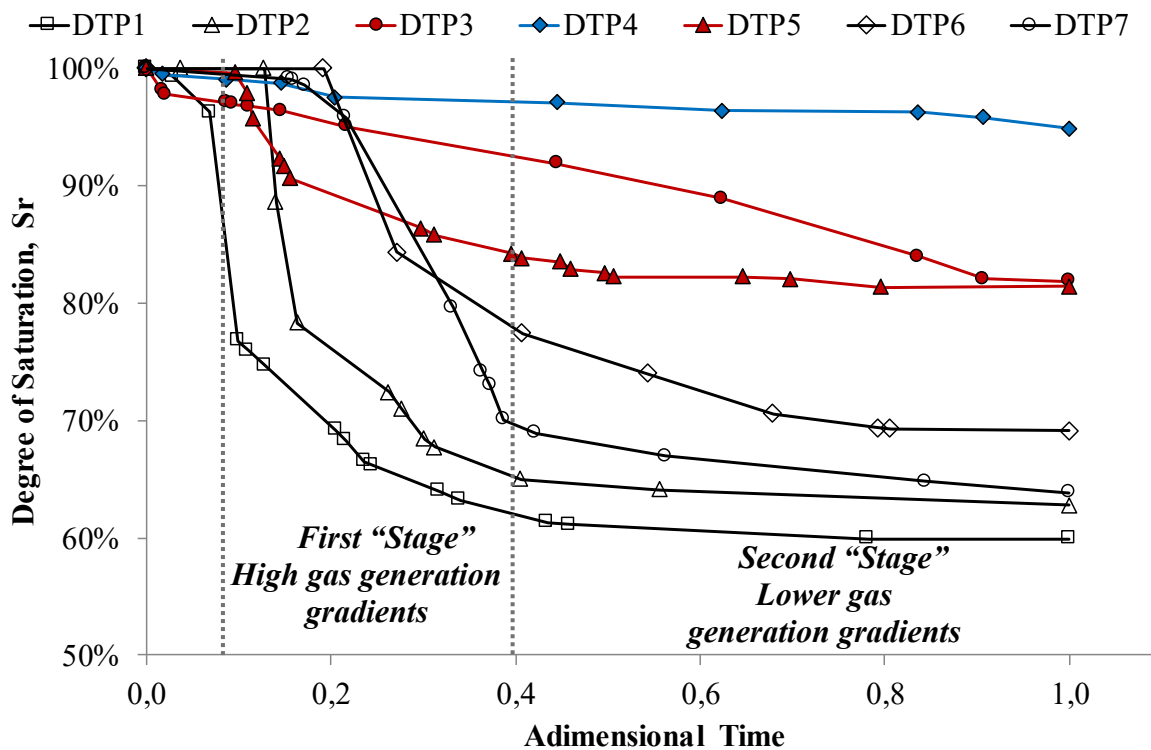


Figure 5-13 Permeameters desaturation tests results – Comparison between the final degrees of saturation

As revealed in advance, an additional apparatus with higher dimension has been used to test the bio-desaturation potential. The increasing in the equipment’s volume was useful to assess if a higher number of voids can influence bacteria metabolism and thus the process’ efficiency. The apparatus, identified by the DTC test (Table 5-2) is shown in Figure 5-14. The desaturation testing cell presents the following dimensions: B=200 mm; L=110 mm, H=120 mm. It has been equipped with two side-placed drainages, connected to graduate burettes allowing to the measurement (by volume in this case) of the expelled pore fluid, to assess time after time the  $S_r$  achieved. The drainages present two porous plates, adequately covered by filter papers, in order to neglect any type of occlusions caused

by the finer content of the silty sand. In addition, a lower drainage, placed in the lower part of the cell, has been adopted to sample liquid pore fluid sample to be further analysed. Even in this test, since the burettes are connected to the atmosphere, the pressure of the pore fluid is equal to the atmospheric one.

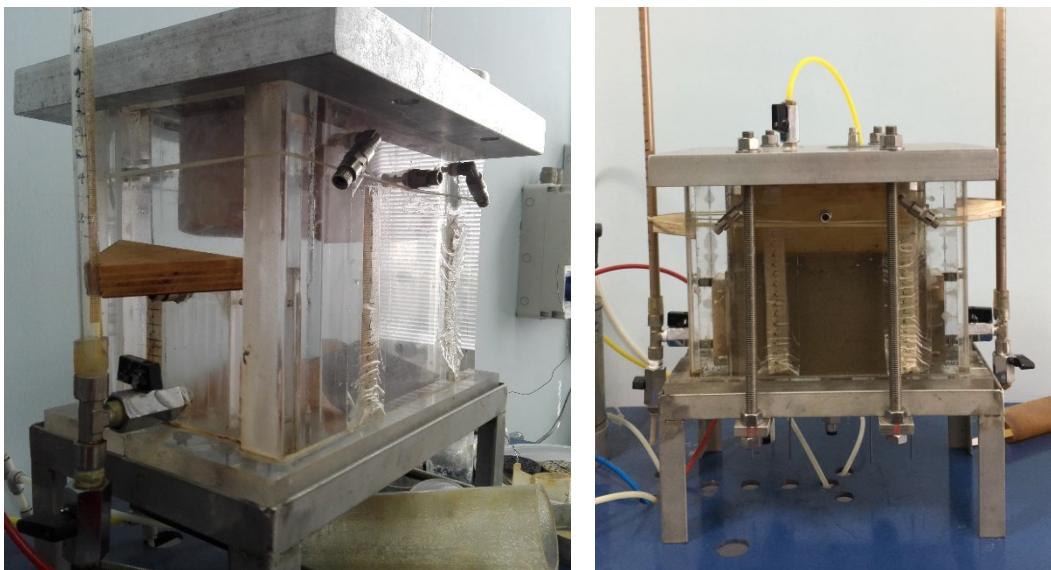


Figure 5-14 Desaturation testing cell equipment

Table 5-4 DTC test

Tests	Bacteria Concentration (C.F.U.)	Nitrate Concentration (mg/L)	Sr (%)	NH <sub>4</sub> <sup>+</sup> Measurements (-)
DTC	1,00E+08	2500	57.15%	✓

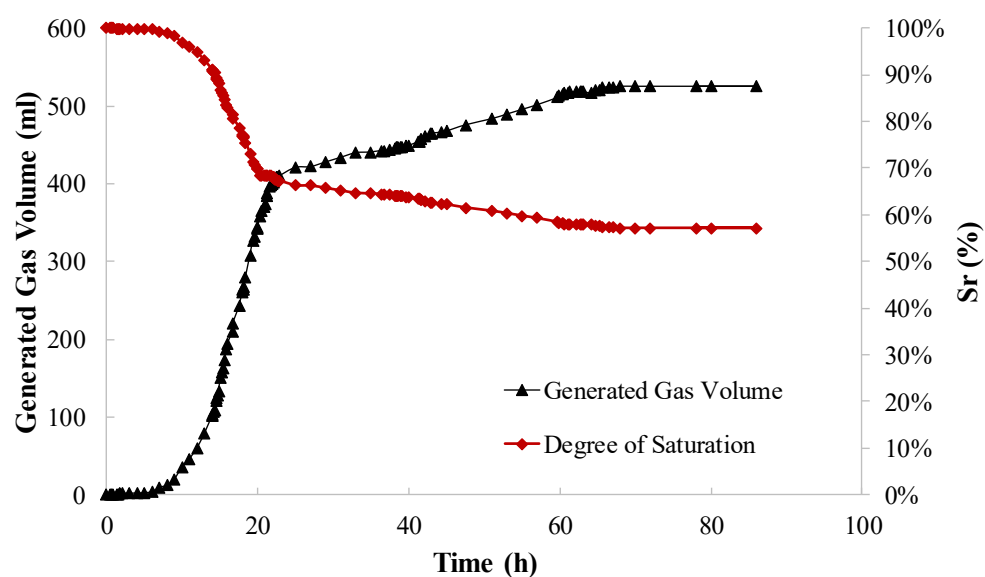


Figure 5-15 DTC test result – Generated gas volume and degree of saturation

In

Table 5-4 the main information about DTC test are reported while, in Figure 5-15, test results are showed- both in terms of generated gas and degree of saturation achieved time after time.

Thanks to the increased volume of the testing cell – if compared with permeameters' dimensions– it has been possible to measure the expelled pore fluid more accurately as well as with a higher sampling ratio, resulting in a more regular trend of the curves. For the DTC test, as reported in

Table 5-4, the same bacteria concentration adopted for the DTP1 test has been used. Besides, regarding the  $NO_3^-$  concentration, DTC test has been initiated by keeping unchanged nitrates quantity, equal to 2500 mg/L, as for the DTP1 and DTP2 tests. Thus, since the tests conditions are quite similar between the above-mentioned three experiments, it is useful to compare their results, as reported in Figure 5-16.

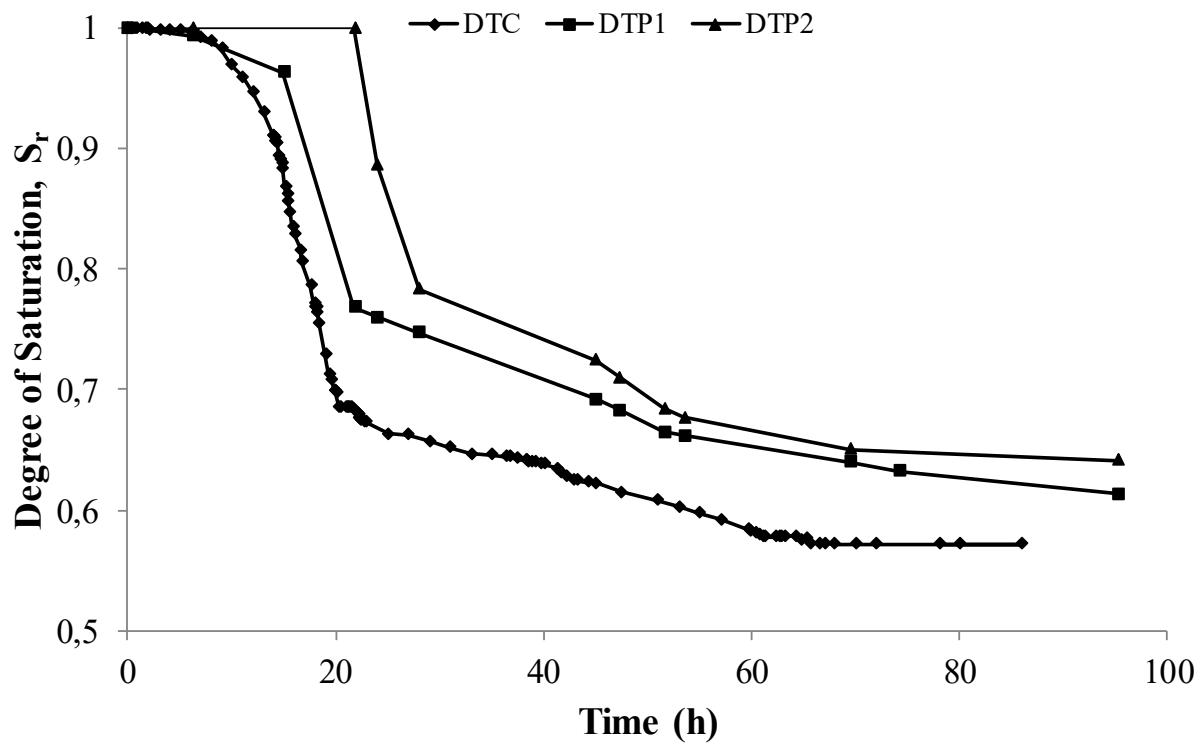


Figure 5-16 Comparison between DTP1, DTP2 and DTC tests

As it can be easily seen, the DTC shows a faster activation of bacteria metabolism, even if compared with the DTP1 test – at the same bacteria concentration. In addition, the final degree of saturation reached by the DTC test is approximately  $S_r \approx 57\%$ , being the lowest achieved in the performed tests. The higher volume of the desaturation testing cell is such to increase the efficiency of bacteria metabolism, probably due to a more effective establishment of the microorganisms'

colonies among the grains. Thus, a first preliminary conclusion deriving from tests shown in Figure 5-16 is that the dimension of the treated volume could affect the bacteria efficiency: the higher is the volume, the higher will be the capability of bacteria to activate their own metabolism – at the same initial concentration, as for DTC and DTP1 tests. On the other hand, if attention is focused on DTP1 and DTP2 tests, if  $NO_3^-$  concentration is kept constant (as it is for the mentioned tests), by lowering bacteria concentration from  $10^8$  to  $10^4$  CFU the final degree of saturation is practically the same. Thus, for such range of tested concentrations, it is possible to reliably assert that the limiting factor for the bio-IPS potential is represented by the  $[NO_3^-]_0$ , rather than bacteria concentration.

Afterwards, ion ammonium measurements  $NH_4^+$ , carried out during several tests, have been interpreted, with the aim to deeper investigate the transient desaturation processes, especially under a bio-chemical point of view. To this purpose, several samples of pore fluid have been analysed, during time, and interpreted with the aid of the back-knowledge about the biochemical paths involved in the process. Such results will be shown and commented in the next section.

### 5.3.2 TIME-DEPENDENT METABOLISM ANALYSIS

The IPS process carried out by bacteria metabolism has been evaluated by means of the desaturation tests discussed above. Once the final results in terms of degree of saturation have been assessed, it is fundamental to deeply investigate the entire process in terms of intermediate products too. Indeed, if the bio-IPS technique wants to be applied in real scale issues, it is necessary to evaluate the time dependent metabolism as well as the chemical compounds resulting from the metabolism itself. To this aim, for the tests reported in Table 5-5, samples of the pore fluid have been analysed, in order to assess the trend of the ion ammonium produced during the bacteria respiratory denitrification. Measurements have been carried out by means of spectrophotometer analyses. In such tests, the absorbances of the solutions, in terms of optical density at a certain wavelength, is evaluated. The concentration of the wanted product is linearly correlated to the absorbances, through the Lambert-Beer law (Swinehart 1962), as follows:

$$C = \frac{A}{(\varepsilon \cdot b)} \quad \text{Equation 5-5}$$

in which:

- $A$  is the absorbance;
- $\varepsilon$  is an absorption coefficient, depending on the type of examined compound as well as the wavelength used;
- $b$  is the optical path of the wave;

- $C$  is the concentration of the wanted compound.

Thus, after sampling several pore fluid specimens in time,  $NH_4^+$  measurement has been carried out. In Figure 5-17 the results of the performed analyses are reported, for the DTC, DTP1 and DTP2 tests.

*Table 5-5 Desaturation tests in which ion ammonium concentration analyses have been performed*

Tests (-)	Bacteria Concentration (C.F.U.)	Nitrate Concentration (mg/L)	Sr (%)	$NH_4^+$ Measurements (-)
DTC	1,00E+08	2500	57,15%	✓
DTP1	1,00E+08	2500	59,90%	✓
DTP2	1,00E+04	2500	62,80%	✓

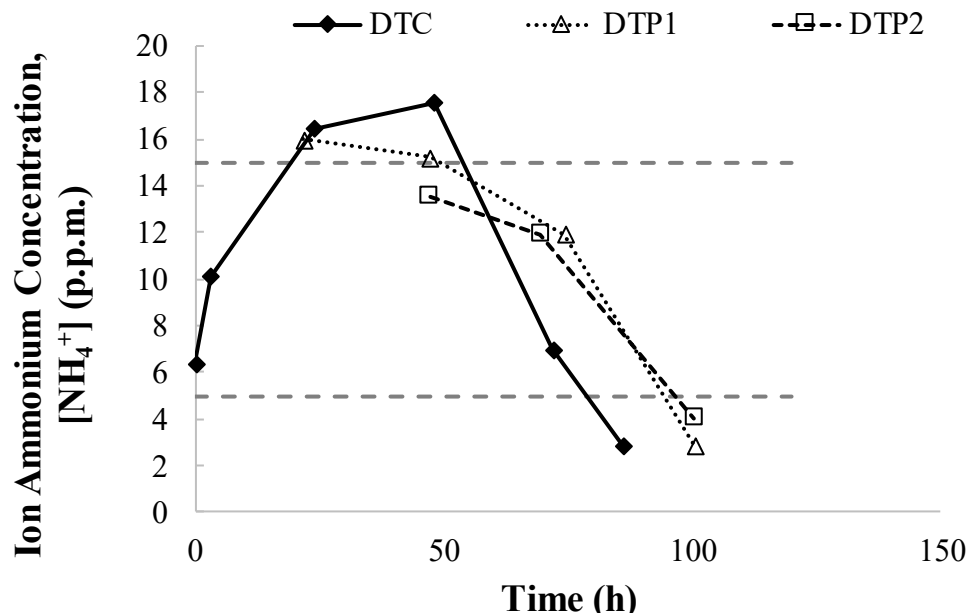


*Figure 5-17 Ion ammonium concentration analyses by means of spectrophotometric tests*

Test results have been compared with the limiting values indicated by the Italian code (*D.Lgs. 11/1999, n. 152*). As it is shown, final values are always lower than the 5 p.p.m, which is the lower bound of the acceptable  $NH_4^+$ . Thus, a first conclusion is that ion ammonium is reliably reduced by bacteria metabolism in such an amount which is compatible with the code's limits.

On the other hand, ion ammonium trend could be useful to investigate deeply the bio-chemical processes involved in the bio-IPS paths. To this aim, it is interesting to superimpose such trend with the desaturation test results, in order to interpret both results in detail. Such comparison is shown in Figure 5-18, in which results for the DTC test are reported.

The high gradient of generated gas corresponds to relatively high values of ammonium concentration. This means that in the initial phase of the test, between 20 and 40 hours, the biochemical production of  $N_2$  is mainly due to the denitrification but simultaneously the ammonification is involved in the process. Then, once the main part of nitrates is already reduced, the formed ammonium is also reduced to  $N_2$  by the anammox reaction. Thus, the gradient of generated gas is lower but  $N_2$  is still generated by the reduction of  $NH_4^+$  itself, corresponding to the time between 40 and 80 hours in the presented test.

Thus, after an initial increment, the  $NH_4^+$  tends to be reduced to 2/3 p.p.m. Since in the first step both denitrification and ammonification are involved in the process, the gradient of  $N_2$  nucleation is high as well as the production of  $NH_4^+$ . Once nitrates are mostly reduced, expelled pore fluid's gradient tends to decrease and the relative production of  $N_2$  is due mainly to the ammonium reduction caused by the anammox reaction.

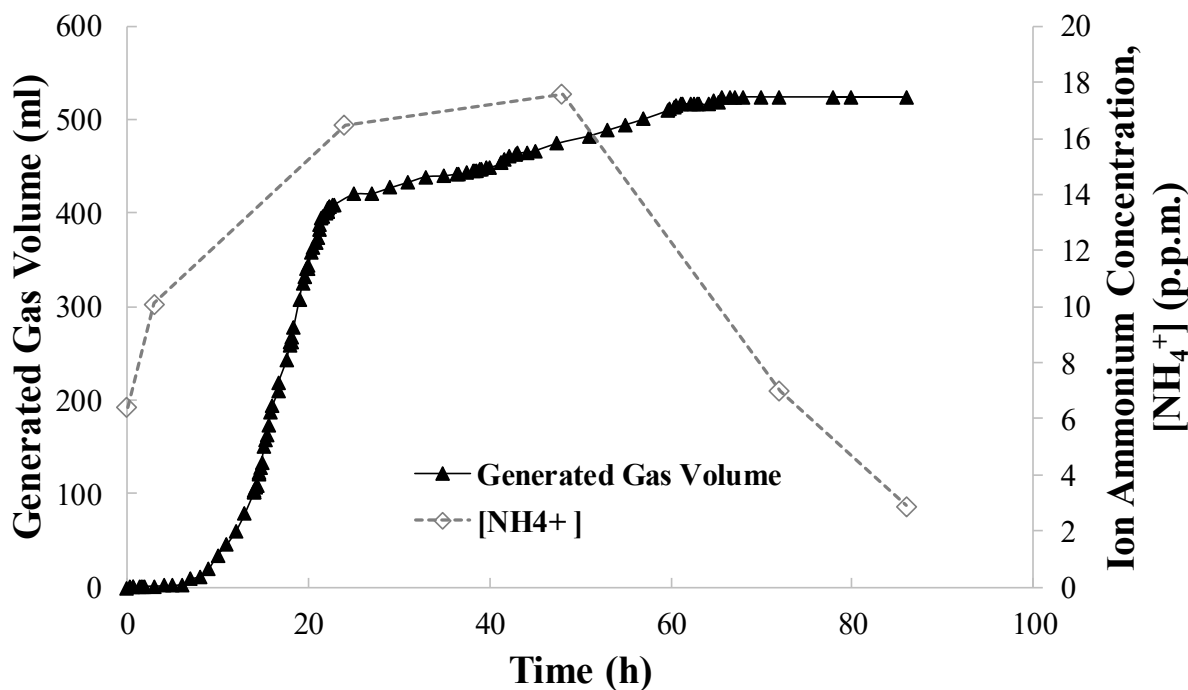


Figure 5-18 DTC test- Comparison between the generated gas volume and the development of ion ammonium concentration

Indeed, recalling the theoretical framework reported in §3.3.3, the experimental results confirm the consistency with the theoretical interpretation. In Figure 5-19 the whole process is summarized, in order to report as schematically as possible the biochemical processes involved in the IPS technique.

Finally, an additional test on nitrate concentration at the end of the DTP2 test has been performed. To this aim, a specimen has been sampled from the expelled pore fluid, once bacteria activity reached the steady state conditions. The results of the ion exchange chromatography test, reported in Figure 5-20, can be compared with the same type of analysis performed on the bio-chemical solution only-as reported in §4.6, Figure 4-13.

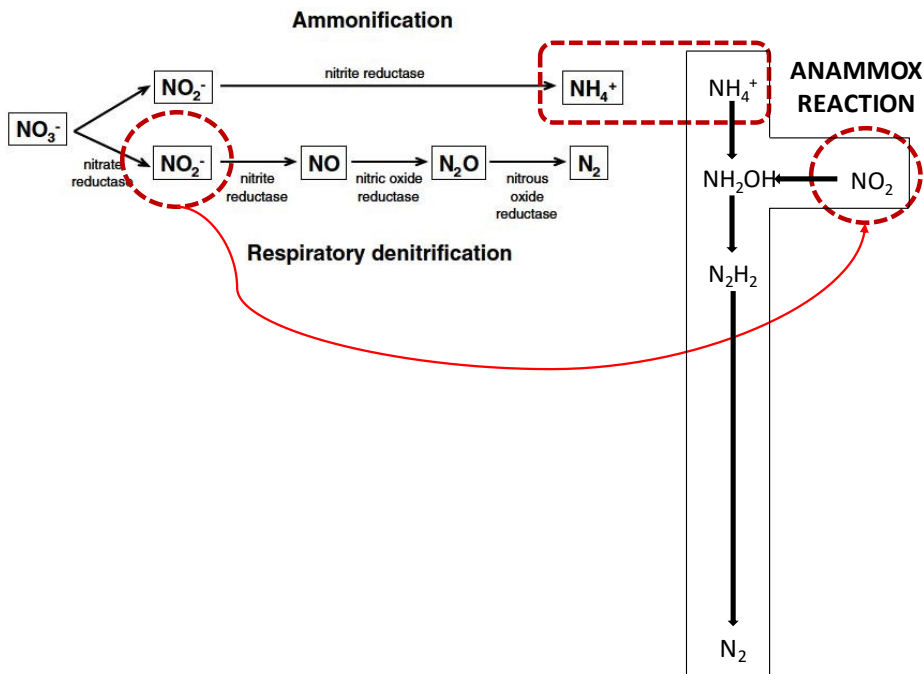


Figure 5-19 Qualitative development of bio-chemical processes

Table 5-6 Ion exchange chromatography test on DTP2 - after steady state condition has been achieved

Test	$[\text{NO}_3^-]$ initial	$[\text{NO}_3^-]$ final
<b>Biochemical Solution (only)</b>	2031.4 p.p.m	3.1 p.p.m.
<b>Soil+bio-chemical solution (DTP2 Test)</b>	$\approx 2500$ p.p.m.	2.51 p.p.m.

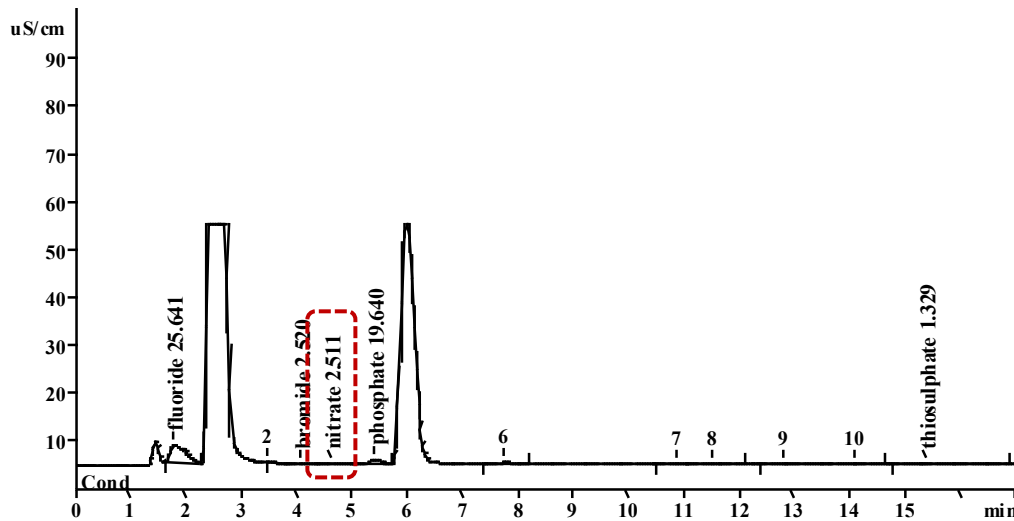


Figure 5-20 Ion exchange chromatography test on DTP2's expelled pore fluid- at the end of the test

The ion exchange chromatography test, performed on DTP2, leads to an assessment of the final nitrates' concentration equal to 2.51 p.p.m.- starting by a  $[NO_3^-]_0 \approx 2500$  p.p.m. Thus, even in this case a very high efficiency in the reduction of nitrates has been achieved by the bacteria activity. Moreover, if such result is compared with the one performed on the bio-chemical solution only, it is interesting to note that a higher efficiency is reached when the denitrification process is activated in presence of the tested soil. The higher efficiency is due to the higher availability of carbon sources, given by the organic matter presented in the PdC silty sand soil. Indeed, by drying the sandy soil in muffle at high temperature, an organic matter equal to 10.06% has been assessed. The presence of a higher amount of carbon sources- make available by the fine content practically- make bacteria metabolism to be faster and more efficient, since more nutrients can be used to reduce nitrates.

The tests performed and discussed so far have been carried out at an atmospheric pore fluid pressure. These tests have ensured the capability of bacteria metabolism to first activate itself, and then to carry on  $N_2$  bubbles nucleation. Since the development of the bio-IPS technique aims to be reliably applicable in real scale field problems, it is necessary to investigate the ability of bacteria to carry on denitrification processes even in presence of higher pore pressures. Indeed, even though liquefaction phenomena are often to be observed in the shallow layers, pore water pressures higher than the atmospheric one will be present in the subsoil, with the possible effect of altering the nucleation process. In order to check if this can be a problem, two desaturation tests on a back-pressured specimen have been performed and will be presented and discussed in the next section.

### 5.3.3 DESATURATION TESTS ON BACK-PRESSURED SAMPLES

In the present section, two desaturation tests in classic triaxial cell will be reported. The aim of the experimentation is to verify the ability of bacteria metabolism to be activated even in presence of back pressures, applied at the liquid phase, different from the atmospheric one. The tested soil is again the PdC silty sand. The sample preparation method has been kept unchanged from the DTP tests, that is the wet pluviation of the dry soil directly within the bio-chemical solution, owning both nitrates and microorganisms. The equipment used, shown entirely in Figure 5-21, is composed by a cell chamber, a water-air interface tank to apply the cell stresses and a volume gauge to quantify the flows of fluid that go inside or outside the soil sample. In fact, the volume gauge is equipped with a micrometer (Figure 5-22) to measure volume change. The tests performed are reported in Table 5-7. The testing conditions have been kept practically unchanged, in order to assess the consistency and repeatability of tests results.

*Table 5-7 Desaturation tests in triaxial apparatus on back-pressured samples*

Test	[NO <sub>3</sub> <sup>-</sup> ] initial	Bacteria Concentration	Applied back pressure	Final Sr
DT-Tx1	≈600 p.p.m	10 <sup>4</sup> C.F.U.	50 kPa	84%
DT-Tx2	≈600 p.p.m.	10 <sup>4</sup> C.F.U.	50 kPa	82%



*Figure 5-21 Desaturation tests equipment for back-pressured samples*



Figure 5-22 Volume gauge system to assess the expelled pore fluid due to bacteria activity

With regards to the sample preparation – prior to wet pluviation – a special filter paper between the soil grains and the porous stones has been used, able to intercept microorganisms which lie within the bio-chemical solution. The used filter papers are glass microfiber Whatman® GF/A. Such an expedient has proven to be necessary because when bacteria nucleate bubbles, a pore pressure gradient triggers the fluid flow - as discussed previously. If the system is closed - as it is in our case - bacteria could migrate from the soil to the drainage system, resulting in additional nucleation within the drainage line itself. If this would occur, there would be an experimental error affecting the measurements carried out by the volume gauge. Thus, if bacteria are not able to leave the soil specimen, drainages connected to measurement system will be continuously fully saturated, as they must be. Obviously, prior the activation of the tests, all the drainages have been carefully saturated.

Thus, by applying such procedures, tests have been performed by imposing a back pressure of 50 kPa and a cell pressure of 100 kPa, resulting easily in an effective stress of 50 kPa. Once consolidation has been fully developed- and taken into account for the further calculations- all readings have been zeroed. Tests results in terms of degree of saturation during time are reported in Figure 5-23.

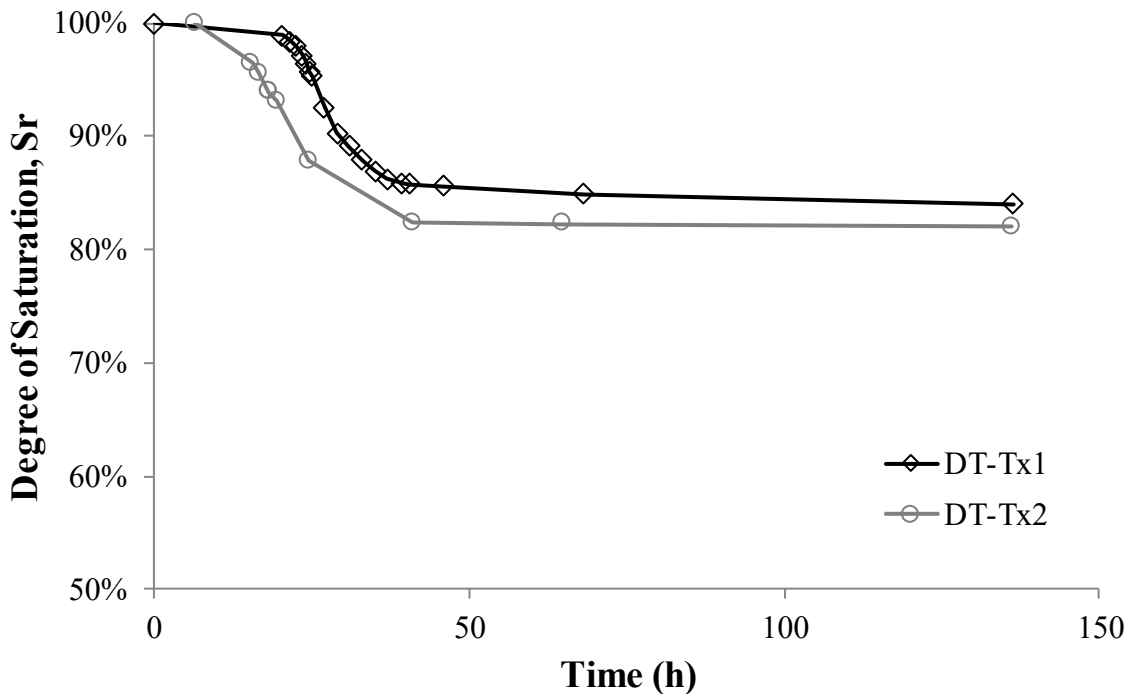


Figure 5-23 DT-Tx desaturation tests results- back pressured samples at 50 kPa

Tests results show an achieved final degree of saturation between 82% and 84% (which is in fact a possible target value of Sr, with respect to the improvement of the cyclic resistance to liquefaction) demonstrating that bacteria metabolism can be activated – and carried on efficiently – even for pore pressures higher than the atmospheric one, and thus making the bio-IPS technique potentially suitable for real scale field improvement actions.

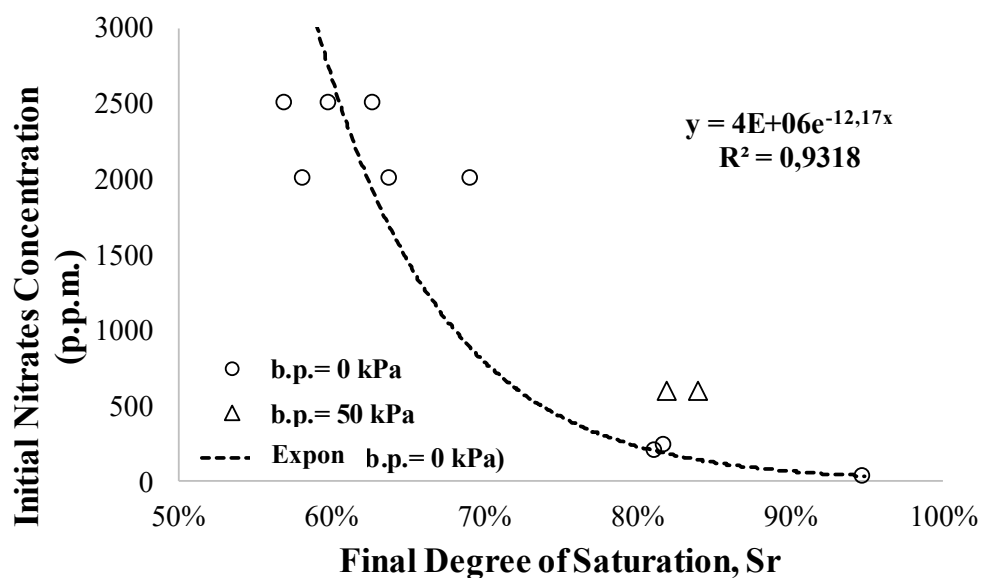


Figure 5-24 Final results of the degree of saturation achieved vs. initial nitrates concentration (dashed line for b.p.=0 kPa)

Finally, in Figure 5-24 a first possible design chart is reported. The dashed line has been drawn as the best fitting curve, using an exponential form, of the desaturation tests carried out at an atmospheric pore fluid pressure. As it was expected, neglecting the natural experimental scatter of the data - which is not particularly high anyway - the DT-Tx tests lie above the fitting curve for b.p.=0 kPa. This is due to the higher pressures applied to the specimen, resulting in a higher amount of N<sub>2</sub> gas that goes under solution. Obviously, the reported chart represents a first starting point: additional tests at different back pressures as well as at different NO<sub>3</sub><sup>-</sup> concentration have to be performed.

In conclusion, desaturation tests as well as all the biological-environmental analyses performed have proven the applicability of the selected bacteria to carry on gas bubbles nucleation (by means of respiratory denitrification mainly) underling their compatibility under an environmental point of view. Different degrees of saturation can be achieved, and the target values can be calibrated in function of both initial nitrates concentration and pore pressure applied- in other words, as a function of the depth of the layer to be treated.

In addition, as previously said, an optical analysis on bubble nucleation has been performed at the *Department of Chemical, Materials and Production Engineering (DICMAPI)*, University of Napoli *Federico II*, trying to investigate the rheology of the process as well as the stability of the bubble itself. Such analysis will be reported in the following section.

#### **5.4 OPTICAL ANALYSES ON BUBBLE NUCLEATION**

The nucleation process of the N<sub>2</sub> gas bubbles has been analysed by means of optical analyses, performed with an equipment of very high-resolution available at the *Department of Chemical, Materials and Production Engineering*, of the University of Napoli *Federico II*. The apparatus is reported in Figure 5-25. It is composed of a high-resolution camera, firmly fixed on a regulation plateable to fix a focal plan to be investigated. The sample to be analysed is arranged in an environmentally controlled sealed box, at a fixed temperature.

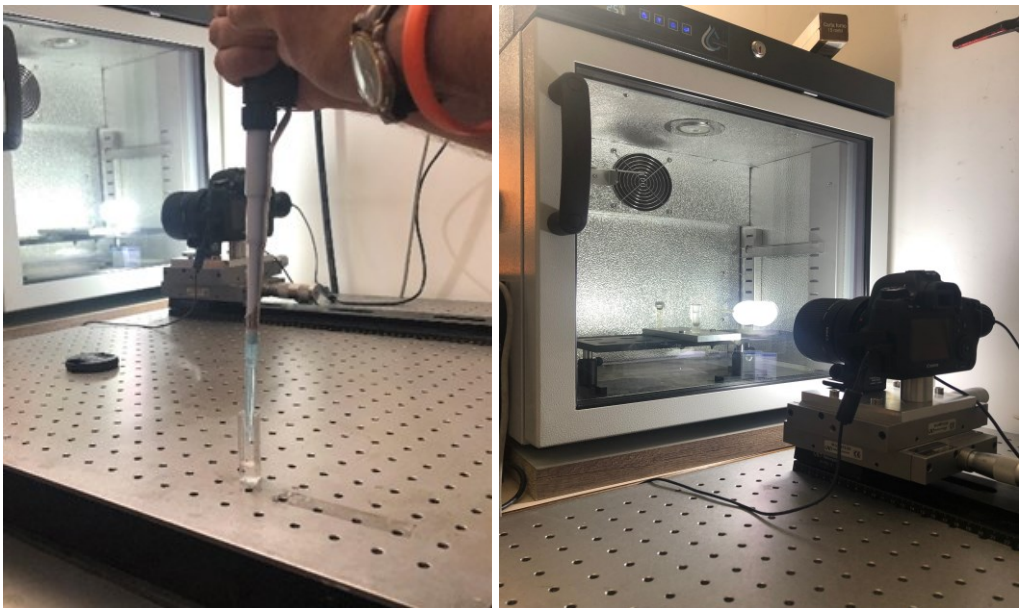
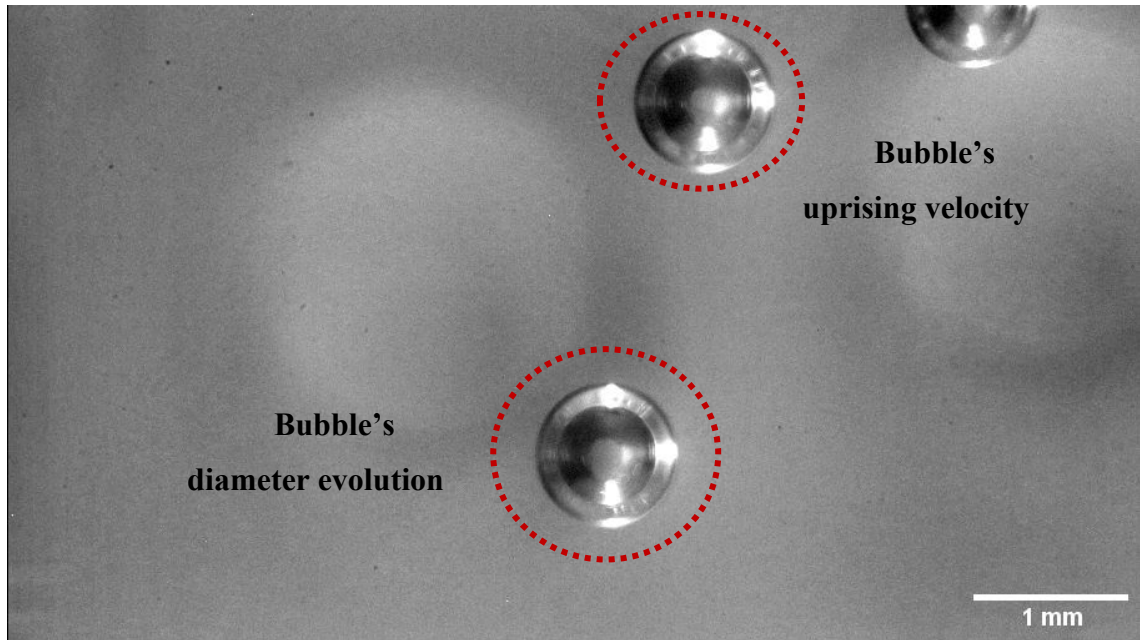


Figure 5-25 Optical analyses equipment

Operatively, the biochemical solution, containing as always nitrates and bacteria, has been gently inserted in a cuvette (Figure 5-25, left) and sealed at the top. Afterwards, the sample has been carefully laid down within the chamber. Before the metabolism was activated, a first focal plane was fixed by the high-resolution camera in order to analyse, by means of a time lapse procedure, the evolution of the nucleation process of the bubbles inside the cuvette. Unfortunately, since the position of any bubble nucleation is regardless unknown, an iterative research of focal plane has been adopted.

Once a suitable focal plane has been established- able to focus on nucleated bubbles- a data interpretation has been performed. In Figure 5-26 the first useful frame is shown, in which are clearly detectable two entire bubbles. On the other hand, Figure 5-27 shows the final frame of the assumed focal plane, in which a unique whole bubble (the lowest one) is still present. Optical analyses results have been than interpreted in terms of bubble's diameter evolution (for the stable bubble) and bubble's uprising velocity (for the unstable one).



*Figure 5-26 Optical analyses at the beginning of the nucleation process*

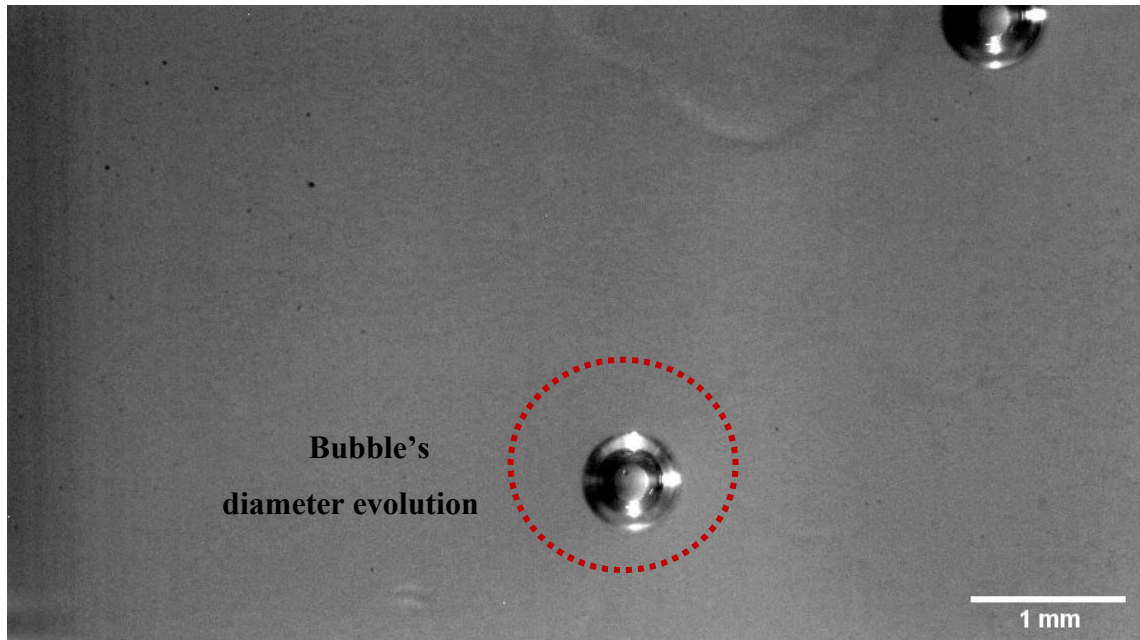


*Figure 5-27 Optical analyses at the end of the nucleation process*

In Figure 5-28 diameter evolution for the stable bubble is reported. As it is shown, bubble's diameter starts from a value of about 0.9 mm. During time, the experimental results show a tendency of the bubble's diameter to decrease, probably due to a gradient of concentration between the gas bubble itself and the solution (in which no- molecular nitrogen is initially present). At the end of the test, the bubble's diameter reaches a stable value, of about 0.6 mm, to remain constant in time. Besides, during the whole test, no displacements of the bubbles have been detected.

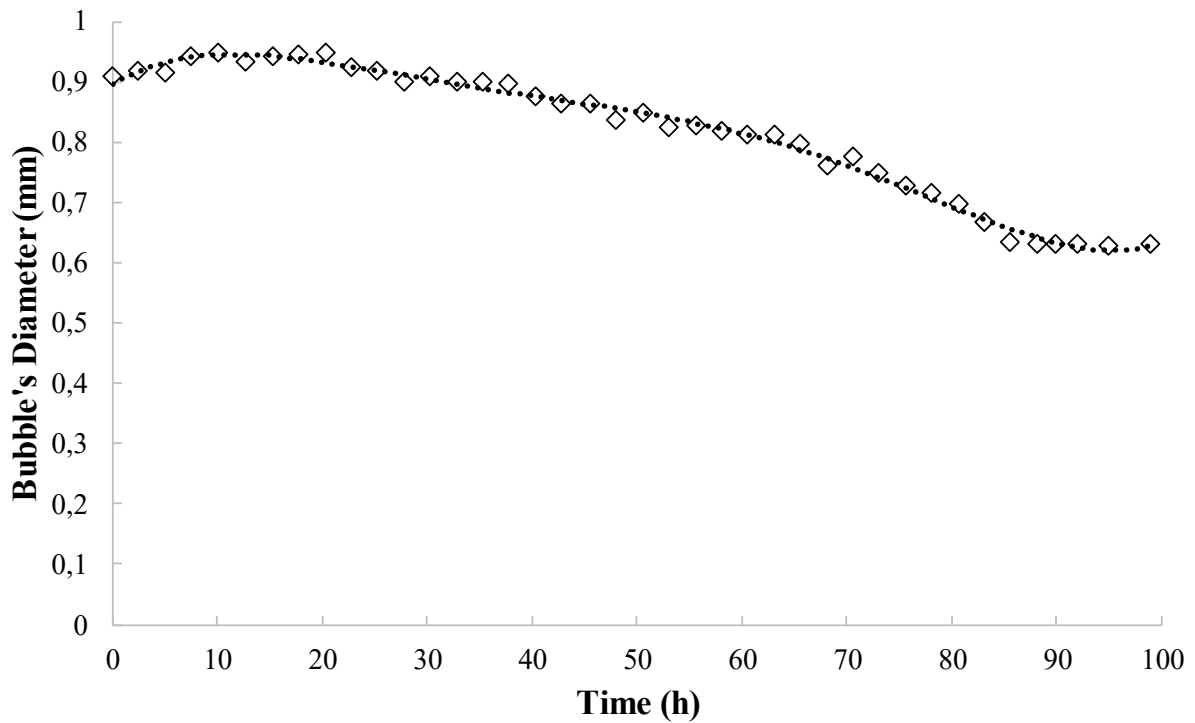


Figure 5-28 Optical analyses results- Bubble's diameter evolution

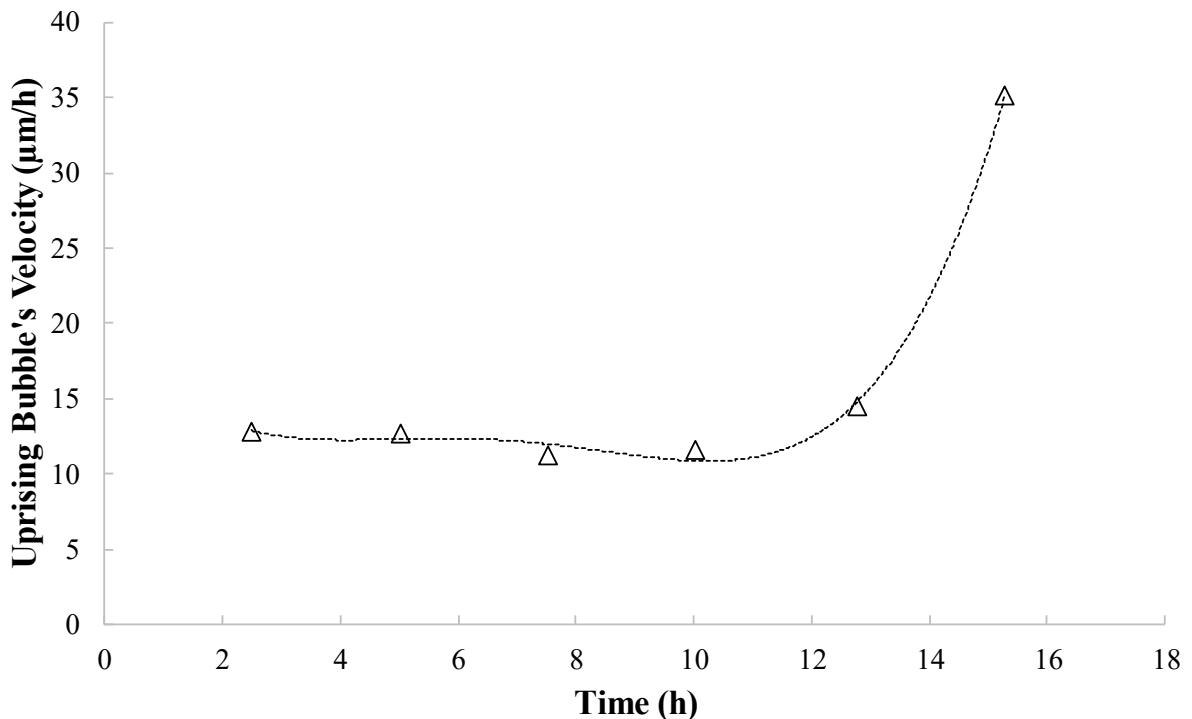


Figure 5-29 Optical analyses results- Bubble's uprising velocity

On the other hand, Figure 5-29 shows the uprising velocity of the unstable bubble (see Figure 5-26). It can be noted that, for such bubble, an instability exists in a relatively little time. The bubble

is such to be stable for few hours, afterwards an uprising velocity arises, and bubble goes upward, to be further expelled from the cuvette.

Thus, optical analyses lead to two interesting but opposite consideration:

- Bubble's uprising velocity shows that some nucleated bubbles could migrate upwards and be expelled by the sample;
- On the other hand, bubble's diameter analyses show that, not only tiny bubbles can be nucleated, but their stability persists for a relative long time, and no uprising flows are detected. In addition, such achievement is even more solid since the performed test has been carried out in a liquid solution only. Indeed, when the bubble nucleates directly within the soil's pores, adhesion forces among grains and the bubble will be established, resulting in an even more stable condition of the bubble itself, boding well for a long-lasting ground improvement action.

However, since the number of observations is limited, the optical analyses represent a starting point that needs to be improved by future additional tests. Number of observations as well as the testing time should be increased, in order to provide a more solid assessment of the nucleation processes.

Therefore, desaturation processes have been widely investigated, under both the bio-chemical and geotechnical point of view. Once the bio-IPS potential has been assessed, an additional- but fundamental- aspect has to be taken into account, that is how to control and monitor the IPS process- even a different technique from the bio-IPS is carried out. To this aim, attention has been focused on possible monitoring techniques that can be used to assess the degree of saturation, achieved with any IPS technique. In the following section, such an important issue is faced, trying to develop reliable monitoring techniques- or at least lay the foundations for them.

## **6 CHAPTER 6**

### **6.1 MONITORING TECHNIQUES**

One of the most relevant issues related to IPS technology is represented by the possibility to reliably assess and monitor the true degree of saturation in the field. It is well known that lowering the degree of saturation of a liquefiable soil results in an increase in its cyclic resistance. Besides, the quantification of the increase in the liquefaction resistance can be assessed by several methods - by means of experimental as well as theoretical approaches, as discussed in *Chapter 2* and *Chapter 3*. Indeed, cyclic resistance improvement can be evaluated in controlled laboratory environments, as well as the corresponding degrees of saturation achieved- for example by means of B-tests or, even more easily, by direct analyses on specimens' state parameter (e.g. void ratio, water content,  $\gamma_s$ ).

On the contrary, when ground improvement techniques are applied in real scale fields, several issues and uncertainties come out, increasing the difficulties to assess the effectiveness of the adopted treatment. Focusing on such issues, it is particularly true when IPS improvements have to be evaluated, in terms of degree of saturation. Several methods to retrieve undisturbed samples- even in cohesionless soils- are available, but they are usually expensive, time-consuming and often complex- an example could be represented by ground freezing sampling methods. Therefore, undirect methodologies are needed to assess the degrees of saturation achieved and, most importantly, they should be the less disturbing as possible, in order to be applicable in a wide range of field conditions. Thus,  $S_r$ -depending parameters have to be first detected and further tested experimentally.

In the present thesis, two possible monitoring techniques have been analysed, in order to lay the foundations for a reliable methodology to evaluate the degree of saturation after an IPS mitigation action. The tested parameters, both  $S_r$ -dependent obviously, are represented by:

- Electrical resistivity,  $\rho$ ;
- P-waves velocity propagation,  $V_p$ .

In the following, the experimental tests performed in the lab are reported, preceded by a brief theoretical framework on both parameters that lead to potential monitoring techniques.

### **6.2 ELECTRICAL RESISTIVITY**

The first parameter that has been tested to potentially assess the achieved degree of saturation is represented by the electrical resistivity,  $\rho$ .

Generally, resistivity is a fundamental property of a material that quantifies how strongly it resists to electric current. In an ideal case, cross-section and physical composition of the examined material

are uniform across the sample, and the electric field and current flow are both parallel and constant everywhere. When such hypotheses are verified, the electrical resistivity  $\rho$  can be calculated as:

$$R = \rho \cdot \frac{L}{A} \quad \rho = R \cdot \frac{A}{L} \quad \text{Equation 6-1}$$

where:

- $R$  is the electrical resistance;
- $L$  is the length of the specimen;
- $A$  is the cross-section through the current is applied (see Figure 6-1).

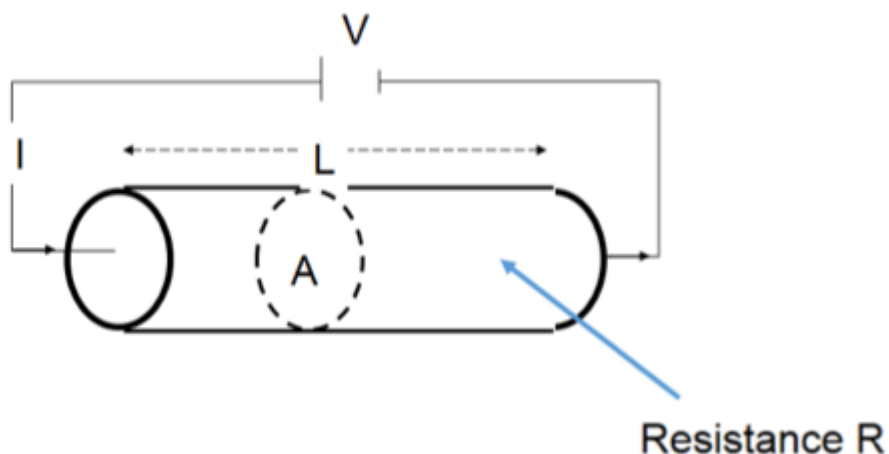


Figure 6-1 Ideal case for electrical resistivity assessment

In particular, if the Ohm's law is considered (*Equation 6-2*), it is possible to calculate the electrical resistivity of a given material as (*Equation 6-3*):

$$V = R \cdot I \quad \text{Equation 6-2}$$

$$\rho = \frac{V}{I} \cdot \frac{A}{L} \quad \text{Equation 6-3}$$

which is an intrinsic property of the tested material itself. Thus, if a homogeneous sample – with a given geometry ( $A, L$ ) – is investigated, it is possible to easily calculate the electrical resistivity by measuring the current intensity,  $I$ , generated by an applied electrical potential,  $V$ .

As for any other material, the measurements of soil resistivity provide information about the ability of an electrical current to flow through the soil itself. Soil resistivity has been found to be directly dependent on several parameters of interest, such as the mineralogy and packing of soil particles (Weil et al. 2011), salinity (Rhoades et al. 1976), porosity and water content (Dannowski and

Yaramanci 1999), composition of the solids, particle shape and orientation (Kandiah and K. 1988). Among them, soil's electrical resistivity is also strongly dependent on the degree of saturation and, particularly, on the electrical resistivity of the pore fluid (Bhatt and Jain 2014). This last dependency will be of fundamental relevance to assess degrees of saturation for soils treated by the bio-IPS technique, as will be shown in the following. Indeed, pore fluid chemistry has to be properly taken into account, to carry out reliable and repeatable measurements.

Therefore, a small size physical model, equipped with an electrical resistivity measurement device, has been set up, in order to experimentally investigate the relationship between such controlling-parameter and the degree of saturation, as reported in the following section.

### **6.2.1 SMALL SIZE PHYSICAL MODEL: ELECTRICAL RESISTIVITY MEASUREMENTS**

In order to investigate the relationship between  $\rho$  and  $S_r$ , an experimental model able to perform resistivity measurements has been developed. The model has geometrical dimensions of  $B=200\text{mm}$ ,  $L=390\text{mm}$  and  $H=150\text{ mm}$ . Besides, it presents three drainages for each side, in order to allow the pore fluid to be expelled during the bio-IPS process (Figure 6-2). As it will be shown, each drainage has been connected to a storage box, in order to further quantify the amount of expelled pore fluid (by weight measurements) and thus to calculate the achieved degree of saturation. In addition, as revealed in advance, a system able to induce an electrical potential has been installed on the model. In particular, the model has been equipped with two lead-plates on the lateral sides, as showed in Figure 6-2 and Figure 6-3. Lead plumbs – installed in the inner part of the model, to be further directly in contact with the soil – have been connected to the outside by means of metal bolts, from which the electrical potential will be practically applied.

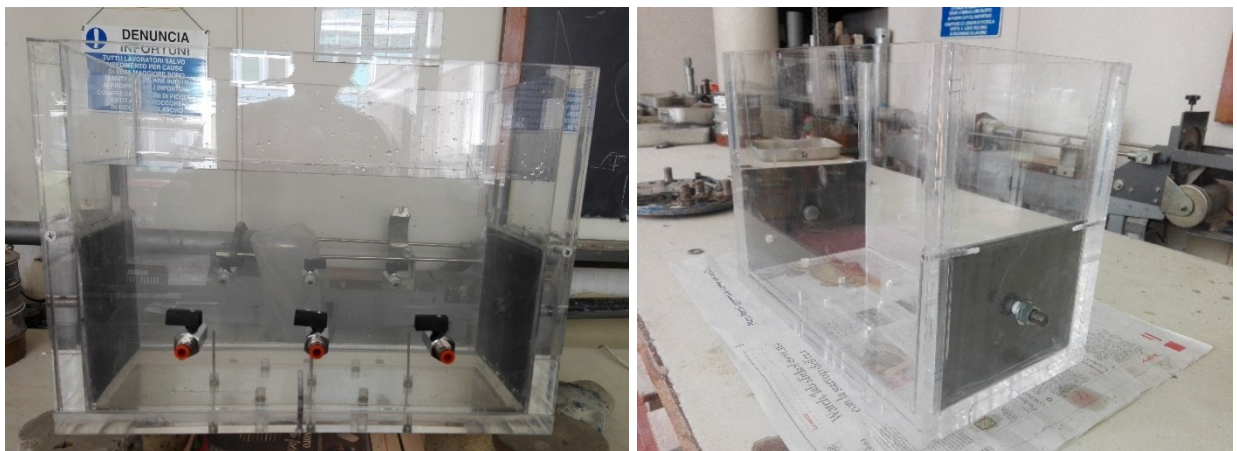


*Figure 6-2 Physical model equipment*

The electrical voltage is imposed by a current generator of nominal voltage equal to 12 Volts, thanks to which the flow current can flow inside the soil. On the other hand, once the  $\Delta V$  is applied, current intensity is measured, allowing to the calculation of  $\rho$  taking advantages of *Equation 6-3*. In particular, for each step of the test, both  $V$  and  $I$  have been measured as follow, thanks to a classic voltmeter:

- Electrical potential by means of parallel measurements across the two external bolts;
- Current intensity by means of series measurements.

Thanks to such apparatus, it has been possible to perform resistivity analyses under partially saturated conditions of tested samples.



Figure 6-3 Lead plate to apply an electrical potential within the sample

Since the experimentation is mainly focused of the investigation of the degree of saturation correlated to the chemistry of the pore fluid, an inert soil- under an electrical point of view- has been tested. Such soil is represented by the Quarto Sand (see §5.2)- its grain size distribution is shown again in Figure 6-4.

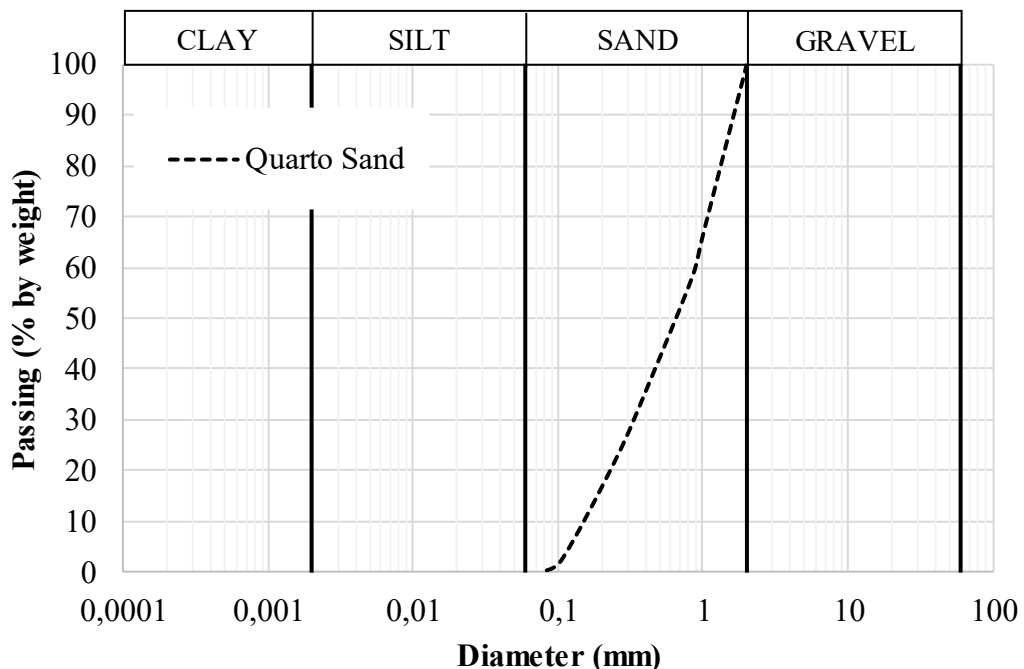


Figure 6-4 Grain size distribution of Quarto Sand

In particular, two different tests on this material have been performed, as reported in Table 6-1. The aim of the tests is to evaluate the key-role of the pore fluid with regards to the electrical resistivity that soil will exhibit. The dependency of the electrical resistivity from the chemistry of the pore fluid filling the voids is fundamental to develop a monitoring technique based on such parameter.

Table 6-1 DRC Tests

Test	Preparation method	Pore-water fluid	Saturation /Desaturation process
DRC-1	Dry pluviation	Tap water	Gradual imbibition
DRC-2	Wet pluviation	Bio-IPS solution	Biologically induced partial saturation

In detail, the DRC-1 test has been performed by pluviating the soil in completely dry condition, by keeping a constant height of drop- as for the tests already mentioned in §5.3. Thus, sample is totally dry initially, to be further wetted by several step of imbibition with fresh water. The imbibition phases have been carried on by gently wetting the specimen from the top by a predetermined quantity of tap water. The employment of tap water rather than distilled one is fundamental: the ability of any material to conduct current is due to the movements of ions (Bhatt and Jain 2014) which lie in the considered material- in the pore fluid solution for the presented case. Since the distilled water is such

to be composed by pure H<sub>2</sub>O, theoretically, it would be not suitable to the goal that needs to be achieved.

Therefore, following the procedures mentioned above, DRC-1 test has been performed and the obtained results are reported in Figure 6-5.

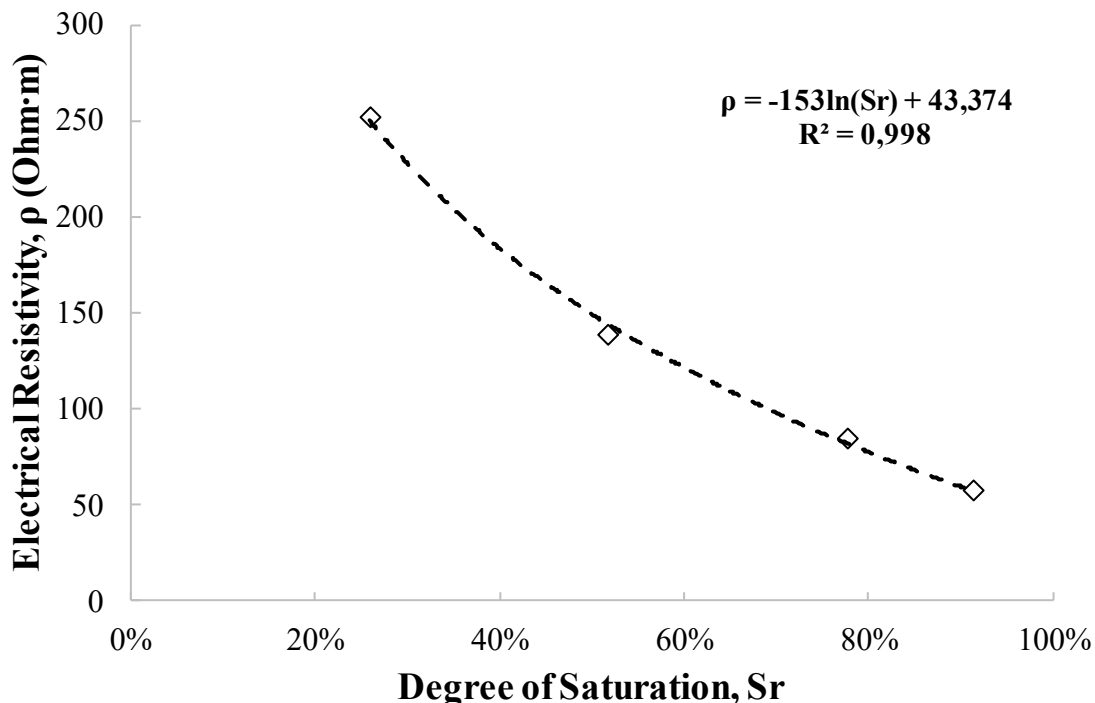


Figure 6-5 DRC-1 test's results- Electrical resistivity vs. degree of saturation

As expected, electrical resistivity decreases as the degree of saturation increases, because of the higher presence of ions within the soil's voids. A logarithmic equation can be used to reliably fit the experimental data, with a very good accuracy. Note that saturation degree equal to 100% cannot be achieved. Since the sample has been set up in completely dry conditions, any imbibition phase implies that the pore fluid starts to fill the initial empty voids. On the other hand, during the imbibition air bubbles will be trapped within the voids unavoidably. This leads to the impossibility to fully saturate the sample. As result, experimental data in Figure 6-5 do not reach the Sr=100%.

Thanks to DRC-1 test, a first correlation between Sr and  $\rho$  has been carried out. As revealed in advance, an additional test taking advantage of the bio-IPS technique has been performed, that is the DRC-2 test (initial biochemical conditions in Table 6-2).

Table 6-2 DRC-2 test- Initial biochemical conditions

Test	Bacteria Concentration (C.F.U.)	Nitrate Concentration (mg/L)	Sr (%)
(-)			
<b>DRC-2</b>	1,00E+04	2000	58.2%

The implementation of DRC-2 is shown in Figure 6-6. Note that, since the box is not sealed at the top, it has been necessary to cover the entire upper surface of the sample with an impervious solution, composed by water + SAP (a Super Absorbent Polymer), in order to ensure the permanence of the nucleated bubbles within the soil's pores. Finally, all the drainages have been connected with storage boxes, in order to evaluate the expelled pore fluid, therefore, to calculate the Sr indirectly.

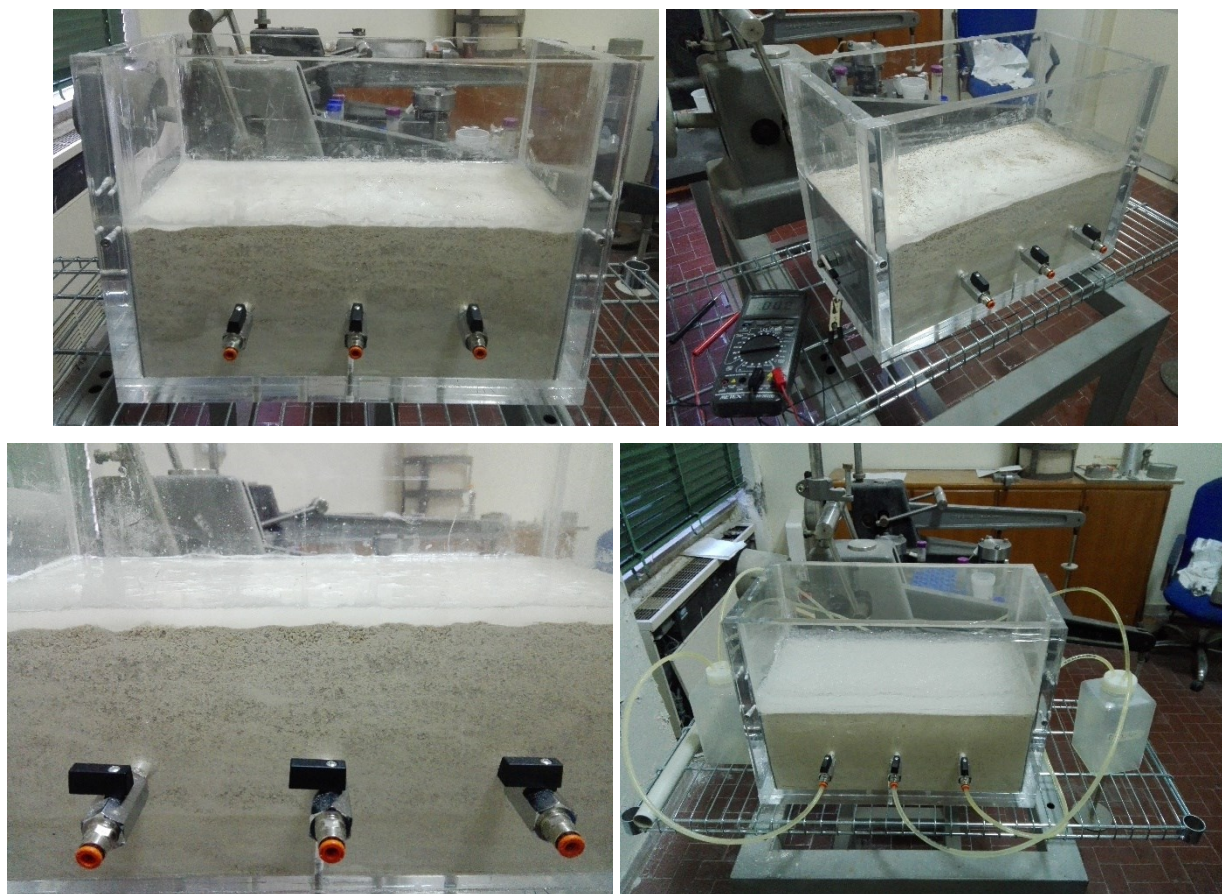


Figure 6-6 DRC-2 test implementation

Test results in terms of Sr and generated gas volume are reported in Figure 6-7. Final degree of saturation has been assessed and equal to 58.2%, in accordance with the desaturation tests already showed. Anyway, electrical resistivity measurements have been performed during the entire duration of the test. Obtained results are reported in Figure 6-8.

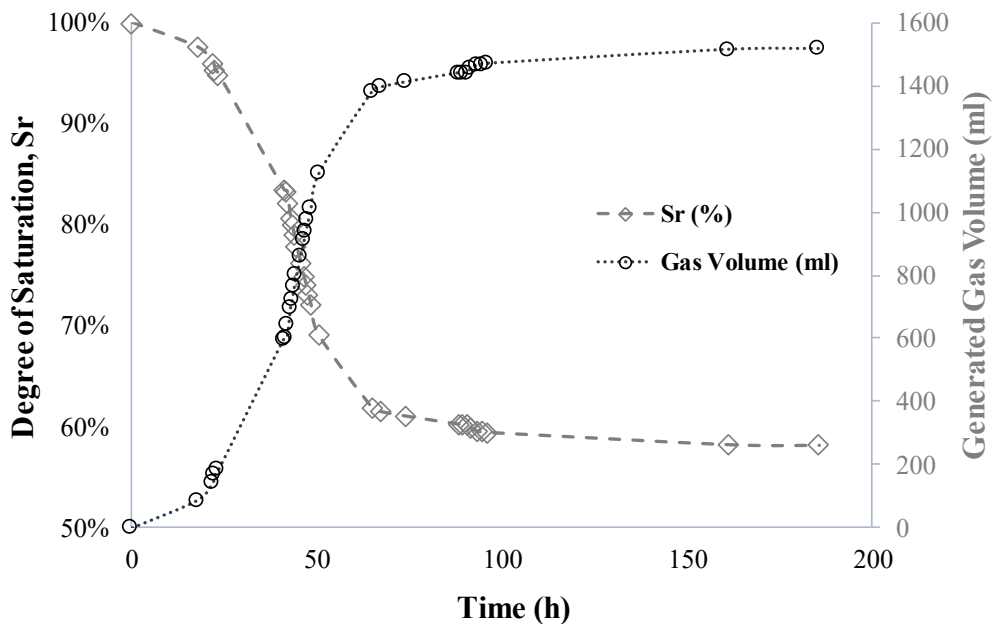


Figure 6-7 DRC-2 test's results- Degree of saturation and generated gas volume vs. time

As it can be seen, the trend obtained for the DRC-2 test is similar to the one reported above for DRC-1 test (Figure 6-5): data are well fitted by a logarithmic equation. Electrical resistivity increases as the degree of saturation decreases, since a lower number of ions are able to conduct current because of the increasing quantity of nucleated gas bubbles during time. Besides, since DRC-2 test starts by fully saturated conditions, electrical resistivity measurements for Sr=100% have been performed.

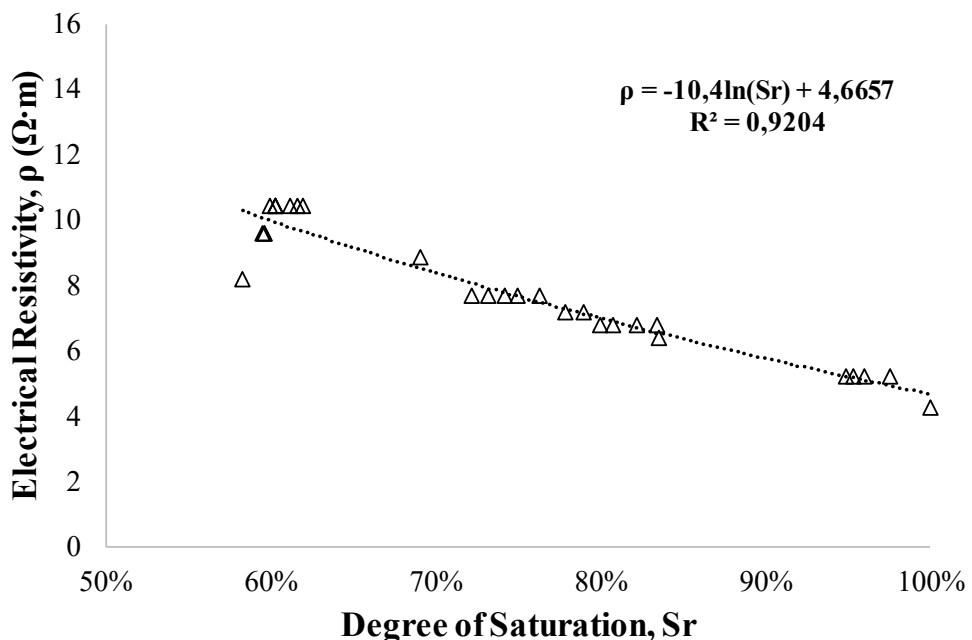


Figure 6-8 DRC-2 test's results- Electrical resistivity vs. degree of saturation

Another interesting result is that, even though the trends between the two performed tests are similar, the order of magnitude of the electrical resistivity is completely different- if the two tests are compared, as shown in Figure 6-9. Thus, apparently, performed tests cannot be compared in a unique chart and no direct information can be extracted by such results.

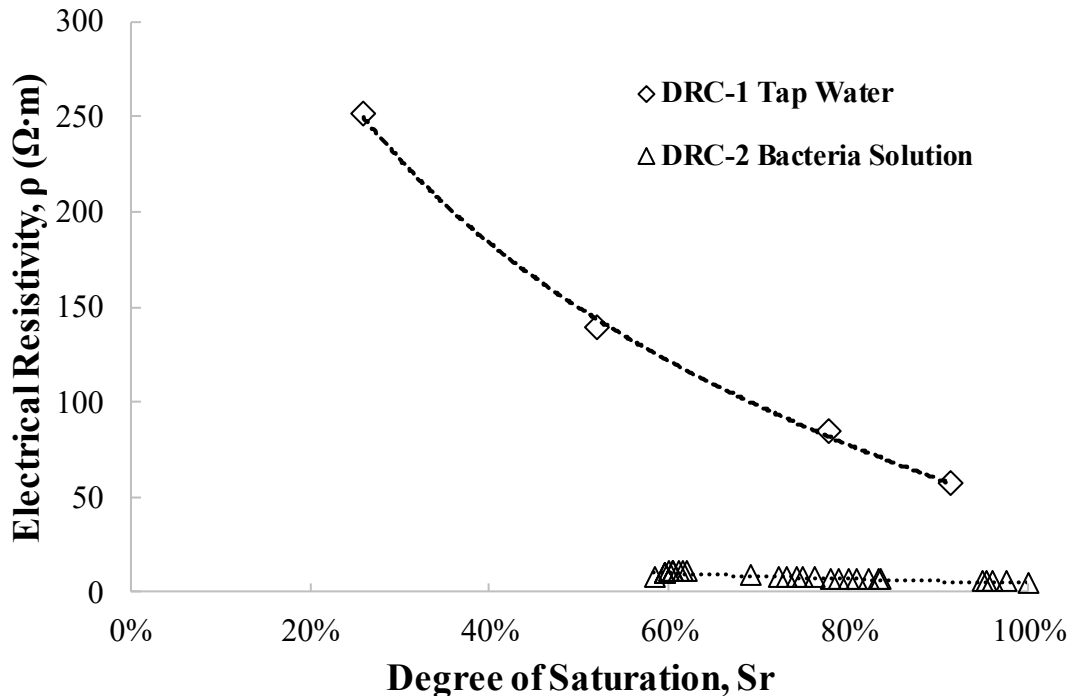


Figure 6-9 Comparison between DRC-1 and DRC-2 tests- Degree of saturation vs. electrical resistivity

Actually, as previously mentioned, if a comparison wants to be performed the pore fluid chemistry must be taken into account. Indeed, the two liquid phases are completely different – under a chemical point of view. This issue can be faced by measuring the pore fluid resistivity for each test, as reported in Table 6-3.

Table 6-3 Electrical resistivity of the pore fluids for DRC-1 and DRC-2 tests

Test	Pore fluid	Electrical resistivity, $\rho_{\text{fluid}}$
DRC-1	Tap water	18.35 Ω·m
DRC-2	Bacteria solution	1.5 Ω·m

Thanks to the knowledge of the electrical resistivity of the pore fluid solutions, it is possible to normalize the data- in terms of  $\rho=f(\text{Sr})$ - in order to remove the effects of pore fluid's chemistry as follow:

$$\rho_{ad} = \frac{\rho_i}{\rho_{fluid}}$$

Equation 6-4

By applying such normalization and comparing data interpretation, results shown in Figure 6-9 are obtained.

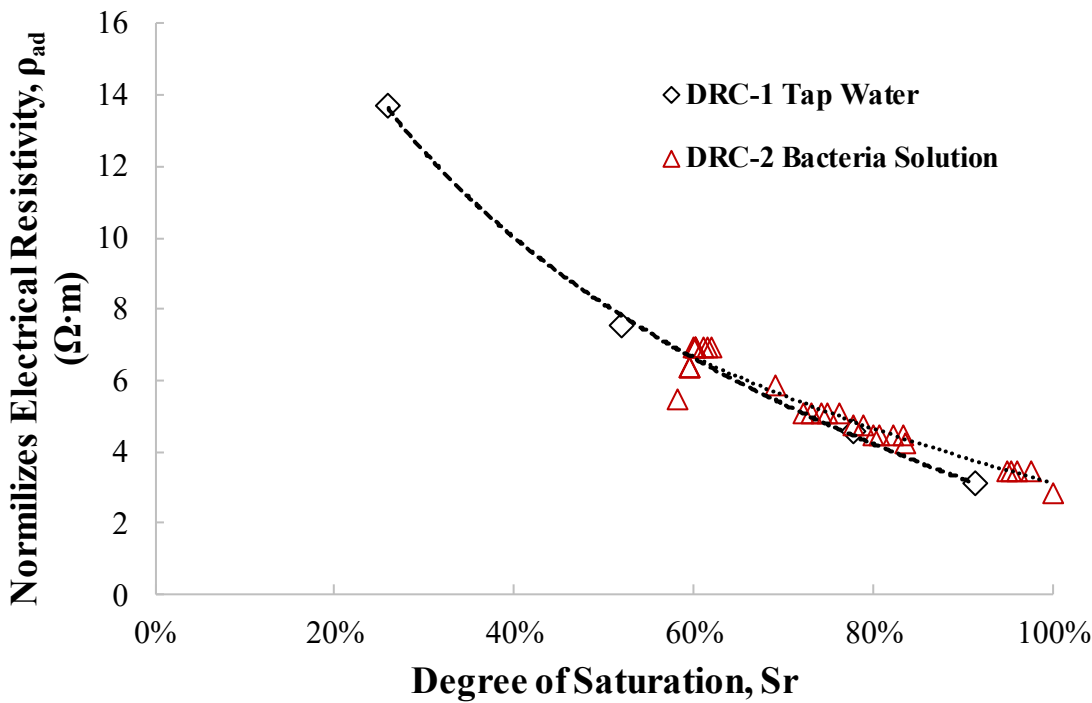


Figure 6-10 DRC tests normalization as a function of the pore fluid resistivity

The normalization is able to remove the influence of the pore fluid's chemistry, resulting in a dependency of  $\rho_{ad}$  from  $S_r$  which is a function of pore space geometry and gas bubbles distribution within the voids. Therefore, it is possible to assert that the electrical resistivity resulting from an IPS mitigation action is not directly connected to a specific degree of saturation, rather it represents a relative response of the "system" *soil+bubbles+pore-fluid-resistivity*. Thus, measurements on pore fluid resistivity have to be preliminary performed, in order to be able to carry out the normalization showed above.

With such an approach it would be possible to assess the degrees of saturation according to the following procedure:

1. Zero reading of the in-situ pore fluid, before any IPS technique application;

2. Injection of bacteria solution- for a bio-IPS technique- or alternatively injection of air bubbles;
3. Preliminary reading of the soil's electrical resistivity immediately after the bio-chemical injection;
4. Readings during time of the soil's electrical resistivity;
5. Performance of a calibration test on the treated soil in the lab (in order to obtain a correlation similar to Figure 6-5 or Figure 6-8), and its normalization (Figure 6-10);
6. Normalization of in-situ readings during time of the soil's electrical resistivity;
7. Assessment of the achieved degree of saturation using both normalized in-situ readings and the normalized calibration test.

Therefore, electrical resistivity tests results seem to be attractive to develop a monitoring procedure as discussed above. Any type of data manipulation is performed in normalized way and calibration tests can be easily developed in the lab. On the other hand, if the procedure itself would be carried out, several practical issues have to be faced:

- The chemistry of both the in-situ and injected pore fluid might be well known, but considerations about the dilution of the chemical itself has to be assessed – for example by sampling pore fluid specimens;
- Treated volumes – e.g. that could be achieved with a low-pressure grouting technique – have to be evaluated in the most precise way, in order to further extract local fluid samples, and therefore to assess the initial pore fluid resistivity.

However, experimental results lay the foundations for a potential reliable monitoring technique based on a parameter,  $\rho_{ad}$ , which has no links – or very low dependency – with the mechanical properties of the soil but mainly depends on the chemistry of the pore fluid.

Besides, an additional parameter potentially suitable to control the degree of saturation has been investigated. Such parameter, as revealed in advance, is represented by the P-waves velocity, which are well-known influenced by the degree of saturation of soils. To this aim, in the next section experimental program carried out at the *Faculdade de Engenharia, of the University of Porto (FEUP)* will be presented and discussed, aiming to evaluate the applicability of measuring  $V_p$  velocities as a monitoring technique.

### 6.3 P-WAVES VELOCITY

In order to assess a relationship between P-waves velocity and the degree of saturation, an experimental program based on bender element tests- equipped on triaxial cells apparatus-, have been performed at “*Faculdade de Engenharia, University of Porto*” (FEUP). Testing program provides a preliminary correlation between  $V_p$  and the well-known Skempton’s parameter, the B-value, which is in turn highly sensitive to a change in the degree of saturation. The final goal of the laboratory experimentation on P-waves’ propagation is to achieve a final correlation able to link directly  $S_r$  and  $V_p$ , providing a suitable relationship to assess any changes in the degree of saturation in field applications.

As a matter of fact, if IPS effectiveness evaluation is needed, direct measurements of degree of saturation are usually inapplicable both in site and in most laboratory model facilities (i.e. shaking table or centrifuge tests). Thus, monitoring techniques of the degree of saturation are required, such as P-waves measurements, since they are highly sensitive to a change in the degree of saturation (Tamura et al. 2002). In laboratory tests, such as triaxial tests, the full saturation can be ensured by B-Values measurements, using a CO<sub>2</sub> flushing and back pressure increments to encourage the complete saturation.

In the literature several works are available to better understand the dependency of the  $S_r$  on P-wave velocity. As it is shown by Nishio (1987), a small change of the B-value between 0.8 and 1 leads to a considerable variation in the P-wave velocity. Similar results were obtained by Kokusho, (2000), by applying Biot’s poro-elasticity theory, leading to the assertion that if soil voids are fully saturated by water, P-waves should be almost equal to the pure water propagation velocity, equal to  $\approx 1500$  m/s. Thus, if a correlation between P-wave-in-situ velocity and B-value is available, a reliable link between the situ and laboratory could be achieved. Nevertheless, on the other hand, other authors’ works pointed out that P-wave velocities are often less sensitive to the degree of saturation, at least, they are not as sensitive as the theory predicts (Ishiiara et al. 1998).

However, since the B-value is a very reliable parameter in laboratory tests, but clearly not applicable in field (Tsukamoto et al. 2002), in-situ measurement techniques have been developed to assess the degree of saturation. Measurements of P-waves velocity are widely used in seismic non-destructive field tests. Thus, validating a relationship between these two  $S_r$ -depending parameters is useful to assess the  $S_r$  achieved with a ground improvement technique (e.g. IPS) in the field: Flora et al. (2020), applied different methodologies during in situ tests, respectively measuring the velocity of compression waves  $V_p$  and the soil resistivity  $\rho$ , both sensitive to a change in the saturation degree.

Moreover, Okamura et al. (2011), carried out P-waves velocity measurements, in field trial tests, to ensure the initial full saturation of the liquefiable soil.

The present study is based on the experimental results carried out in triaxial cells equipped with bender elements in order to investigate the correlation between the generated P-waves velocity and the exhibited B-value of the specimen at different level of degree of saturation. The data have been processed to filter out the effects of interference among the generated waves, that can mask the real value of saturation degree. The processing procedure is described and discussed. As a final outcome an experimental correlation between  $V_p$  and  $S_r$  is provided, that can be adopted to interpret the results of in situ tests. The aim of the testing programme is thus to define an experimental relationship between the P-wave velocity and the Skempton's value B, in order to define a final relationship linking  $V_p$  and  $S_r$  directly. The knowledge of such relationship can be useful to assess the degree of saturation of a partially saturated soil, in laboratory tests as well in in-situ mitigation action. In addition, some remarks on the signal interpretation are considered, defining a correction procedure to avoid any interferences due to technical issues.

### **6.3.1 BENDER ELEMENTS TESTS AND TESTING PROGRAMME**

The bender element is a piezoelectric transducer composed of two layers: it has two conductive outer electrodes, two piezoceramic sheets, and a conductive metal plate at the centre (Lee and Santamarina 2005). The use of bender elements in laboratory and field investigations has been widely used in the geotechnical practice, since they are able to induce an elastic stress-strain response in practically all soils (Viana Da Fonseca et al. 2009), without attain the non-linear behaviour of the material. Due to the capability of the bender to induce a very low strain level within the soil, the elastic properties of the material can be measured and this enables non-destructively monitoring (Weil et al. 2011). The most common methodologies for interpreting BE results are generally grouped into time-domain and frequency- domain methods. In the present study, a time domain approach is adopted since it is more immediate, and closer to the field geophysical testing especially (Jovičić et al. 1996). Moreover, no cross-correlation has been used to determine the travel time, since its application supposes the input and output signals to be of the 'same nature'. Indeed, such a procedure is not warranted in case of multiple travel paths and diffraction effects (Viggiani and Atkinson 1995), resulting in a more complex output signal. However, a solid and standardized interpretation procedure of the signals is still not available, because of the intrinsic complexity of the wave propagation process within the specimen and of the distortion of the wave during its travel (Mitaritonna et al. 2010).

When the bender is excited by an input pulse, both P and S waves are generated, also depending on the input frequency of the signal. Usually, P waves are clearly generated for frequencies higher

than 15-20 kHz, that is why a wide range of frequency has been covered in this study, as shown later. A schematic representation of the induced waves is shown in Figure 6-11 (adapted from Lee and Santamarina 2005): two P-wave side lobes normal to their plane, and an S-wave frontal lobe are generated. In the elastic range, the ratio between the P and S waves' velocity can be expressed as a function of the Poisson's ratio:

$$\frac{V_p}{V_s} = \sqrt{\frac{2(1-\nu)}{1-2\nu}} \quad \text{Equation 6-5}$$

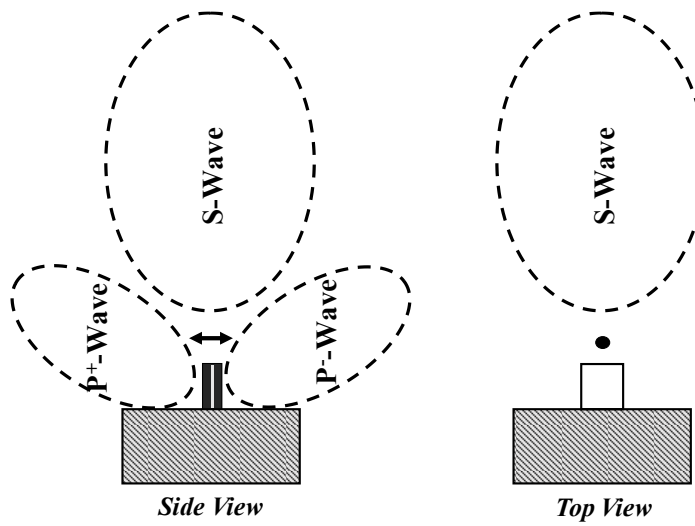


Figure 6-11 Generated waves from bender elements (Lee & Santamarina, 2005)

Due to the complexity of the waves' propagation, some interferences can affect either the S or P arrival time. Lee & Santamarina show that the P-wave reflected from the cell wall can arrive earlier than the direct S-wave, and this is not supposed to be a near field effect (Lee and Santamarina 2005). Since the target of the experiments is the dependency of the compression waves on the degree of saturation, the reflection of P-waves from the cell wall should be taken into account in the interpretation of the results, as far as it can alter the output signal, hiding the wave that propagates within the tri-phase material.

The tested soil is the monogranular clean sand, *Quartz Sand* (Figure 6-13, Table 6-4). In order to verify its susceptibility to liquefaction, several cyclic tests (both triaxial and simple shear tests, see *Appendix* for data interpretation) have been performed at *FEUP*. Its cyclic resistance curve is reported in Figure 6-12. With regards to BE tests, two different apparatuses have been used. These triaxial cells, equipped with bender elements, are reported in Figure 6-14 and Figure 6-15.

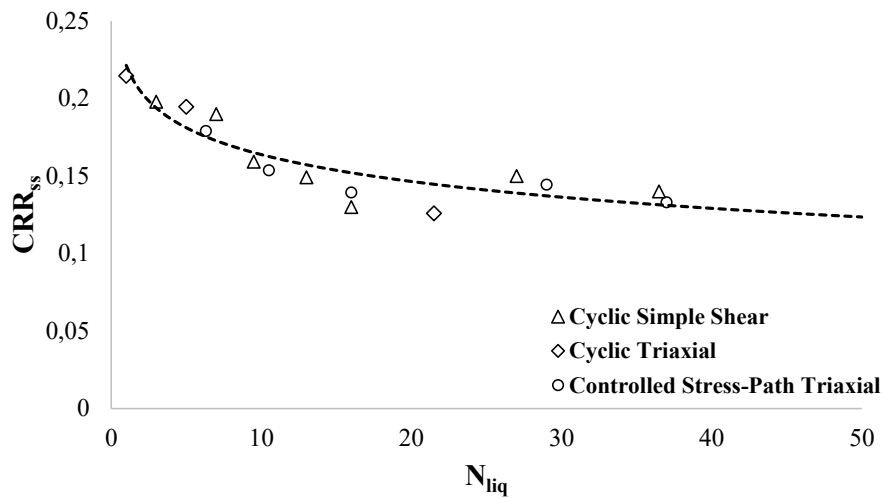


Figure 6-12 Cyclic resistance curve for Quartz sand

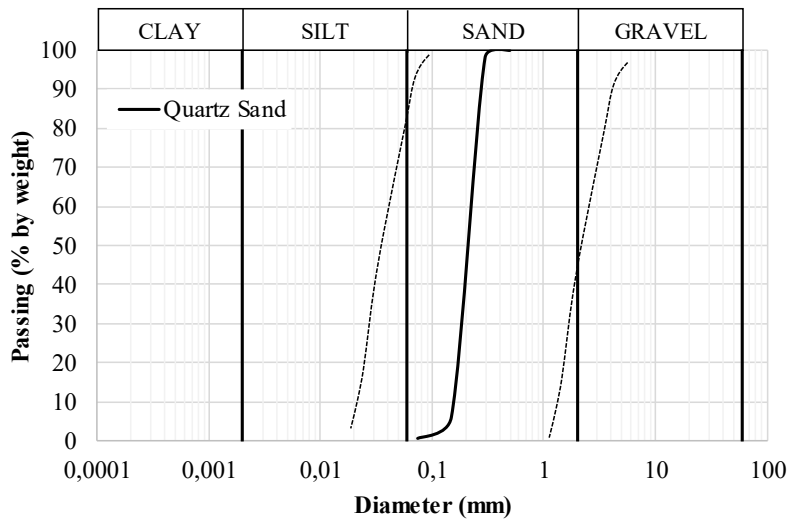


Figure 6-13 Quartz sand for granulometric distributions for  $U_c < 3.5$

Table 6-4 Quartz sand parameters

Soil (-)	G <sub>s</sub> (-)	e <sub>max</sub> (-)	e <sub>min</sub> (-)	D <sub>50</sub> (mm)	U <sub>c</sub> (-)	FC (%)
Quartz Sand	2.640	0.769	0.512	0.215	1.45	0



Figure 6-14 Controlled stress-path triaxial cell

The controlled stress-path triaxial cell (Figure 6-14) is able to test specimens with a diameter  $\Phi=50$  mm, while the triaxial one (Figure 6-15) has a specimen diameter of  $\Phi=70$  mm. In particular, as will be reported in detail later, in the triaxial cell direct measurements of Sr have been performed (additionally to  $V_p$  and B-values). On the other hand, in the controlled stress-path apparatus B-value measurements have been carried out only.



Figure 6-15 Cyclic triaxial cell

The tested samples, flushed with CO<sub>2</sub> and partially saturated with water, have been subjected to a progressive increase of the back pressure until the full saturation has been achieved. The average relative density is 40.7%. During this process, carried out at very low effective confinement stresses of 15 kPa, both P-waves velocities and B-tests have been performed. The experimental program is shown in Table 6-5. As previously anticipated, two tests have been performed in order to assess, during the entire duration of the test, the degree of saturation achieved in the specimen. Such measurements are carried out in the 70 mm cell because the greater volume of the specimen allows a higher sensitivity to changes in the water content.

*Table 6-5 Bender elements experimental program*

Test	Relative Density (%)	Specimen Diameter (mm)	S <sub>r</sub> Measurements (-)	σ' <sub>c</sub> (kPa)	Sample preparation method (-)
ST1	37,9%	50	No	15	Moist tamping
ST2	42,5%	50	No	15	Moist tamping
ST3	42,4%	50	No	15	Moist tamping
ST5	46,1%	50	No	15	Moist tamping
ST6	37,5%	50	No	15	Moist tamping
ST7	34,4%	50	No	15	Moist tamping
ST8	39,9%	50	No	15	Moist tamping
Tx1	41,9%	70	Yes	15	Dry pluviation
Tx2	43,6%	70	Yes	15	Dry pluviation

A preliminary estimation of the P-wave velocities has been made by measuring the first arrival time. Moreover, a Fast Fourier Transformation has been performed to investigate the frequency content, of both input and output signals. Then, such data have been associated with the B-values. Such association is necessary to ensure a realistic interpretation of the first arrival time, since the B-test represents an integral response of the sample and it is the most reliable parameter to assess the full saturation. As it will be shown, a correction of the first arrival time is needed to neglect the P-waves cell wall interferences. Furthermore, a direct dependency between V<sub>p</sub> and S<sub>r</sub> has been performed, by calibrating experimental data carried out in the 70 mm diameter triaxial cell. Besides, the non-linearity of the soil has been taken into account to estimate the degrees of saturation by using the experimental values of the Skempton's parameter, B, as it will be shown in detail in §6.3.2.3. Moreover, a cyclic characterization of the material has been performed, by means of several cyclic tests in different apparatus. Such a characterization is reported in detail in *Appendix 1*.

### 6.3.2 EXPERIMENTAL RESULTS

Since the whole study is based on the assumption of “occluded gas bubbles” configuration- i.e. *Partially Saturated Soils*- a first assessment of the soil-water characteristic curve for the tested soil has been performed. To that aim, preliminary tests on pressure plate needed to be carried out to obtain the soil-water characteristic curve, in order to ensure that during all the tests the suction remains negligible. Such tests have been conducted in the equipment shown in Figure 6-16. Tests are conducted by preparing the specimens in steel rings and fully saturating them by a continuous imbibition of deaired water, following the ASTM recommendation (ASTM D6836-16 2016). Afterwards, specimens are arranged in the pressure pens. Thanks to a ceramic plate with high air entry pressure, it is possible to apply a desired suction by applying directly a specific air pressure. Thus, being the water pressure equal to the atmospheric one, the suction is easily imposed and equal to the air pressure inside the chamber (*i. e.*  $s=u_a-u_w=u_a$ ).



Figure 6-16 Pressure plates equipment



Figure 6-17 Performed tests in the pressure pens equipment

The results, shown in Figure 6-18, confirm that for such clean sand even a very low degree of saturation leads to a negligible value of suction. Therefore, for the values of interest of  $S_r$ , it is reasonable to consider that the gas phase distribution is discontinuous, bubbles are occluded, and no additional (suction-induced) normal forces are involved to significantly change the shear strength of the soil.

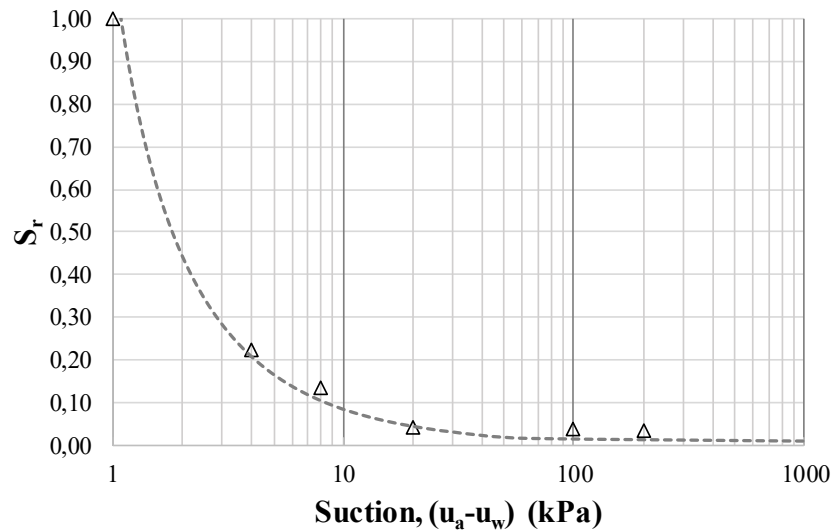
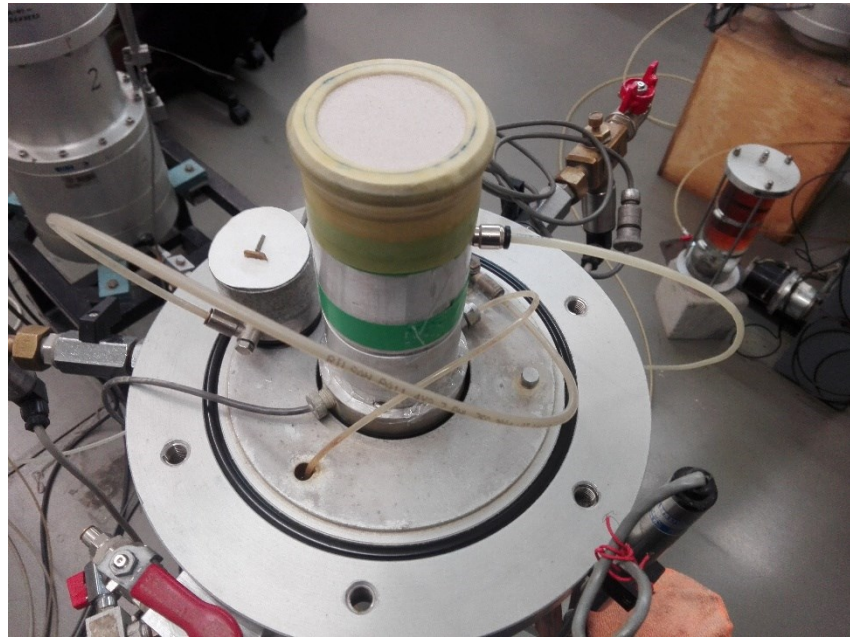


Figure 6-18 Pressure plate: experimental results

Once the no-suction dependency of the soil has been ensured- for the desired degrees of saturation that want to be tested- the BE testing program can be carried on. Starting by the bender element tests performed in the controlled stress-path apparatus, each test has been conducted by following the procedure discussed below:

- Specimen preparation by means of moist tamping technique: soil is mixed with a water content,  $w=7.5\%$ . Afterwards, soil is tamped within the latex membrane- previously solidarized within the mould by means of applied suction. Height of the soil has been subdivided in six layers in order to control, as precisely as possible, the desired void ratio. For each layer, indeed, a careful measurement of the soil tamped weight and height is performed.
- Once the specimen has been tamped, and sealed at the top, the chamber is closed and filled with water. During this filling stage, the specimen has been subjected to a confinement stress of 15 kPa by means of applied suction from the back-pressure line.
- At the end of the filling stage, the specimen is always subjected to a  $\sigma_c'=15$  kPa, by gradually reducing the applied suction and, at the same time, by increasing the water cell pressure.
- Afterwards, a  $CO_2$  flush to further encourage the saturation is carried out.  $CO_2$  flush is performed by applying a low gas pressure at the bottom of the specimen, allowing the gas to pass through the entire sample- substantially replacing the entrapped air with carbon dioxide, which is of higher solubility in water, resulting in an easier saturation of the specimen itself.
- At the end of any  $CO_2$  flushing, first measurements of both P and S waves are performed;
- Afterwards, a water flush is carried on, to increase the degree of saturation. At the end of any water flushing, a second measurement of P and S wave velocities is performed again;
- Once the water flushing is over, a first B-test is performed. Waves velocities measurements are carried out too;
- Then, the back pressure is applied and gradually increased. At each increasing step, B-value, P and S waves measurements are performed, in order to obtain the desired relationship discussed above;
- Once the specimen is fully saturated, consolidation is performed at  $\sigma_c'=50$  kPa to further apply a cyclic stress ratio, leading to liquefaction failure (such results will be reported in *Appendix*).



*Figure 6-19 Sample preparation by means of moist tamping technique*

Focusing on the signal interpretation, from the time histories of the output displacement measured at the receiving bender element in the time scale, the P-waves velocity can be easily calculated by measuring the first arrival time, since the travel distance is assumed equal to the bender's tip-to-tip distance (specimen height of  $H_{\text{nominal}}=110$  mm). In all the tests, the specimen has been excited by a sinusoidal pulse of the bender with frequency of 25, 50 and 75 kHz. These frequency values ensure that the movement of the bender is able to induce a compression strain in the specimen, thus the first arrival to the receiving bender corresponds to the propagating P wave. Measurements of S-waves arrival times have been also performed by using lower input frequencies of 1, 2, 4, 6 and 8 kHz. This also permitted to determine the elastic shear stiffness modulus,  $G_0$ , avoiding any possible interferences with the P wave propagation.

#### 6.3.2.1 Time-Domain Analyses

In Figure 6-20 the time history of the output signals is shown for the ST1 test at different back pressures, as summarized in Table 6-6. It is easy to ascertain that the increase in the back pressure leads to a lower arrival time of the P wave, since it is increasing both the degree of saturation and the volumetric stiffness of the equivalent pore fluid. Furthermore, the first arrival time of about 70  $\mu\text{s}$ , associated with a velocity of about 1360 m/s, is reached under a back pressure of 150 kPa, and remains quite constant afterwards, as shown in Table 6-6.

Table 6-6 ST1 Bender elements test

First arrival time ( $\mu$ s)	b.p. (kPa)	$V_p$ (m/s)
343	0	286
254	10	386
216	50	454
72	150	1362
72	200	1362
67	250	1464
65	400	1509

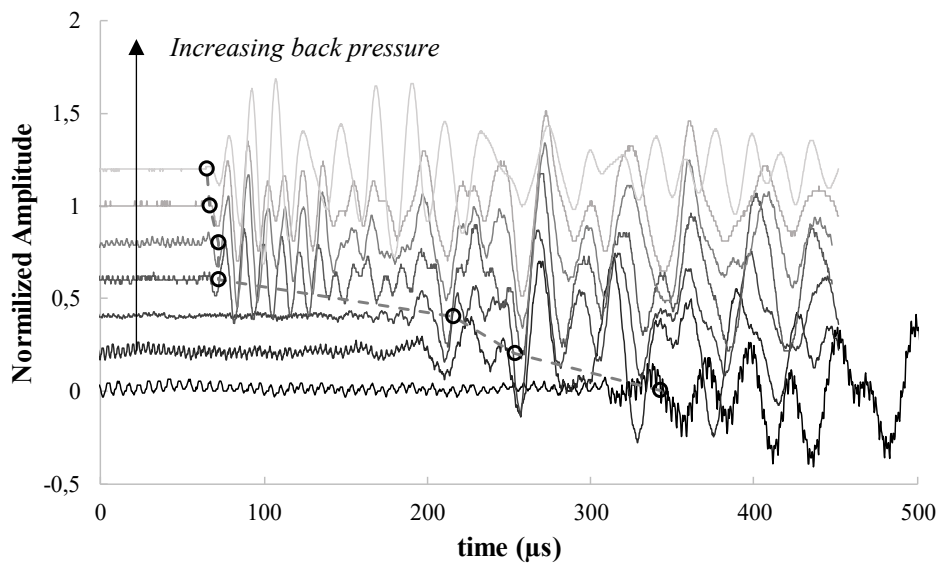


Figure 6-20 STI BE test- evolution of output signals at increasing back pressures

In Figure 6-21 the ST1 output signal measured for a back pressure of 200 kPa is shown. In Figure 6-22 both frequency contents of the input (dot line) and output (solid line) signals are shown, for a nominal input frequency of 50 kHz. The presence of a peak related to a frequency of about 75 kHz is evident, higher than the input frequency of 50 kHz (dot line). This has been interpreted as an interference of the propagated wave with possible refracted waves at the specimen boundaries or possibly of a coupled effect of the bubbles-water path within the sample, resulting in a propagation of the wave itself through a saturated path (i.e. no bubbles are crossed by the P-wave, as schematically represented in Figure 6-23).

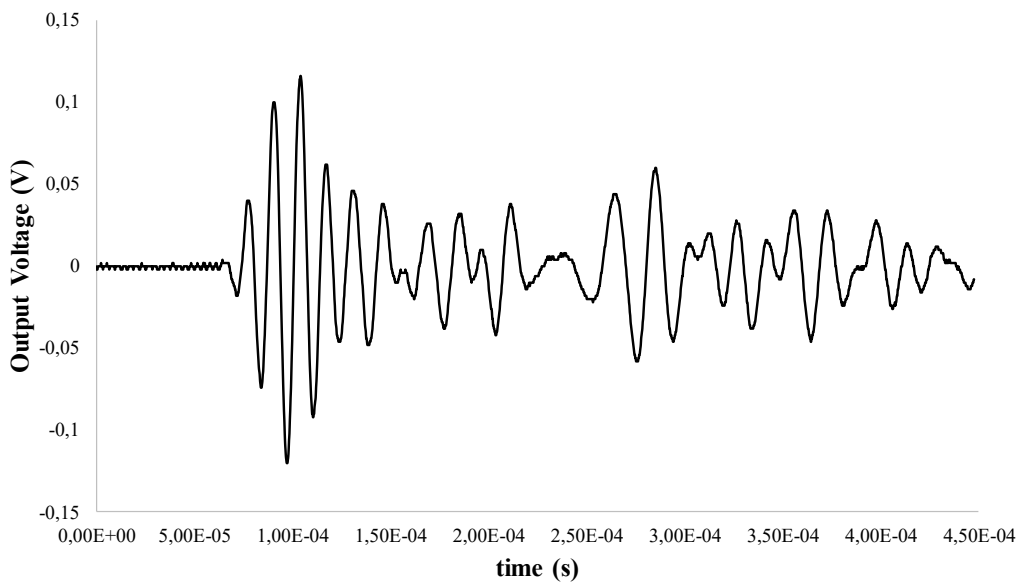


Figure 6-21 ST1 output signal

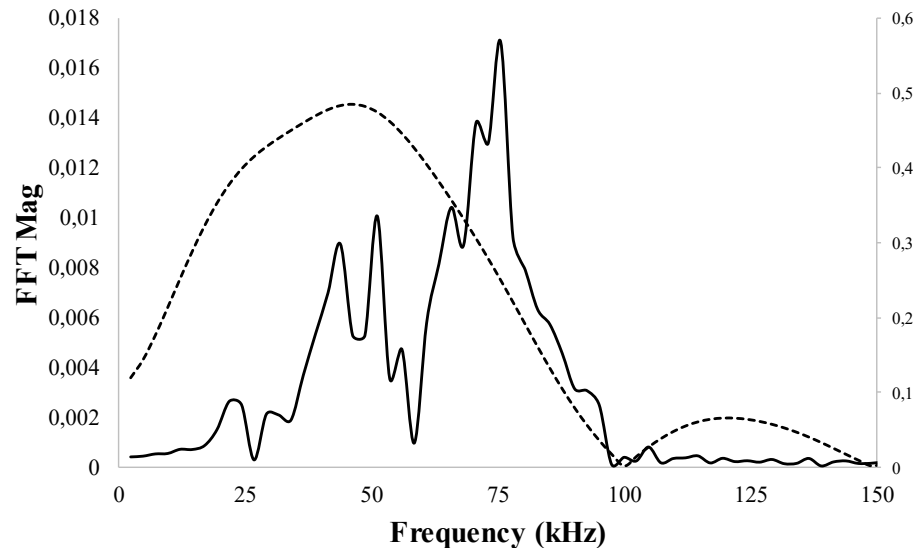


Figure 6-22 ST1 Fast Fourier Transformation for input sinusoidal pulse (dot line) and output signal (solid line)

To verify the consistency of the output data, the experimental data are plotted and shown in Figure 6-24, in terms of  $V_p$ -B. It is clear to see that even for relatively low values of B ( $\approx 0.70$ ), the P-velocities reach 1400-1500 m/s, which is the velocity of propagation of a P wave in a fully saturated specimen (the well-known velocity of propagation through water). Since the B-test is an integral response of the sample, and a reliable parameter to ensure the complete saturation (i. e.  $B=0.95-0.98$ ), such high values of  $V_p$  for B close to 0.70 are not realistic.

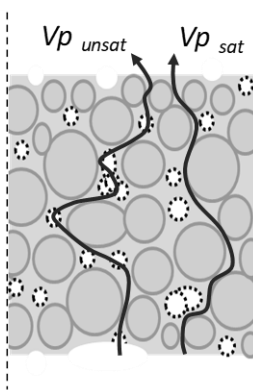


Figure 6-23 Possible schematic paths of the propagated waves

It is likely that waves propagate through a stiffer path that is not representative of the whole specimen. The above calculation of  $V_p$  is therefore misleading since it clearly depends on the path the waves follow while propagating. It is highly possible that the trend shown in Figure 6-24 is affected by the interference with the propagation of refracted waves along the cell wall, at the interface between the membrane and the cell water, or is a consequence of a preferential saturated travel-path randomly located within the sample (Figure 6-23).

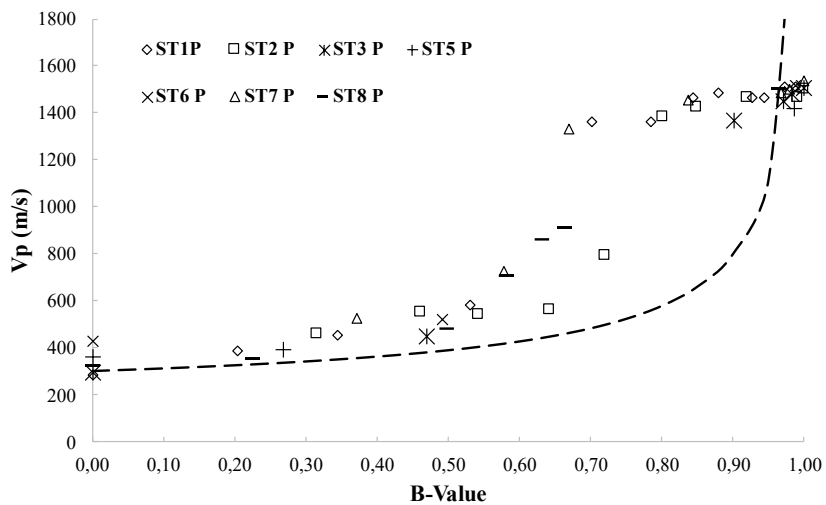


Figure 6-24 Correlation between  $V_p$  and  $B$  without any signal correction or interpretation

With the aim to provide further evidence of the effect of wave interference on the output signal, Figure 6-25 compares the *FFT* of the input signal (dashed line) to that of the output signal (solid line). While the former shows a clear peak at 50 Hz, that is the nominal frequency of the input signal, in the latter two peaks can be detected, the first at about 50 kHz (which is comparable with the input frequency) and the second at a higher value of about 75 kHz. This second peak indicates that higher

frequency content arises in the recorded signal, possibly due to the superimposition of wavefronts, as mentioned before.

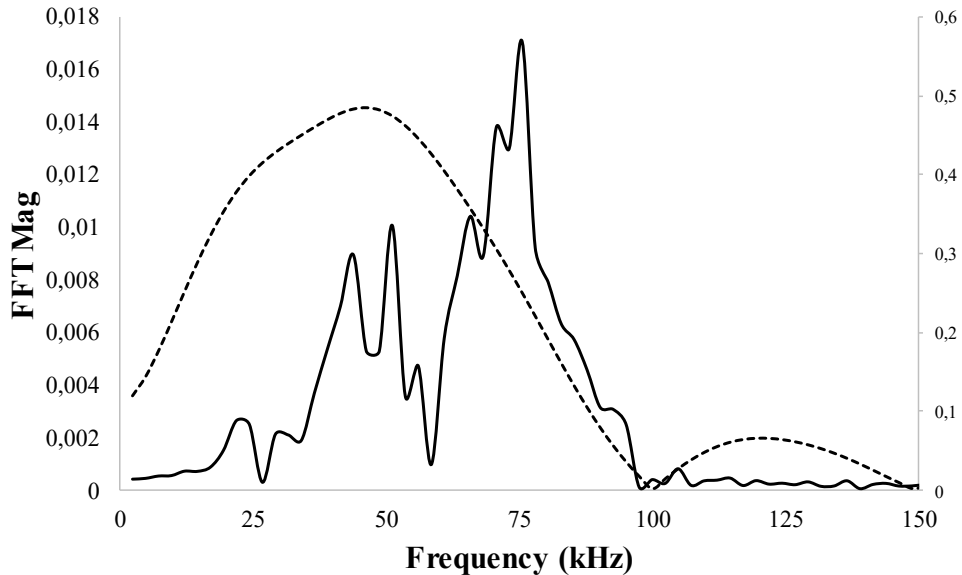


Figure 6-25 Fast Fourier transformation of the input (dashed line) and the entire output signal (solid line)

Therefore, a frequency content analysis of the output signal can be useful to filter out spurious waves from the interpretation of the results. Such interpretation is discussed in the following section.

#### 6.3.2.2 Frequency-Domain Analyses- Corrected Output Signals

The output signals for ST1 test at back pressure  $u_{bp}=200$  kPa and ST7 test at  $u_{bp}=150$  kPa are presented herewith, for the purpose of validating a procedure to correct the signal before carrying out data interpretation in the time domain.

Figure 6-26 shows the output signal referred to an input sinusoidal wave of 50 kHz. It may be seen that two main branches of the signal can be detected. This may be justified, according to what has been observed in the previous section, by assuming that two propagating wave fronts affect the receiver bender. Only the second of them arises from the propagation within the partially saturated soil sample, while the first is affected either by refraction at the boundaries or by randomly distributed preferential saturated paths. Indeed, the first wave front would indicate  $V_p \approx 1350$  m/s, for a  $B \approx 0.78$  under a backpressure = 200 kPa, while the second indicates  $V_p = 632$  m/s, which is consistent with the experimental value of  $B$  and the predicted theoretical value as well. Therefore, a subdivision of the signal has been made, as shown in Figure 6-26, by isolating the effect of the first wavefront and considering the residual one to be representative of the real soil response. *FFT* has been applied to the two sub-signals and the results are plotted in Figure 6-27. The spectrum of the first train (dot line)

shows the same peak at about 75 kHz, while no significant peak is detected for lower frequencies. On the other hand, the frequency content of the residual signal (solid line) shows the peak for a frequency close to 50 kHz (i. e. the input frequency). A peak close to 75 kHz is still present, because of the reflection effect of the surfaces waves that arrived at the receiver bender anyway.

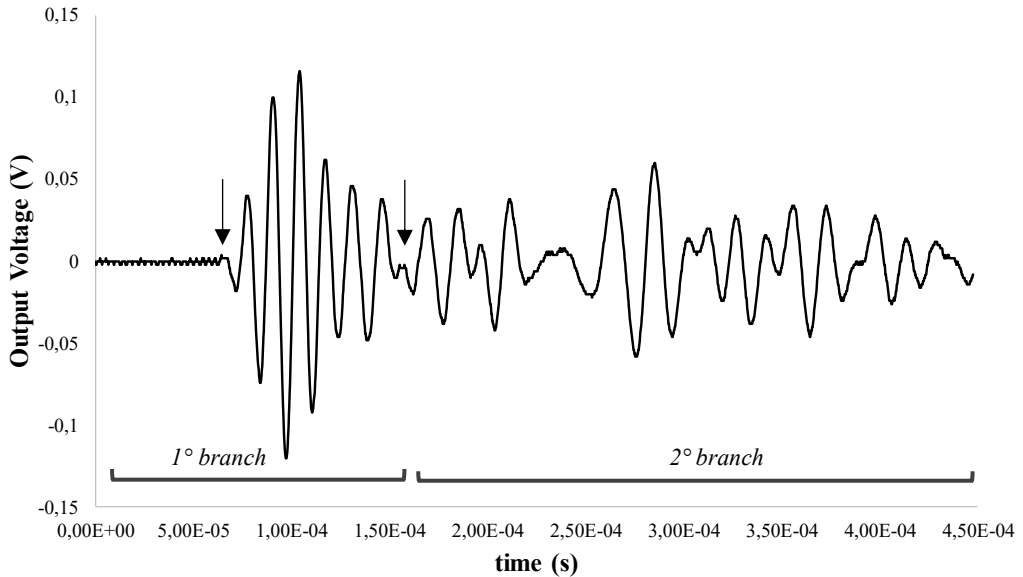


Figure 6-26 Output signal for ST1 test at back-pressure  $u_{bp}=200 \text{ kPa}$

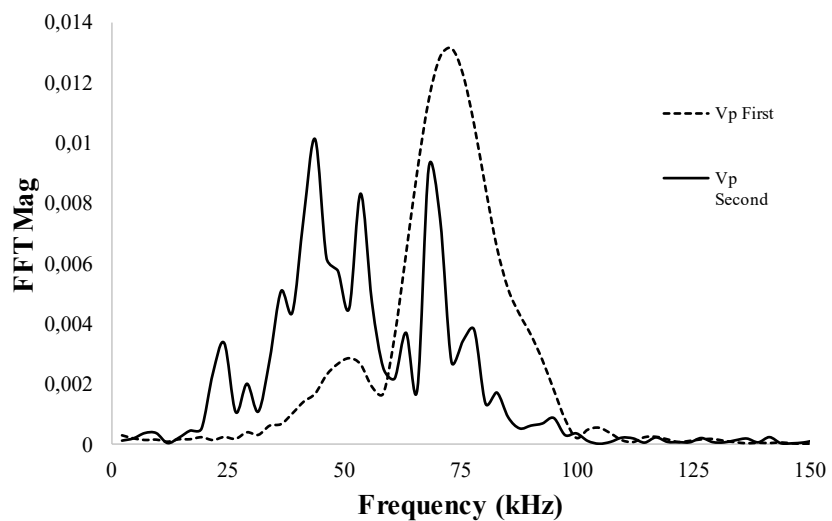


Figure 6-27 Fast Fourier transformation for the two sub-signals (ST1 Test)

Furthermore, an analysis of a signal referred to ST7 test is shown. Such a test is carried out during a saturation stage of 150 kPa of back pressure, and an input frequency of the signal of 75 kHz. In Figure 6-28, the output signal (and its FFT in Figure 6-29) is presented, in which two events can still be detected. For such test, a B-Value equal to 0.83 has been measured, ensuring the partially saturated

condition of the sample. As previously discussed, the first arrival time, close to  $65 \mu\text{s}$  (first arrow), would lead to  $V_p \approx 1490 \text{ m/s}$ , so that the specimen should be fully saturated. If the first sub-signal is neglected, and the second sub-signal showed in Figure 6-28 is considered, the arrival time measured leads to  $V_p \approx 854 \text{ m/s}$ , in accordance with the measured B-Value.

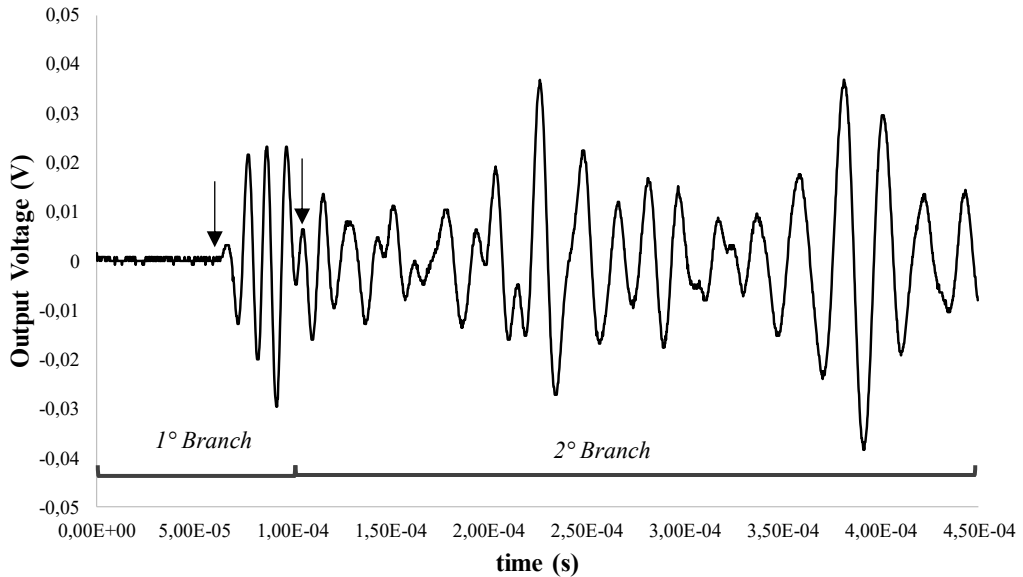


Figure 6-28 ST7 output signal for  $b.p.=150 \text{ kPa}$

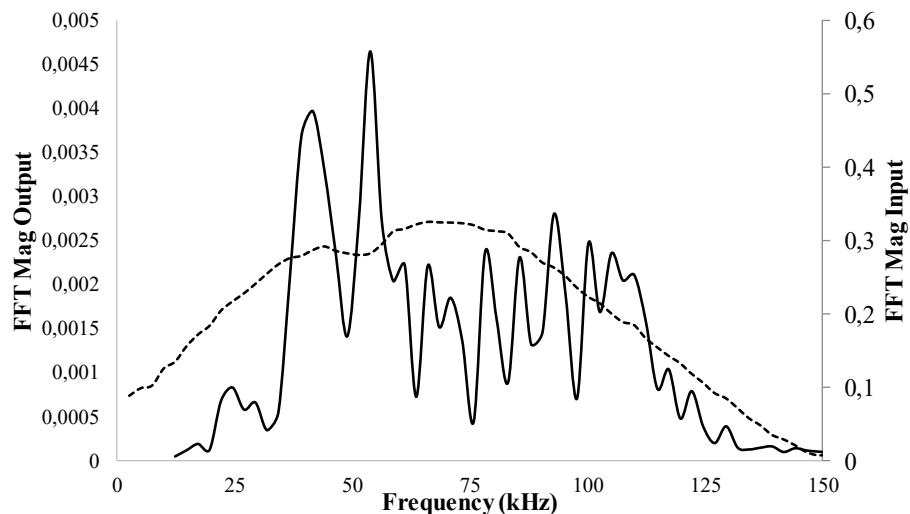


Figure 6-29 ST7 frequency content for  $b.p.=150 \text{ kPa}$

By applying the Fast Fourier transformation for the entire signal, different peaks can be detected: the first, close to  $50 \text{ kHz}$ , and the second close to  $100 \text{ kHz}$ , higher than the input frequency applied. Thus, a frequency content analysis has been performed by dividing the output signal, isolating the interference waves that affects the interpretation. In Figure 6-30 the *FFT* of the two events are shown.

If the first sub-signal is neglected, the frequency content of the residual signal shows a peak close to 50 kHz, similar to the one shown in the ST1 test, while the interference waves present a peak to 100 kHz.

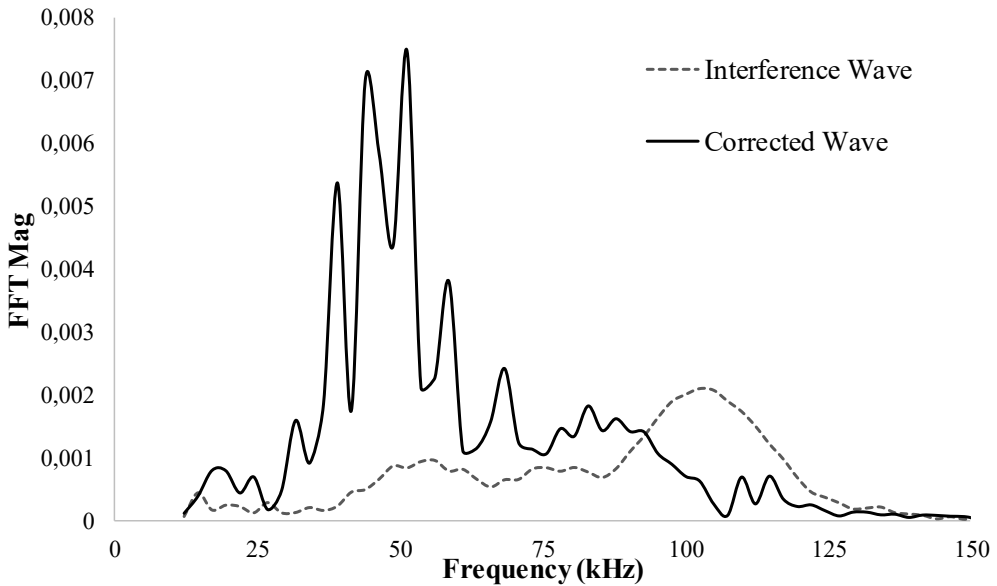


Figure 6-30 Fast Fourier transformation for the two sub-signals (ST7 Test)

This result leads to an interesting consideration: the partially saturated soil response seems to be almost frequency independent and included between 30 and 50 kHz, while a higher frequency content affects the signal, probably due to any interferences with the boundary conditions (e.g. membrane-water interface or with randomly distributed preferential saturated paths).

This issue has suggested to investigate separately the role of the soil skeleton and the pore water as well, by performing two different additional tests. Such tests are carried out for a dry specimen, to assess the soil skeleton response, and for a completely water-filled chamber without any sample, to simulate the pore water response as well. Both tests are performed with an input frequency of 25 kHz, lower than the other ones, in order to investigate the frequency-independent response.

The results, in terms of *FFT*, are shown in Figure 6-31. For the dry sample, a peak is detected for a frequency between 10 and 20 kHz and represents the soil skeleton response under the applied frequency input. With regards to the test on the chamber filled with water, a higher frequency content included between 30 and 50 kHz is clear, regarding the water response under the applied input frequency; this response can be associated with the pore water response in a partially saturated sample test.

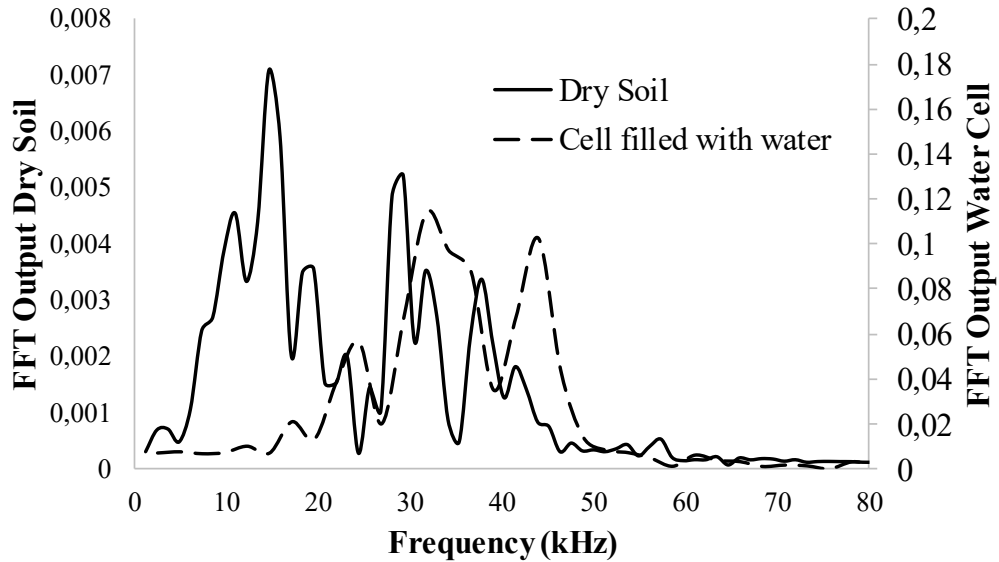


Figure 6-31 FFT for dry sample and chamber completely filled with water

Thus, the results in Figure 6-31 confirm that there are two different response, in terms of frequencies, of the soil skeleton and the pore water. When a partially saturated sample is subjected to BE pulse, the pore water response becomes predominant, and the most representative peak is due to the propagation of the wave through the bi-phase pore fluid. The soil skeleton response, at lower frequencies, is not appreciable (Figure 6-27, Figure 6-30). Such results also confirm that the higher frequencies of 75 and 100 kHz obtained in the previous tests are due to an interference with the apparatus or to the water-membrane interface, and they must be neglected during the signal manipulation.

Thus, the subdivision of the signals in different branches, and the respectively analysis on the *FFT*, can support to the neglection of interferences, which result in frequency peaks higher than the input frequency content. The knowledge of the nominal frequency of the input signal, and its frequency content as well, is necessary to manipulate the output, by deleting the wavefronts resulting in higher frequency peaks in the *FFT*.

With such type of interpretation, carried out for all the tests, a correction in the experimental data has been performed. Therefore, the final values of the BE tests are shown in Figure 6-32. The results shown a very good fitting with the theoretical values, using *Equation 6-6* (that will be later discussed in detail), in which the parameters used are shown in Table 6-7, and previously calculated thanks to the  $V_s$  measurements, coming from the BE tests at lower frequencies (between 1 kHz and 8 kHz).

$$V_p = \left( \frac{\frac{4G_0}{3} + \frac{K_{b,0}}{(1-B)}}{(1-n)\rho_s + n\rho_f} \right)^{1/2} \quad \text{Equation 6-6}$$

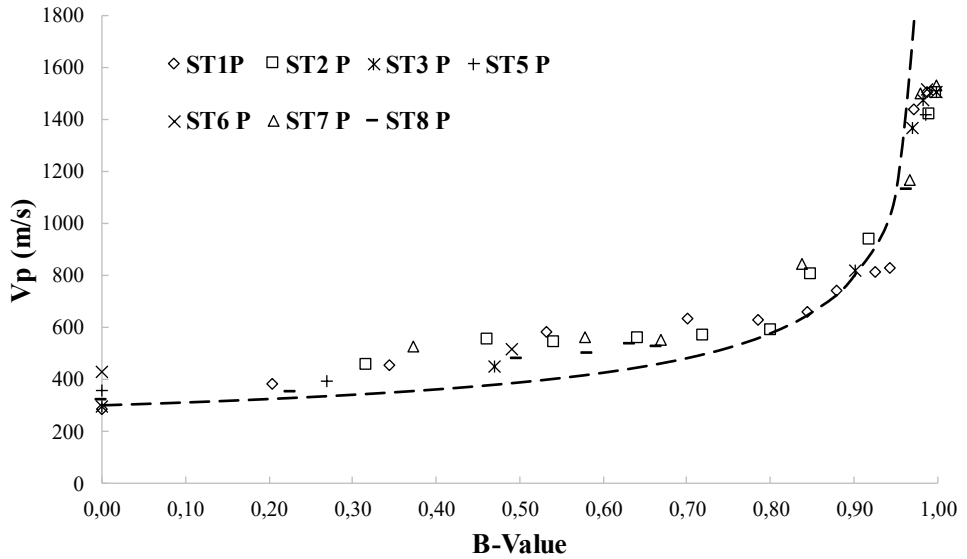


Figure 6-32 Correlation between  $V_p$  and  $B$  after frequency analysis correction

Table 6-7 Elastic parameters for Quartz tested sand

n (-)	$V_p$ (m/s)	$V_s$ (m/s)	$\rho_s$ (g/cm <sup>3</sup> )	$G_0$ (MPa)	v (-)	$K_{b,0}$ (Mpa)
0.410	276	136	1.59	29.41	0.34	82

Therefore, data interpretation by means of frequency content analyses provides a reliable experimental relationship between the measured B-value and P-wave velocity, for each performed test. On the other hand, no direct information linking directly  $V_p$  and  $S_r$  are obtained yet. To this purpose, additional tests on the cyclic triaxial equipment (Figure 6-15) have been performed. Experimental measurements of  $S_r$  have been carried out, to be later linked with the observed P-waves velocity, as it will be shown in the following.

### 6.3.2.3 Experimental correlation between P-waves velocity and degree of saturation

In order to achieve a direct relationship between the P-wave velocity and the degree of saturation, two tests on the 70 mm triaxial cell equipped with bender elements have been performed (Tx-1 and Tx2 tests in Table 6-5). In such tests, the degree of saturation has been experimentally measured

thanks to a balance of the water flow during the entire tests, represented by the initial flushing and the saturation stages, under the increasing of the back pressure.

As for the tests in the 50 mm apparatus, the degree of saturation has been changed by changing the back-pressure values. The experimental data in terms of  $S_r$  have been related to the  $V_p$  velocity. In order to have a theoretical relationship to best-fit the experimental values, a theoretical equation  $V_p-S_r$  is needed.

As it is well known, Skempton's parameter B is usually used to ensure the fully saturated condition in both static and cyclic tests. Its measurement, carried out in undrained condition, represents an integral response of the specimen under the increment of the total stresses, in radially symmetric conditions, and can be experimentally determined as  $B=\Delta u/\Delta \sigma$ . On the other hand, the B parameter can be theoretically expressed as (Skempton 1954):

$$B = \frac{1}{1 + n \cdot \frac{K_b}{K_f}} \quad \text{Equation 6-7}$$

where n is porosity,  $K_b$  the bulk modulus of the soil skeleton and  $K_f$  the bulk modulus of the pore fluid. When a specimen is considered to be partially saturated, as defined above, the equivalent pore fluid bulk modulus,  $K_f$ , can be expressed as a function of the degree of saturation as follow (Yang and Sato 2000):

$$K_f = \frac{1}{\frac{1}{K_w} + \frac{(1 - S_r)}{P_{w,abs}}} \quad \text{Equation 6-8}$$

with  $K_w$  bulk modulus of water and  $P_{w,abs}$  absolute water pressure. With such basis, B is considered to be a linking parameter to the degree of saturation (Yang 2002):

$$B = \frac{1}{1 + n \frac{K_b}{K_w} + n \cdot \frac{K_b}{P_{w,abs}} \cdot (1 - S_r)} \quad \text{Equation 6-9}$$

Many authors have used a theoretical simplified relationship based on the P-waves velocity (e. g. (Yang and Sato 2000) linked with the bi-phase nature of the pore fluid and the B-value:

$$V_p = \left( \frac{\frac{4G_0}{3} + \frac{K_{b,0}}{(1-B)}}{(1-n)\rho_s + n\rho_f} \right)^{1/2} \quad \text{Equation 6-10}$$

in which  $(1-n)\rho_s + n\rho_f$  is the total density of the soil,  $\rho$ , and  $G_0$  the shear stiffness at low strain levels.

Thus, by substituting *Equation 6-9* in *Equation 6-10*, a direct link between  $V_p$  and  $S_r$  is obtained. Note that in both equations the bulk modulus of the soil skeleton is needed. Since the B-tests are related to a strain level higher than the one referred to the BE tests, two values have been used, respectively  $K_b$  (*Equation 6-9*) and  $K_{b,0}$  (*Equation 6-10*). In addition, the increasing in the back-pressure must be taken into account, since it changes the compressibility of the bubbles and the response of the soil in terms of B as well. Therefore, thanks to the large number of data, an experimental relationship between the back-pressure and B-value has been obtained, as it is shown in Figure 6-33.

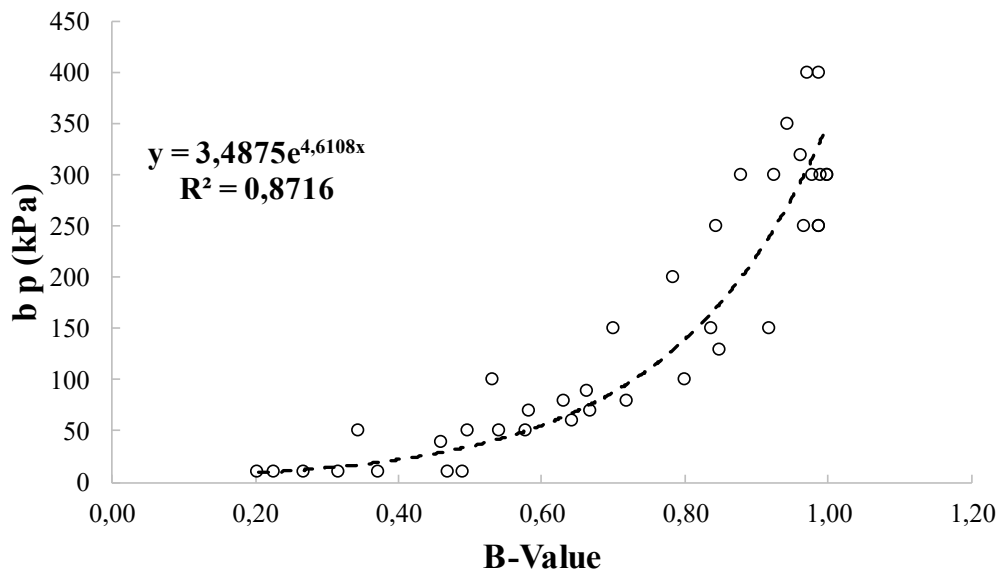


Figure 6-33 Experimental correlation between applied back pressures and achieved B-Values

Finally, the  $V_p-S_r$  relationship is plotted in Figure 6-34. It has been obtained by using the parameters shown in Table 6-8, in which the compressibility,  $K_b$ , has been reasonably changed to obtain the best fitting with the experimental data. Note that the ratio between the  $K_b$  and  $K_{b,0}$  is about 0.18 which is, as order of magnitude, the decrease of the stiffness from very low strain level, to higher ones.

Table 6-8 Elastic parameters from BE tests

$G_0$ (MPa)	$\nu$ (-)	$K_{b,0}$ (MPa)	$K_b$ (MPa)
29	0.34	82	15

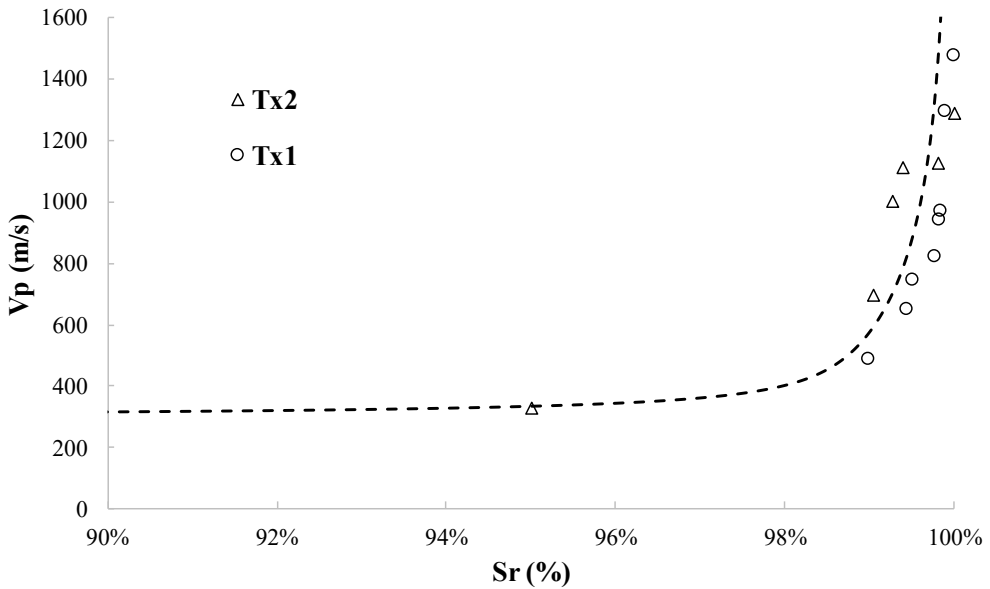


Figure 6-34 Tx1 and Tx2 tests results- experimental relationship between P-waves velocity and. degree of saturation

Thanks to this calibration in terms of  $K_b$ ,  $S_r$  values could be obtained from  $B$  values, by using Equation 6-11, in which the  $P_{w,abs}$  has been considered as a function of  $B$ , using the experimental correlation shown in Figure 6-33.

$$S_r = \frac{\left\{ B \cdot \left[ 1 + n K_b \cdot \left( \frac{1}{K_w} + \frac{1}{P_{w,abs}} \right) \right] - 1 \right\}}{B \cdot n \cdot K_b} \cdot P_{w,abs} \quad \text{Equation 6-11}$$

The results are shown in Figure 6-35. In order to stress out the effect of the pore pressure, i. e. the compressibility of the bubbles, in Figure 6-35 the trend of the theoretical curves for constant values of the back-pressure (respectively  $u_{bp}=0$  kPa and  $u_{bp}=300$  kPa) are shown. By considering the real increments of the back pressure, the theoretical curve fit better the data, since it is taking into account the changes in pore fluid stiffness.

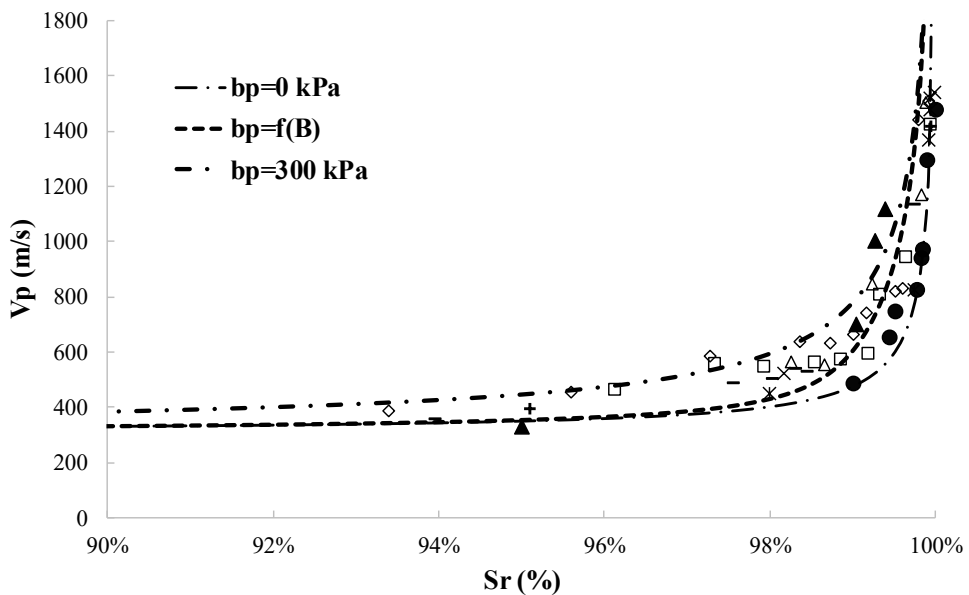


Figure 6-35 Final correlation between  $P$ -waves velocity and the degree of saturation, for different paths of back pressures

Then, the sensitivity of both B-Value and P-wave velocity has been examined. B-tests represent an integral response of the specimen, in terms of degree of saturation, while bender element tests, although they show a high sensitivity to the degree of saturation, need a careful interpretation of the data. The stiffer path the wave propagates through, or apparatus-effects such surface waves across the water cell, can significantly affect the experimental data interpretation. The frequency content analysis leads to a reasonable correction of the first arrival time, based on the neglection of the wave-trains at higher frequency content, probably due to an amplification of the frequency itself at the interface water cell-membrane, or a stiffer-fully saturated path. Frequency content analysis on the dry soil and water cell tests also shows that the pore fluid response is predominant in BE tests, (until a certain level of  $S_r$  is achieved), and almost frequency independent, demonstrating that higher frequency contents are related to interferences within the test apparatus. The relationship between  $V_p$  and  $S_r$  must take into account the non-linear behaviour of the soil due to different strain level induced in BE and B-value tests, and the effects of the back pressure as well. Anyway, with a view to a practical use of the  $V_p$  to check the degree of saturation in real scale problems, the results show that they are not able to verify degree of saturation lower than  $\approx 95\%$ , since the role of the soil skeleton becomes predominant compared to the equivalent pore fluid, in contrast to almost saturated conditions ( $95 < S_r < 100\%$ ).

### 6.3.3 NUMERICAL MODELLING OF BENDER ELEMENTS TESTS

After the experimental study on bender elements tests, a numerical modelling on the propagation of P-waves has been performed. Soil specimen has been modelled by means of the PLAXIS 2D software, the well-known finite element code widely used in ordinary and non-ordinary geotechnical numerical analyses. The aim of the numerical modelling is to verify and validate the signals correction and interpretation performed in the previous section. To this purpose, a simplified plane strain numerical model has been carried out. Plane strain condition is suitable to model the P-wave propagation across the specimen neglecting any type of reflection and refraction waves at the boundary of the model itself.

Therefore, a specimen with  $B=50$  mm and  $H=100$  mm has been modelled (Figure 6-36), by applying a confinement effective stress of 15 kPa. The pore fluid pressure has been kept equal to the atmospheric one. The generated mesh has been developed in order to avoid any numerical error due to the relative dimensions of mesh/wavelength. Every time a numerical analysis is performed, the mesh influence must be taken into account. Kuhlmeyer and Lysmer, 1973, suggested to assume a size of element not larger than  $\lambda/8$ , where  $\lambda$  is the wavelength corresponding to the maximum frequency of interest. Wavelengths shorter than the element length will obviously not be properly accounted for if interpolation between adjacent nodes is linear (Smith 1975).

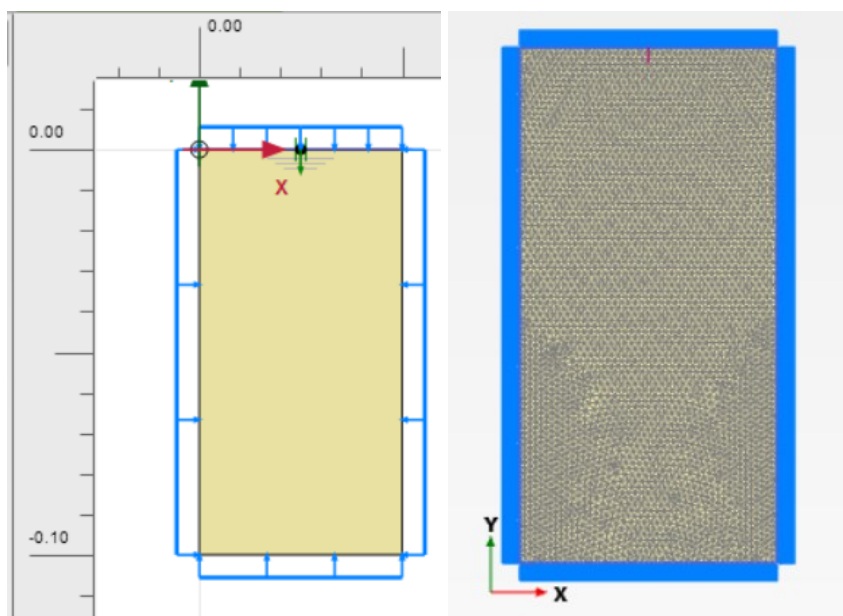


Figure 6-36 Numerical model- Geometry and generated mesh

The bender element has been modelled by applying, at the top of the modelled sample, a point displacement. The displacement itself has been fixed to propagate along the  $y$  axis, to the aim of inducing a compression displacement, i.e. modelling the propagation of P-waves across the specimen.

With regards to the constitutive model used in the numerical analyses, an elastic-linear one has been adopted, since BE tests are such to induce very low strain levels. Indeed, as discussed already, displacements induced by the excitations of the benders lead to such strains able to investigate, actually, all the elastic properties of the tested material. The elastic parameters used for the numerical modelling are reported in Table 6-9, inferred from the experimental data of BE tests. The imposed input displacement has been fixed equal to the experimental one, with a nominal frequency of 50 kHz (Figure 6-37).

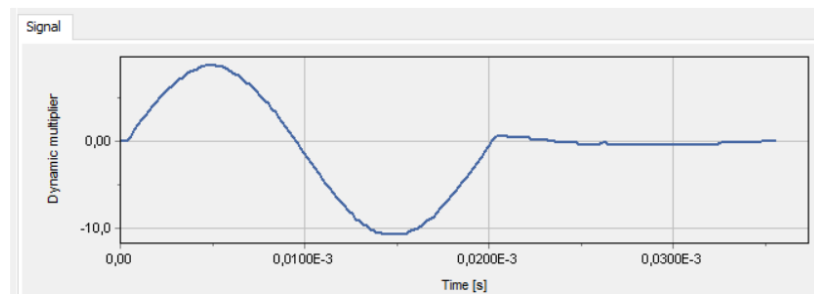


Figure 6-37 Numerical input displacement

Table 6-9 Numerical modelling elastic parameters

$V_p$ (m/s)	$E_{ed}$ (MPa)	$\nu$ (-)
295.8	160.5	0.34

Operatively, if BE tests want to be modelled, a numerical expedient is needed to simulate the partially saturated conditions, since the PLAXIS 2D code is not able to model directly the bi-phase nature of the pore fluid (*water + bubbles*). Such an issue can be easily faced by changing the bulk modulus of the pore water: the changes in the water volumetric compressibility,  $K_w$ , is sufficiently able to model partially saturated conditions, resulting in an equivalent pore fluid owning a higher compressibility. Therefore, several analyses have been performed for different values of  $K_w$  and, consequently, B-values. Numerical analyses are reported in Table 6-10.

Table 6-10 Numerical Analyses

Numerical Analysis	$K_w$	B	First arrival time	$V_p$
(-)	(MPa)	(-)	(s)	(m/s)
<b>PS1</b>	5	0,103	3,33E-04	300,3
<b>PS2</b>	100	0,696	2,17E-04	460,8
<b>PS3</b>	160	0,785	1,83E-04	546,4
<b>PS4</b>	250	0,851	1,53E-04	653,6
<b>PS5</b>	500	0,919	1,05E-04	952,4
<b>FS</b>	3000	0,970	6,36E-05	1572,3

Numerical results are then shown in Figure 6-38, in terms of evolution of the signal with the increasing  $K_w$  values. In order to preliminary validate the numerical model, a comparison between experimental and numerical data of ( $V_p$ ;B-value) has been performed (Figure 6-39). Obviously, numerical results fit exactly the theoretical curve of ( $V_p$ ;B-value) (given by *Equation 6-10*), since both the theoretical expression as well as the constitutive model are based on the poro-elasticity theory. However, since an optimum fitting is achieved, numerical model's consistency has been ensured.

Afterwards, a comparison between the output signals of both experimental and numerical results has been performed. In particular, for similar B-values, numerical outputs have been compared with experimental outputs of ST1 test (Table 6-11).

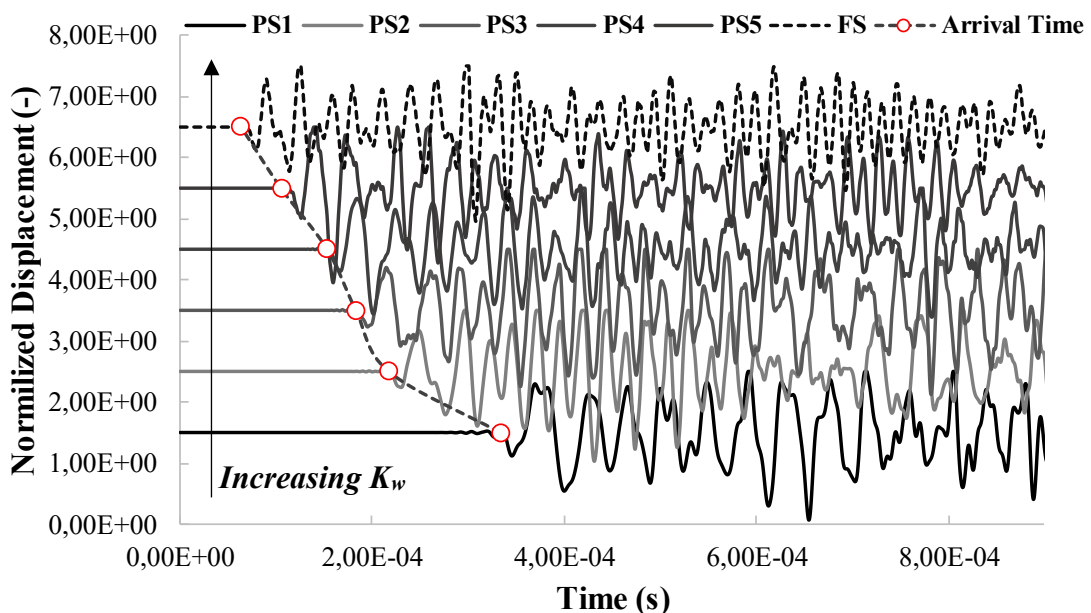


Figure 6-38 Numerical modelling on BE tests- Signals evolution

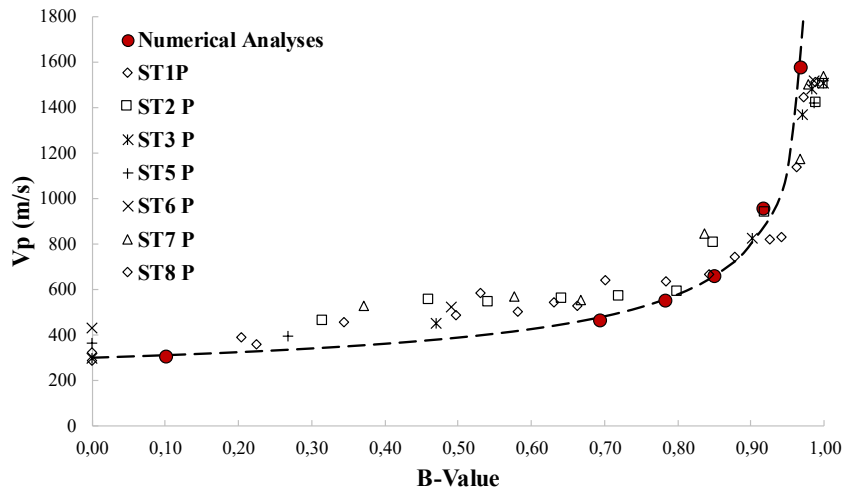


Figure 6-39 Numerical vs. experimental values of  $V_p$  as a function of B-value

The performed comparison aims to the validation of the first arrival time in the time domain, by superimposing the numerical and experimental output signals, as reported in Figure 6-40, Figure 6-41 and Figure 6-42.

Table 6-11 Comparison between numerical and experimental  $V_p$ -propagation tests

Numerical	Experimental
PS3 B=0.785	ST1, b.p.=200 kPa B=0.785
PS4 B=0.851	ST1, b.p.=250 kPa B=0.844
PS5 B=0.920	ST1, b.p.=300 kPa B=0.926

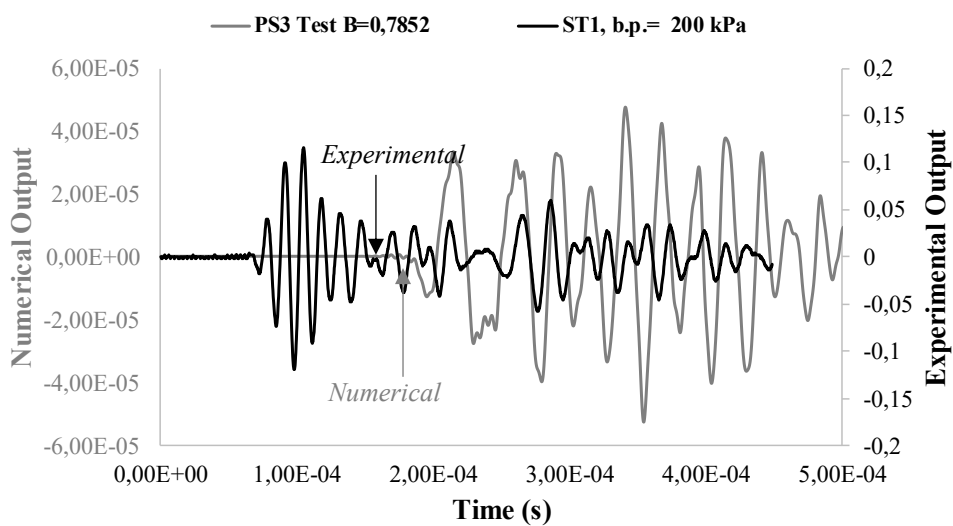


Figure 6-40 Numerical vs. experimental first arrival time (PS3)

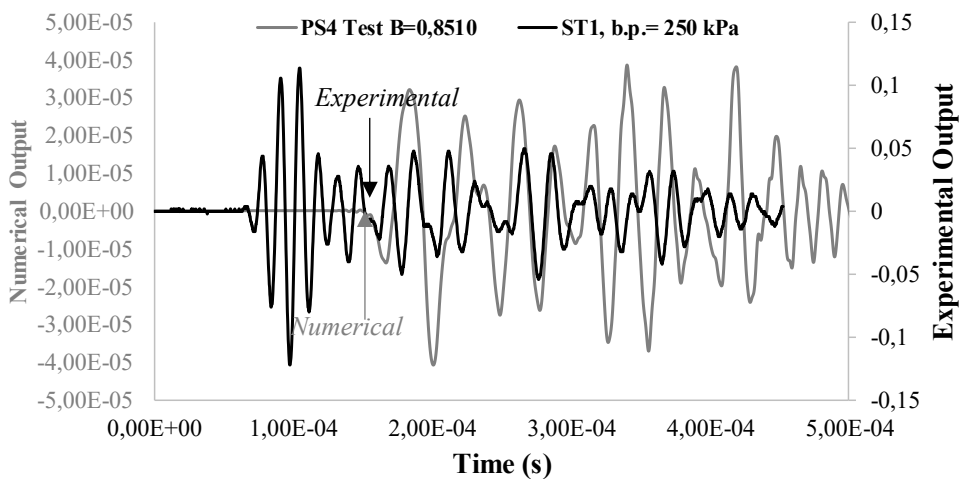


Figure 6-41 Numerical vs. experimental first arrival time (PS4)

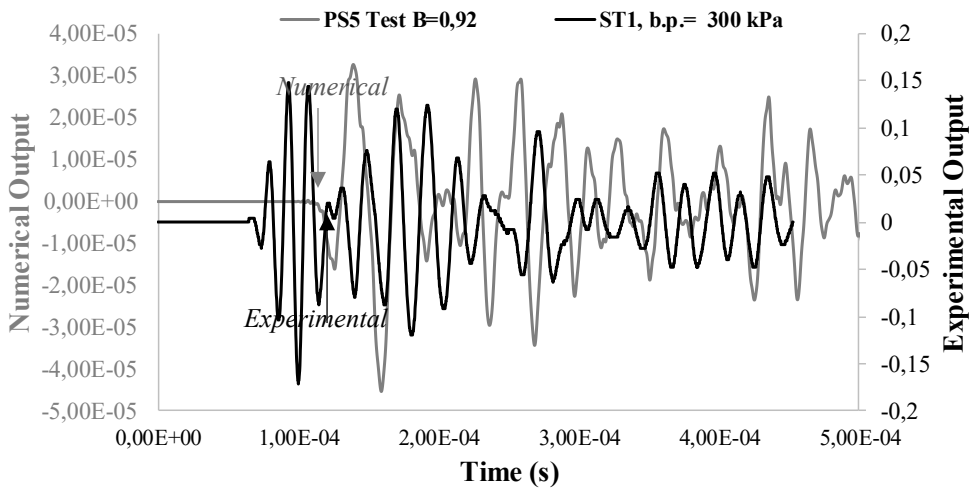


Figure 6-42 Numerical vs. experimental first arrival time (PS5)

Numerical results show that the first arrival times are consistent with the ones predicted by the theoretical relationship. More important, if numerical and experimental outputs are compared, the data interpretation carried out on experimental output signals leads to a very good fitting with the numerical ones. Experimental output interpretation, performed on time domain analyses and based on the identification of different branches (Figure 6-26 and Figure 6-28), needs a careful data manipulation, since experimental errors can occur as a consequence of external interferences not related to the waves propagating across the bi-phase fluid. Numerical analyses in plane strain conditions confirm that, by applying an equivalent pore fluid compressibility, the first arrival times

are very close to the experimental ones - after the branches identification is performed. The imposition of a unique compressibility of the pore fluid, the plane strain conditions as well as the absence of the cell water around the numerical specimen, are such to not generate any type of interferences during the propagations of the waves. More precisely, by modelling the pore fluid as an equivalent one-phase fluid, it is possible to avoid the waves' propagation through paths at different stiffness (saturated and partially saturated paths, Figure 6-23) that can affect the first arrival time, as demonstrated by the experimental BE tests.

Moreover, to additionally support the experimental data manipulation, a final comparison between the frequency content of both numerical and experimental outputs is performed and shown in Figure 6-43. The comparison has been carried out between the ST1 (b.p.=200 kPa, experimental) and PS3 (numerical), for  $B=0.785$ .

As it can be seen, the frequency content of the numerical test is in good agreement with the experimental one, for frequencies not higher than 50-60 kHz. At higher frequencies, in particular close to 75 kHz, the numerical frequency content does not show any significant peak, while the experimental one does.

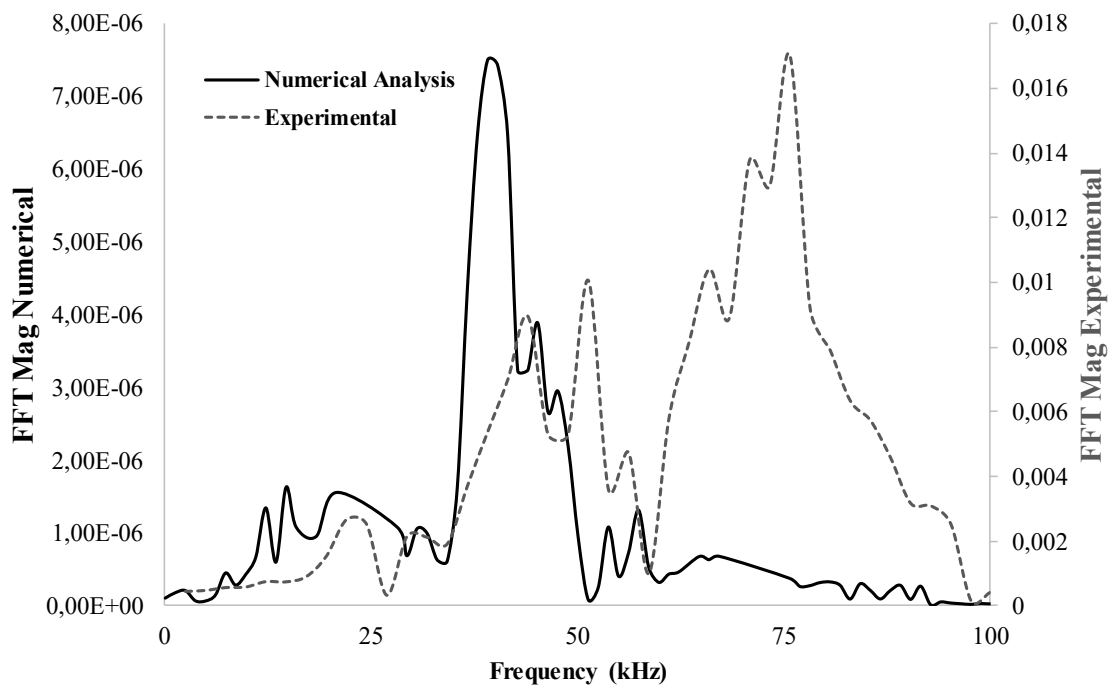


Figure 6-43 Frequency content comparison between numerical and experimental tests(PS3 and ST1, for an equal  $B$ -Value=0.785))

This result confirms that experimental signals are affected by laboratory interferences due to the complexity of the physical propagation of the P-waves across the specimen (which can present

saturated and partially saturated travel paths simultaneously) and/or at the interface water cell-membrane. Therefore, the first branch detected in the experimental output signal- responsible of the frequency peak at higher frequencies- is not related to a water-gas travel path, and it should be neglected during data interpretation, to ensure a reliable assessment of the P-wave and, as a consequence, to the degree of saturation

## 7 CHAPTER 7

### CONCLUSIONS AND REMARKS

The induced partial saturation represents an appealing mitigation technique to face liquefaction phenomena, and its effectiveness has been deeply investigated, proved and verified in a wide amount of research works. As a consequence, the advantages provided by the IPS lead to the necessity of developing a methodology to induce the partial saturation within the soil. The Thesis work, aiming to this purpose, has focused attention and efforts on a multidisciplinary approach, represented by the proposed bio-IPS technology, leading to the development of a bio-chemical solution able to generate gas bubbles. Since the chemical can be easily injected within the soil, (e.g. by means of low-pressure injections) bubbles nucleation develops directly within the voids, inducing a discontinuous gas phase distribution highly homogeneous among the soil's voids. In addition, the nucleation of occluded gas bubbles allows to assume the effective stresses principle still valid, resulting in a very low invasive application, strongly appealing for existing structures.

The experimentation presented in the thesis work has tried to cover the entire process, from the development of the bio-chemical solution to possible monitoring techniques. Starting by the biochemical tests, obtained results have demonstrated that selected bacteria can be suitable to an IPS technology for several reasons. First of all, selected bacteria are non-pathogenic, and their metabolic properties are able to nucleate gas bubbles. The selected bio-chemical reaction carried out by bacteria metabolism, which is represented by respiratory denitrification, is particularly appealing since nitrogen gas,  $N_2$ , represents the final metabolic product. Indeed,  $N_2$  presents several advantages, since it is chemically inert, of low solubility in water and is completely environmentally compatible.

Nitrogen gas bubbles nucleation has been ensured by the gas chromatography analyses, providing a high efficiency of bacteria to generate  $N_2$  in large amount, proving that even if a low quantity of  $CO_2$  is generated, it lies under solution in the chemical.

With regards to the performed environmental analyses, it has been proved that bacteria own a very high efficiency for reducing nitrates, necessary to activate bacteria metabolism itself. In addition, final values of nitrates concentration, evaluated by means of ion exchange chromatography tests, are compatible with the lower limits imposed by the Italian code, resulting in an environmental applicability. Moreover, the time-dependent metabolism analysis confirms a good consistency between the theory and the experimental observations, in terms of bio-chemical paths involved in the process, supported by the transient analyses performed on the formation- and consecutive reduction-of the ion ammonium,  $NH_4^+$ .

On the other hand, with regard to the performed desaturation tests, it has been demonstrated that a wide range of degrees of saturation can be achieved, depending on the initial nitrates' concentration used in the bio-chemical solution. In addition, desaturation tests performed in back-pressured specimens confirm that, even in presence of pore pressures higher than the atmospheric one, bacteria metabolism can be activated anyway, and thus applicable in real scale mitigation actions. Optical analyses, neglecting the upward flow of one of the selected bubbles, demonstrate that tiny bubbles can be nucleated, and they result relatively stable during time.

The tested monitoring techniques suitable to predict the final degrees of saturation, achieved by the bio-IPS technique, are represented by the electrical resistivity and P-waves velocity, both depending on  $S_r$ . The electrical resistivity has been proved to be highly sensitive to the chemistry of the pore fluid. The tests on the physical model (*DRC tests*) have been performed using two different types of pore fluids: water (*DRC-1 test*) and bio-chemical solution (*DRC-2 test*). In both cases, electrical resistivity changes with  $S_r$ : the lower is the degree of saturation, the higher is the measured electrical resistivity. This is due to the presence of the gas phase, resulting in a higher difficulty of the material to conduct current. In fact, even if the general relationship between  $\rho$  and  $S_r$  is similar between the two tests, the order of magnitude of the measured resistivity has been proved to be completely different. Indeed, for the *DRC-2* test, the high number of ions in the bio-chemical solution, essential for providing nutrients to bacteria and activate their metabolism, leads to a considerable decrease of  $\rho$ . As a consequence, it is necessary to normalize the electrical response of the soil with regards to the chemistry of the pore fluid. Thus, the relationship ( $\rho$ ;  $S_r$ ) must take into account the pore fluid electrical resistivity. By normalizing the measured resistivity with the ones of the pore fluids, a unique relationship is obtained (for a given material and same state properties), as it has been proved by the performed tests.

The experimentation carried out at *FEUP* is based on the P-waves velocity instead. First of all, tests on pressure plates demonstrate that, for the tested quartz sand, by achieving the desired degrees of saturation (about 80% with regards to the increase in the *CRR*), no significant suctions are involved, resulting in a discontinuous gas phase distribution. Afterwards, bender element tests confirm that P-waves velocity are strongly dependent on a slight change in the degree of saturation itself. On the other hand, experimental measurements of the output signals present several issues related to the complexity of the waves' propagation within the specimen. If a first calculation in time domain is performed, the calculation of  $V_p$  can be misleading. It is highly possible that the trend obtained without any output signal interpretation is affected by the interference with the propagation of refracted waves along the cell wall, at the interface between the membrane and the cell water, or is a consequence of a preferential saturated travel-path randomly located within the sample. Such an issue

can be faced by carrying out a signal interpretation, identifying different branches of the output signals. A second wave, slower than the first one, must be detected and correlated to a travel path represented by water + bubbles, and thus referred to the partially saturated conditions within the soil. A good tool to encourage the interpretation is to perform a frequency analyses of both input and output signal. Performed tests as well as *FFT* show that the faster waves, leading to the water P-wave velocity propagation, own a peak in the frequency content higher than that of the input signal, and they should be neglected from the data interpretation. All the made assumptions are confirmed by the B-values, performed for each measurement of  $V_p$ . The B-value is indeed a reliable parameter to assess the saturation of the specimen and, more important, it represents an integral response of the tested specimen itself, rather  $V_p$  is a local response and strongly dependent on the stiffness of the travel path. Moreover, numerical plane strain analyses lead to  $V_p$  values that are consistent with the ones obtained with signals interpretation. Indeed, the plane strain conditions has been fixed in order to avoid any type of refraction and reflection of the generated waves at the boundary of the specimen. However, P-waves velocity shows a very high dependency from  $S_r$  only in a restricted range of the degree of saturation, between the 95% and 100%. For this reason,  $V_p$  values only cannot be used to predict the achieved  $S_r$ .

A reliable monitoring technique can be represented by the combination of such  $S_r$ -depending parameters:  $V_p$  is not able to quantify  $S_r$  lower than 95%, but it is very sensitive when initially saturated soils start to decrease their water content. For this reason,  $V_p$  represents a reliable parameter to ensure the beginning of the desaturation process. On the other hand, by priorly characterizing properly the chemistry of the pore fluid, electrical resistivity can instead provide a reliable estimation of the degree of saturation achieved with the bio-IPS technique.

## 8 REFERENCES

- Acar, Y. B., and Alshawabkeh, A. N. (1993). "Principles of electrokinetic remediation." *Environmental Science & Technology*, American Chemical Society, 27(13), 2638–2647.
- Aislalie, J., Deslippe, J. R., and Dymond, J. R. (2013). "Soil microbes and their contribution to soil services." *Ecosystem services in New Zealand - conditions and trends*, (Figure 2), 143–161.
- Alessio, G., Alfonsi, L., Brunori, C. A., Burrato, P., Casula, G., Cinti, F. R., Civico, R., Colini, L., Cucci, L., De Martini, P. M., Falcucci, E., Galadini, F., Gaudiosi, G., Gori, S., Mariucci, M. T., Montone, P., Moro, M., Nappi, R., Nardi, A., Nave, R., Pantosti, D., Patera, A., Pesci, A., Pezzo, G., Pignone, M., Pinzi, S., Pucci, S., Salvi, S., Tolomei, C., Vannoli, P., Venuti, A., and Villani, F. (2013). "Liquefaction phenomena associated with the Emilia earthquake sequence of May-June 2012 (Northern Italy)." *Natural Hazards and Earth System Science*, 13(4), 935–947.
- Ambraseys, N. N. (1988). "Engineering Seismology." *Earthquake Engineering and Structural Dynamics*, 17, 1–105.
- ASTM-D6836-16. (2016). "Standard Test Method for Determination of the Soil Water Characteristic Curve for Desorption using Hanging Column, Pressure Extractor, Chilled Mirror Hygrometer, or Centrifuge, ASTM International, 100 Barr Harbor Drive, P.O. Box C700, West Conshohocken." *Subcommittee D18.04*.
- Astuto, G., Bilotta, E., Flora, A., Carraturo, F., and Guida, M. (2019). "Induced partial saturation for liquefaction mitigation by bio-gas bubbles nucleation." *Proc. of the 7th International Conference on Earthquake Geotechnical Engineering, 7ICEGE, Rome (Italy), June 2019*, (1).
- Bachofen, R. (1991). "Gas metabolism of microorganisms." *Experientia*, 47(6), 508–513.
- Baharuddin, I. N. Z., Omar, R. C., and Devarajan, Y. (2013). "Improvement of engineering properties of liquefied soil using Bio-VegeGrout." *IOP Conference Series: Earth and Environmental Science*, 16(1).
- Been, K., Crooks, J. H. A., Becker, D. E., and Jefferies, M. G. (1986). "The cone penetration test in sands: Part I, state parameter interpretation." *Geotechnique*, 36(2), 239–249.
- Been, K., Hachey, J., and Jefferies, M. G. (1991). "The critical state of sands." *Geotechnique*, 41(3), 365–381.
- Been, K., and Jefferies, M. G. (1985). "A state parameter for sands." *Geotechnique*, 35(2), 99–112.
- Bhatt, S., and Jain, P. K. (2014). "Correlation between electrical resistivity and water content of sand – a statistical approach." *American International Journal of Research in Science, Technology, Engineering & Mathematics*, 6(2), 115–121.
- Blander, M., and Katz, J. L. (1975). "Bubble nucleation in liquids." *AIChE Journal*, 21(5), 833–848.
- Boulanger, R. W., Asce, M., Idriss, I. M., and Asce, M. (2006). "Liquefaction Susceptibility Criteria for Silts and Clays." *Journal of Geotechnical and Geoenvironmental Engineering*, 132(November), 1413–1426.
- Boulanger, R. W., and Idriss, I. M. (2014). "CPT-based liquefaction triggering procedure." *Journal of Geotechnical and Geoenvironmental Engineering*, 142(2), 04015065.
- Bruce, D. (2000). "An Introduction to the Deep Soil Mixing Methods as Used in Geotechnical Applications." (E. C. O. Geosystems, ed.).

- Casagrande, A. (1936). "Characteristics of cohesionless soils affecting the stability of slopes and earth fills." *J. Boston Society of Civil Engineers*, 23(1), 13–32.
- Casagrande, A. (1976). *Liquefaction and cyclic mobility of sands: a critical review*. Harvard Soil Mechanics Series 88, Cambridge, Massachusetts.
- Castro, G. (1969). "Liquefaction of sands." *ph. D. Thesis, Harvard Soil Mech.*
- Castro, G., and Poulos, S. J. (1977). "Factors affecting liquefaction and cyclic mobility." *Journal of Geotechnical and Geoenvironmental Engineering*, 103(6).
- Cetin, K. O., Youd, T. L., Seed, R. B., Bray, J. D., Stewart, J. P., Durgunoglu, H. T., Lettis, W., and Yilmaz, M. T. (2004). "Liquefaction-Induced Lateral Spreading at Izmit Bay During the Kocaeli (Izmit)-Turkey Earthquake." *Journal of Geotechnical and Geoenvironmental Engineering*, 130(12), 1300–1313.
- Chu, D. B., Stewart, J. P., Lee, S., Tsai, J. S., Lin, P. S., Chu, B. L., Seed, R. B., Hsu, S. C., Yu, M. S., and Wang, M. C. H. (2004). "Documentation of soil conditions at liquefaction and non-liquefaction sites from 1999 Chi-Chi (Taiwan) earthquake." *Soil Dynamics and Earthquake Engineering*, 24(9–10), 647–657.
- Chu, J. (2016). "Solutions to Sustainability in Construction: Some Examples." *Procedia Engineering*, Elsevier B.V., 145, 1127–1134.
- Chung, Y. C., and Chung, M. S. (2000). "BNP test to evaluate the influence of C/N ratio on N<sub>2</sub>O production in biological denitrification." *Water Science & Technology*, 42(3–4), 23–27.
- Ciardì, G. (2017). "Microbially Induced Partial Saturation As Remedial Measure Against Liquefaction : A Review Of Fundamental Concepts." *Incontro Annuale dei Ricercatori di Geotecnica 2017- IARG 2017*.
- Dannowski, G., and Yaramancı, U. (1999). "Estimation of water content and porosity using combined radar and geoelectrical measurements." *European Journal of Environmental and Engineering Geophysics*, 4(1), 71–85.
- Davidson, A. E. A., Matson, P. A., Vitousek, P. M., Riley, R., Dunkin, K., and Maass, J. M. (1993). "Processes Regulating Soil Emissions of NO and N<sub>2</sub>O in a Seasonally Dry Tropical Forest." *Ecology*, 74(1), 130–139.
- DeAlba, P., Chan, C. K., and Seed, H. B. (1975). "Determination of soil liquefaction characteristics by large-scale laboratory tests." *Report EERC 75-14, Earthquake Engineering Research Center, University of California, Berkeley*.
- DeJong, J. T., Fritzges, M. B., and Nüsslein, K. (2006). "Microbially Induced Cementation to Control Sand Response to Undrained Shear." *Journal of Geotechnical and Geoenvironmental Engineering*, 132(11), 1381–1392.
- DeJong, J. T., Soga, K., Banwart, S. A., Whalley, W. R., Ginn, T. R., Nelson, D. C., Mortensen, B. M., Martinez, B. C., and Barkouki, T. (2011). "Soil engineering in vivo: Harnessing natural biogeochemical systems for sustainable, multi-functional engineering solutions." *Journal of the Royal Society Interface*, 8(54), 1–15.
- El-Kelesh, A. M., Matsui, T., and Tokida, K. (2012). "Field Investigation into Effectiveness of Compaction Grouting." *Journal of Geotechnical and Geoenvironmental Engineering*, 138(4), 451–460.
- El-Kelesh, A. M., Mossaad, M. E., and Basha, I. M. (2001). "Model Of Compaction Grouting." *Journal of Geotechnical and Geoenvironmental Engineering*, 127(11), 955–964.

- Elias, V., Welsh, J., Warren, J., Lukas, R., Collin, J. G., and Berg, R. R. (2008). "Ground Improvement Methods." *Structural Foundation Designers' Manual*, 124–139.
- Eseller-bayat, E., Yegian, M. K., and Alshawabkeh, A. (2013). "Liquefaction Response of Partially Saturated Sands. I: Experimental Results." *Journal of Geotechnical and Geoenvironmental Engineering*, 139(6), 863–871.
- Fasano, G., De Sarno, D., Bilotta, E., and Flora, A. (2019). "Design of horizontal drains for the mitigation of liquefaction risk." *Soils and Foundations*, Japanese Geotechnical Society, 59(5), 1537–1551.
- Flora, A., Bilotta, E., Chiaradonna, A., Lirer, S., Mele, L., and Pingue, L. (2020). "A field trial to test the efficiency of induced partial saturation and horizontal drains to mitigate the susceptibility of soils to liquefaction." *Bulletin of Earthquake Engineering*.
- Flora, A., Lirer, S., and Silvestri, F. (2012). "Undrained cyclic resistance of undisturbed gravelly soils." *Soil Dynamics and Earthquake Engineering*, Elsevier, 43, 366–379.
- Flora, A., Modoni, G., Lirer, S., and Croce, P. (2013). "The diameter of single , double and triple fluid jet grouting columns : prediction method and field trial results." *Geotechnique*, 63(11), 934–945.
- Da Fonseca, A. V., Ferreira, C., and Fahey, M. (2009). "A framework interpreting bender element tests, combining time-domain and frequency-domain methods." *Geotechnical Testing Journal*, 32(2), 91–107.
- Gallagher, P. M., Pamuk, A., and Abdoun, T. (2007). "Stabilization of Liquefiable Soils Using Colloidal Silica Grout." *Journal of Materials in Civil Engineering*, 19(1), 33–40.
- Gerth, W. A., and Hemmingsen, E. A. (1980). "Heterogeneous nucleation of bubbles at solid surfaces in gas-supersaturated aqueous solutions." *Journal of Colloid and Interface Science*, 74(1), 80–89.
- Hanzawa, H., Itoh, Y., and Suzuki, K. (1979). "Shear Characteristics of a Quick Sand in the Arabian Gulf." *Soils and Foundations*, 19(4), 1–15.
- Hemmingsen, E. A. (1977). "Spontaneous formation of bubbles in gas-supersaturated water." *Nature*, 267(5607), 141–142.
- Huang, Y., and Wen, Z. (2015). "Recent developments of soil improvement methods for seismic liquefaction mitigation." *Natural Hazards*, 76(3), 1927–1938.
- Ishihara, K., Huang, Y., and Tsuchiya, H. (1998). "Liquefaction resistance of nearly saturated sand as correlated with longitudinal wave velocity." *Poromechanics*, Balkema, 583–586.
- Ishihara, K. (1993). "Liquefaction and flow failure during earthquakes." *Geotechnique*, 43(3), 351–415.
- Ishihara, K., and Koga, Y. (1981). "Case Studies of Liquefaction in the 1964 Niigata Earthquake." *Soils and Foundations*, 21(3), 35–52.
- Johns, D. H. W. K. F. and S. W., Williams, H., Farrish, K., and Wagner, S. (2004). "Denitrification and soil characteristics of wetlands created on two mine soils in east Texas, USA." *Wetlands*, 24(1), 57–67.
- Jovičić, V., Coop, M. R., and Simić, M. (1996). "Objective criteria for determining Gmax from bender element tests." *Géotechnique*, ICE Publishing, 46(2), 357–362.

- Kamata, T., Tsukamoto, Y., and Ishihara, K. (2009). "Undrained Shear Strength of Partially Saturated Sand in Triaxial Tests." *Bulletin of the New Zealand Society for Earthquake Engineering*, 42(1).
- Kandiah, A., and K., M. K. (1988). "Level Ground Soil-Liquefaction Analysis Using in Situ Properties: I." *Journal of Geotechnical Engineering*, American Society of Civil Engineers, 114(7), 753–770.
- Karim, M. E., and Alam, M. J. (2014). "Effect of non-plastic silt content on the liquefaction behavior of sand-silt mixture." *Soil Dynamics and Earthquake Engineering*, Elsevier, 65, 142–150.
- Khodadadi, H., and Bilsel, H. (2012). "Application of microorganisms for improvement of liquefiable sand." *3rd International Conference on New Developments in Soil Mechanics and Geotechnical Engineering*, (June), 857–863.
- Kokusho, T. (2000). "CORRELATION OF PORE-PRESSURE B-VALUE WITH P-WAVE VELOCITY AND POISSON'S RATIO FOR IMPERFECTLY SATURATED SAND OR GRAVEL." *Soils and Foundations*, 40(4), 95–102.
- Konrad, J.-M. (1988). "Interpretation of flat plate dilatometer tests in sands in terms of the state parameter." *Géotechnique*, ICE Publishing, 38(2), 263–277.
- Kramer, S. (1996). *Geotechnical Earthquake Engineering*.
- Kramer, S., and Seed, B. (1988). "Initiation of soil liquefaction under static loading conditions." *Journal of Geotechnical Engineering*, 114(4), 412–430.
- Kuhlmeyer, R. L., and Lysmer, J. (1973). "Finite Element Method Accuracy for Wave Propagation Problems." *Journal of the Soil Mechanics and Foundation Division*, 99(5), 421–427.
- Lai, C. G., Bozzoni, F., Mangriots, M.-D., and Martinelli, M. (2015). "Soil liquefaction during the 20 may 2012 M5. 9 Emilia earthquake, northern Italy: field reconnaissance and post-event assessment." *Earthquake Spectra*, SAGE Publications Sage UK: London, England, 31(4), 2351–2373.
- Lee, J.-S., and Santamarina, J. C. (2005). "Bender Elements: Performance and Signal Interpretation." *Journal of Geotechnical and Geoenvironmental Engineering*, 131(January), 987–1003.
- Lee, K. L., and Albaisa, A. (1974). "Earthquake induced settlements in saturated sands." *Journal of the Soil Mechanics and Foundations Division, ASCE*, 100(GT4).
- Leroueil, S., Hight, D. W., and Cabral, A. R. (2015). "Practical implications of gas-water interactions in soils." *PCSMGE - 15th Pan-American Conference on Soil Mechanics and Geotechnical Engineering*, 209–259.
- Lirer, S., and Mele, L. (2019). "On the apparent viscosity of granular soils during liquefaction tests." *Bulletin of Earthquake Engineering*, 17(11), 5809–5824.
- Lombardi, D., and Bhattacharya, S. (2014). "Liquefaction of soil in the Emilia-Romagna region after the 2012 Northern Italy earthquake sequence." *Natural hazards*, Springer, 73(3), 1749–1770.
- Lubetkin, S. D. (2003). "Why is it much easier to nucleate gas bubbles than theory predicts?" *Langmuir*, 19(7), 2575–2587.
- Lukas, R. G. (1995). *Dynamic compaction*. Federal Highway Administration, Office of Engineering, Office of Technology ....
- Martin, J. R., Olgun, C. G., Mitchell, J. K., Hon, M., and Durgunoglu, T. H. (2004). "High-Modulus Columns for Liquefaction Mitigation." *Journal of Geotechnical and Geoenvironmental*

- Engineering*, 130(6), 561–571.
- Marulanda, C., Culligan, P. J., and Germaine, J. T. (2000). “Centrifuge modeling of air sparging — a study of air flow through saturated porous media.” *Journal of Hazardous Materials*, 72(2), 179–215.
- Mele, L., and Flora, A. (2019). “On the prediction of liquefaction resistance of unsaturated sands.” *Soil Dynamics and Earthquake Engineering*, Elsevier Ltd, 125(June), 105689.
- Mele, L., Tian, J. T., Lirer, S., Flora, A., and Koseki, J. (2018a). “Liquefaction resistance of unsaturated sands: experimental evidence and theoretical interpretation.” *Géotechnique*, 69(6), 541–553.
- Mele, L., Tian, J. T., Lirer, S., Flora, A., and Koseki, J. (2018b). “Liquefaction resistance of unsaturated sands: experimental evidence and theoretical interpretation.” *Géotechnique*, ICE Publishing, 69(6), 541–553.
- Mele, L., Tian, J. T., Lirer, S., Flora, A., and Koseki, J. (2019). “Liquefaction resistance of unsaturated sands: Experimental evidence and theoretical interpretation.” *Geotechnique*, 69(6), 541–553.
- Middlebrooks, T. A. (1942). “Fort Peck Slide.” *Transactions of the American Society of Civil Engineers*, 107(1), 723–742.
- Miller, E. A., and Roycroft, G. A. (2004). “Compaction Grouting Test Program for Liquefaction Control.” *Journal of Geotechnical and Geoenvironmental Engineering*, 130(4), 355–361.
- Mitaritonna, G., Amorosi, A., and Cotecchia, F. (2010). “Multidirectional bender element measurements in the triaxial cell: equipment set-up and signal interpretation.” *Rivista Italiana di Geotecnica*.
- Nishio, S. (1987). “Effect of saturation on elastic wave velocities of sand and gravel.” *Proc. of Recent Advances in Study of Engrg. Properties of Unsaturated Soil, JGS*, 221–224.
- Okamura, M., and Soga, Y. (2006). “Effects of pore fluid compressibility on liquefaction resistance of partially saturated sand.” *Soils and Foundations*, 46(5), 695–700.
- Okamura, M., Takebayashi, M., Nishida, K., Fujii, N., Jinguiji, M., Imasato, T., Yasuhara, H., and Nakagawa, E. (2011). “In-Situ Desaturation Test by Air Injection and Its Evaluation through Field Monitoring and Multiphase Flow Simulation.” *Journal of Geotechnical and Geoenvironmental Engineering*, 137(7), 643–652.
- Van Paassen, L. A., Pham, V., Mahabadi, N., Hall, C., Stallings, E., and Kavazanjian, E. (2018). “Desaturation via biogenic gas formation as a ground improvement technique.” *Geotechnical Special Publication*, 2017-Novem(GSP 300), 244–256.
- Papadopoulos, G. A., and Lefkopoulos, G. (1993). “Magnitude-distance relations for liquefaction in soil from earthquakes.” *Bulletin - Seismological Society of America*, 83(3), 925–938.
- Poulos, S., Castro, G., and France, J. (1988). “Liquefaction evaluation procedure.” *Journal of Geotechnical Engineering*, 111(6), 772–792.
- Poulos, S. J. (1981). “The steady state of deformation.” *Journal of Geotechnical and Geoenvironmental Engineering*, 107(ASCE 16241 Proceeding).
- Rasouli, R., Hayashi, K., and Zen, K. (2016). “Controlled permeation grouting method for mitigation of liquefaction.” *Journal of Geotechnical and Geoenvironmental Engineering*, 142(11), 1–11.
- Rebata-Landa, V., and Santamarina, J. C. (2012). “Mechanical Effects of Biogenic Nitrogen Gas

- Bubbles in Soils." *Journal of Geotechnical and Geoenvironmental Engineering*, 138(2), 128–137.
- Rhoades, J. D., Raats, P. A. C., and Prather, R. J. (1976). "Effects of Liquid-phase Electrical Conductivity, Water Content, and Surface Conductivity on Bulk Soil Electrical Conductivity." *Soil Science Society of America Journal*, 40(5), 651–655.
- Ronen, D., Berkowitz, B., and Magaritz, M. (1989). "The development and influence of gas bubbles in phreatic aquifers under natural flow conditions." *Transport in Porous Media*, 4(3), 295–306.
- Ben Salem, Z., Frikha, W., and Bouassida, M. (2015). "Effect of Granular-Column Installation on Excess Pore Pressure Variation during Soil Liquefaction." *International Journal of Geomechanics*, 16(2), 04015046-1–8.
- Sciarra, A., Cantucci, B., Buttinelli, M., Galli, G., Nazzari, M., Pizzino, L., and Quattrocchi, F. (2012). "Soil-gas survey of liquefaction and collapsed caves during the Emilia seismic sequence." *Annals of Geophysics*, 55(4).
- Skempton, A. W. (1954). "The Pore-Pressure Coefficients A and B." *Géotechnique*, ICE Publishing, 4(4), 143–147.
- Smith, W. D. (1975). "The Application of Finite Element Analysis to Body Wave Propagation Problems." *Geophysical Journal of the Royal Astronomical Society*, 42(2), 747–768.
- Soga, K. (1998). "Soil Liquefaction Effects Observed in The Kobe Earthquake of 1995." *Proceedings of the Institution of Civil Engineers - Geotechnical Engineering*, 131(1), 34–51.
- Swinehart, D. F. (1962). "The Beer-Lambert Law." *Journal of Chemical Education*, American Chemical Society, 39(7), 333.
- Tamura, S., Tokimatsu, K., Abe, A., and Sato, M. (2002). "Effects of Air Bubbles on B-Value and P-Wave Velocity of a Partly Saturated Sand." *Soils and Foundations*, 42(1), 121–129.
- Taylor, M. L., Cubrinovski, M., and Bradley, B. A. (2012). "Characterisation of Ground Conditions in the Christchurch Central Business District." *Australian Geomechanics Journal*, 47(4), 43–57.
- Topolnicki, M. (2004). *Ground Improvement*. Second edition published 2004 by Spon Press.
- Towhata, I. (2008). "Mitigation of Liquefaction-Induced Damage." *Geotechnical Earthquake Engineering*, Springer Berlin Heidelberg, Berlin, Heidelberg, 588–642.
- Triantafyllidis, T., and Kimmig, I. (2019). "A simplified model for vibro compaction of granular soils." *Soil Dynamics and Earthquake Engineering*, Elsevier Ltd, 122, 261–273.
- Tsukamoto, Y. (2018). "Degree of saturation affecting liquefaction resistance and undrained shear strength of silty sands." *Soil Dynamics and Earthquake Engineering*, Elsevier Ltd, (March), 0–1.
- Tsukamoto, Y., Ishiara, K., Nakazawa, H., Kamada, K., and Huang, Y. (2002). "Resistance of Partly Saturated Sand to Liquefaction with Reference to Longitudinal and Shear Wave Velocities." *Soils and Foundations*, 42(6), 93–104.
- Tsukamoto, Y., Kawabe, S., Matsumoto, J., and Hagiwara, S. (2014). "Cyclic resistance of two unsaturated silty sands against soil liquefaction." *Soils and Foundations*, Elsevier, 54(6), 1094–1103.
- Tveit, A. T., Urich, T., Frenzel, P., and Svenning, M. M. (2015). "Metabolic and trophic interactions modulate methane production by Arctic peat microbiota in response to warming." *Proceedings*

- of the National Academy of Sciences*, 112(19), E2507–E2516.
- Vaid, Y. P., and Chern, J. C. (1983). “Effect of Static Shear on Resistance to liquefaction.” *Soils And Foundations*, 23(1), 47–60.
- Vannucchi, G., Crespellani, T., Facciorusso, J., Ghinelli, A., Madiai, C., Puliti, A., and Renzi, S. (2012). “Soil liquefaction phenomena observed in recent seismic events in Emilia-Romagna Region, Italy.” *International Journal of Earthquake Engineering*, 2(3).
- Vaughan, P. R. (2003). “Observations on the behaviour of clay fill containing occluded air bubbles.” *Géotechnique*, 53(2), 265–272.
- Viggiani, G., and Atkinson, J. H. (1995). “Interpretation of bender element tests.” *Geotechnique*, 45(1), 149–154.
- Wang, W. (1979). “Some findings in Soil Liquefaction.” *Water Conservancy and Hydroelectric Power Scientific Research Institute, Beijing, China*.
- Weil, M. H., DeJong, J. T., Martinez, B. C., and Mortensen, B. M. (2011). “Seismic and Resistivity Measurements for Real-Time Monitoring of Microbially Induced Calcite Precipitation in Sand.” *Geotechnical Testing Journal*, 35(2), 330–341.
- Wheeler, S. J., and Karube, D. (1995). “State of the Art Report: Constitutive Modeling.” *Proc. 1st Int. Conf. Unsaturated Soils, Paris*, 1323–1356.
- Wong, H. Y. (1974). “Discussion of Compaction Grouting.” *Journal of Geotechnical Engineering*, 100(5), 556–559.
- Wu, S. (2015). “Mitigation of liquefaction hazards using the combined biodesaturation and bioclogging method.”
- Yang, J. (2002). “Liquefaction resistance of sand in relation to P-wave velocity.” *Géotechnique*, 52(4), 295–298.
- Yang, J., and Sato, T. (2000). “Interpretation of seismic vertical amplification observed at an array site.” *Bulletin of the Seismological Society of America*, 90(2), 275–285.
- Yegian, M. K., Eseller-Bayat, E., Alshawabkeh, A., and Ali, S. (2007). “Induced-Partial Saturation for Liquefaction Mitigation: Experimental Investigation.” *Journal of Geotechnical and Geoenvironmental Engineering*, 133(3), 295–305.
- Yoshimi, Y., Tanaka, K., and Tokimatsu, K. (1989). “Liquefaction Resistance of a Partially Saturated Sand.” *Soils and Foundations*, 29(3), 157–162.
- Youd, L. T. (1984). “Recurrence of liquefaction at the same site.” *Proc. 8th World Conf. Earthq. Engng*, Prentice-Hall Inc, 3, 231–238.
- Youd, L. T. (1991a). “Mapping of earthquake-induced liquefaction for seismic zonation.” *Proceedings, 4th International Conference on Seismic Zonation, Earthquake Engineering Research Institute, Stanford University*, 1, 111–147.
- Youd, L. T. (1991b). “Mapping of Earthquake-Induced Liquefaction for Seismic Zonation.” *Proceedings, 4th International Conference on Seismic Zonation, Earthquake Engineering Research Institute, Stanford University*, 111–147.
- Yu, H. S. (1994). “State Parameter from Self-Boring Pressuremeter Tests in Sand.” *Journal of Geotechnical Engineering*, 120(12), 2118–2135.
- Zeybek, A., and Madabhushi, S. P. G. (2017). “Influence of air injection on the liquefaction-induced

deformation mechanisms beneath shallow foundations.” *Soil Dynamics and Earthquake Engineering*, Elsevier Ltd, 97(October 2015), 266–276.

## 9 APPENDIX- QUARTZ SAND CYCLIC CHARACTERIZATION

The material used for the bender elements experimental program, at “*Faculdade de Engenharia, University of Porto*“ has been mechanically characterized by means of cyclic tests in three different apparatuses. Regardless the low-strain level soil response, investigated by BE tests, the cyclic resistance of the quartz sand has been evaluated by means of mechanical testing in the following equipment:

- Controlled stress path triaxial cell equipment (Figure 6-14);
- Cyclic triaxial cell equipment (Figure 6-15);
- Cyclic simple shear equipment (Figure A-9-1).

Prior to the cyclic characterization, static triaxial tests have been performed in order to assess the shear strength angle of the monogranular sand. As shown in

Figure A-9-2, an M coefficient of 1.42 has been evaluated, leading to a  $\phi_{cv}'=35.1^\circ$ .

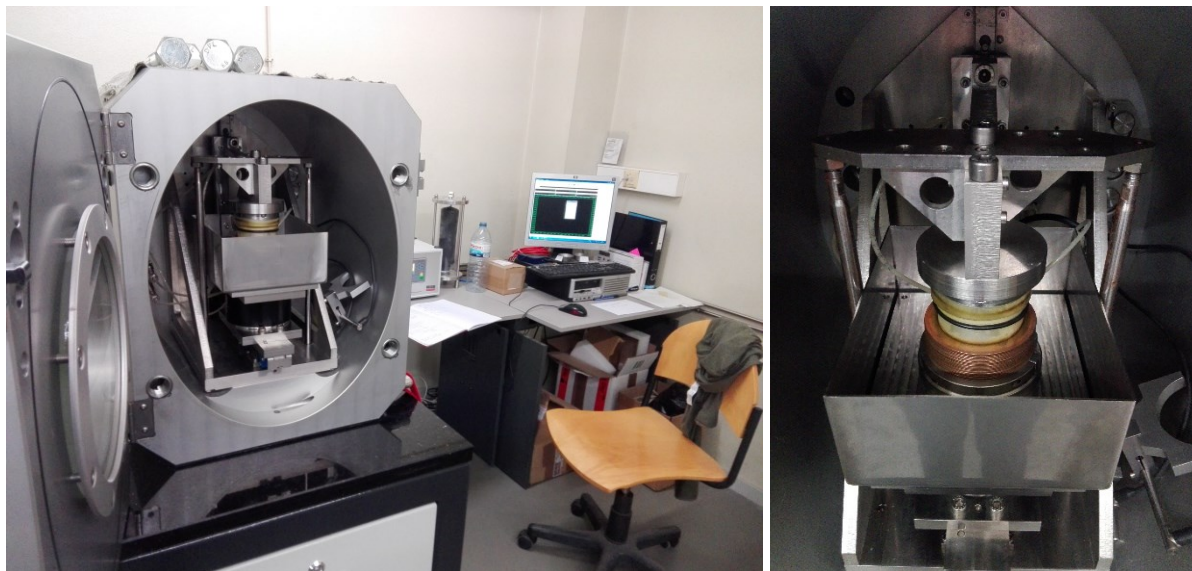


Figure A-9-1 Cyclic simple shear equipment at the geotechnical laboratory of FEUP

Triaxial cells have been already mentioned in the §6.3, since they have been necessary to implement the BE experimental setup. On the other hand, for mechanical characterization only, a cyclic simple shear apparatus has been additionally used. As it will be shown in the following, all the three equipments own several differences in terms of applied cyclic stresses or specimen conditions. Thus, a careful output interpretation was needed, in order to finally assess a cyclic resistance curve for the tested material.

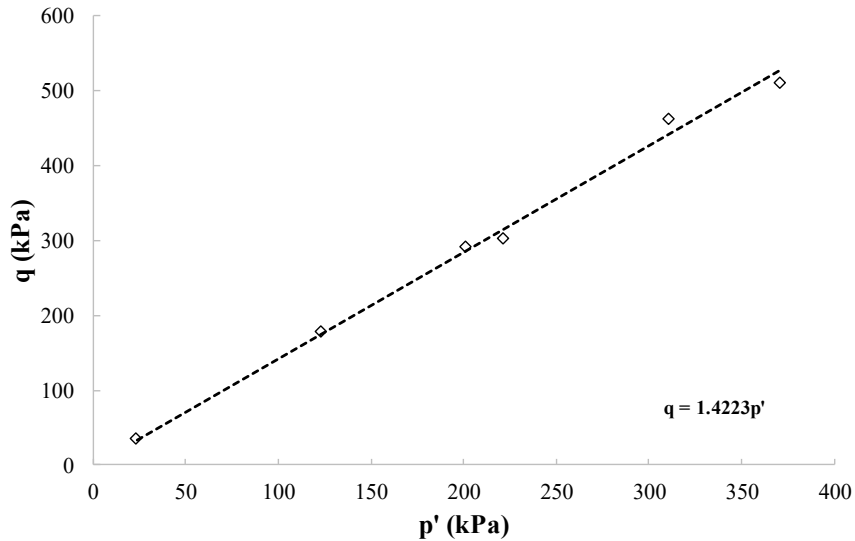


Figure A-9-2 Failure envelop for Quartz sand

Coming back to the cyclic characterization, it is fundamental to underline several peculiarities-regarding testing apparatus- that will affect the present study. As it is well known, when cyclic tests are performed, output data are usually manipulated in terms of cyclic stress ratio,  $CSR$ , vs. number of cycles needed to reach liquefaction,  $N_{liq}$ . In case of cyclic triaxial tests, the applied cyclic stress ratio can be defined as:

$$CSR_{tx} = \frac{\tau_d}{\sigma'_{ref}} = \frac{q_d}{2 \cdot \sigma'_{ref}} \quad \text{Equation A-1}$$

where  $q_d$  is the deviatoric stress, equal to  $(\sigma_a - \sigma_r)$  and  $\sigma'_{ref}$  is defined as:

$$\sigma'_{ref} = \frac{\sigma'_{1,c} - \sigma'_{3,c}}{2} \quad \text{Equation A-2}$$

with  $\sigma'_{1,c}$  and  $\sigma'_{3,c}$  are respectively the maximum and minimum principal effective stresses acting at the end of the consolidation stage.

On the other hand, in case of cyclic simple shear tests, the CSR can be defined as:

$$CSR_{ss} = \frac{\tau_d}{\sigma'_{v,0}} \quad \text{Equation A-3}$$

In the present work, since both equipment have been used, a comparison between triaxial and simple shear cyclic tests needs to be performed. To this aim, the Castro's correlation between  $CSR_{tx}$

and  $CSR_{ss}$  has been used, able to compare different applied stress paths tests thank to the following equation:

$$CSR_{ss} = C_r \cdot CSR_{tx} \quad \text{Equation A-4}$$

$$C_r = 2 \cdot \frac{1 + k_0}{3\sqrt{3}} \quad \text{Equation A-5}$$

Therefore, theoretical instruments are widely available to compare cyclic tests performed in different equipment. The testing program on cyclic characterization is reported in Table A-1 and Table A-2, respectively for triaxial and simple shear tests.

*Table A-1 Triaxial Cells Tests*

Equipment	Test	Relative density, $D_r$	$CSR_{tx}$
<b><i>Controlled stress path triaxial</i></b>	<b>ST2</b>	43%	0,213
	<b>ST3</b>	42%	0,231
	<b>ST6</b>	37%	0,246
	<b>ST7</b>	34%	0,286
	<b>ST8</b>	40%	0,223
	<b>TxS2</b>	46%	0,279
	<b>TxS3</b>	47%	0,253
	<b>TxS4</b>	34%	0,164

*Table A-2 Cyclic simple shear tests*

Equipment	Test	Relative density, $D_r$	$CSR_{ss}$
<b><i>Cyclic Simple Shear</i></b>	<b>CSS1</b>	39%	0,190
	<b>CSS2</b>	38%	0,150
	<b>CSS3</b>	41%	0,140
	<b>CSS4</b>	35%	0,198
	<b>CSS5</b>	31%	0,159
	<b>CSS6</b>	34%	0,149
	<b>CSS7</b>	35%	0,130

As it is shown, an average relative density of 39% ( $\pm 5\%$ ) is achieved for all the tests, leading to the possibility of reasonably comparing data for a unique cyclic resistance curve, with an acceptable scatter of data.

Therefore, starting by the triaxial tests, a first comparison in terms of  $(CRR; N_{liq})$  is made. To this aim, a stress approach to assess the number of cycles needed to reach liquefaction has been adopted, defining soil's failure when:

$$r_u = \frac{\Delta u}{\sigma'_{c,0}} = 0.9$$

Equation A-6

where  $\sigma'_{c,0}$  represent the effective confinement stress at the end of the consolidation stage, equal to 50 kPa.

In Table A-9-3 the applied CSR as well as  $N_{liq}$  values are reported, while relative results are plotted in Figure A-9-3.

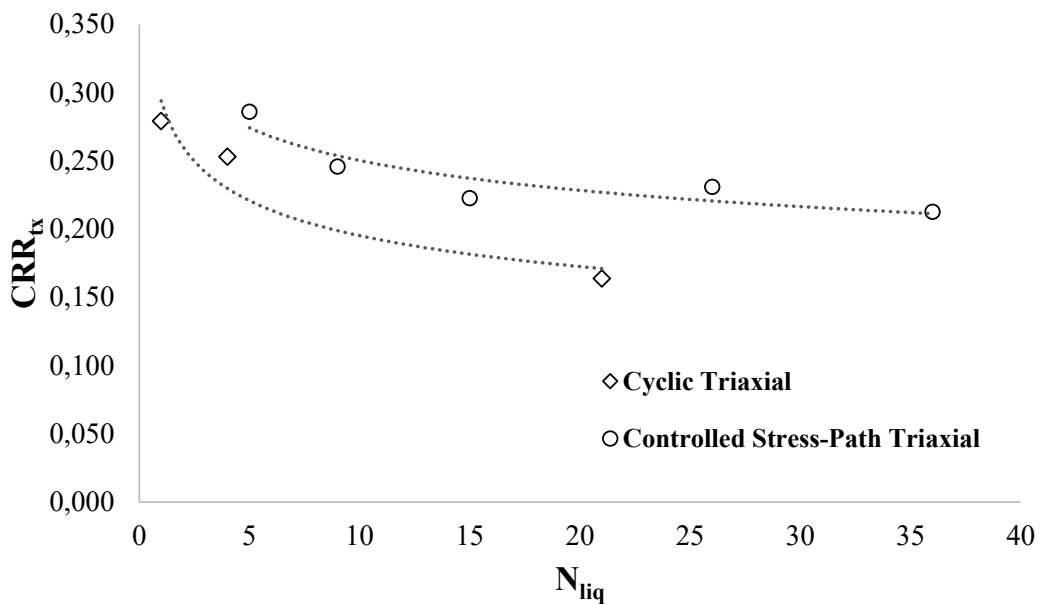


Figure A-9-3 Cyclic triaxial tests results for cyclic and controlled stress path equipment

Table A-9-3 Triaxial tests results

Equipment	Test	Relative density, $D_r$	CSR <sub>tx</sub>	$N_{liq}$ ( $r_u$ approach)
<i>Controlled Stress-Path Triaxial</i>	<b>ST2</b>	43%	0,213	36
	<b>ST3</b>	42%	0,231	26
	<b>ST6</b>	37%	0,246	9
	<b>ST7</b>	34%	0,286	5
	<b>ST8</b>	40%	0,223	15
<i>Cyclic Triaxial</i>	<b>TxS2</b>	46%	0,279	1
	<b>TxS3</b>	47%	0,253	4
	<b>TxS4</b>	34%	0,164	21

Clearly, liquefaction tests results do not lie on a unique CRR curve. Such result leads to an evaluation of the applied CSR history, since the two equipment present differences in terms of applied

cyclic stress. Indeed, the main difference between the tested apparatus, with regards to  $CSR(N_{cyc})$  is that:

- For the cyclic triaxial apparatus, the equipment is able to apply a sinusoidal cyclic stress of a given amplitude;
- For the controlled stress path apparatus, the equipment is not able to apply a sinusoidal cyclic stress, rather the deviatoric time history oscillates in linear increments (and decrements), related to a given amplitude.

Therefore, a technical issue has to be faced: for a given amplitude, the evaluation of the CSR for each apparatus would lead to a unique value of CSR itself, calculable by using *Equation A-1*. Actually, although the deviatoric peak is the same, the applied time-stress history for the two apparatuses is such to impose different cyclic loading during time, resulting in a kind of “*applied energy*” which is different for the two tests. Thus, a correcting factor must be adopted in order to take into account the applied CSR during time. To this purpose, a comparison between two CSR time histories is reported in Figure A-9-4, respectively for bi-linear and sinusoidal shape.

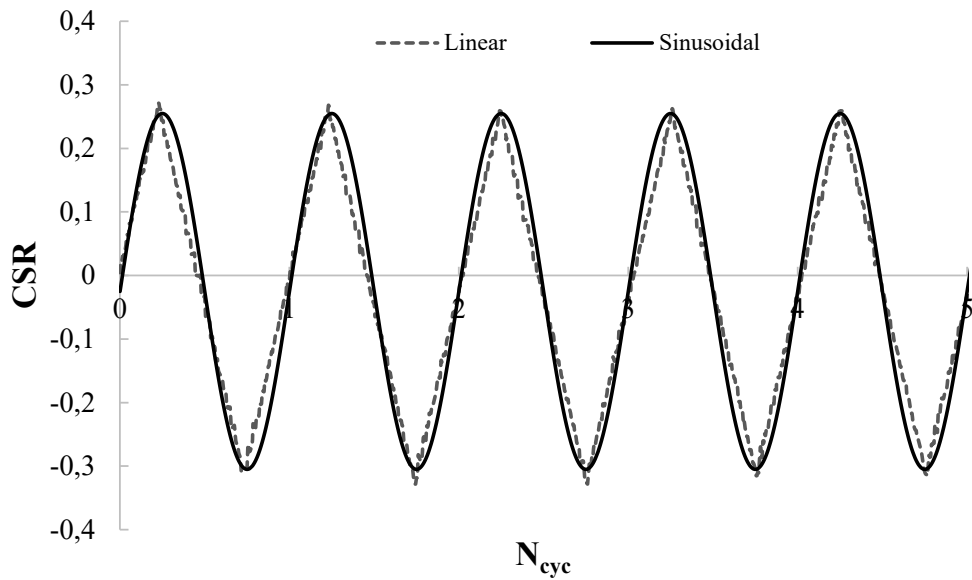


*Figure A-9-4 Comparison between bi-linear and sinusoidal CSR time history*

Operatively, a correction factor needs to be calculated, in order to link a bi-linear to a sinusoidal CSR as follows:

$$CSR_{sin} = \frac{CSR_{bi-linear}}{k_{CSR}}. \quad \text{Equation A-7}$$

To this purpose, an evaluation of the area subtended by the two CSR functions ( $A_{CSR}$ ) has been carried out numerically as follow:

$$A_{CSR} = \sum_{N_{Cyc}=0}^n CSR_{N_{Cyc}} \cdot \Delta N_{Cyc} \quad \text{Equation A-8}$$

which could be conceptually associated to a sort of applied deviatoric energy. By applying *Equation A-8* with regards to the  $CSR(N_{cyc})$  curves, results shown in Figure A-9-5 are obtained.

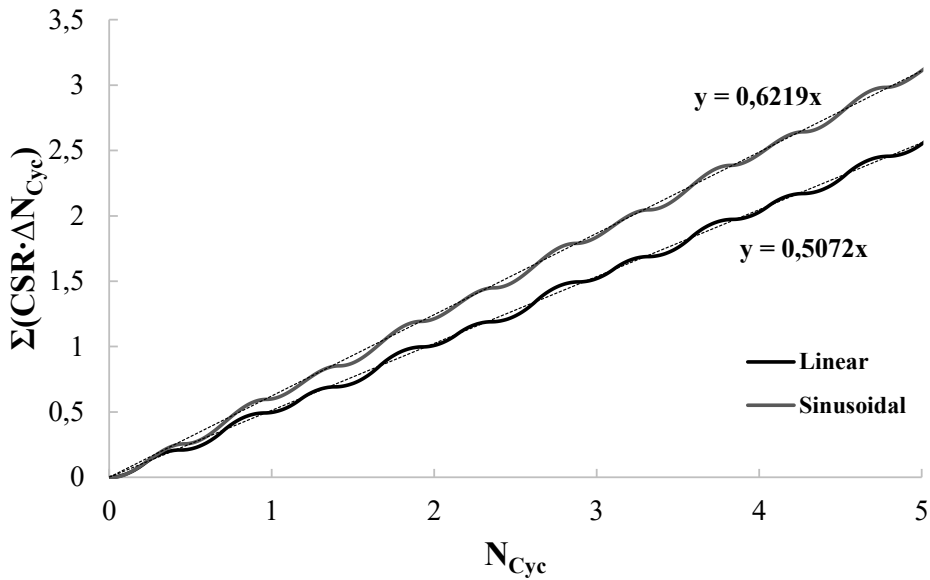


Figure A-9-5 Evolution of Equation A-8

Starting by Figure A-9-5's results, the evolution of the CSR during time (i.e.  $N_{cyc}$ ) is different for the two time histories. This discrepancy leads to different area subtended by the sinusoidal and bi-linear applied CSR. If a normalization between  $(\sum_{N_{Cyc}=0}^n CSR_{N_{Cyc}} \cdot \Delta N_{Cyc})$ - respectively for sinusoidal and bi-linear function- is performed, the correction factor needed can be expressed as:

$$k_{cyc} = \frac{0.6219}{0.5072} = 1.23 \quad \text{Equation A-9}$$

which is simply given by the ratio between the two angular coefficients showed in Figure A-9-5.

Thus, by using the correction factor as reported in *Equation A-7*, the following manipulation of the data is carried out, in which are additionally reported the  $N_{liq}$  measured by adopting a strain criterion approach (i.e. double amplitude axial strain,  $\epsilon_a^{DA}$  equal to 5%).

Table A-4 Triaxial tests results after the application of  $k_{cyc}$

Equipment	Test	Relative density, $D_r$	CSR bi-linear	CSR <sub>sin</sub>	N <sub>liq</sub> ( $r_u$ approach)	N <sub>liq</sub> ( $\epsilon_a^{DA}$ approach)
<b>Controlled Stress-Path Triaxial</b>	<b>ST2</b>	43%	0,213	0,173	36	37
	<b>ST3</b>	42%	0,231	0,188	26	29
	<b>ST6</b>	37%	0,246	0,200	9	10,5
	<b>ST7</b>	34%	0,286	0,233	5	6,3
	<b>ST8</b>	40%	0,223	0,181	15	16
<b>Cyclic Triaxial</b>	<b>TxS2</b>	46%	-	0,279	1	1
	<b>TxS3</b>	47%	-	0,253	4	5
	<b>TxS4</b>	34%	-	0,164	21	21,5

Therefore, by plotting all the tests in terms of (CSR<sub>sin</sub>; N<sub>liq</sub>), results shown in Figure A-9-6 and Figure A-9-7 are obtained, respectively for stress and double amplitude strain criteria.

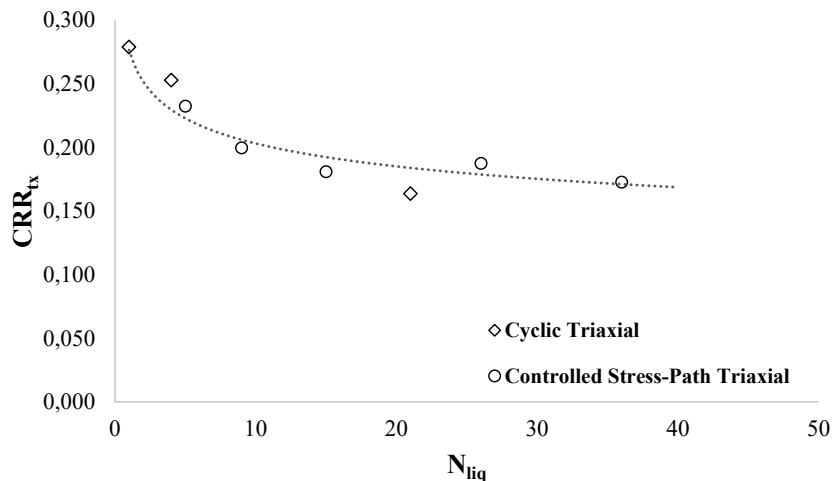


Figure A-9-6 Cyclic resistance curve for triaxial tests after  $k_{cyc}$  correction ( $r_u$  criteria)

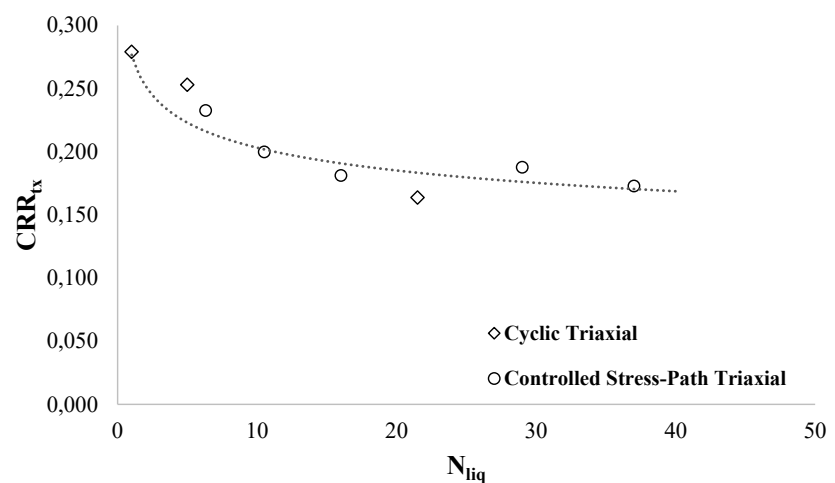


Figure A-9-7 Cyclic resistance curve for triaxial tests after  $k_{cyc}$  correction ( $\epsilon_a^{DA}$  criteria)

Output results show a good correlation between the two apparatus test results, demonstrating that, for a similar relative density tested, the cyclic resistance curve is highly dependent on the CSR time history. If different shapes of the CSR vs. time are applied, this must be taken into account with regards to the cyclic resistance of the liquefiable soil.

Afterwards, to validate such data interpretation, an energy-based approach has been adopted to reliably assess the consistency of the applied correction. The energy-based method has been widely investigated in the last years by several authors, resulting in a high reliability of the obtained results.

The method is based on the definition of the specific energy needed to cause soil liquefaction and it is can be defined as the sum of two components (Mele and Flora 2019):

$$E_{tot,liq} = E_{v,liq} + E_{s,liq} \quad \text{Equation A-10}$$

in which  $E_{v,liq}$  is the volumetric specific energy and  $E_{s,liq}$  is the deviatoric specific energy to reach liquefaction. In fact, *Equation A-10* represent the total energy to be applied to the specimen to reach liquefaction, thus is valid for any type of performed test. Obviously, when fully saturated tests are performed, no volumetric deformations will affect the sample during the cyclic deviatoric phase, resulting in  $E_{v,liq}=0$ . As a consequence, if the energy-based approach wants to be adopted to interpret the present tests, definition and calculation of  $E_{s,liq}$  only is needed. To this purpose,  $E_{s,liq}$  is defined as the sum of the areas of all the cycles in the  $\epsilon_s$ - $q$  plane until liquefaction is reached, where  $\epsilon_s$  is the deviatoric strain and  $q$  is the cyclic deviatoric stress.  $E_{s,liq}$  can be formally defined as follows, with regards to Figure A-9-8 stress-strain relationship (Mele et al. 2018b):

$$E_{s,liq} = \iint_D dq d\epsilon_s \quad \text{Equation A-11}$$

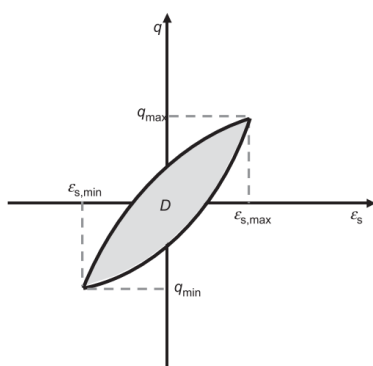


Figure A-9-8 Cycle in  $q$ - $\epsilon_s$  plane (Mele et al. 2018b)

Therefore, since by definition the  $E_{s,liq}$  represents the subtended area of stress-strain curve at each cycle, it is highly dependent on the applied CSR, thus strongly appropriate to face the present issue. Afterwards, such an energy-based approach has been adopted for the above reported tests results, by calculating the  $E_{s,liq}$  as a function of the stress-strain relationship until  $N_{liq,ea}$  is reached. Results are reported in Figure A-9-9.

Table A-5 Energy-based approach results

Equipment	Test	Relative density, $D_r$	$CSR_{sin}$	$N_{liq} r_u$	$N_{liq} \epsilon_a$	$E_{s,liq} \epsilon_a (kJ/m^3)$
Controlled Stress-Path Triaxial	ST2	43%	0,173	36	37	0,773
	ST3	42%	0,188	26	29	0,442
	ST6	37%	0,200	9	10,5	0,948
	ST7	34%	0,233	5	6,3	1,197
	ST8	40%	0,181	15	16	0,744
Cyclic Triaxial	TxS2	46%	0,279	1	1	1,638
	TxS3	47%	0,253	4	5	1,106
	TxS4	34%	0,164	21	21,5	0,822

The results can be well fitted, with a low scatter, by a unique curve, related to the cyclic resistance one (except for the ST3 test which lies relatively below in Figure A-9-9). Therefore, since the energy-based method is able to prescind from the numerical definition of the CSR (thus of the CRR for the cyclic resistance curve), the data interpretation carried out by means of the correcting factor  $k_{cyc}$  can be validated, since a good agreement of the experimental results is achieved with the energy-based approach itself.

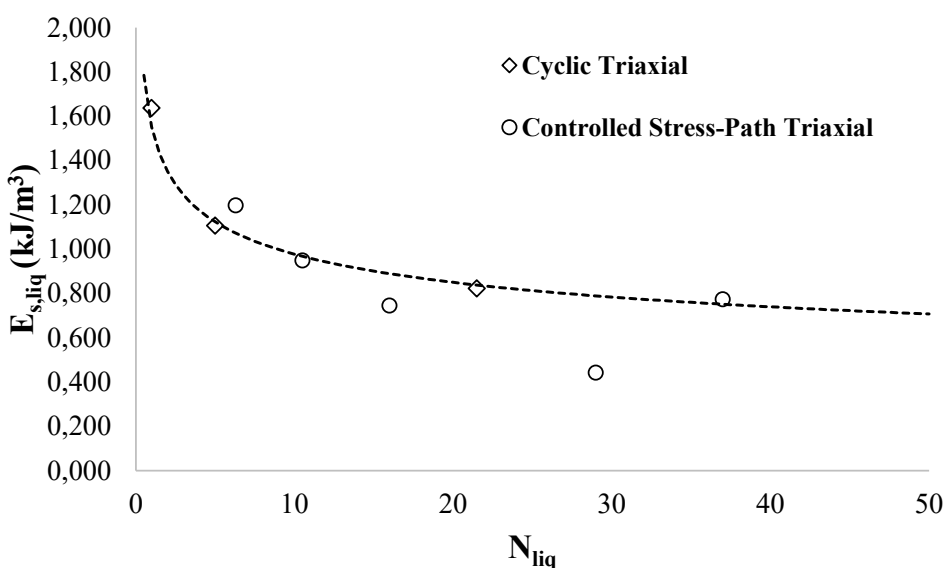


Figure A-9-9 Energy-based approach- Experimental results

As revealed in advance, after the triaxial tests additional cyclic simple shear tests have been performed- in the apparatus already shown in Figure A-9-1. The peculiarity of the performed tests is that fully saturated conditions are not tested physically, rather moist tamped specimens have been realized and sheared at a given confinement stress. The purpose of such experimentation is to evaluate the possibility of testing dry specimens- therefore reducing drastically the testing times- and successively correlate test results to the cyclic resistance curve for fully saturated conditions. The opportunity of testing dry specimens to assess fully saturated cyclic resistances is possible thanks to the imposition, during the shearing phase, of zero-volumetric strain.

Operatively, the testing procedure is reported in the following:

1. Specimen preparation by means of moist tamping technique, by using an initial water content avoiding any additional interlocking forces due to suction (by referring to soil-water characteristic curve, Figure 6-18);
2. Specimen assembly within the shear stress apparatus. Soil is assembled within steel rings (Figure A-9-1, right side), resulting in a  $k_0$  consolidation phase, carried out at  $\sigma'_v=50\text{ kPa}$ ;
3. Application of cyclic shear stresses by neglecting any vertical displacement, in order to impose  $\varepsilon_z=0$ . Since a  $k_0$  condition is initially ensured thanks to the presence of steel rings, it results  $\varepsilon_z=\varepsilon_v=0$ , in order to model fully saturated conditions.

With this procedure, fully saturated conditions can be theoretically achieved in short times. The experimental programme in the cyclic simple shear apparatus is reported in Table A-6, while tests results for strain criterion are showed in Figure A-9-10.

*Table A-6 Cyclic simple shear testing program*

Equipment	Test	Relative density, $D_r$	$\text{CSR}_{ss}$	$N_{\text{liq}} \varepsilon_a$
<i>Cyclic Simple Shear</i>	<b>CSS1</b>	39%	0,190	7
	<b>CSS2</b>	38%	0,150	27
	<b>CSS3</b>	41%	0,140	36,5
	<b>CSS4</b>	35%	0,198	3
	<b>CSS5</b>	31%	0,159	9,5
	<b>CSS6</b>	34%	0,149	13
	<b>CSS7</b>	35%	0,130	16

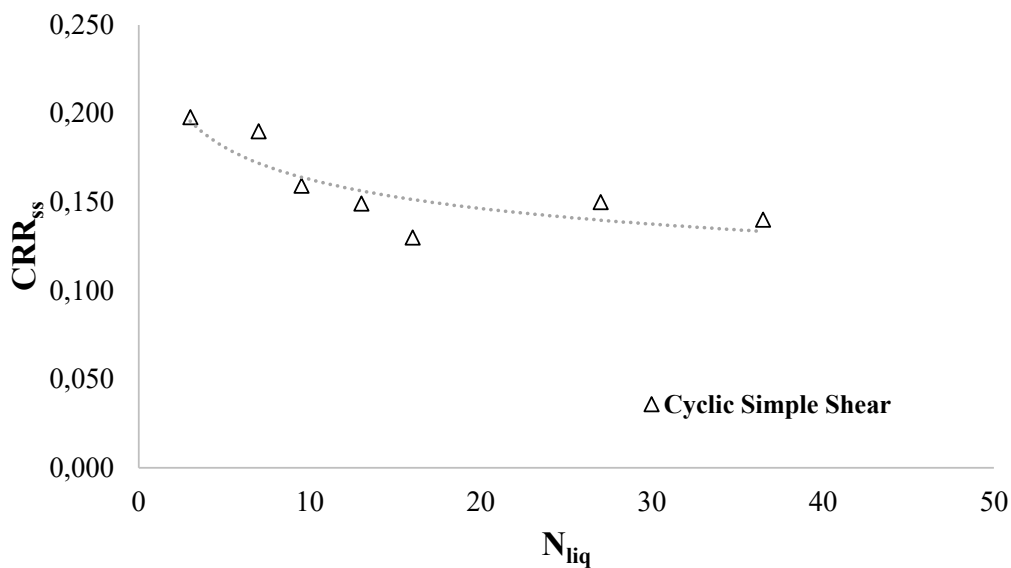


Figure A-9-10 Cyclic resistance curve for cyclic simple shear tests on moist tamped specimens (strain criterion)

In order to confirm the reliability of testing almost dry specimen for the definition of the fully saturated CRR of the soil, a comparison between cyclic simple shear and triaxial tests has been performed. Prior to the comparison, it has been necessary to modify  $CSR_{tx}$  values to simple shear stress conditions. To this purpose, the Castro's correlation (*Equation A-4* and *Equation A-5*) has been used by adopting a  $k_0=0.5$ , leading to a  $c_r=0.77$ . In addition, even for the cyclic simple shear tests, calculation of the energy needed to reach liquefaction has been carried out. The whole final data are then reported in Table A-7.

Table A-7 Final results of cyclic tests on Quartz sand

Equipment	Test	Relative density, $D_r$	$CSR_{ss}$	$N_{liq} \varepsilon_a$	$E_{s,liq} \varepsilon_a (\text{kJ/m}^3)$
<b>Controlled Stress-Path Triaxial</b>	<b>ST2</b>	43%	0,133	37	0,773
	<b>ST3</b>	42%	0,145	29	0,442
	<b>ST6</b>	37%	0,154	10,5	0,948
	<b>ST7</b>	34%	0,179	6,3	1,197
	<b>ST8</b>	40%	0,139	16	0,744
<b>Cyclic Triaxial</b>	<b>TxS2</b>	46%	0,215	1	1,638
	<b>TxS3</b>	47%	0,195	5	1,106
	<b>TxS4</b>	34%	0,126	21,5	0,822
<b>Cyclic Simple Shear</b>	<b>CSS1</b>	39%	0,190	7	1,078
	<b>CSS2</b>	38%	0,150	27	0,846
	<b>CSS3</b>	41%	0,140	36,5	0,923
	<b>CSS4</b>	35%	0,198	3	1,315
	<b>CSS5</b>	31%	0,159	9,5	1,092
	<b>CSS6</b>	34%	0,149	13	0,981
	<b>CSS7</b>	35%	0,130	16	0,810

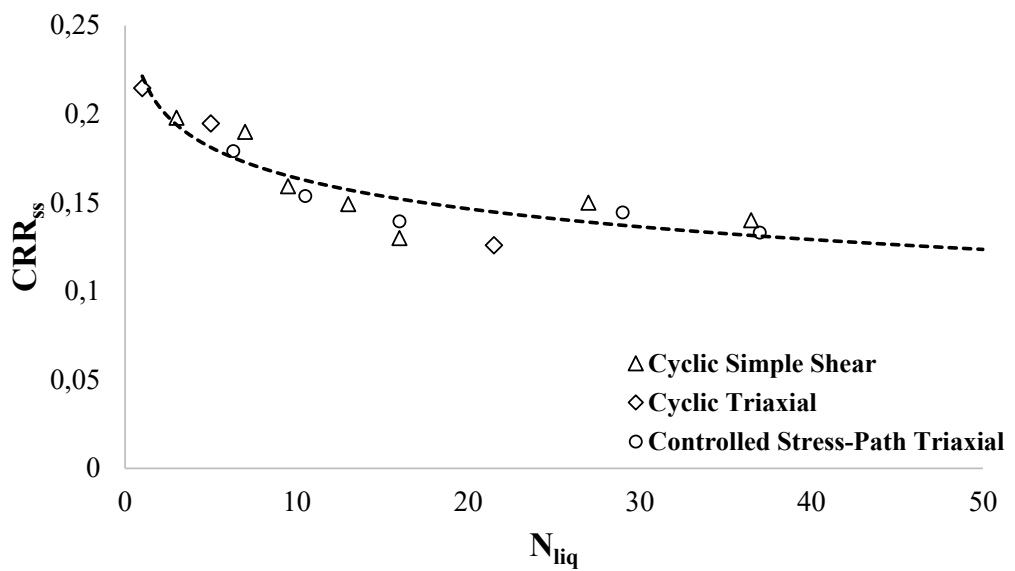


Figure A-9-11 Final cyclic resistance curve for quartz sand

In Figure A-9-11 final results are reported, showing a very good correlation between different types of performed tests. Finally, in Figure A-9-12, the energy-based method calculations are reported, demonstrating the consistency of the cyclic resistance results for all the tested equipments.

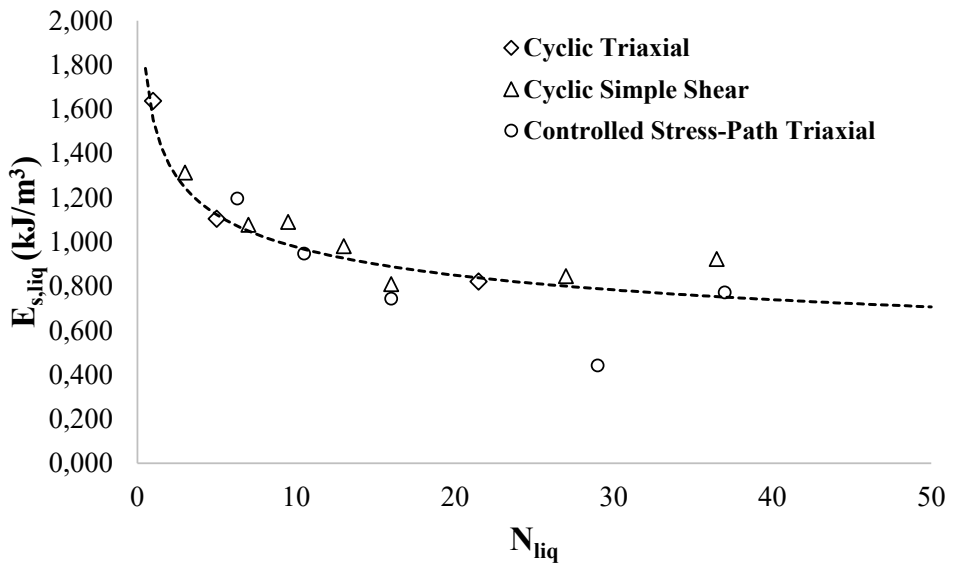


Figure A-9-12 Energy-based method results for the entire experimental program

In conclusion, the cyclic characterization of the tested soil has been carried out by means of different approaches. The cyclic resistance curve has been obtained taking into account the

differences of the applied CSR, in terms of shape- bi-linear vs. sinusoidal- regarding the triaxial tests. In addition, cyclic simple shear tests on moist tamped samples seem to be sufficiently able to model the cyclic behavior of fully saturated specimens, resulting in a lower spending-time of the performed tests. Finally, the energy-based approach, more reliable thanks to the availability of recent published research results, confirms the physical assumption on the data interpretation, regarding the dependency of the CRR from the applied stress ratio.